A COMBINED GAS-PHASE AND SURFACE REACTION MECHANISTIC MODEL OF DIESEL SURROGATE REFORMING FOR SOFC APPLICATION

by

RAJESH DAHYALAL PARMAR

A thesis submitted to the
Department of Chemical Engineering
in conformity with the requirements for
the degree of Doctor of Philosophy

Queen's University
Kingston, Ontario, Canada
April 2013

Abstract

This study presents a detailed gas-phase and surface kinetic model for n-tetradecane autothermal reforming to deconvolute the complex reaction network that provides the mechanistic understanding of reforming chemistry in a packed-bed reactor.

A thermodynamic analysis study for diesel reforming was performed to map the carbon formation boundary for various reforming processes. Through a Langmuir-Hinshelwood-Hougen-Watson (LHHW) type of kinetic model, which was derived using a simple mechanistic study, the need for a detailed kinetic study including both gas-phase reactions and surface reactions was identified.

Pt-CGO (Pt on Gd doped CeO_2) and Rh-pyrochlore catalysts were synthesized and characterized. In an accelerated test for reforming of commercial-diesel, Rh-pyrochlore catalyst showed stable performance for 24 hrs, whereas Pt-CGO catalyst deteriorated in 4 hrs. Minimum structural change in Rh-pyrochlore catalyst compared to Pt-CGO catalyst was observed using redox experiments. An experimental kinetic study with an inert silica bed provided clear evidence that the gas-phase reactions are important to the kinetics of hydrocarbon reforming.

“Reaction Mechanism Generator” (RMG) software was employed to generate a detailed gas-phase kinetic model containing nine thousand three hundred and forty-seven elementary reactions and four hundred and fifty-nine species. The model was validated against n-tetradecane ignition delay data, and inert bed autothermal reforming data. The RMG model was also extended to capture the high pressure and low temperature pyrolysis chemistry to predict pyrolysis experimental data. The reactor simulation using the RMG model identified the detailed chemistry of the reactions in the pre-catalytic zone. Gas-phase oxidation/pyrolysis converts the heavier hydrocarbons and oxygen in the pre-catalytic zone to lower molecular weight products prior to reaching the catalyst surface. The steam reforming reactions that are dominant on the surface of the catalyst primarily involve lower molecular weight oxidation/pyrolysis products.

A multi-component micro-kinetic model containing two hundred and seventy surface reactions and fifty-two adspecies was developed using a semi-empirical Unity Bond Index-Quadratic Exponential Potential (UBI-QEP) method. Transition State Theory estimates were used for elementary reactions up to C_3 species, and simple fragmentation reactions were assumed for higher hydrocarbon species. Model simulations indicated on the catalyst surface that hydrogen is initially produced by the water-gas-shift reaction and subsequently by steam reforming reactions. A major reaction path for ethylene formation from 1,3 butadiene in the post-catalytic zone of the reactor was also identified.

Co-Authorship

I hereby declare that I am the sole author of the thesis. Dr. Kunal Karan (supervisor) and Dr. Brant A. Peppley (co-supervisor) provided valuable technical input and editorial feedback and are co-authors of the manuscripts presented in this thesis.

Acknowledgements

I would like to extend my deepest gratitude to my supervisors, my family, and all those directly and indirectly associated with this thesis.

I would like to thank my parents, Bhagwatiben and Dahyalal Parmar, my mother-in-law, Manglaben Keshubhai Solanki, my wife, Nila, my son, Ronak and my brother and sisters for their unconditional love, emotional support throughout my graduate degree.

I am thankful to Dr. Kunal Karan (supervisor) for his support and patience throughout the thesis. This thesis could not have been accomplished without the additional support, continuous encouragement and leadership from Dr. Brant A. Peppley (co-supervisor). I am sincerely thankful to Dr. James McLellan for his guidance, suggestions, and help as and when required. Also, I would like to express my sincerest gratitude to my Ph.D. committee: Dr. Marten Ternan, Dr. J. Scott Parent, Dr. Gabriel Ciccarelli, Dr. James McLellan, Dr. Brant A. Peppley, Dr. Kunal Karan, and Dr. Colin MacDougall for valuable discussion and providing inputs in refining the thesis.

I am grateful to Dr. Dushyant Shekhawat and Dr. David Berry (National Energy Technology Laboratory, US DOE, WV, USA) for accepting my proposal to perform experimental studies at their facility. Discussions with Mr. Daniel Haynes and Mr. Mark Smith were extremely helpful for catalyst characterization and kinetic study experiments. Special thanks to Mr. Donald Floyd for his hard work, troubleshooting the experiments, and help with experimental studies. Dr. Dushyant Shekhawat is also the co-author of the manuscript Chapters – 5, 6, and 7.

I am sincerely thankful to Prof. William H. Green (Massachusetts Institute of Technology, Cambridge, USA) for accepting me to his facility to learn more about Reaction Mechanism Generator (RMG), for allowing MIT computational facility to perform calculations and guiding through the gas-phase kinetic model generation. I met wonderful colleague at MIT, Mr. Amrit Jalan, who deserve appreciation for all brainstorming, debugging exercise that helped me to gain more insight into the gas-phase kinetics of combustion, pyrolysis, and reforming. I am grateful to

the RMG development team, especially Prof. Richard H. West, for helpful discussions and help with using RMG. I also thank Prof. Jim Wallace and Dr. Charles Westbrook for useful discussions for gas-phase kinetic study. Mr. Amrit Jalan and Dr. William H. Green are the co-authors of the manuscript Chapter 6.

I wish to express my appreciation to Dr. Ashish Mhadeshwar (Sr. Research Engineer, Exxon Mobile) for his guidance through surface kinetic study.

I wish to thank all past and present students and researchers at Queens-RMC Fuel Cell Research Centre (FCRC) for making FCRC enjoyable and productive work place do to research.

I would also like to acknowledge the NSERC Solid Oxide Fuel Cell Canada Strategic Research Network for funding my visit to NETL and MIT.

Table of Contents

List of Figures

List of Tables

List of Symbols

Symbol	**Description**
Cp_g	Gas specific heat [j/mol·K]
Cp_p	Particle thermal conductivity [j/mol·K]
d_p	Diameter of particle [m]
d_t	Diameter of reactor [m]
g	Gravitational acceleration [m/s^2]
i	Number of reactions [-]
K_{bed}	Packed bed thermal conductivity without flow [W/m·K]
$K_{bed,flow}$	Thermal conductivity of packed bed with flow [W/m·K]
K_g	Gas-phase thermal conductivity [W/m·K]
K_{min}	Mineral thermal conductivity [W/m·K]
K_P	Quartz sand particle thermal conductivity [W/m·K]
K_{quartz}	Quartz particle thermal conductivity [W/m·K]
K_1	Thermal conductivity of quartz perpendicular to quartz optic axis [W/m·K]
K_2	Thermal conductivity of quartz parallel to quarts optic axis [W/m·K]
L	Length of reactor [m]
n	Number of species [-]
n_{wm}	Fluid fraction in series path of flow [-]
P	Pressure [Pa]
$P_{E,o}$	Molecular Peclet number [-]
$P_{E,r}$	Radial Peclet number [-]
$\dot{Q}$	Volumetric heat gain / loss [W/m^3]
r	Radial coordinate [m]
r_j	Rate of reaction [mol/s]
T	Temperature [K]
T_{bed}	Temperature at bed center (or at the center of the reactor) [K]
u_x^l	Interstitial velocity [m/s]
u_x^s	Superficial velocity [m/s]

x	Axial coordinate [m]
ΔH_r	Heat of reaction [j/mol·K]
θ	Volumetric content of quartz
ε	Porosity [-]
ρ_g	Density of gas-phase [kg/m^3]
μ	Molecular viscosity [Pa·s]
μ_{eff}	Effective turbulent viscosity [Pa·s]

Chapter 1

General Introduction

Commercialization of fuel cells depends not only on efficient and low cost design but also on the availability of hydrogen, either from a storage tank or from an on-board reforming unit processing hydrocarbon fuel. Although developed countries are investing in hydrogen energy, it is projected that the deployment of this infrastructure will take at least a couple of decades. Even in developed countries such as Canada, over 200,000 Canadians living in 300+ remote communities rely on diesel generators for producing electricity at costs that vary from $0.15 to $1.50 per kWh [1, 2]. The costs of diesel fuel, risks of fuel spill, local air quality, and long term sustainability are often cited as reasons for communities to look into alternative solutions [3]. In addition to diesel electricity production being relatively inefficient and expensive, it is also responsible for the emission of 1.2 million tons of greenhouse gases (GHG) annually in Canada alone [4]. With growing concern over efficient utilization of existing fuel supply, numerous alternatives have been proposed including: novel fuel additives, biofuel blends and improved design of combustion systems. Alternative methods of power generation, such as fuel cells, with minimal pollution and high conversion efficiency have attracted significant attention as possible solutions.

Power demand in passenger cars is constantly on the rise. Due to low storage capacities of conventional lead-acid batteries, use of modern electrical equipment in vehicles is fairly limited [5]. The practice to idling to power the electronic equipment of heavy diesel trucks used in military and commercial application has been identified as a major economic and environmental concern. In 2009, a report by Argonne National Laboratories estimated that long-haul trucks typically idle 6 hours per day, or 1,830 hours per year. However, actual practice varies, from idling 1-2 nights per week to hardly ever turning the engine off [6]. Trucks are typically kept running to heat and cool the cab and sleeper, keep the fuel warm in the winter, avoid cold starting, power electrical systems for refrigeration, lighting, computers and personal safety, and other electronic devices [7, 8]. With more than 680,000 trucks in the United States [9], each year about 20 million barrels of diesel fuel are consumed by idling long-haul trucks overnight. Truck emissions from idling total about 10 million tons of CO_2, 50,000 tons of nitrogen oxides, and 2,000 tons of particulate matter per year. Exhaust gases are known to cause severe environmental and health problems: nitrogen oxides are among causes of forest dieback and together with emitted hydrocarbons, are precursors of photo-oxidants, which give rise to photo-chemical smog; benzene and particulate matters are carcinogenic substances at high concentrations [10]. Van Den Berg [11] estimated the total electric demand of a parked commercial truck to be around 4.2 kW which is difficult to meet using batteries alone. Today, the generation of electric power from internal combustion engines limits the efficiency of conversion of fuel to electricity to values far below 20% [12]. The efficiency of truck diesel engines producing 4.2 kWe via the standard on-board alternator is only about 4 to 11% at idling [13].

Solid Oxide Fuel Cell (SOFC)-Diesel reforming technology is a promising technology that has potential to replace existing low efficiency and high polluting diesel generators/engines for low power, distributed power applications. Fuel cell systems coupled with an upstream diesel reformer have efficiencies in the 25-40% range [12] which makes them an attractive option. SOFC systems using conventional fuels for stationary and Auxiliary Power Unit (APU) applications have been projected as initial market penetration opportunities for fuel cells [14].

Use of fuel cells is expected to reduce emissions of air pollutants such as nitrogen oxides, carbon monoxide, volatile organic compounds and particulate matters. In addition CO_2 release will be lower because of higher efficiencies. Realizing the environmental benefits and efficiency gains, however, will require significant reduction in manufacturing costs and improvement in reliability such that commercialization is viable. A better understanding of process chemistry is essential to identifying better catalysts and optimizing the design of the diesel reformer. This is the main driving force behind the current effort performed under the umbrella of the NSERC strategic network SOFC Canada to get the mechanistic and kinetic understanding of diesel reforming for optimized APU design.

1.1 **Thesis Objectives**

The scientific aim of the present work was to gain insight into diesel autothermal reforming process by combining experimental work and mechanistic kinetic model development. To achieve the goal, following sub-theme targets were identified:

a. Perform thermodynamic analysis study to obtain the carbon formation boundary for diesel reforming at different operating conditions.
b. Test and characterize several commercial diesel reforming catalysts and select the catalyst for kinetic studies.
c. Carry out reaction kinetics experiments with and without catalyst in a packed bed reactor for model validation and to assess the importance of gas-phase kinetics.
d. Construct the gas-phase reactions kinetic model under autothermal reforming conditions using Reaction Mechanism Generator (RMG) and validate the model with literature data and experimental data from sub-theme c. Also, identify the major reaction pathways for different

species formation (especially ethylene which is the precursor to carbon formation) in the pre-catalytic zone.

e. Develop a surface micro-kinetic model using the semi-empirical unity bond index-quadratic exponential potential (UBI-QEP) approach for the gas-phase species reaching the catalyst surface and validate the model against experimental data.

f. Simulate the packed bed reactor using combined gas-phase and surface reaction kinetic models and get insight into major surface reactions for hydrogen production and assess the importance of gas-phase chemistry in the post-catalytic zone.

1.2 **Thesis Structure**

The structure of this thesis is shown in Figure 1.1. Chapter-1 describes the need for better technology for efficient utilization of fossil energy. Chapter 2 discusses in detail current research being done in reforming technology development and identifies the current research needs. Thermodynamic analysis of diesel reforming over a range of operating conditions is given in Chapter 3 and defines the theoretical no carbon formation zone to be used in the experimental kinetic study discussed in Chapter 5. A generalized LHHW kinetic model developed in Chapter 4 reveals the need for the detailed gas-phase and surface kinetic study that will be discussed in Chapter 6 and Chapter 7, respectively. Chapter 5 presents the catalyst characterization, long term stability tests, and kinetic data from a test reactor, with and without catalyst, that are useful for the gas-phase kinetic model validation in Chapter 6 and surface kinetic model validation in Chapter 7. Chapter 6 describes the experimental packed bed reactor design, generation of the gas-phase kinetic model in autothermal reforming (ATR) conditions using Reaction Mechanism Generator (RMG), validating the model in combustion, pyrolysis and ATR regions, and different reaction paths for major products formation in the pre-catalytic zone. Chapter 7 presents a multi-component surface micro-kinetic model. The gas-phase kinetic model discussed in Chapter 6 along with surface kinetic model validated against experimental data at various operating conditions. The importance of gas-phase reactions in the post-catalytic zone is also identified. Chapter 8 gives overall summary, conclusion and contribution of the present work with recommendations for future study.

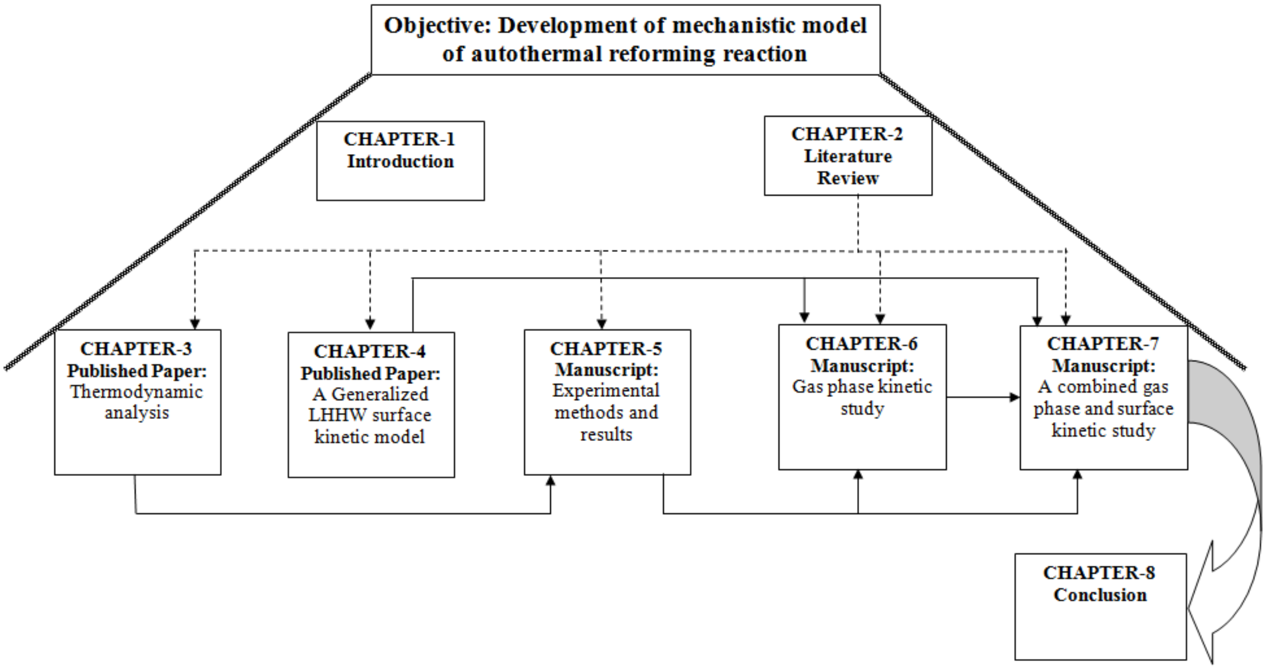

Figure 1.1: Framework of thesis.

References

[1] S. Henderson, Renewable energy and off-gird housing in the Yukon - Baseline report, Canada, 2005.

[2] H. Ibrahim, R. Younès, A. Ilinca, D. Ramdenee, M. Dimitrova, J. Perron, M. Adegnon, D. Boulay, C. Arbez, Potential of a Hybrid Wind-Diesel-Compressed air system for Nordic Remote Canadian Areas, Energy Procedia, 6 (2011) 795-804.

[3] T.M. Weis, A. Ilinca, J.P. Pinard, Stakeholders' perspectives on barriers to remote wind–diesel power plants in Canada, Energy Policy, 36 (2008) 1611-1621.

[4] H. Ibrahim, R. Younès, A. Ilinca, M. Dimitrova, J. Perron, Study and design of a hybrid wind-diesel-compressed air energy storage system for remote areas, Applied Energy, 87 (2010) 1749-1762.

[5] J. Marie-Francoise, H. Gualous, R. Outbib, A. Berthon, 42V Power Net with supercapacitor and battery for automotive applications, Journal of Power Sources, 143 (2005) 275-283.

[6] Reducing Vehicle Idling, Argonne National Laboratory: Transportation Technology R&D Center, http://www.transportation.anl.gov/engines/idling.html, Accessed - 25-Oct-2008.

[7] C.J. Brodrick, T.E. Lipman, M. Farshchi, N.P. Lutsey, H.A. Dwyer, D. Sperling, S.W. Gouse, D.B. Harris, F.G. King, Evaluation of fuel cell auxiliary power units for heavy-duty diesel trucks, Transportation Research Part D: Transport and Environment, 7 (2002) 303-315.

[8] S. Jain, H.Y. Chen, J. Schwank, Techno-economic analysis of fuel cell auxiliary power units as alternative to idling, Journal of Power Sources, 160 (2006) 474-484.

[9] H.C. Frey, P.Y. Kuo, C. Villa, Effects of Idle Reduction Technologies on Real World Fuel Use and Exhaust Emissions of Idling Long-Haul Trucks, Environmental Science & Technology, 43 (2009) 6875-6881.

[10] A. Cutillo, S. Specchia, M. Antonini, G. Saracco, V. Specchia, Diesel fuel processor for PEM fuel cells: Two possible alternatives (ATR versus SR), Journal of Power Sources, 154 (2006) 379-385.

[11] A.J. Van den Berg, Truckstop electrification: Reducing CO2 emissions from mobile sources while they are stationary, Energy Conversion and Management, 37 (1996) 879-884.

[12] A. Lindermeir, S. Kah, S. Kavurucu, M. Mühlner, On-board diesel fuel processing for an SOFC–APU—Technical challenges for catalysis and reactor design, Applied Catalysis B: Environmental, 70 (2007) 488-497.

[13] C.J. Brodrick, H.A. Dwyer, M. Farshchi, D.B. Harris, F.G. King Jr, Effects of engine speed and accessory load on idling emissions from heavy-duty diesel truck engines, Journal of the Air & Waste Management Association, 52 (2002) 1026-1031.

[14] M.C. Williams, J.P. Strakey, W.A. Surdoval, The US department of energy, office of fossil energy stationary fuel cell program, Journal of Power Sources, 143 (2005) 191-196.

Chapter 2

Literature Review

The reforming of conventional liquid hydrocarbon fuels such as diesel and gasoline is facing a number of challenges that are hindering the commercialization of this technology in spite of high volumetric and gravimetric hydrogen density and a well-established delivery infrastructure. Various designs have been proposed and tested for diesel reforming by various industries and research institutes such as Eltron Research and Development Inc. (USA) [1], InnovaTek Inc. (USA) [2], PowerCell in collaboration with Volvo Technology Corporation and KTH – Royal Institute of Technology (Sweden) [3, 4], Webasto AG (Germany) [5], Delphi Automotive System (USA) [6], Precision Combustion Inc. (USA) [7], Institute für Mikrotechnik Mainz GmbH[8], and Forschungszentrum Jülich GmbH (Germany) [9, 10].

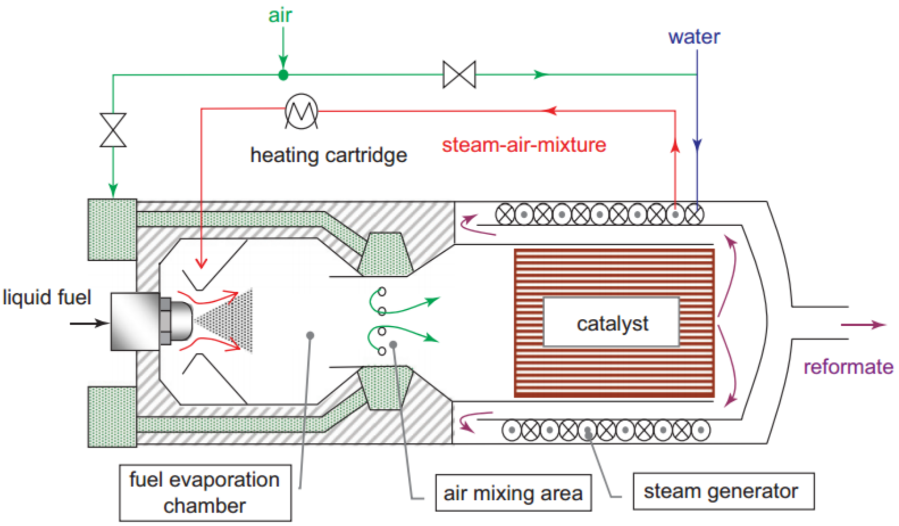

Figure 2.1: Fuel reformer design by Forschungszentrum Jülich GmbH (Germany) [9].

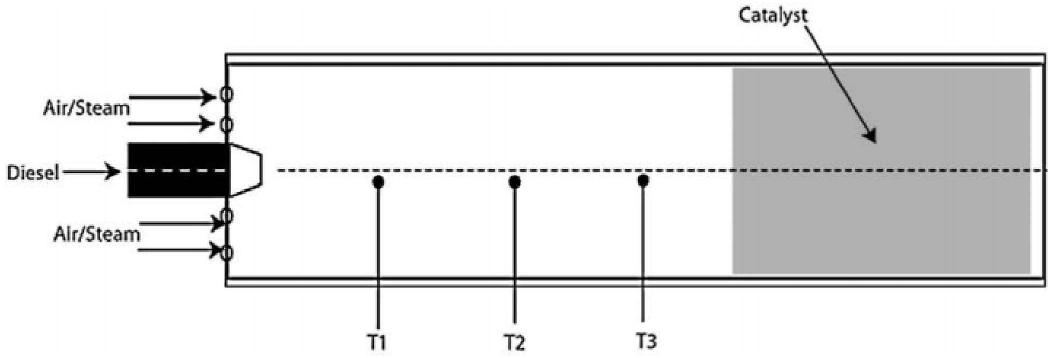

Figure 2.2: Fuel reformer design by PowerCell (Sweden) [3].

The reformer design by Forschungszentrum Jülich GmbH and by PowerCell is shown in Figures 2.1 and 2.2 respectively. In any reformer design, the basic concept is same. The fuel is atomized and mixed with other reactants such as air and/or steam in a mixing zone before entering the catalyst zone. The evaporated fuel mixes with the other reactants and the temperature is increased to the reaction temperature before the homogeneously mixed reactants reach the catalyst surface. The catalyst zone can be a packed bed reactor, a monolith or a micro-channel reactor coated with an active metal dispersed or substituted in the support structure which must be highly active and stable for diesel reforming. Apart from system design issues for energy integration, three core technical issues for diesel reforming are: (a) efficient homogeneous mixing of reactants in the mixing zone, (b) controlling gas-phase reactions in the mixing zone and in the hot zone after the catalyst that is responsible for ethylene generation which is precursor to coke formation, (c) designing a stable, highly active diesel reforming catalyst that is sulfur poisoning-resistant, carbon tolerant and capable of high hydrogen yields. The technical targets of the U.S. Department of Energy (US-DOE) requires a durability of 5,000 hrs [11].

Gas-phase reactions can have significant impact on reformer performance. Gas-phase chemistry in the upstream mixing region is often cited as a major source of ethylene, a precursor for carbonaceous deposits [12-16]. Gas-phase reactions also contribute to catalytic partial oxidation of light hydrocarbons in short contact time millisecond reactors [17-19]. However, there are limited studies directed towards the understanding of combined gas-phase reactions and surface reactions at reforming conditions that equally favour gas-phase reactions. An optimal reformer should provide homogeneous mixing of diesel with steam and air, and sufficiently high temperatures before the gas-phase products reach the catalyst surface. Many mixing zone designs have been proposed by various groups using both experimental and Computational Fluid Dynamic (CFD) studies of mixing of reactants in diesel and gasoline reforming reactors [3, 8, 10, 16, 20]. Although there are continuous improvements in diesel reformer designs based on CFD simulations, the understanding and incorporation of gas-phase kinetics in the mixing region upstream of the catalyst zone in these models has been very limited. Recently, Dean and co-workers pointed out the importance of modeling the upstream mixing region using n-hexane and n-dodecane as diesel surrogates [21]. They obtained a kinetic model based on combustion modeling work of Westbrook and co-workers at the Lawrence Livermore National Laboratory (LLNL) [22]. It should be noted that these models were used to predict the gas-phase concentrations and temperature profiles at high equivalence ratios (equivalence ratio is defined as the ratio of the fuel-to-oxidizer ratio to the stoichiometric fuel-to-oxidizer ratio) where their validity is unclear. They proposed that the mixture must reach the catalyst surface in less than 0.1 sec to avoid formation of troublesome quantities of ethylene (1000 ppm) assuming the reactants are perfectly mixed at 800 K. In a related study, Deutschmann and co-workers used kinetic models from the literature for gas-phase partial oxidation of iso-octane [23, 24]. They used a 10 mm heat shield before and after the catalyst zone and assumed that no isooctane conversion occurs before the heat-shield (*i.e.*, non-catalytic monolith). They concluded that the homogeneous and heterogeneous chemistry was an important element in modeling CPOX (Catalytic Partial Oxidation). Recently, Deutschmann and coworkers have shown that understanding the homogeneous gas-phase chemistry is very important for isooctane reforming as it leads to coke precursor (*i.e.*, olefins, particularly ethylene and propylene) formation and subsequently coke formation down-steam of the reactor [25]. However, most alkane chemistry models in the literature are not developed specifically for autothermal reforming (ATR) conditions.

A variety of approaches for modeling surface kinetics for higher hydrocarbon (*i.e.*, diesel or gasoline surrogate) reforming have been employed. These models usually do not consider the co-occurrence of gas-phase reactions or occurrence of the gas-phase reaction in the pre- and post-catalytic zones. One of the first approaches used was assuming an overall reaction for system design purposes and fitting a power law type equation to experimental data [26-31]. Later studies adapted the Xu and Froment's [32] Langmuir-Hinshelwood-Hougen-Watson (LHHW) type methane reforming kinetic model for higher hydrocarbon reforming and estimated the parameters of the model by fitting to experimental data [33-35]. A third approach used was to make various reaction schemes based on experimental observations or surface science studies and assume the rate determining step and most abundant surface species to determine the LHHW or Eley-Rideal (ER) kinetic model. Rostrup-Neilsen [36, 37] proposed one of the earliest such generalized mechanisms for higher hydrocarbon steam reforming, which was later used for modeling heptane reformers by various groups [38, 39]. Idem and co-workers [40-42] used similar approach in which they assumed various reaction mechanisms and rate determining steps to propose LHHW and ER models for isooctane and synthetic diesel partial oxidation. The model that gave lowest

AAD (Average Absolute Deviation) was then selected to represent the partial oxidation. Praharso *et al.* [43] and Huang *et al.* [44] used LHHW models to fit experimental data to the steam reforming of isooctane and partial oxidation of heavy hydrocarbons, respectively. In 2009, Deutschmann and co-workers studied the kinetics of hexadecane steam reforming in a micro-channel coated with Rh/CeO$_2$ catalyst [45]. They used an elementary reaction kinetic model based on C$_1$ mechanism that was developed for Rh/Al$_2$O$_3$ catalyst, and added a global reaction for dissociative adsorption of hexadecane over the catalyst surface. The proposed micro-kinetic surface reaction mechanism assumed no gas-phase reactions and predicted the outlet composition very well qualitatively. Using similar approach they also proposed the mechanism for ethane, propane, and butane reforming on Rh catalsyst [46]. Using the Hickman and Schmidt's[47] methane oxidation mechanism, Rickenbach *et al.*[48] added more parameters (*i.e.*, reactions), replaced methane adsorption step with butane adsorption, and proposed a simple 23 step mechanism for butane reforming. All of the work discussed so far assumed no gas-phase reactions and proposed the surface kinetic mechanism for heavy hydrocarbons. As discussed before, Deutschmann and co-workers used the available kinetic models from literatures for gas-phase reactions and modeled the heterogeneous partial oxidation of iso-octane by using a detailed surface reaction mechanism for partial oxidation of C$_1$-C$_3$ species coupled with lumped reactions for adsorption of iso-octane [23, 24] . They concluded that the homogeneous gas-phase chemistry is very important and there is need to have more detailed model for both gas-phase reactions and surface reactions. Dorazio *et al.* [49] proposed a gas-phase mechanistic study model for n-tetradecane reforming on Pt/Al$_2$O$_3$ catalyst. The proposed mechanism could qualitatively capture some of the behavior of the process but failed to quantitatively predict the experimental data.

Several experimental studies on catalysts have been reported for generating hydrogen from gasoline, diesel fuel and its surrogates [11, 28, 50-52]. Based on progress made so far, no non-noble metal catalysts have shown long term activity and stability for heavy hydrocarbon reforming. Platinum group metals such as Pt and Rh are found to be an excellent candidate for heavy hydrocarbon reforming. Krumpelt and co-workers at Argonne National Laboratory (ANL) developed Pt on doped ceria catalyst that gave promising results for autothermal reforming of isooctane for 47 days [53, 54]. Based on ANL's study, Bae and co-workers used 0.5 wt% Pt – on 20 mol% Gd doped ceria (CGO) for gasoline and diesel autothermal reforming [15, 55]. They observed that homogeneous mixing of the reactants lead to long term stability as generation of carbon precursor (*i.e.*, ethylene) was suppressed [16]. Also Pt was reported to show better performance over Rh and Ru when CGO was used. Later they recommended to use post reforming stage (3 wt% Ru/CGO) to remove light hydrocarbons (over C_1) to get stable operation for synthetic diesel reforming [56, 57]. Schmidt and coworkers used Rh-α-Alumina coated monoliths for n-decane, n-hexadecane, JP-8, and isooctane autothermal reforming [13]. However, they observed carbon, ethylene and propylene due to gas-phase cracking. Roychoudhary and coworkers used Pt on La-Al_2O_3 and Rh on Ce-Zr microlith short-contact time reactor for isooctane autothermal reforming [58]. Later they used their proprietary catalyst for 50 hr autothermal reforming of JP-8 fuel. The catalyst activity was found to decrease initially and the performance was recovered when the catalyst was exposed to air after 45 hrs [7]. Kolb and coworkers reported declining of catalytic activity for iso-octane autothermal reforming in 1wt% Rh/Al_2O_3 coated micro-structured reactor [59]. The activity recovered to initial level after short oxidation. Thormann *et al.* [60, 61] reported 15 hr stable operation for steam reforming of diesel surrogate (hexadecane) in microchannel reactor coated with Rh/CeO_2. They observed that the activity declined at 645 °C, but remained constant at 700 °C. Pettersson and coworkers used two layers of monometallic Rh and bimetallic (Rh-Pt) washcoats (*i.e.*, Ce and La doped alumina) for diesel autothermal reforming [62]. In their XPS analysis, they observed lower amount of Rh/Al, Pt/Al and La/Al ratio at the entrance of reactor possibly due to oxidation reactions at the entrance of the catalyst that causes sintering. The present literature study shows that until now only Pt/CGO catalyst has given a better performance for long term operation of diesel reformer. However, none of the work presented so far identified the effect of reducing and oxidizing environment on the catalyst activity. Sehested [63] reported four major challenges for reforming catalysts (Figure 2.3). These challenges are strongly interconnected. Apart from carbon formation and sulfur poisoning, the sintering of the catalyst is the major concern, which particularly happens in redox environment. Desirable catalysts are those whose structure as well as properties do not change or change only minimally with time, particularly at high operating temperatures and during redox cycles.

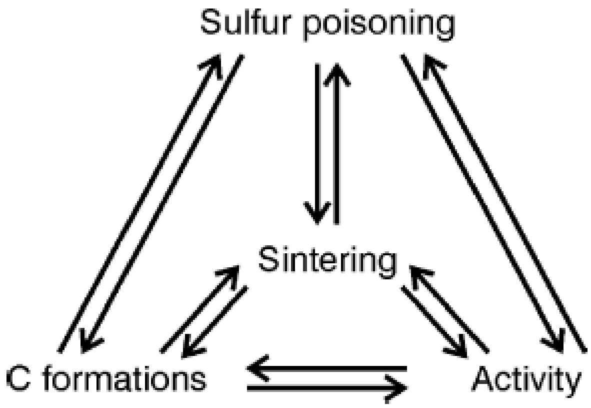

Figure 2.3: Four major challenges for reforming catalyst [63].

Summary

Literature review on the kinetics of heavy hydrocarbon reforming revealed that there are limited studies that consider gas-phase reaction and that no validated gas-phase reaction model exist for high equivalence ratio (*i.e.,* low O_2/C ratio) for larger alkane molecules (or diesel surrogates). High equivalence ratio is pertinent to autothermal reforming whereas low equivalence ratio is relevant to combustion processes. This review has also found that elementary reaction based surface kinetic model for diesel reforming is not available. For better design of the reformer and the catalyst, understanding the process gas-phase and surface chemistry in terms of the elementary reactions is important. The development of micro-kinetic models to predict the chemistry and understand the reaction pathways leading to hydrogen production and ethylene formation, which is a precursor to coke formation, is also crucial for improved reformer models. Literature studies on fossil liquid fuel reforming catalysts suggest that there is need to identify the suitable catalyst and test it under redox environment for stable performance.

References

[1] M. Mundschau, C.G. Burk, D.A. Gribble, Diesel fuel reforming using catalytic membrane reactors, Catalysis Today, 136 (2008) 190-205.

[2] Q. Ming, T. Healey, L. Allen, P. Irving, Steam reforming of hydrocarbon fuels, Catalysis Today, 77 (2002) 51-64.

[3] B. Lindström, J. Karlsson, P. Ekdunge, L. De Verdier, B. Häggendal, J. Dawody, M. Nilsson, L. Pettersson, Diesel fuel reformer for automotive fuel cell applications, International Journal of Hydrogen Energy, 34 (2009) 3367-3381.

[4] X. Karatzas, M. Nilsson, J. Dawody, B. Lindström, L.J. Pettersson, Characterization and optimization of an autothermal diesel and jet fuel reformer for 5kWe mobile fuel cell applications, Chemical Engineering Journal, 156 (2010) 366-379.

[5] A. Lindermeir, S. Kah, S. Kavurucu, M. Mühlner, On-board diesel fuel processing for an SOFC–APU—Technical challenges for catalysis and reactor design, Applied Catalysis B: Environmental, 70 (2007) 488-497.

[6] J. Zizelman, S. Shaffer, S. Mukerjee, Solid oxide fuel cell auxiliary power unit–a development update, SAE paper, (2002) 0411.

[7] S. Roychoudhury, M. Lyubovsky, D. Walsh, D. Chu, E. Kallio, Design and development of a diesel and JP-8 logistic fuel processor, Journal of Power Sources, 160 (2006) 510-513.

[8] M. O'Connell, G. Kolb, K. Schelhaas, J. Schuerer, D. Tiemann, A. Ziogas, V. Hessel, Development and evaluation of a microreactor for the reforming of diesel fuel in the kW range, International Journal of Hydrogen Energy, 34 (2009) 6290-6303.

[9] J. Pasel, J. Meißner, Z. Porš, R. Samsun, A. Tschauder, R. Peters, Autothermal reforming of commercial Jet A-1 on a scale, International Journal of Hydrogen Energy, 32 (2007) 4847-4858.

[10] Z. Porš, J. Pasel, A. Tschauder, R. Dahl, R. Peters, D. Stolten, Optimised mixture formation for diesel fuel processing, Fuel Cells, 8 (2008) 129-137.

[11] G. Kolb, Fuel processing: for fuel cells, Wiley-VCH, Weinheim, 2008.

[12] S. Yoon, I. Kang, J. Bae, Suppression of ethylene-induced carbon deposition in diesel autothermal reforming, International Journal of Hydrogen Energy, 34 (2009) 1844-1851.

[13] B. Dreyer, I. Lee, J. Krummenacher, L. Schmidt, Autothermal steam reforming of higher hydrocarbons: n-Decane, n-hexadecane, and JP-8, Applied Catalysis A: General, 307 (2006) 184-194.

[14] S. Yoon, I. Kang, J. Bae, Effects of ethylene on carbon formation in diesel autothermal reforming, International Journal of Hydrogen Energy, 33 (2008) 4780-4788.

[15] I. Kang, J. Bae, S. Yoon, Y. Yoo, Performance improvement of diesel autothermal reformer by applying ultrasonic injector for effective fuel delivery, Journal of Power Sources, 172 (2007) 845-852.

[16] I. Kang, S. Yoon, G. Bae, J.H. Kim, J. Bae, D. Lee, Y. Song, The micro-reactor testing of catalysts and fuel delivery apparatuses for diesel autothermal reforming, Catalysis Today, 136 (2008) 249-257.

[17] D.K. Zerkle, M.D. Allendorf, M. Wolf, O. Deutschmann, Understanding homogeneous and heterogeneous contributions to the platinum-catalyzed partial oxidation of ethane in a short-contact-time reactor, Journal of Catalysis, 196 (2000) 18-39.

[18] A. Beretta, L. Piovesan, P. Forzatti, An investigation on the role of a Pt/Al2O3 catalyst in the oxidative dehydrogenation of propane in annular reactor, Journal of Catalysis, 184 (1999) 455-468.

[19] A. Beretta, E. Ranzi, P. Forzatti, Oxidative dehydrogenation of light paraffins in novel short contact time reactors. Experimental and theoretical investigation, Chemical Engineering Science, 56 (2001) 779-787.

[20] G. Kolb, T. Baier, J. Schürer, D. Tiemann, A. Ziogas, S. Specchia, C. Galletti, G. Germani, Y. Schuurman, A micro-structured 5kW complete fuel processor for iso-octane as hydrogen supply system for mobile auxiliary power units: Part II—Development of water–gas shift and preferential oxidation catalysts reactors and assembly of the fuel processor, Chemical Engineering Journal, 138 (2008) 474-489.

[21] I. Kang, H.H. Carstensen, A.M. Dean, Impact of gas-phase reactions in the mixing region upstream of a diesel fuel autothermal reformer, Journal of Power Sources, 196 (2011) 2020-2026.

[22] C.K. Westbrook, W.J. Pitz, O. Herbinet, H.J. Curran, E.J. Silke, A comprehensive detailed chemical kinetic reaction mechanism for combustion of n-alkane hydrocarbons from n-octane to n-hexadecane, Combustion and Flame, 156 (2009) 181-199.

[23] M. Hartmann, L. Maier, H. Minh, O. Deutschmann, Catalytic partial oxidation of iso-octane over rhodium catalysts: An experimental, modeling, and simulation study, Combustion and Flame, 157 (2010) 1771-1782.

[24] L. Maier, M. Hartmann, S. Tischer, O. Deutschmann, Interaction of heterogeneous and homogeneous kinetics with mass and heat transfer in catalytic reforming of logistic fuels, Combustion and Flame, 158 (2011) 796-808.

[25] T. Kaltschmitt, L. Maier, M. Hartmann, C. Hauck, O. Deutschmann, Influence of gas-phase reactions on catalytic reforming of isooctane, Proceedings of the Combustion Institute, 33 (2011) 3177-3183.

[26] T. Phillips, J. Mulhall, G. Turner, The kinetics and mechanism of the reaction between steam and hydrocarbons over nickel catalysts in the temperature range 350–500° C, part 1, Journal of Catalysis, 15 (1969) 233-244.

[27] K. Sjostrom, Steam Reforming of n-Heptane at Low Concentration for Hydrogen Injection into Internal Combustion Engines, Industrial & Engineering Chemistry Process Design and Development, 19 (1980) 148-153.

[28] D. Shekhawat, D.A. Berry, T.H. Gardner, J.J. Spivey, Catalytic reforming of liquid hydrocarbon fuels for fuel cell applications, Catalysis, 19 (2006) 184-254.

[29] A.B. Shigarov, V.V. Kireenkov, V.A. Kuzmin, N.A. Kuzin, V.A. Kirillov, Autothermal reforming of diesel fuel in a structured porous metal catalyst: Both kinetically and transport controlled reaction, Catalysis Today, 144 (2009) 341-349.

[30] D. Creaser, X. Karatzas, B. Lundberg, L.J. Pettersson, J. Dawody, Modeling study of 5 kWe-scale autothermal diesel fuel reformer, Applied Catalysis A: General, 404 (2011) 129-140.

[31] F. Gökaliler, Z.I. Önsan, A.E. Aksoylu, Power-law type rate equation for propane ATR over Pt–Ni/Al2O3 catalyst, International Journal of Hydrogen Energy, 37 (2012) 10425-10429.

[32] J. Xu, G.F. Froment, Methane steam reforming, methanation and water-gas shift: I. Intrinsic kinetics, AIChE Journal, 35 (1989) 88-96.

[33] M. Pacheco, J. Sira, J. Kopasz, Reaction kinetics and reactor modeling for fuel processing of liquid hydrocarbons to produce hydrogen: isooctane reforming, Applied Catalysis A: General, 250 (2003) 161-175.

[34] J.R. Lattner, M.P. Harold, Comparison of conventional and membrane reactor fuel processors for hydrocarbon-based PEM fuel cell systems, International Journal of Hydrogen Energy, 29 (2004) 393-417.

[35] L. Shi, D.J. Bayless, M.E. Prudich, A CFD model of autothermal reforming, International Journal of Hydrogen Energy, 34 (2009) 7666-7675.

[36] J.R. Rostrup-Nielsen, Activity of nickel catalysts for steam reforming of hydrocarbons, Journal of Catalysis, 31 (1973) 173-199.

[37] J.R. Rostrup-Nielsen, Catalytic steam reforming, Catalysis, Science and Technology, 5 (1984) 1-117.

[38] Z. Chen, Y. Yan, S.S.E.H. Elnashaie, Hydrogen production and carbon formation during the steam reformer of heptane in a novel circulating fluidized bed membrane reformer, Industrial & Engineering Chemistry Research, 43 (2004) 1323-1333.

[39] C.Y. Nah, S. Palanki, Analysis of heptane autothermal reformer to generate hydrogen for fuel cell applications, International Journal of Hydrogen Energy, 34 (2009) 8566-8573.

[40] H.H. Ibrahim, R.O. Idem, Kinetic studies of the partial oxidation of isooctane for hydrogen production over a nickel–alumina catalyst, Chemical Engineering Science, 61 (2006) 5912-5918.

[41] H.H. Ibrahim, R.O. Idem, Kinetic studies of the partial oxidation of gasoline (POXG) over a Ni-CeO2 catalyst in a fixed-bed flow reactor, Chemical Engineering Science, 62 (2007) 6582-6594.

[42] M.F.A. Khan, A. Khan, H. Ibrahim, R. Idem, Kinetic Study of the Catalytic Partial Oxidation of Synthetic Diesel over 5 wt % $Ni/Ce_{0.5}Zr_{0.33}Ca_{0.085}Y_{0.085}O_{2-\delta}$ Catalyst for Hydrogen Production, Energy & Fuels, 26 (2012) 5421-5429.

[43] A.A.A. Praharso, D. Trimm, N. Cant, Kinetic study of iso-octane steam reforming over a nickel-based catalyst, Chemical Engineering Journal, 99 (2004) 131-136.

[44] H. Huang, Z. Wang, H. Liu, H. Sun, Y. Wei, X. Zhou, A kinetic model for analyzing partial oxidation reforming of heavy hydrocarbon over a novel self-sustained electrochemical promotion catalyst, International Journal of Hydrogen Energy, 37 (2012) 15125-15134.

[45] J. Thormann, L. Maier, P. Pfeifer, U. Kunz, O. Deutschmann, K. Schubert, Steam reforming of hexadecane over a Rh/CeO_2 catalyst in microchannels: Experimental and numerical investigation, International Journal of Hydrogen Energy, 34 (2009) 5108-5120.

[46] B.T. Schädel, M. Duisberg, O. Deutschmann, Steam reforming of methane, ethane, propane, butane, and natural gas over a rhodium-based catalyst, Catalysis Today, 142 (2009) 42-51.

[47] D. Hickman, L. Schmidt, Steps in CH4 oxidation on Pt and Rh surfaces: High temperature reactor simulations, AIChE Journal, 39 (1993) 1164-1177.

[48] J.V. Rickenbach, M. Nabavi, I. Zinovik, N. Hotz, D. Poulikakos, A detailed surface reaction model for syngas production from butane over Rhodium catalyst, International Journal of Hydrogen Energy, 36 (2011) 12238-12248.

[49] L. Dorazio, M.J. Castaldi, Autothermal reforming of tetradecane (C14H30): A mechanistic approach, Catalysis Today, 136 (2008) 273-280.

[50] D. Shekhawat, D.A. Berry, D.J. Haynes, J.J. Spivey, Fuel constituent effects on fuel reforming properties for fuel cell applications, Fuel, 88 (2009) 817-825.

[51] D. Shekhawat, J.J. Spivey, D. Berry, Fuel Cells: Technologies for Fuel Processing, Elsevier Science, Oxford, 2011.

[52] R.M. Navarro Yerga, M.C. Álvarez-Galván, N. Mota, J.A. Villoria de la Mano, S.M. Al-Zahrani, J.L.G. Fierro, Catalysts for hydrogen production from heavy hydrocarbons, ChemCatChem, 3 (2011) 440-457.

[53] M. Krumpelt, R. Wilkenhoener, D.J. Carter, J.M. Bae, J.P. Kopasz, T. Krause, S. Ahmed, Catalytic autothermal reforming, US DOE Annual Progress Report, 2000.

[54] M. Krumpelt, T. Krause, D.J. Carter, J.M. Mawdsley, J.M. Bae, S. Ahmed, C. Rossignol, Catalytic autothermal reforming, US DOE Annual Progress Report, 2001.

[55] I. Kang, J. Bae, G. Bae, Performance comparison of autothermal reforming for liquid hydrocarbons, gasoline and diesel for fuel cell applications, Journal of Power Sources, 163 (2006) 538-546.

[56] S. Yoon, J. Bae, A diesel fuel processor for stable operation of solid oxide fuel cells system: I. Introduction to post-reforming for the diesel fuel processor, Catalysis Today, 156 (2010) 49-57.

[57] S. Yoon, J. Bae, S. Lee, T.V. Pham, S.P. Katikaneni, A diesel fuel processor for stable operation of solid oxide fuel cells system: II. Integrated diesel fuel processor for the operation of solid oxide fuel cells, International Journal of Hydrogen Energy, 37 (2012) 9228-9236.

[58] S. Roychoudhury, M. Castaldi, M. Lyubovsky, R. LaPierre, S. Ahmed, Microlith catalytic reactors for reforming iso-octane-based fuels into hydrogen, Journal of Power Sources, 152 (2005) 75-86.

[59] G. Kolb, T. Baier, J. Schürer, D. Tiemann, A. Ziogas, E. Hermann, P. Alphonse, A micro-structured 5kW complete fuel processor for iso-octane as hydrogen supply system for mobile auxiliary power units: Part I—Development of water–gas shift and preferential oxidation catalysts reactors and assembly of the fuel processor, Chemical Engineering Journal, 137 (2008) 653-663.

[60] J. Thormann, P. Pfeifer, U. Kunz, K. Schubert, Reforming of diesel fuel in a micro reactor, International Journal of Chemical Reactor Engineering, 6 (2008) 1-18.

[61] J. Thormann, P. Pfeifer, K. Schubert, U. Kunz, Reforming of diesel fuel in a micro reactor for APU systems, Chemical Engineering Journal, 135 (2008) S74-S81.

[62] X. Karatzas, J. Dawody, A. Grant, E.E. Svensson, L.J. Pettersson, Zone-coated Rh-based monolithic catalyst for autothermal reforming of diesel, Applied Catalysis B: Environmental, 101 (2011) 226-238.

[63] J. Sehested, Four challenges for nickel steam-reforming catalysts, Catalysis Today, 111 (2006) 103-110.

Chapter 3

Thermodynamic Analysis of Diesel Reforming Process: Mapping of Carbon Formation Boundary and Representative Independent Reactions

3.1 **Preface**

This chapter presents a thermodynamic chemical equilibrium analysis using a Gibbs free energy minimization technique for diesel reforming. The goal of the analysis was to map the carbon formation boundary and identify the operation window for maximum hydrogen yields in carbon-free zone. The chapter was published in “Journal of Power Sources, 194 (2009) 1007-1020”

The work examines carbon formation under various operating conditions in different parts of the reactor for three different reforming processes - steam reforming (SR), partial oxidation (POX), and autothermal reforming (ATR). The chapter presents a mapping of carbon formation boundary and possible reforming operations and conditions that ultimately lead to higher hydrogen yield. This study shows that despite the high hydrogen yields, the endothermic steam reforming of diesel is a highly energy intensive process that could lead to overall lower efficiency of the system. Partial oxidation of diesel is not suitable as it needs very high temperatures in order to be in the carbon free region as per thermodynamic analysis. Elevated temperatures (> 1000 °C) are also not desired from material of construction selection point of view. Thermodynamic analysis suggests autothermal reforming as the best choice as it can be carried out at low temperatures than POX and can have a sufficiently higher hydrogen yield than POX process. However, it is not possible to operate the ATR process at thermoneutral point in the carbon-free operation region. The thermodynamic study provides supporting reason for pursuing further studies on autothermal reforming of diesel. This analysis also helped in deciding the operating conditions for experimental study discussed in Chapter 5.

3.2 **Abstract**

This paper presents thermodynamic analysis of commercial diesel with 50 ppm sulfur content for the three common modes of reforming operations. Thermodynamic analysis is done to get boundary data for carbon formation and to get the composition of various species for all modes and entire range of operations. For steam reforming operation, steam-to-carbon (S/C) ratio equal to or greater than 2 is required for carbon-free operation in entire temperature range (400–800 °C). However, selection of S/C ratio requires the balance between maximizing the hydrogen yield and minimizing the energy input both of which increase with increasing S/C ratio. For partial oxidation operation, O_2/C ratio of 0.75 is preferable to maximize hydrogen yield but carbon formation can occur if regions of reactor experience temperatures lower than 700 °C. In the case of autothermal reforming, for carbon-free operation, temperature higher than 750 °C, O_2/C ratio in the range of 0.125–0.25 and S/C ratio greater than 1.25 and ideally 1.75 is recommended. However, enthalpy analysis indicates that it is not possible to reach to thermoneutral point at this condition so it is better to operate O_2/C ratio 0.25 or little higher with constant heat supply. A set of three independent reactions is proposed that along with element balance equations can adequately describe the equilibrium composition of six major species – H_2, CO_2, CO, H_2O, CH_4, and C for the entire range of reforming operation.

Keywords: Thermodynamic analysis; Diesel reforming; Gibbs' minimization; Carbon free operation; Independent reactions

1. Introduction

Diesel is a common fuel source for transportation application worldwide and it is used in generators as the main source for electricity generation in the Northern communities of Canada. Conversion of chemical energy of diesel into either motive power or electricity is achieved in combustion engines, which generates in addition to a known greenhouse gas – carbon dioxide – unwanted byproducts such as nitrogen oxides (NO_x) and particulate matter. A recent report in Canada has shown that health cost associated with exposure to particulate matter emissions is significant [1]. Without changing the fuel, it is possible to significantly reduce or even completely eliminate the impact of particulate emissions if hydrogen-rich stream generated from diesel reforming can be used as a fuel for low-temperature proton exchange membrane fuel cell (PEMFC) for automotive applications and for high-temperature solid oxide fuel cell (SOFC) for remote electricity generation [2-4]. It is pertinent to point out that reformed-diesel-fed-SOFCs are also being considered as auxiliary power units in transport trucks which require power to heat or to cool the cabin areas and to power electrical systems for refrigeration, lighting, computers and other electronic devices [5].

However, reactor design for reforming diesel into a hydrogen rich stream is a challenging problem that includes finding an active, stable catalyst. Another problem is deactivation of supported-metal catalysts due to carbon/coke formation and by the presence of sulfur compounds in the feed [5-8]. Carbon formation fouls the metal surfaces, blocks the catalyst support pores and voids, causes physical disintegration of catalyst support, and may also promote undesirable side reactions [4, 6, 7]. From operational standpoint, the objective is to identify operating conditions that avoid carbon formation and maximizes the production of hydrogen while simultaneously minimizes the formation of CO, CH_4, and other hydrocarbons. Depending on the reforming process chosen, an additional interest is to minimize the reactor energy input. Such conditions can be identified using chemical reaction equilibrium and thermo-chemical analyses.

There is limited literature on the chemical equilibrium analysis of diesel reforming processes. The work of Ahmed *et al.* [2] examines three diesel reforming processes – steam reforming (SR), autothermal reforming (ATR) and partial oxidation (POX) – in context of application as a reformer for solid oxide fuel cell system. Thermodynamic analysis results were presented in the form of product distribution over a wide range of temperature (300–800 °C) but for selected feed compositions, *i.e.* steam to carbon (S/C) and oxygen to carbon (O_2/C) ratios. For ATR operations, only three S/C ratios of 1.2, 1.5 and 1.8 were examined, each at two O_2/C ratios. For POX operation, only three O_2/C ratios – 0.5, 0.75 and 1.0 – and for SR operation, three S/C ratios – 1.5, 1.8 and 2.0 – were examined. Whereas the carbon formation temperature at these specified operating conditions could be derived from the product distribution data, carbon formation boundary for the entire spectrum of temperature and feed composition (defined by O_2/C and S/C ratios) was not explicitly presented.

In other studies, equilibrium compositions have been reported at conditions specific to the experimental work carried out using surrogate fuels [7, 9-12] or particular C:H ratio [4] of diesel to compare with experimentally observed product compositions results. However, no detailed study of thermodynamic analysis of commercial diesel has been reported.

1.1. Objective

The objective of the present work is to *map* the thermodynamic region where the carbon formation is favoured. It should be noted that kinetic effects are not addressed in this analysis and that coke formation is possible by kinetically driven processes in the region where the carbon formation is not thermodynamically favoured. Unlike Ahmed *et al.*'s work wherein four feed composition for ATR, three feed composition for SR and three feed composition for POX were examined, carbon formation boundary for the entire range of feed composition covering three different reforming processes was carried out. The carbon formation boundary is determined from gas-solid chemical reaction equilibrium computations using Gibbs free energy minimization routine implemented in Matlab^{TM}. In addition, the influence of pressure on carbon formation boundary is also examined. From the analysis of equilibrium composition of reaction product, it is shown that the composition of the six dominant species can be predicted by considering three independent reactions and the known elemental balance.

2. Diesel: Composition and Reforming Reactions/Products

2.1. Diesel fuel composition

Diesel fuel is a complex mixture of around 400 hydrocarbon species, some 20 organic compounds of sulfur, and additives. The distribution of the carbon number of the hydrocarbon molecules peaks in the range of 15–25 carbon atoms per molecule [13]. Diesel fuel contain mainly iso-paraffins, but also n-paraffins, mono-, di-, tri-, tetra cycloparaffins, alkylbenzenes, naphthalenes and phenanthrenes and even pyrenes [14]. Aromatic compounds may comprise 20 vol.% of the mixture. Different chemical formulae for diesel have been reported: $C_{14.342}H_{24.75}O_{0.0495}$[15], $CH_{1.86}$[4], $C_{13.4}H_{26.3}$[12], $C_{13.57}H_{27.14}$[16], $C_{16.2}H_{30.6}$[10], $C_{13.6}H_{27.1}$[14].

Ahmed *et al.*[2] performed thermodynamic analysis on commercial diesel having the same composition reported in Amphlett *et al.*[17], who simulated diesel composition that has similar heat of formation, Gibbs free energy and distillation curve to type D2 diesel. It has been reported that hexadecane is the predominant hydrocarbon in U.S. certified grade diesel (38.7 wt.%), however overall composition and heat of combustion of typical diesel fuel are more closely represented by dodecane [3, 12]. The chemical equilibrium composition by definition is not path dependent; the final composition is simply a function of the thermodynamic state defined by temperature, pressure, and elemental composition (atomic ratios of C:H:O in the feed). In the present study, we have considered $C_{13.6}H_{27.1}$ to be representative of commercial diesel with 50 ppm sulfur content (as per European regulation 2005) [14]. The properties of commercial diesel are summarized in Table 3.1.

Table 3.1: Properties of diesel fuel

Fuel	**Formula**	**Sulfur content [wt. ppm]**	**L.H.V. [kJ/mol]**	**F.L. Lower, Higher [Vol %]**	ρ **kg/m^3**	**B.P. or B.R. [^{o}C]**	**H.V. [kJ/mol]**	**Cp [J/mol·K] at 20 °C**
Diesel	$C_{13.6}H_{27.1}$	50	8,080	1, 6	856	120-430	47	340

L.H.V - Lower heating value; F.L.- Flammability limits; B.P.- Boiling Point
B.R.- Boiling Range; H.V.- Heat of vaporization

2.2. Reactions and products

The general scheme of reforming diesel with subsequent usage of the reformate in a SOFC is depicted in Figure 3.1. The general idea is to operate the reformer such that reformate stream with as high hydrogen content as possible is generated while minimizing unwanted species–unreacted and unsaturated hydrocarbons. The practical reformers usually operate at temperatures greater than 600 °C to ensure that reactions proceed with sufficiently fast kinetics. Since the SOFCs are designed to operate in the 600-900 °C range, the upstream reformer may have to be operated at higher temperatures (> 600 °C) in consideration of heat losses [10]. The ability to operate the reformer at thermally desirable conditions also depends on the type of the reforming process, which will influence the choice of catalyst and the product composition.

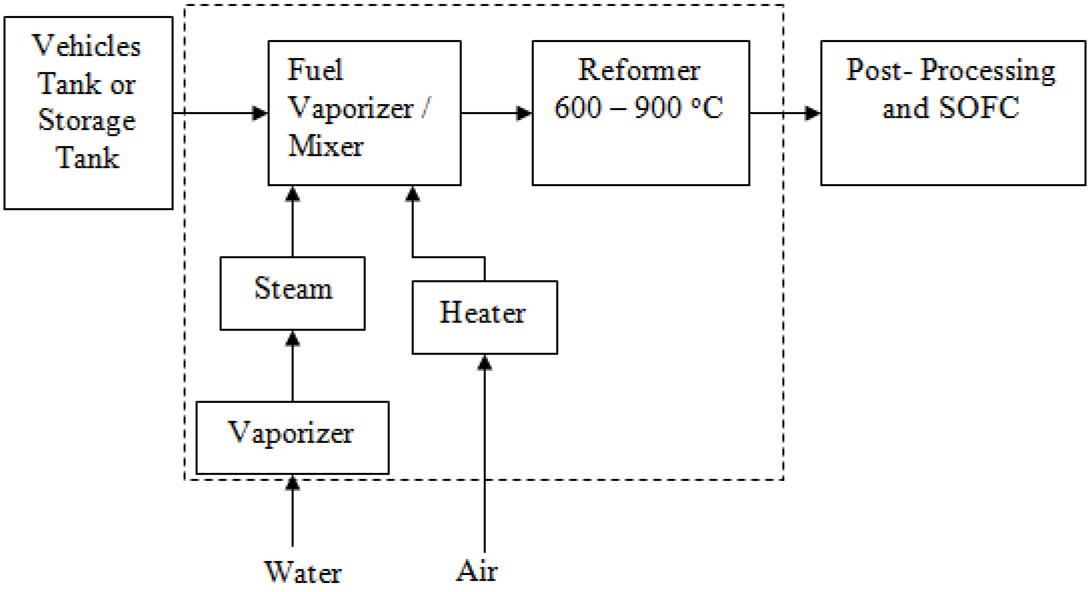

Figure 3.1: Schematic diagram for reforming process and dotted line represents system boundary considered for the energy balance calculations.

Reforming of hydrocarbons including diesel can be classified into three different types of processes – SR, POX, and ATR. Under idealized conditions, hydrocarbon is stoichiometrically converted to CO and H_2 in POX, and to CO_2 and H_2 in ATR and SR (assuming water-gas-shift [WGS]). Thus, the overall reaction can be represented as shown below:

$$\text{SR:}\, C_nH_m + S\cdot n\cdot H_2O \rightarrow \left(\frac{m}{2}+2n\right)H_2 + n\cdot CO_2 + (S-2)n\cdot H_2O \qquad \Delta H > 0 \tag{1}$$

$$\text{POX:}\ C_nH_m + A\cdot n\cdot O_2 \rightarrow \left(\frac{m}{2}\right)H_2 + 2\cdot A\cdot n\cdot CO \qquad \Delta H < 0 \quad \text{(valid for } A = 0.5\text{)} \tag{2}$$

ATR:

$$C_nH_m + A\cdot n\cdot O_2 + S\cdot n\cdot H_2O \rightarrow nCO_2 + \left(\frac{m}{2}+2\cdot n(1-A)\right)H_2 + \left(S-2(1-A)\right)n\cdot H_2O \quad \Delta H \approx 0 \tag{3}$$

where S is steam to carbon ratio and A is oxygen to carbon ratio. From stoichiometric conversions, $S = 2$ for SR, $A = 0.5$ for POX reaction, and $S = 2\cdot(1-A)$ for ATR.

It must be recognized that the aforementioned reforming processes do not proceed with the idealized stoichiometries of Equations (1)–(3) because of the occurrence of numerous chemical reactions - the reverse water-gas-shift reaction (RWGS), methanation, thermal cracking and gasification - shown below. As a result, the reformate streams typically contains CO, CH_4, carbon (C) and other species not included in Equations (1)–(3). Depending on the operating conditions and the catalyst employed, the kinetics can be sufficiently fast such that the reformate composition approaches chemical equilibrium at the given temperature and pressure. It is generally accepted that the diesel reforming process involves hundreds or thousands of gas-phase radical reactions as well as surface reactions. The list of selective key overall reactions presented below provides an indication of complexity although complete list consist of thousands of reactions.

$CO + H_2O \rightarrow CO_2 + H_2$ $\Delta H^o_{298} = -42.2$ kJ/mol (WGS) (4)

$CO + 3H_2 \rightarrow CH_4 + H_2O$ $\Delta H^o_{298} = -205.3$ kJ/mol (Methanation) (5)

$CO_2 + 4H_2 \rightarrow CH_4 + 2H_2O$ $\Delta H^o_{298} = -163.1$ kJ/mol (6)

$2CO + 2H_2 \rightarrow CH_4 + CO_2$ $\Delta H^o_{298} = -123.8$ kJ/mol (7)

$C_mH_n \rightarrow CH_4 + C_{m-1}H_{n-4}$ (8)

$C_mH_n + H_2 \rightarrow CH_4 + C_{m-1}H_{n-2}$ (9)

$C_mH_n \rightarrow mC + \frac{n}{2}H_2$ (10)

$CH_4 \rightarrow C + 2H_2$ $\Delta H^o_{298} = 74.9$ kJ/mol (11)

$C_2H_2 \rightarrow 2C + H_2$ $\Delta H^o_{298} = -226.9$ kJ/mol (12)

$C_2H_4 \rightarrow 2C + 2H_2$ $\Delta H^o_{298} = -52.3$ kJ/mol (13)

$C_3H_6 \rightarrow 3C + 3H_2$ $\Delta H^o_{298} = -20.4$ kJ/mol (14)

$C_4H_8 \rightarrow 4C + 4H_2$ $\Delta H^o_{298} = 0.13$ kJ/mol (15)

$Cis2 - C_4H_8 \rightarrow 4C + 4H_2$ $\Delta H^o_{298} = 7.0$ kJ/mol (16)

$trans2 - C_4H_8 \rightarrow 4C + 4H_2$ $\Delta H^o_{298} = 11.2$ kJ/mol (17)

$2CO \rightarrow C + CO_2$ $\Delta H^o_{298} = -86.3$ kJ/mol (Boudouard) (18)

$CO + H_2 \rightarrow C + H_2O$ $\Delta H^o_{298} = -130.4$ kJ/mol (Rev-gasification) (19)

$$C + O_2 \rightarrow CO_2 \qquad \Delta H^o_{298} = -393.8 \text{ kJ/mol} \tag{20}$$

$$S + O_2 \rightarrow SO_2 \qquad \Delta H^o_{298} = -574.3 \text{ kJ/mol} \tag{21}$$

$$SO_2 + \frac{1}{2}O_2 \rightarrow SO_3 \qquad \Delta H^o_{298} = -98.9 \text{ kJ/mol} \tag{22}$$

$$SO_3 + H_2O \rightarrow H_2SO_4 \qquad \Delta H^o_{298} = -98.2 \text{ kJ/mol} \tag{23}$$

$$H_2 + S \rightarrow H_2S \qquad \Delta H^o_{298} = -297.3 \text{ kJ/mol} \tag{24}$$

Thermal Cracking of hydrocarbon:

$$\begin{aligned} C_nH_m \rightarrow\ & C + H_2 + CH_4 + C_2H_6 + C_3H_8 + C_4H_{10} + \\ & C_5H_{12} + C_6H_{12}\left(\text{cyclohexane}\right) + C_6H_6\left(\text{benzene}\right) + \\ & C_8H_{18}\left(\text{isooctane}\right) + \text{........} \end{aligned} \tag{25}$$

Hexadecane, which is major component of diesel, also reacts with O_2 [7]:

$$C_{16}H_{34} + O_2 \rightarrow C_{14}H_{10}\left(S\right) + 2CO + 12H_2 \tag{26}$$

$$C_{16}H_{34} + \frac{7}{2}O_2 \rightarrow \frac{1}{2}C_{18}H_{12}\left(S\right) + 7CO + 14H_2 \tag{27}$$

2.2.1. Carbon and coke formation

As discussed earlier, a significant problem in reforming process is the formation of carbon-rich solid phase which is often referred to as carbon and coke. The definition of carbon and coke is somewhat arbitrary and by convention related to their origin. Carbon is generally considered to be a product of CO disproportionation (Boudouard reaction; Equation (18) [6] while coke is produced by decomposition or condensation of hydrocarbons [6, 7]. Coke forms may vary from higher molecular weight hydrocarbons such as condensed polyaromatics to carbons such as graphite, depending upon the conditions under which the coke was formed and aged [6]. In the reforming of hydrocarbons, different types of carbon or coke have been observed. Elemental carbon (whisker carbon, filamentous carbon) is formed from the decomposition of hydrocarbons (Equations (11)–(17)) [6, 7], Boudouard reaction (Equation (18)) and reverse gasification (Equation (19)) [7]. Dissociation of hydrocarbons such as methane and higher hydrocarbons ($n \geq 4$) is favoured at high temperatures, whereas carbon formation by Boudouard reaction and reverse gasification is favoured at low temperatures. Pyrolytic carbon (Equation (25)) is formed by thermal cracking of hydrocarbons. The formation of coke typically, not necessarily always, proceeds through the following sequence [7].

$$C_nH_m \rightarrow \text{Olefins} \rightarrow \text{Polymers} \rightarrow \text{Coke} \rightarrow \text{Amorphous Carbon} \rightarrow \text{Graphitic Carbon} \qquad (28)$$

It should be emphasized that amorphous carbon (filamentous) is favoured at low temperature (< 600 °C) whereas graphitized carbon (also whisker type) is favoured at high temperature (>600 °C). Compounds which approximates the structure of coke, such as anthracene ($C_{14}H_{10}$; Equation (26)) and naphthacene ($C_{18}H_{12}$; Equation (27)), are thermodynamically favourable even at POX conditions [7].

In a reformer system, there is a potential for coke/carbon formation in the catalytic reactor (reformer) as well as in its upstream and downstream units, for example, carbon/coke formation is possible and observed in the vaporizer unit. Furthermore, if the transfer line downstream of the reformer is not catalytically inert, carbon formation at low temperature via Boudouard reaction and reverse gasification reaction (Equations (18)–(19)) can occur. As such, prior to operating a reformer (lab-scale or industrial) it is useful to assess the conditions under which carbon formation is thermodynamically favoured. If the reformer is operated outside this thermodynamic carbon formation region, the carbon formation may be avoided. In practice, further considerations to non-idealities, such as inadequate mixing, must be given and it must be recognized that the reformer operation may be limited by reaction kinetics.

One of the reformer process units wherein there is significant potential for carbon formation is the vaporizer or injector. It must be noted that diesel fuel is liquid at ambient conditions and would have to be either vaporized or directly injected into another reacting stream, irrespective of the type of reforming process chosen. Since diesel is a hydrocarbon mixture, it has a boiling point temperature range. The least stable components of the diesel fuel crack into free radicals at the auto-ignition temperature, which may be as low as 250 °C for some fuels. If insufficient oxygen or steam is present, the free radicals can initiate chain polymerization reactions forming carbon-rich phase or tars.

2.2.2. Sulfur compound formation

Small amounts of sulfur in diesel fuel is a potential poison for many reforming catalyst, however it also minimizes coke formation [4, 7]. Expected sulfur products during the reforming of sulfur containing-diesel are SO_2 and H_2S (Equations (21), and (24)). However SO_3 and H_2SO_4 (Equations (22), and (23)) may also exist at conditions encountered in the cold exhaust lines of reformer. Further, H_2S can interact with metal catalyst resulting either in surface adsorbed sulfur (at low H_2S concentrations) or in bulk metal sulfide (at high H_2S concentrations) [18]. The loss of catalyst activity due to presence of SO_2 and H_2S has been reported [19]. In fact, one method of catalyst selection involves the use of Ellingham diagram, which plots the Gibbs free energy of formation of various bulk sulfides as a function of temperature and H_2S/H_2 molar ratio in the system [4, 7]. In the present study, we have not considered the formation of bulk metal sulfides.

2.2.3. CO and CH_4 formation

The primary goal of the hydrocarbon reforming process is to generate hydrogen, however, CO and/or CH_4 are always observed in the reformate stream and are the undesired products. Reactions involving these two species are shown in Equations (4) -(7). CO formation is favoured at high temperature because of reverse WGS reaction (Equation (4)), reverse methanation reaction (Equation (5)), and methane dry reforming reaction (reverse Equation (7)), whereas CH_4 formation is favoured at low temperature (Equations (5)–(7)). Hence, if the reformer exhaust lines are not catalytically inert and if they are at low temperature then undesired product like CH_4 is formed. Reactions which are responsible for formation of methane from hydrocarbon fuels are Equations (8) and (9) [14].

2.3. Summary

In summary it can be stated that diesel is a complex mixture of myriads of hydrocarbons and its reformation to hydrogen can be attained by one of the three possible processes. From the consideration of overall reaction stoichiometries, it can be deduced that the yield of hydrogen will depend on the choice of the reforming process. Moreover, highly undesirable products such as solid carbon/coke may form in the reformer or in the upstream/downstream units depending on the operating conditions. Detailed kinetic simulation of diesel reforming process and in particular prediction of carbon-formation is complicated owing to the large number of elementary reactions that must be considered and for which the kinetic rate laws are not known. However, carbon-free operational conditions that also favour high hydrogen yield can be identified by carrying out chemical reaction equilibrium study.

3. Chemical Reaction Equilibrium Calculations

In this work, the equilibrium composition of reacting mixture is computed by the non-stoichiometric approach, in which the equilibrium composition is found by the direct minimization of Gibbs free energy, which uses scalar parameter (Lagrange multipliers) for a given set of species [20]. The advantages of this method are: (a) a previous selection of the possible chemical equations is not necessary, (b) by applying constraint, no divergence appears during computation and (c) an accurate estimation of initial equilibrium composition is not necessary [21].

3.1. Governing equations

The chemical equilibrium for a system at constant temperature and pressure satisfies the following equation:

$$dG_{total} = -S \cdot dT + V \cdot dP + \sum_{components} \mu_i dn_i = 0 \xrightarrow{const.T,P} \sum_{components} \mu_i dn_i = 0 \tag{29}$$

where G is Gibbs free energy in Joules, S is entropy in Joules/K, T is temperature in K, V is the volume in m^3, P is pressure in N/m^2, μ_i is the chemical potential of species i in J/mol and n_i is the number of moles of species i.

For equilibrium composition computation, the objective is to find the values of n_i that minimizes the value of G. From Equation (29) total Gibbs free energy of the system is given as,

$$G_{total} = \sum_{components} n_i \overline{G}_i = \sum_{components} n_i \mu_i \tag{30}$$

where $\overline{G}_i$ is the partial molar Gibbs free energy, which is equal to chemical potential.

For system comprising two phases,

$$G_{total} = \sum_{gases} \mu_i n_i + \sum_{condensed} \mu_i n_i \tag{31}$$

$$G_{total} = G_{gas} + G_{condensed} = \sum_{i=1}^{i=n_c} n_i \left(\mu_i^{o} + RT \ln\left(a_i\right)\right) + \sum_{i=n_{c+1}}^{i=n_s} \mu_i n_i \tag{32}$$

where n_c is number of gas-phase species, n_{c+1} to n_s is number of condensed species, the activity of the substance, a_i, can be given as:

$$a_i = \frac{\hat{f}_i}{f_i^{o}} = \frac{\hat{\phi}_i y_i P}{P^{o}} = \frac{n_i}{n_{total-gas}} \frac{\hat{\phi}_i P}{P^{o}} \tag{33}$$

Considering gas-phase behavior as ideal, $\phi_i \approx 1$ and standard state is taken to be 1 bar, *i.e.*, $P^{o} = 1 \text{ bar}$. Equation (32) can be transformed into:

$$\frac{G_{total}}{RT} = g = \sum_{i=1}^{i=n_c} n_i \left({\frac{\mu_i}{RT}}^{o} + \ln\left(a_i\right)\right) + \sum_{i=n_{c+1}}^{i=n_s} \frac{\mu_i n_i}{RT} \tag{34}$$

$$g = \sum_{i=1}^{i=n_c} n_i \left(C_i + \ln\left(\frac{n_i}{n_{total-gas}} \right)\right) + \sum_{i=n_{c+1}}^{i=n_s} \frac{\mu_i n_i}{RT} \tag{35}$$

where $C_i = g_i^{o} + \ln\left(\frac{P}{P^{o}}\right)$, $g_i^{o} = {\frac{\mu_i}{RT}}^{o}$ and μ_i^{o} is the molar Gibbs free energy of species *i* at standard state.

The last term on the right hand side of Equation (35) representing the solids or condensed-phase species (carbon and/or sulfur) is equal to zero as all elements' Gibbs energy of formation is set to zero at standard state.

Further, the elements in the system must be conserved, resulting in additional *m* material balance equations for *m* elements:

$$b_j - \sum_{i=1}^{i-n_s} a_{ji} n_i = 0 \quad for\ j = 1, 2, ..., m \qquad \text{(Equality constraint)} \tag{36}$$

where a_{ji} is the number of atoms of element *j* in molecule *i*, and b_j is the total amount of element *j* in the mixture. Equation (36) considers solids for element balance.

Thus, the equilibrium calculation problem is the determination of the minimum of a constrained function. In terms of Lagrange multiplier (λ), the constraint function to be minimized is:

$$f = g + \sum_{j=1}^{j=m} \lambda_j \left(b_j - \sum_{i=1}^{i-n_s} a_{ji} n_i \right) \tag{37}$$

At the minimum, the derivatives with respect to number of moles of the species are zero. Thus, the derivatives with respect to mole numbers are:

$$\frac{\partial f}{\partial n_{i,gases}} = C_i + \ln\left(\frac{n_i}{n_{total-gas}} \right) - \sum_{k=1}^{k=m} a_{ik} \lambda_k = 0 \qquad i = 1, 2, ..., n_c \tag{38}$$

$$\frac{\partial f}{\partial n_{i,solids}} = -\sum_{k=1}^{k=m} a_{ik}\lambda_k = 0 \qquad i = n_{c+1}, \ldots\ldots, n_s \tag{39}$$

The non-linear systems of equations described by Equations (38) and (39) can be solved by using Newton-Raphson method. In this study, the fsolve function of Matlab^{TM} was employed to solve the set of equations.

For each S/C and O_2/C ratio, the equilibrium composition is computed in the temperature range of 400 to 1000 °C at an interval of 50 °C. This gave the temperature range of 50 °C where carbon disappears. Then the calculations are repeated with increment of 0.5 °C in the observed 50 °C span. The temperature at which, the carbon content is less than 1×10^{-100} moles is reported as zero carbon for that C:H:O feed ratio.

3.2. Input data

The input data for simulation includes specification of elemental composition (dictated by the feed composition), temperature, and pressure as well as the standard state free energy of formation of all species.

The standard state free energy or chemical potential (μ_i^o) for all elemental species, *e.g.*, C (graphite), O_2, N_2, and H_2, is set equal to zero. Accordingly, for chemical compounds $\mu_i^o = \Delta G_{f_i}^o$, *i.e.*, standard Gibbs energy of formation of species *i*. In this work, standard Gibbs energy of formation data is obtained from JANAF data tables [22], Pamidimukkala *et al.* [23], and Yaws [24].

3.3. Selection of chemical species for inclusion in equilibrium calculations

For computation of equilibrium composition by free energy minimization approach, any chemical species can be included in the list of potential products (made of the constituent elements of the feed species), the thermodynamically unfavourable species simply end up with negligible mole number. However, to gain some insight into which species may be favoured to exist, the free energy of formation (ΔG_f^o) of several C–H–O and sulfur species were examined as a function of temperature as shown in Figures 3.2 and 3.3, respectively .

From Figure 3.2, it can be noted that CO, CO_2 and H_2O are the most favourable oxygenated

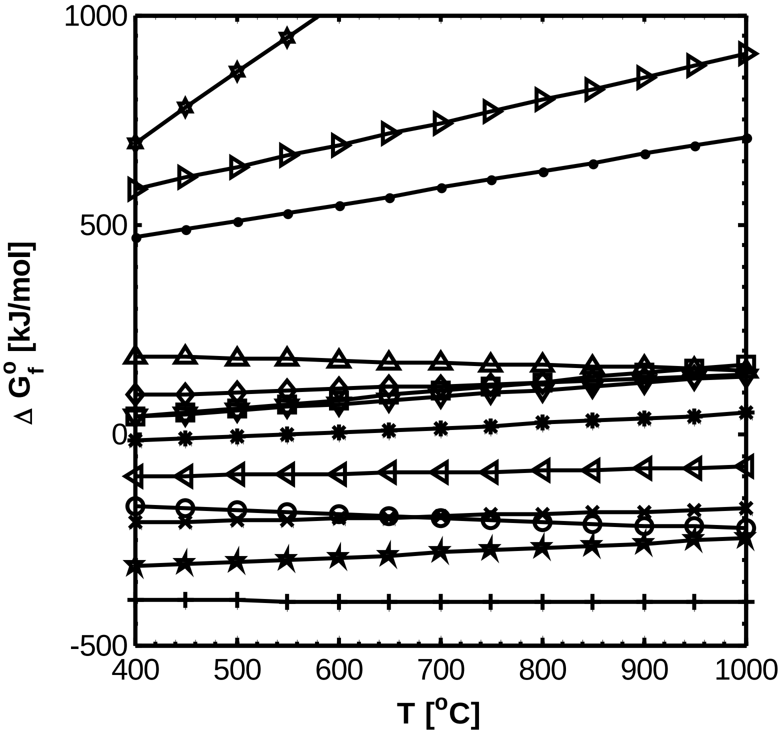

Figure 3.2: Gibbs energy of formation of key carbon-containing species. o, CO; +, CO_2;∗, CH_4; x, H_2O; □, C_2H_6; ◊, C_2H_4; ⊔ , C_2H_2; ▽, C_2H_4O; •, $C_{14}H_{10}$; ▷, $C_{18}H_{12}$; ◁, CH_2O; ★, CH_2O_2; ✸, $C_{16}H_{34}$.

compounds. Acetaldehyde is highly unfavourable with respect to CO_2 and formaldehyde is highly unfavourable with respect to CO and CO_2. Hence these species could be possible intermediate species. C_2H_6, C_2H_4, C_2H_2, C_2H_4O, $C_{14}H_{10}$ and $C_{18}H_{12}$ are unfavourable with respect to CO, CO_2 and CH_4. Formation of $C_{14}H_{10}$, and $C_{18}H_{12}$ (as per Equations (26) and (27)) from hexadecane is highly favourable at all temperatures but thermodynamically it should decompose into CO, CO_2 in the presence of oxygen.

From Figure 3.3, it can be noted that H_2SO_4 has lower Gibbs energy of formation compared to SO_2, which is lower than that for H_2S. Without considering the elemental constraints to be

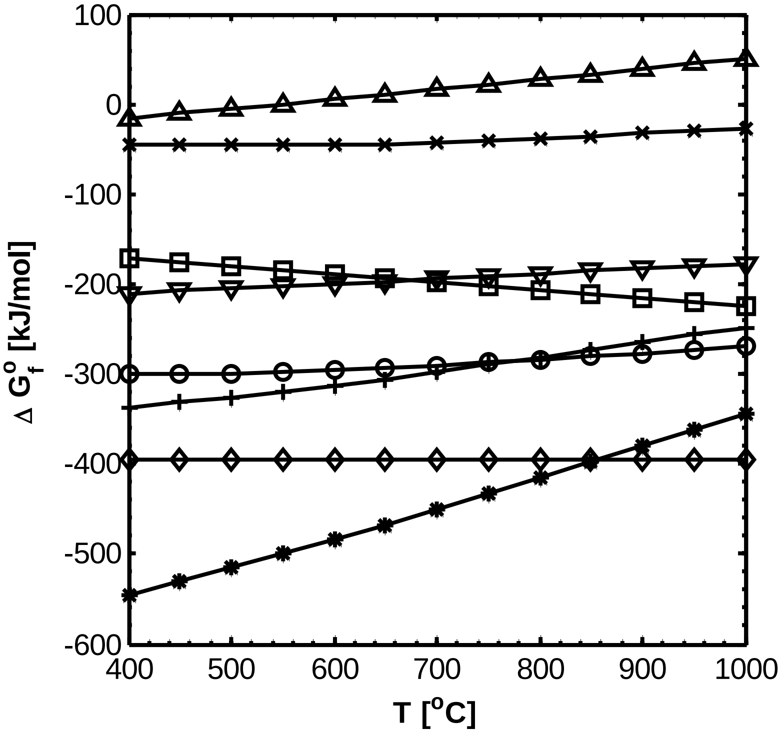

Figure 3.3: Gibbs energy of formation of sulfur-containing and other key species. o, SO_2; +, SO_3; ∗, H_2SO_4; x, H_2S; □, CO; ◊, CO_2; ⊔ , CH_4; ▽, H_2O.

satisfied, it may appear that sulfur in the product will preferably be present as H_2SO_4 and SO_2 rather than H_2S. However, other oxygen-containing species must be considered in the assessing which species would be more favourable. For instance, among oxygen-containing species, thermodynamically CO_2 would be favoured over both H_2SO_4 and SO_2. Thus, it would be expected that oxygen in the reaction feed would end up as CO_2 rather than SO_2 and H_2SO_4. Therefore, it may be expected that sulfur ends up as H_2S rather than H_2SO_4 or SO_2 in the equilibrium product. It must be recognized that the ultimate presence of species in the equilibrium mixture would depend, in addition to free energy of formation, on the elemental constraints imposed.

From the above arguments, the possible species that might be found in the final product were selected to be the following 19 species - H_2, CO, CO_2, CH_4, H_2O, O_2, C_2H_6, C_2H_4, C_2H_2, C_2H_4O, $C_{14}H_{10}$, $C_{18}H_{12}$, SO_2, SO_3, H_2SO_4, H_2S, S (alpha (solid), beta(liquid), gamma(gas)), C (graphite). Formic acid and formaldehyde were initially added into calculations but later on removed as their equilibrium composition was very negligible (almost zero).

It is useful to point out that amorphous carbon may be favoured kinetically at low temperature but thermodynamically graphite carbon is highly favourable. Reported standard Gibbs free energy change for transformation of amorphous carbon into graphite carbon varies from -11.054 kJ/mol to -3.220 kJ/mol [25]. Cimenti *et al.*[25] analyzed the equilibrium composition using thermodynamic data for amorphous carbon and graphite and it showed negligible amount of amorphous carbon as energy content of amorphous carbon is higher than that of graphite. Hence, for the current equilibrium calculations only graphite carbon was considered.

4. Results and Discussion

Chemical equilibrium computations were carried out to map the carbon formation boundaries in diesel reforming system and to assess the hydrogen yield in carbon-free operational region. The entire range of thermodynamic operating variables (temperature, pressure and composition) of practical interest was examined. The temperature range of interest is 400–1000 °C with the lower range relevant to the temperatures encountered in the vaporizer and the higher end temperatures expected in the exothermic partial oxidation process. For the compositional range, the steam to carbon ratio (S) and oxygen to carbon ratio (A) are parameters of interest. These ratios based on stoichiometries for SR, ATR and POX reactions of Equations (1)–(3) have been discussed earlier. In practical operations, values higher and lower than the ratios determined from the ideal stoichiometries are possible and, more importantly, as will be shown, necessary for carbon-free operation. The studied compositional range spanning the entire spectrum of reforming processes is indicated in Figure 3.4. For fuel vaporizer where no steam and oxygen is present, the process would be depicted as a point at the origin of the plot corresponding to S/C=0 and O_2/C=0. It is to be noted that the vaporizer feed may be a mixture of oxidant and fuel or water and fuel, in such case the depiction of vaporizer at the origin of Figure 3.4 would not be valid. Similarly, for SR process, there is no free oxygen present (O_2/C=0) in the feed and, thereby, the operating region coincides with the y-axis whereas for POX process wherein no steam (S/C=0) is present in the feed, the operating region coincides with the x-axis.

Finally, it is useful to remind that 19 chemical species, including condensed phases, identified in section 3.3 were considered in all free energy minimization computations.

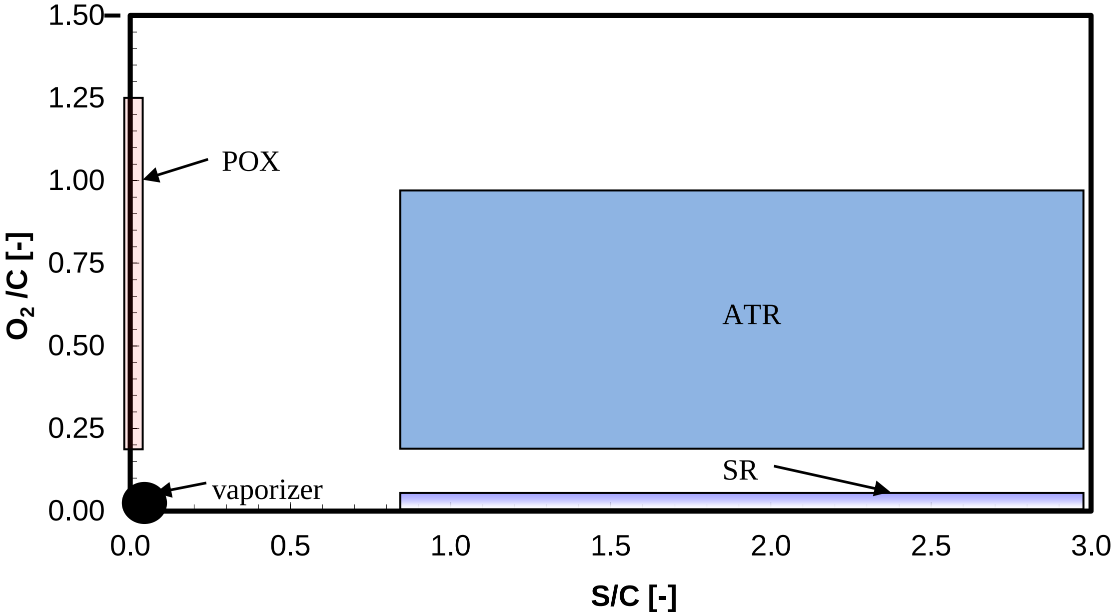

Figure 3.4: Schematic representation of studied compositional operational range for various reforming processes.

4.1. Carbon/Coke formation boundary

Carbon formation boundary for vaporizer unit and that for various diesel reforming process is reported in this section. As discussed previously, only graphite carbon is considered in product species list and the coke, which is represented as anthracene ($C_{14}H_{10}$) and naphthacene ($C_{18}H_{12}$), is found negligible.

4.1.1. Carbon formation in vaporizer/injector

To assess the carbon formation potential in the vaporizer or injector line of the reformer, equilibrium calculations for diesel thermal cracking were carried out. All C–H species among the selected 19 species (see section 3.3) were considered in the calculations. As expected, the dominant species were methane and hydrogen, in addition to carbon as shown in Figure 3.5. It can be noted that significant amount of carbon is favoured to be formed even at low temperatures. However, the kinetics of the carbon-forming reactions is likely too slow to be cause of concern. Nonetheless, if the vaporizer/injector is operated or exposed to higher temperatures – carbon formation would be favoured both kinetically and thermodynamically. In the case of steam

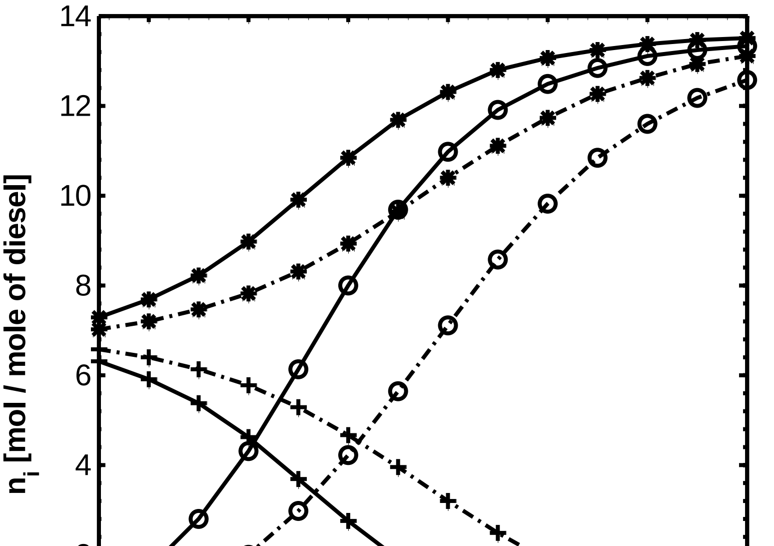

Figure 3.5: Equilibrium composition in thermal cracking of diesel. — ,1 atm; -·-, 5 atm; o, hydrogen; +, CH_4; ∗; carbon.

reforming, it may be possible to premix the diesel with water and then vaporize the mixture. However, the immiscibility of water and hydrocarbons dictates that local composition may be significantly different than the overall composition and, thereby, result in carbon formation.

4.1.2. Carbon formation boundary for diesel reforming processes

To map the carbon-free operational regime, based on thermodynamic consideration, carbon formation boundary over the entire range of operating conditions spanning the three different diesel reforming processes was computed. The results are presented in Table 3.2 wherein the carbon formation boundary temperatures at two different pressures is provided and in Figure 3.6 where carbon formation boundary for various S/C ratios is shown. In Figure 3.6, for a given S/C ratio, the region on the right-side or above the line represents the carbon-free conditions. Figure 3.6 also shows (as boxes) the potential range of operating conditions for the three different diesel reforming processes – SR, POX and ATR. The part of the box filled with hatched line then denotes the carbon-free operational conditions for typical reforming operation.

For steam reforming (O_2/C = 0), it can be concluded from Figure 3.6 that if S/C ratio is greater than 1.75, the operation is thermodynamically predicted to be carbon free for the expected operational temperature (600-800 °C). A much lower S/C ratio (~1.25) can be tolerated if the operational temperature is 800 °C. On the other hand, for partial oxidation (S/C ratio = 0), carbon-free operations is possible for the complete operational temperature range (600-1000 °C) as long as the O_2/C ratio is higher than 1.1. However, higher O_2/C ratio can have adverse affect on hydrogen yield as will be discussed in section 4.2.b. Similarly, the choice of S/C ratio for SR operations will also be influenced by energy input requirements and hydrogen yields.

Table 3.2: Carbon formation boundary (Temperature in °C) for different operating conditions

At *P* = 1 atm

	S/C						
O_2/C	**0.00**	**0.75**	**1.00**	**1.25**	**1.50**	**1.75**	**2.00**
0.00	>>1276	>>1023	974.9	711.1	649.4	583.4	238.3
0.125	>>1276	1023.4	717.3	657.0	600.4	315.4	231.9
0.25	>>1276	722.7	663.2	611.1	528.8	282.8	219.9
0.50	1276.0	624.7	570.1	443.8	292.8	229.4	187.9
0.75	678.8	514.1	371.9	273.8	217.4	178.6	149.4
1.00	584.9	300.4	230.3	178.9	150.6	125.0	104.7
1.25	396.1						

At *P* = 5 atm

	S/C						
O_2/C	**0.00**	**0.75**	**1.00**	**1.25**	**1.50**	**1.75**	**2.00**
0.00	>>1282	>>1027.1	977.2	770.3	680.0	317.1	234.1
0.125	>>1282	1027.1	784.8	704.4	576.5	298.0	229.1
0.25	>>1282	797.0	720.9	639.3	384.5	275.8	218.3
0.50	1282.0	679.7	592.7	394.0	287.6	228.2	187.5
0.75	756.5	525.7	361.5	272.1	217.1	178.5	149.4
1.00	645.6	300.1	230.3	184.0	150.6	125.0	104.8
1.25	412.1						

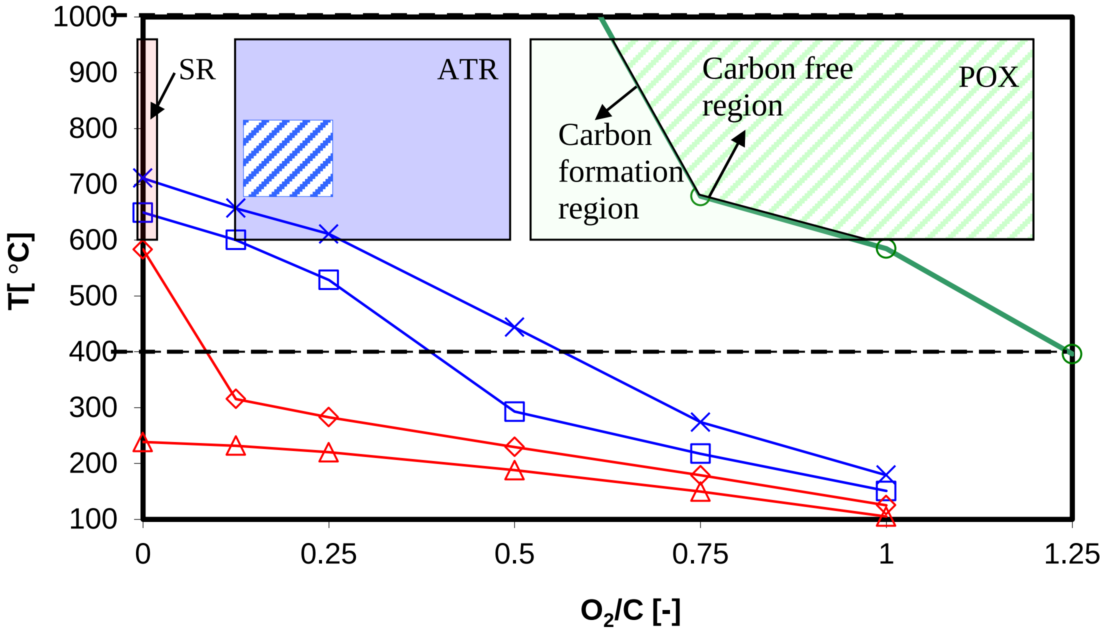

Figure 3.6: Carbon formation boundary for SR, POX, and ATR at 1 atm: o, S/C = 0; x, S/C = 1.25; □, S/C = 1.50; ◊, S/C = 1.75; Δ S/C = 2.0. Dotted box represents thermodynamically recommended region.

For ATR operations, considering the realistic operational region to be O_2/C ratio of 0.25-0.5 and temperature range of 600-1000 °C, it can be noted from Figure 3.6 that carbon-free operations are predicted if S/C ratio of 1.5 or higher is maintained. Again, a lower S/C ratio is tolerable if the operating temperatures are on the higher end. For example, if the ATR operates at 900 °C, a S/C ratio of 1.0 is indicated to allow carbon-free operation. Apart from considerations of carbon-free operations, the choices of O_2/C and S/C ratios would further depend on the desire to maximize hydrogen yield and to operate near the thermo-neutral point. The latter points are discussed in sections 4.2 and 4.3.

4.1.3. Influence of pressure on the carbon formation boundary in SR process

The reforming operations may occur at pressures higher than atmospheric. It was of interest to get insight into the influence of pressure on the carbon-forming boundaries. Recognizing multiple variables (S/C and O_2/C ratios, temperature) and their wide range spanning different diesel reforming processes, computations were carried out for a single diesel reforming process – steam reforming – at various S/C ratios and two pressures – 1 and 5 atmospheres. It is recognized that 5 atm may be significantly higher pressure than those being considered for diesel reforming but it was chosen so as to easily discern the influence of pressure on carbon formation behavior. The amount of carbon formed as a function of temperature is presented in Figure 3.7. The carbon formation boundaries can be noted as the intercept of the plot with the x-axis. A number of interesting observations can be made from the Figure 3.7. First, it can be deduced that the carbon-formation boundary temperature increases with increase in pressure. A shift of nearly 50 °C is observed for S/C ratios lower than 1.75. Second, it can be observed that the effect of pressure on the amount of carbon formed at lower temperature is opposite to that at higher temperatures for a fixed S/C ratio. It is useful to mention that similar thermodynamic trends are observed for carbon formation boundary at various temperatures and pressures for POX and ATR processes.

In principle, by the very nature of free energy minimization approach these effects cannot be explained simply in terms of reactions because a large number and combination of independent reactions can describe the observed equilibrium. However, if we consider the carbon formation/consumption to occur by the known reaction pathways described by the dissociation of

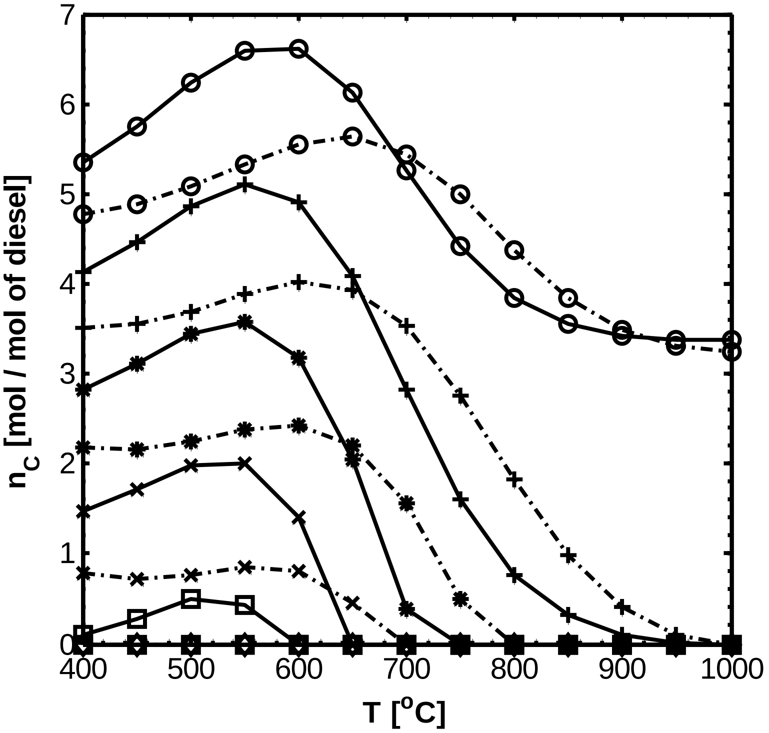

Figure 3.7: Equilibrium composition of carbon in steam reforming showing the effect of system pressure. — ,1 atm; -·-, 5 atm; o, S/C = 0.75; +, S/C = 1.00; ∗, S/C = 1.25; x, S/C = 1.50; □, S/C = 1.75.

hydrocarbons (Equation (10)), Boudouard reaction (Equation (19)) and gasification reaction (Equation (20)), then the observed behavior can be explained as follows. As the temperature is increased, more carbon is formed because of dissociation of hydrocarbons (Equation (10)), however at high temperature, reverse Boudouard reaction (Equation (19)) and gasification reaction (Equation (20)) consume carbon. Thus, it can be thought that these equilibrium reactions determine the moles of carbon over the temperature range.

The different influences of pressure at low and high temperatures can be explained by considering the simultaneous occurrence of the reactions (Equations (11)–(19)). It was argued above that the Boudouard and Reverse gasification reactions are responsible for formation of carbon at low temperature. At high pressure, these reactions should yield higher amount of carbon. However it is observed that, at low temperature, there is a lower amount of carbon at high pressure, which is in contradiction with our previous argument. So only the reactions which could consume the carbon are reverse dissociation reactions (Equations (11)–(17)). Among Equations (11)–(17), it can be shown that the thermodynamic behavior of carbon formation at various temperatures and pressures could be represented by one independent Equation (11).

4.2. Hydrogen yield and product composition of diesel reforming

As stated above, identifying the conditions for carbon-free operation is only one of the metrics for determining the operational regime for reforming processes. Hydrogen yield, defined as moles of hydrogen produced per mole of diesel in the feed is another metric. Furthermore, it is useful to gain understanding of the distribution of other chemical species in the reformate stream. In the following sub-sections, the equilibrium hydrogen yield and product compositions for each of the three different reforming processes are presented.

For all conditions examined, the equilibrium mixture comprised primarily six species – hydrogen, carbon monoxide, carbon dioxide, water vapor, methane and carbon. The other species were present at mole levels less than 1×10^{-5} moles corresponding to less than 0.001 ppm.

4.2.1. Steam reforming

The gas-phase equilibrium mole fraction for key four species – hydrogen, carbon monoxide, carbon dioxide and methane – is presented in Figure 3.8 as a function of temperature and S/C ratio. It is useful to recall that the temperature range of interest for steam reforming is 600-800 °C and that the carbon-free operation requires S/C ratio of 1.75 or greater for this temperature range. However, to avoid carbon formation over the entire temperature range spanning the cooler temperatures in the upstream and downstream process units and tubings, a S/C ratio equal to or greater than 2 would be preferable. The influence of S/C ratio on (gas-phase) hydrogen mole fraction can be seen in Figure 3.8(a). Over 600-800 °C, the hydrogen mole fraction decreases with an increase in S/C ratio. In the same temperature range, the carbon monoxide and methane mole fraction also decreases whereas carbon dioxide mole fraction increases with an increase in S/C ratio. However, the methane mole fraction is less than 0.1 for S/C ratio o,f 1.75 or greater. Thus, the decrease in hydrogen mole fraction appears to be at the cost of increase in carbon dioxide and water mole fractions. H_2S as high as 16 ppm (by volume), which is equivalent to 9.7×10^{-3} ppm (by weight), is observed at low temperatures carbon formation region (*i.e.*, at 400 °C). Negligible amounts of SO_2 are observed.

In systems where the total mole numbers change, assessing the reaction performance in terms of mole fraction can be misleading. Instead, the yield of the desirable product is a metric that should be considered. In Figure 3.9, the hydrogen yield as a function of temperature for different S/C ratio is presented. Indeed, the hydrogen yields exhibit very interesting trends both with respect to S/C ratio and temperature effects. Unlike the hydrogen mole fraction trend, the hydrogen yield increases with an increase in S/C ratio. This would imply that both from carbon-free operation point-of-view and to enhance the hydrogen yields, it would be preferable to operate

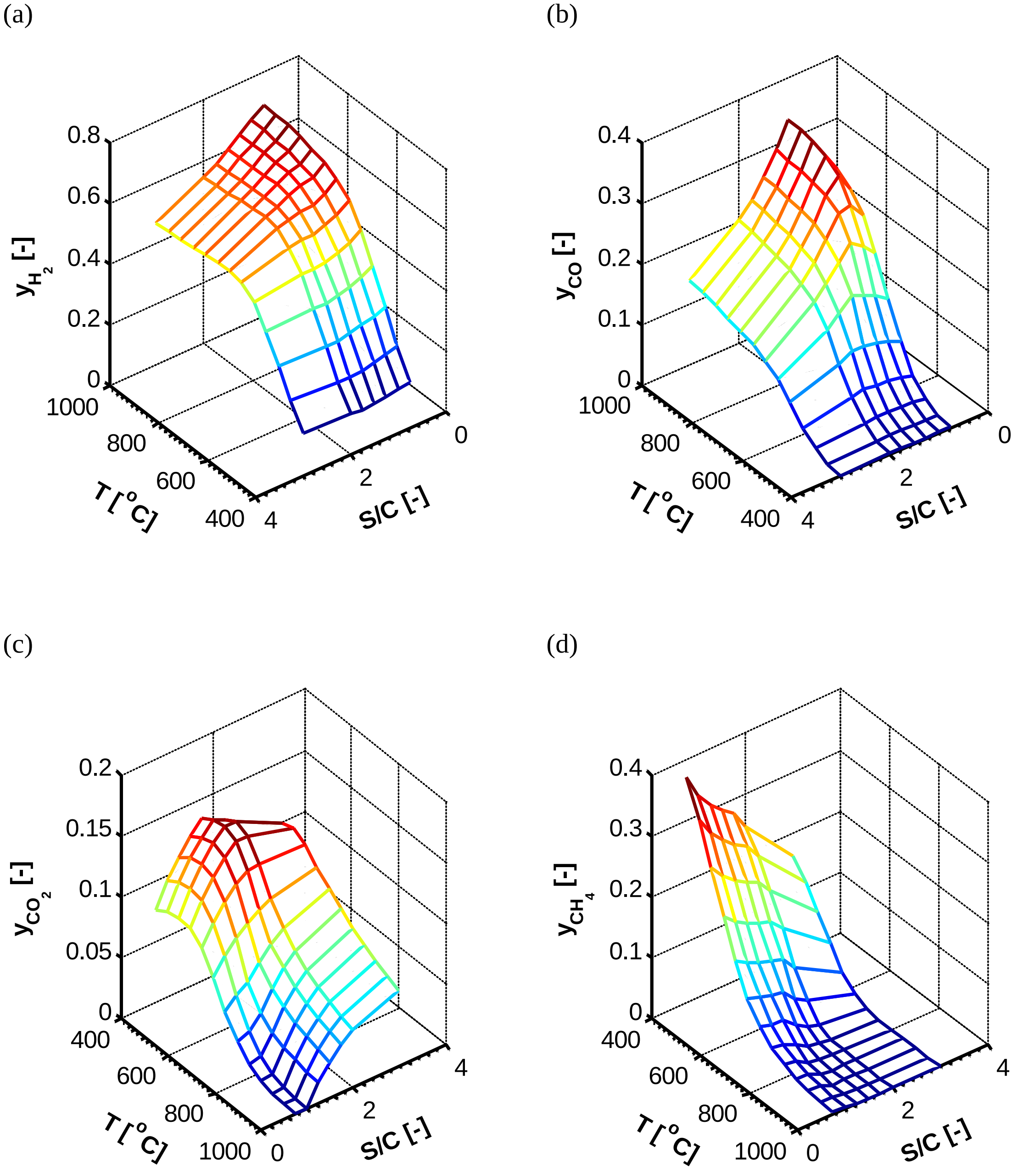

Figure 3.8: Thermodynamic equilibrium gas-phase product mole fraction of H_2, CO, CO_2 and CH_4 for steam reforming at 1 atm. (Note- for Figures (a) and (b) S/C varies from 3 to 0 and for Figures (c) and (d) S/C varies from 0 to 3).

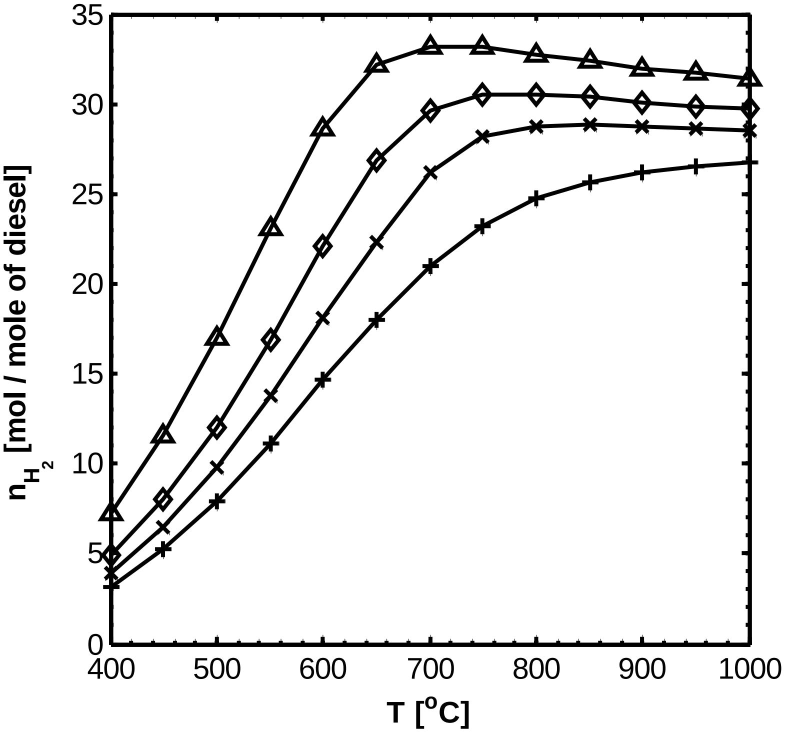

Figure 3.9: Hydrogen yield for SR at 1 atm: +, S/C = 1.00; x, S/C = 1.50; ◊, S/C = 2.00; ⊔ , S/C = 3.00.

at S/C ratios significantly higher than 2. However, higher S/C ratio would also mean higher energy requirements for steam generation. It is also noted that over the S/C ratios of interest, the hydrogen yields level off at higher temperatures. Since, the energy requirements for high temperature operations would also be high, as will be discussed in section 4.3, it would be preferable to operate in the 700–800 °C range.

4.2.2. Partial oxidation

In section 4.1, it was identified that the carbon-free operation for partial oxidation is possible for the entire temperature range of interest 600–1000 °C, if O_2/C ratio is 1.1 or greater. If the POX reactor is operated at higher temperatures (900–1000 °C), a lower O_2/C ratio of 0.75 would allow carbon-free operation. The choice of O_2/C ratio should consider the hydrogen yield. The gas-phase equilibrium mole fraction of key species for POX system is presented in Figure 3.10 as a function of temperature and O_2/C ratio. The hydrogen mole fraction as a function of temperature for O_2/C ratio of up to 1.25 is shown in Figure 3.10(a). Over 600–1000 °C, a dramatic decrease in gas-phase hydrogen mole fraction is seen with an increase in O_2/C ratio. For a given O_2/C ratio, as expected, the hydrogen mole fraction increases with an increase in temperature. Correspondingly, it can be seen from Figure 3.10(b) that the carbon dioxide mole fraction increases and then decreases with O_2/C ratio for a given temperature and increases with an increase in temperature. The mole fraction of carbon monoxide shows a maximum around O_2/C ratio of 0.5 consistent with stoichiometry of reaction (2). Only a small amount of methane is observed at O_2/C ratio greater than 0.5 over the temperature range of operational interest (600-1000 °C). Similar to SR equilibrium compositions, H_2S concentration as high as 20 ppm (by volume), which is equivalent to 1.2×10^{-2} ppm (by weight), was observed at low temperatures (*i.e.*, at 400 °C) and negligible amounts of SO_2 were observed at low temperatures.

Since hydrogen yield is an important metric for assessing reforming process, again, the hydrogen yield as a function of temperature for various O_2/C ratios is presented in Figure 3.11. Several interesting observations can be made from Figure 3.11. At low O_2/C ratios (<0.5), the hydrogen yields are independent of the O_2/C ratio but increase with increasing temperature. Intuitively, it was expected that for the low O_2/C ratio (<0.5), an increase in O_2/C ratio will result in a decrease in hydrogen yield since oxygen would increasingly associate with hydrogen

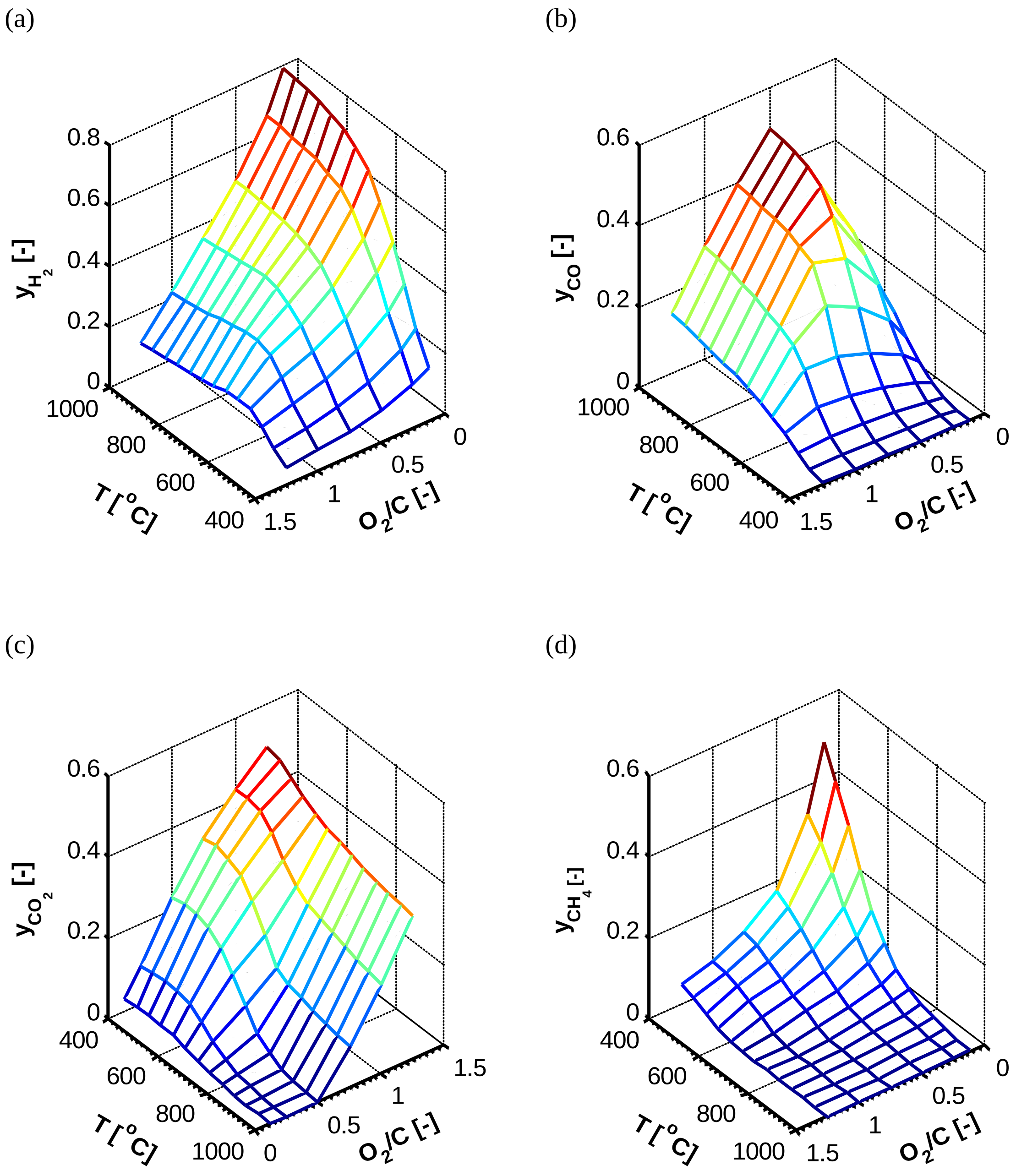

Figure 3.10: Thermodynamic equilibrium gas-phase product mole fraction of H_2, CO, CO_2 and CH_4 for partial oxidation at 1 atm.

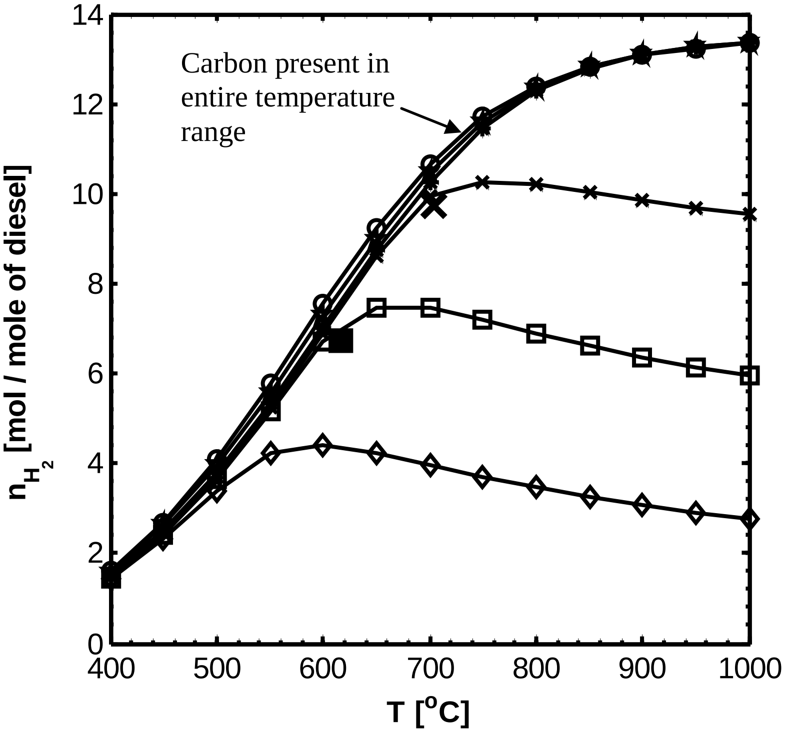

Figure 3.11: Hydrogen yield for partial oxidation at 1 atm: o, $O_2/C = 0.125$; +, $O_2/C = 0.25$; ∗, $O_2/C = 0.5$; x, $O_2/C = 0.75$; □, $O_2/C = 1.00$; ◊, $O_2/C = 1.25$. (Note -Dark marker for $O_2/C = 0.75$ and $O_2/C = 1.0$ indicates the carbon formation boundary).

resulting in an increase in water and a decrease in hydrogen yield. However, for these low O_2/C ratios, an increase in O_2/C ratio results in an increase in CO formation instead of H_2O formation. In fact, for O_2/C ratio ≤ 0.5, CO constitutes over 90% of oxygen-containing species.

For higher O_2/C ratios, the hydrogen yield increases rapidly with the temperature up to a certain temperature and then is nearly invariant for a further small temperature increase but thereafter decreases with an increase in temperature. The temperature at which hydrogen yields exhibits lower change in yields with temperature seems to correspond to the carbon formation boundary temperature. Further, it can be noted that at higher temperatures, for O_2/C ratios greater than 0.5, the hydrogen yields decrease with an increasing O_2/C ratio. These results show that although low O_2/C ratio would appear to be favourable for high hydrogen yields, such operating compositions offer the risk of carbon formation.

The challenge of finding the optimum O_2/C ratio for POX operations is apparent on examining the influence of O_2/C ratio in potentially carbon-free operation region. To ensure carbon-free operation in a POX reactor system, temperature in the upstream and downstream units should also be considered. In particular, the cooler entrance region of POX reactor where temperatures of 600–700 °C may exist, an O_2/C ratio of 1.2–1.25 would be required. The hydrogen yield at these high O_2/C ratios is less than half of that for other O_2/C ratios, for example, of 0.75 at a temperature of 800 °C. On the other hand, despite the high yield at 800 °C for O_2/C ratio of 0.75 thermodynamically carbon-formation can still occur. Even higher temperature operations would overcome this problem but realization of the temperature would again depend on the heat generated during the reaction which is lower for lower O_2/C ratio. Thus, a balance between carbon-free operation and maximization of hydrogen yield is required. It is recognized that these analyses do not consider kinetic effect such that carbon-free operation at lower O_2/C ratio may be possible due to kinetic suppression of carbon formation although thermodynamically this is not the case.

The results discussed above were for oxygen introduced as pure oxygen, which is commercially possible by use of pressure swing adsorption. For simplicity of operation, air instead of oxygen may be employed for generating reformate stream for fuel cell. However, there are two drawbacks of using air as oxygen source. First, in the case of improper reactor operation if the oxygen goes through the reactor unreacted and ends up in the fuel cell anode, it will get oxidized at the anode creating hot spots and can damage the anode or even a cell. Second, the dilution due to the presence of nitrogen also translates into significant lowering of hydrogen partial pressure or concentration which adversely affects the reversible potential and anode electrochemical kinetics. Simulations were carried out to compute equilibrium compositions by using air instead of oxygen as a source of O_2. Similar trends with respect to temperature and O_2/C ratios were observed (results not presented) with the only observation that the hydrogen mole fraction, expectedly, were reduced.

4.2.c. Autothermal reforming

Autothermal reforming is a combination of steam reforming and partial oxidation processes. Thus, both O_2/C and S/C ratios are available as operational parameter for control of the process output. This, however, also expands the region for exploring desirable operating conditions. To minimize redundancy, only the hydrogen yield results are discussed. Figure 3.12(a–c) presents the hydrogen yields a function of S/C ratio and temperature for O_2/C ratio of 0.125, 0.25 and 0.5, respectively. From Table 3.2, the carbon–free operations for O_2/C ratios of 0.125, 0.25 and 0.5 is noted to be for values of S/C ratios exceeding 1.5, ~1.3 and ~0.85, respectively. Thus, examining the hydrogen yields over the temperature range of interest (600–1000 °C) in the carbon-free region, it is noted that the yields do not increase significantly with an increase in the S/C ratios. Thus, it would appear that the S/C ratio should be kept at levels as low as possible to practically avoid carbon formation. For the ease of observing the influence of O_2/C ratio, the hydrogen yield at S/C ratio of 1.75 as a function of temperature for the three

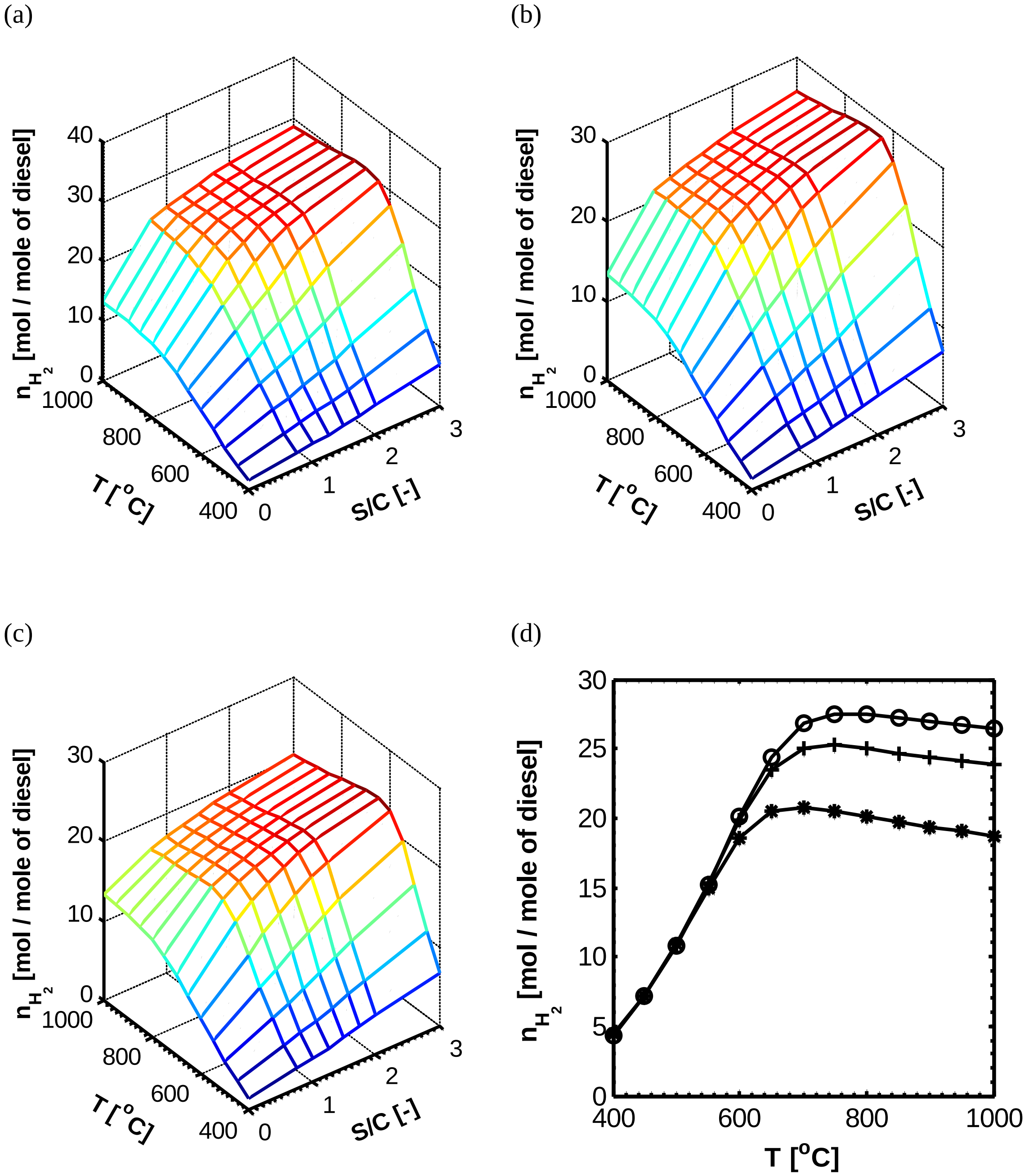

Figure 3.12: Hydrogen yield (moles of hydrogen per mole of diesel) for ATR at 1 atm for S/C=0-3 and (a) O_2/C=0.125, (b) O_2/C=0.25, (c) O_2/C=0.5 and (d) hydrogen yield at S/C = 1.75; and o, O_2/C = 0.125; +, O_2/C = 0.25; ∗, O_2/C = 0.5.

different O_2/C ratios is presented (Figure 3.12(d)). Similar to the POX results, increasing O_2/C ratio results in a significant decrease in the hydrogen yields. In summary, the equilibrium analyses would indicate that it is preferable to operate reactor as low as 750 °C and keep the O_2/C low (0.125–0.25) with S/C greater than 1.25 and ideally 1.75 in order to have no carbon in the entire temperature region.

4.3. Energy requirement and thermo-neutral operation

In the preceding section, the ATR performance was examined purely from chemical equilibrium point. However, it is also important to consider that the ATR operations, by definition, are thermoneutral. That is, there is no external energy requirement for operating the ATR at the desirable state. To assess the energy requirements and viability of thermoneutral operation for recommended operational regime (O_2/C and S/C ratio), enthalpy calculations were carried out. The feed enthalpy was calculated assuming liquid diesel and liquid water and/or air to be fed at 25 °C as shown the system boundary in Figure 3.1. The enthalpy of the equilibrated mixture at a given temperature was computed from the enthalpy data and known composition. Enthalpy data are taken from UniSim package. Diesel property was computed as that of mixture of pure hydrocarbons $C_{14}H_{30}$, $C_{15}H_{32}$, and $C_{10}H_8$ in the molar ratio 0.65: 0.20: 0.15, respectively.

The results of the computations for ATR and steam reforming processes are presented in Figure 3.13. The energy is expressed as kJ per mole of diesel in the feed. The energy requirement of steam reforming process at various S/C ratios is presented in Figure 3.13(a) for information sake and that for ATR at O_2/C ratios of 0.125, 0.25 and 0.5 are presented in Figure 3.13(b,c, and d) respectively. The zero enthalpy change line indicates thermoneutral point. As expected, there is no feasible thermoneutral point for the endothermic steam reforming process. The energy

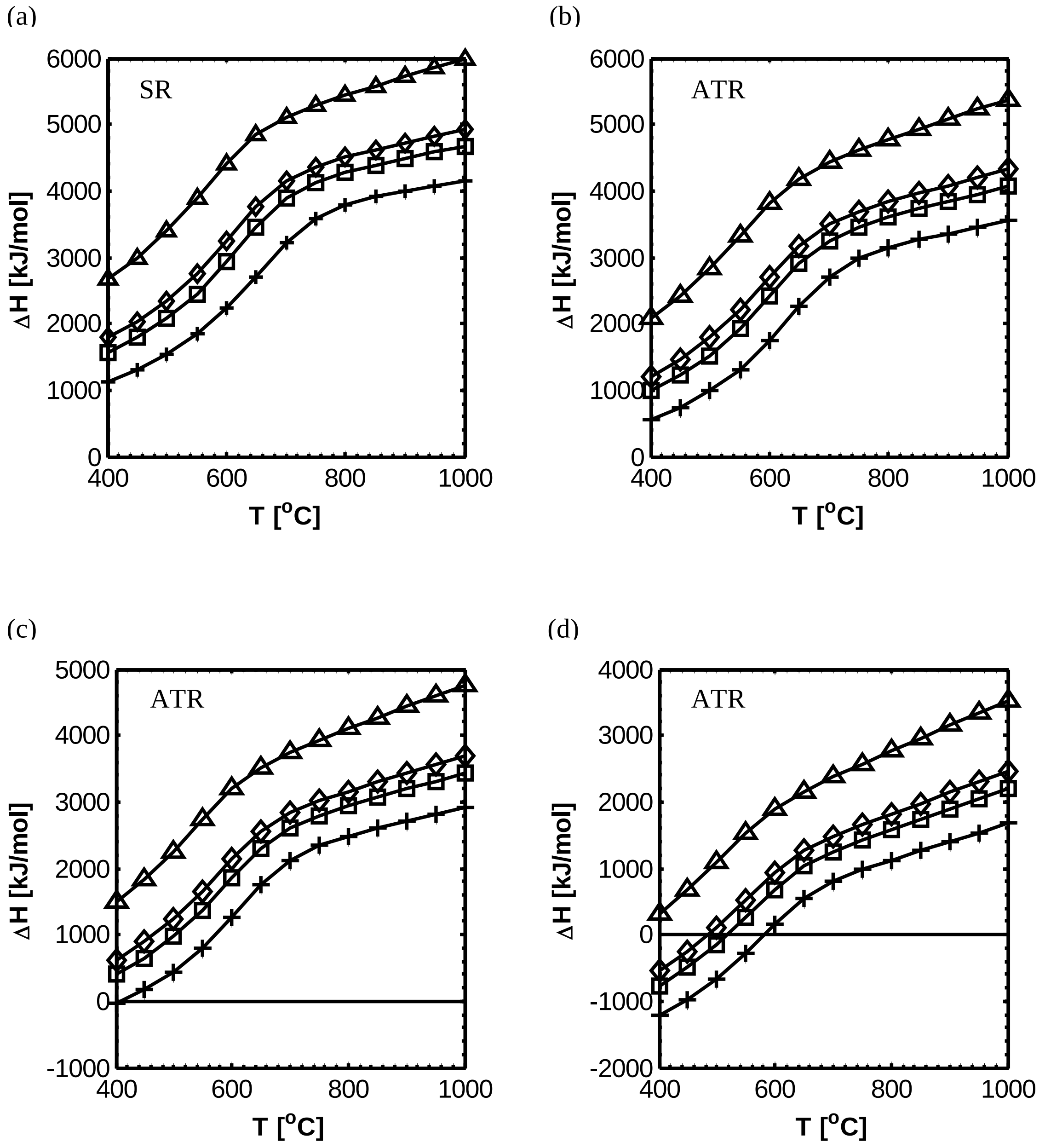

Figure 3.13: Enthalpy change for SR and ATR reactor at 1 atm pressure. Feed is at 25 °C and product is at reactor temperature. (a) O_2/C = 0; (b) O_2/C = 0.125; (c) O_2/C = 0.25; (d) O_2/C = 0.50; +, S/C = 1.25; □, S/C = 1.75; ◊, S/C = 2.00; ⊔ , S/C = 3.00. (Note- Feed contains air).

requirements for SR process are significant with a considerable energy required (>30%) for vaporization of water. For example, for S/C = 1.75, *T*=800 °C, heating of water from 25 °C to 800 °C requires 1739 kJ, which represents 41 % of total endothermic heat of 4200 kJ/mole of diesel for the process.

For the ATR operation, expectedly, the energy inputs are lower than that for SR. The energy requirement reduces with an increase in O_2/C ratio. This is expected since increase in oxygen promotes presence of products of oxidation, an exothermic process. Nonetheless, it can be noted that for O_2/C ratio of 0.125, the operation is endothermic for entire temperature range and S/C ratio greater than 0.75. Upon increasing the O_2/C ratio to 0.25, thermoneutral operation at unfeasibly low temperature of 400 °C is indicated and that too at S/C ratio of 1.0 which is not high enough to avoid carbon-free operation (Figure 3.13(c)). At a further higher O_2/C ratio of 0.5 (Figure 3.13(d)), thermo-neutral operation is possible for S/C ratios of 1.0–2.0. However, the thermo-neutral operation temperature is still low in the range of 500-600 °C, which may not be feasible because of kinetic limitations of the reactions unless appropriate catalysts are found. It can be concluded that the determination of desirable operating conditions wherein carbon-free operation is ensured and hydrogen yield is maximized while energy input is minimized remains a challenging task and requires multi-variable optimization. However, we recommend that it is preferable to operate ATR at O_2/C ratio of 0.25 or little higher by supplying heat to the reformer such that hydrogen yields are maximized.

It is important to recognize that analysis in this work is on one process unit–the diesel reformer. In a larger system, energy flows for all units would have to be considered for overall process optimization. Further, many different system configurations or system integration strategies are possible requiring rigorous process system analysis. Furthermore, for a reformer coupled with a downstream fuel cell unit, different amounts of direct (*e.g.*, radiative heat from SOFC stack to the reformer) and indirect heat (*e.g.*, exhaust gas) will be available depending upon the type of fuel cell, its operating temperature, and its operating point (current density and cell potential). The determination of operating conditions that maximizes either the system output or the system efficiency becomes a non-trivial task with a configuration/operating condition specific solution.

4.4. Reactions representing the overall chemical equilibrium

A few possible overall reactions for reforming are described in section 2.2. It should be noted that the actual reaction mechanism and each reaction described in section 2.2 comprises hundreds of elementary reactions – both surface and gas-phase reactions [7]. From thermodynamics point of view, if one is interested in equilibrium composition of stable species, either a complete knowledge of reaction pathway or an intensive Gibbs minimization calculation is required. However, from the Gibbs free energy minimization calculations presented in this study, it is observed that the major species produced during reforming of diesel are hydrogen, CO, CO_2, CH_4, water and carbon. Thus, it appears that the equilibrium behavior of all three diesel reforming processes can be approximated by computing the composition of 6 species made of 3 elements – C, H and O. In other words, the equilibrium behavior of reforming process can be approximately defined if three independent reactions relating the 6 species are specified with 3 constraint equations imposed by the element balance. In carbon formation region, 6 major reforming species made of 3 elements can be used to describe the equilibrium behavior. That is, the degree of freedom is 6-3=3 requiring only 3 independent reactions relating the 6 species.

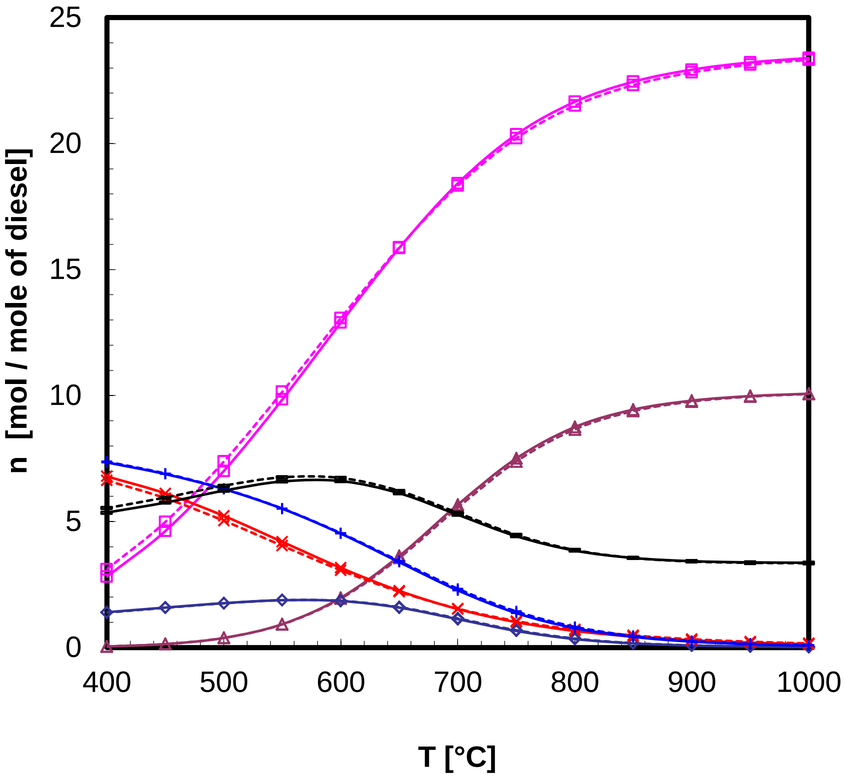

Figure 3.14: Comparison of equilibrium composition predicted by Gibbs minimization and by three independent equations for major products of the reforming. S/C=0.75, —, calculated by Gibbs minimization; ---, calculated by solving 3 independent reactions; □, H_2; ⊔ , CO; ◊, CO_2; x, CH_4, +, H_2O; -, C.

Instead of choosing the reactions either *ad hoc* or by applying statistical methods, we decided to consider Equations (5), (6) and (11) based on the knowledge of reforming processes. However, it should be noted that any two equations out of Equations (4)–(7) can represent the equilibrium composition. Equilibrium computations were carried out in UniSim by considering equilibrium reactor operation and specifying the occurrence of the reactions (5), (6) and (11). The

S/C ratio of 0.75 was selected to ensure the computations were inside the carbon-formation region. The equilibrium composition computed from Gibbs free energy minimization (which considers all 19 species selected in section 3.3) is presented along with the results from the 3 reactions equilibrium reactor operation in Figure 3.14. It can be noted that the composition of the six species predicted from the two different methods compares very well with each other.

Thus, the equilibrium composition for diesel reforming processes can be readily determined by applying the stoichiometric method considering the three reactions (5), (6) and (11) for which the equilibrium constant is given as follows:

$$\ln (K_{eq,5}) = 26194/T - 29.4 \quad (40)$$

$$\ln (K_{eq,6}) = 21791/T - 25.4 \quad (41)$$

$$\ln (K_{eq,11}) = -10171/T + 12.5 \quad (42)$$

It should be noted that the equilibrium constants are unit-less and can be related to the equilibrium activities (defined by Equation (33)) of reactants and products.

5. Conclusions

A thermo-chemical study of reforming of commercial diesel with 50 ppm sulfur content was completed. Equilibrium composition for SR, POX and ATR was obtained by Gibbs free energy minimization routine, implemented in Matlab. A total of 19 chemical species were considered which included in addition to the expected C–H–O species - naphthacene, anthracene, graphite carbon, elemental sulfur, sulfur dioxide, sulfur trioxide, hydrogen sulfide, and sulfuric acid vapor.

Equilibrium calculations for a wide range of temperature 400–1000 °C, steam to carbon ratio (S/C) of 0–3, and oxygen to carbon ratio (O_2/C) of 0–1 spanning the entire range of operations for the three modes of reforming was completed. Carbon formation boundaries were mapped and allowed the identification of carbon-free operating regimes. H_2S is found to be more favourable than SO_2 for all reforming operations and its equilibrium composition as high as 20 ppm (by volume), which is equivalent to 1.2×10^{-2} ppm (by weight), was observed at low temperatures.

In the case of steam reforming, high hydrogen yield with increase in temperature and S/C ratio is observed. In order to avoid the carbon formation for entire range of temperatures S/C ratio should be ≥ 2. It is also found that increasing the S/C ratio increases the hydrogen yield. However, the selection of S/C ratio requires a balance between maximizing hydrogen yield and minimizing energy input both of which increase with S/C.

Thermodynamic analysis suggests that partial oxidation of diesel is least favourable option as it forms high amount of carbon and in order to remain outside the carbon formation boundary, very high temperature and high O_2/C ratio is required. High O_2/C ratio further decreases the hydrogen yield. Dilution by nitrogen, if air is used, makes the process worst and mole fraction of hydrogen in the product stream is lower than 0.2.

In the case of autothermal reforming, for all O_2/C ratios greater than 0.125, S/C ratio of 1.75 is ideal in order to remain in carbon free boundary for entire range of operation. For any O_2/C ratio, S/C above 1.25 marginally increases the hydrogen yield. Above 750 °C, there is very little increase in hydrogen with temperature at the cost of more CO at high temperature. The best operating condition is O_2/C in the range of 0.125–0.25 and S/C greater than 1.25, ideally 1.75 in order to have no carbon in the entire temperature region. Enthalpy analysis indicates that thermoneutral operation of ATR in carbon-free region at temperatures sufficiently high (>700 °C) for reasonable kinetics is not possible. Thus, a recommended ATR operating conditions are 750 °C with O_2/C ratio 0.25 or little higher, S/C greater than 1.25 (ideally 1.75) and with constant heat supply.

Analysis of equilibrium composition for all three reforming modes indicated that only six major species – H_2, CO_2, CO, H_2O, CH_4, and C – exist. Thus, a set of three independent reactions is proposed that along with element balance equations can adequately describe the equilibrium composition for the entire range of reforming operation.

References

[1] No breathing room - national illness costs of air pollution, Summary Report, Canadian Medical Association, August 2008.

[2] K. Ahmed, K. Föger, Thermodynamic analysis of diesel reforming options for SOFC systems, Proceedings-Electrochemical Society, 7 (2003) 1240-1249.

[3] D.-J. Liu, T.D. Kaun, H.-K. Liao, S. Ahmed, Characterization of kilowatt-scale autothermal reformer for production of hydrogen from heavy hydrocarbons, International Journal of Hydrogen Energy, 29 (2004) 1035-1046.

[4] M. Mundschau, C.G. Burk, D.A. Gribble, Diesel fuel reforming using catalytic membrane reactors, Catalysis Today, 136 (2008) 190-205.

[5] Reducing Vehicle Idling, Argonne National Laboratory: Transportation Technology R&D Center, http://www.transportation.anl.gov/engines/idling.html, Accessed - 25-Oct-2008.

[6] C.H. Bartholomew, Carbon deposition in steam reforming and methanation, Catalysis Reviews Science and Engineering, 24 (1982) 67-112.

[7] D. Shekhawat, D.A. Berry, T.H. Gardner, J.J. Spivey, Catalytic reforming of liquid hydrocarbon fuels for fuel cell applications, Catalysis, 19 (2006) 184-254.

[8] A.E. Lutz, R.W. Bradshaw, J.O. Keller, D.E. Witmer, Thermodynamic analysis of hydrogen production by steam reforming, International Journal of Hydrogen Energy, 28 (2003) 159-167.

[9] A.E. Lutz, R.W. Bradshaw, L. Bromberg, A. Rabinovich, Thermodynamic analysis of hydrogen production by partial oxidation reforming, International Journal of Hydrogen Energy, 29 (2004) 809-816.

[10] A. Lindermeir, S. Kah, S. Kavurucu, M. Mühlner, On-board diesel fuel processing for an SOFC–APU—Technical challenges for catalysis and reactor design, Applied Catalysis B: Environmental, 70 (2007) 488-497.

[11] I. Kang, J. Bae, Autothermal reforming study of diesel for fuel cell application, Journal of Power Sources, 159 (2006) 1283-1290.

[12] I. Kang, J. Bae, G. Bae, Performance comparison of autothermal reforming for liquid hydrocarbons, gasoline and diesel for fuel cell applications, Journal of Power Sources, 163 (2006) 538-546.

[13] G.A. Olah, A. Molnar, Hydrocarbon Chemistry, Wiley-Interscience, New Jersey, 2003.

[14] G. Kolb, Fuel processing: for fuel cells, Wiley-VCH, Weinheim, 2008.

[15] Z. Sahin, Experimental and theoretical investigation of the effects of gasoline blends on single-cylinder diesel engine performance and exhaust emissions, Energy & Fuels, 22 (2008) 3201-3212.

[16] L. F. Brown, A comparative study of fuels for on-board hydrogen production for fuel-cell-powered automobiles, International Journal of Hydrogen Energy, 26 (2001) 381-397.

[17] J. Amphlett, R. Mann, B. Peppley, P. Roberge, A. Rodrigues, J. Salvador, Simulation of a 250 kW diesel fuel processor/PEM fuel cell system, Journal of Power Sources, 71 (1998) 179-184.

[18] J.-H. Wang, M. Liu, Computational study of sulfur–nickel interactions: A new S–Ni phase diagram, Electrochemistry communications, 9 (2007) 2212-2217.

[19] P.K. Cheekatamarla, A.M. Lane, Catalytic autothermal reforming of diesel fuel for hydrogen generation in fuel cells: II. Catalyst poisoning and characterization studies, Journal of Power Sources, 154 (2006) 223-231.

[20] W.R. Smith, R.W. Missen, Chemical Reaction Equilibrium Analysis: Theory and Algorithms, Wiley, New York, 1982.

[21] E. Garcia, M. Laborde, Hydrogen production by the steam reforming of ethanol: thermodynamic analysis, International Journal of Hydrogen Energy, 16 (1991) 307-312.

[22] M.W. Chase, J.A.N.A. Force, NIST-JANAF Thermochemical Tables, 1998.

[23] K.M. Pamidimukkala, D. Rogers, G.B. Skinner, Ideal gas thermodynamic properties of CH, CD, CD, CD, CD, CD, CH, CHNCH, and CDNCD, Journal of Physical and Chemical Reference Data, 11 (1982) 83-99.

[24] C.L. Yaws, Chemical Properties Handbook: Physical, Thermodynamic, Environmental, Transport, Safety, and Health Related Properties for Organic and Inorganic Chemicals, McGraw-Hill, New York, 1999.

[25] M. Cimenti, J. Hill, Thermodynamic analysis of solid oxide fuel cells operated with methanol and ethanol under direct utilization, steam reforming, dry reforming or partial oxidation conditions, Journal of Power Sources, 186 (2009) 377-384.

Chapter 4

Kinetic Studies of the Autothermal Reforming of Tetradecane Over Pt/Al_2O_3 Catalyst in a Fixed-Bed Reactor

4.1 **Preface**

This chapter was the first step in the overall goal of developing a mechanistic model for diesel surrogate autothermal reforming. The chapter presents a Langmuir-Hinshelwood-Hougen-Watson (LHHW) type of kinetic model based on ideal surfaces with equivalent adsorption sites and adsorbate species that are randomly mixed and do not interact. Based on a literature surface science study, a simple mechanistic scheme for hydrocarbon (n-tetradecane) reforming on the Pt-Al_2O_3 catalyst is proposed. Several simplifications have been introduced both at the kinetic model development stage and at reactor modeling stage. Next, by applying the physical constraints on the parameters, the model parameter estimation procedure and thermodynamic consistency test are described. With the simplified assumption of constant temperature profile inside the reactor (as the only single point temperature was available), the model predictions show that it can capture the major products (H_2, CO and CO_2) molar flow within 25% of the experimental value and model simulation shows that total oxidation reaction is dominant at the inlet of the reactor catalyst zone. This work was published in “Fuel, 89 (2010) 1212-1220”.

Overall, the model development presented in this chapter and its predictions suggest that to get insight into the n-tetradecane autothermal reforming process a proper understanding of gas-phase reactions before the catalyst, on the catalyst, and after the catalyst is important as these are the reactions that lead to the formation of lower hydrocarbons ($< C_6$) that are normally observed during experimental study. Also, assuming a uniform temperature profile across the reactor bed is not a close depiction of the real reactor temperature. Accordingly, to get the deeper understanding of the n-tetradecane autothermal reforming process, this study indicates the need for detailed gas-phase kinetic model, surface kinetic model, as well as a detailed packed bed reactor model to get an accurate temperature profile.

4.2 **Abstract**

Kinetics of autothermal reforming (ATR) of tetradecane on Pt–Al_2O_3 catalyst over the temperature range 750-900 °C is investigated. Experimental results obtained from NETL (US–DOE) are used for model parameter estimation and validation. Two Langmuir–Hinshelwood–Hougen–Watson (LHHW) type rate models are developed and subjected to parameter estimation and model discrimination. LHHW model in which hydrocarbon is adsorbed on the catalyst surface as alkyl intermediate species by scission of C-H bond gave physically meaningful parameters. Parameters are estimated by using generalized reduced gradient method in spreadsheet and sequential quadratic programming in Matlab. The estimated parameters for the selected model are thermodynamically consistent. The developed kinetic model could capture the experimental behavior of the process and could predict the major components outlet flow rates within 25%.

Keywords: Autothermal reforming; Tetradecane; Kinetics; LHHW model; Thermodynamic consistency

1. Introduction

Liquid hydrocarbons such as diesel possess high energy density, which coupled with existing transportation/storage infrastructure offer an attractive option as fuels for generation of hydrogen-rich stream by reforming. For example, reformate from diesel can serve as a fuel for solid oxide fuel cells (SOFCs), which are being considered as auxiliary power units (APU) in transportation application. APUs can provide the power to heat or to cool the cabin areas and to power electrical systems for refrigeration, lighting, computers and other electronic devices [1] in transportation trucks. Such a diesel-fueled-SOFC based APU system can reduce idling time of primary engine, fuel consumption, emissions and provide longer engine life. Reformation of diesel into hydrogen rich-stream can be attained via three different processes – steam reforming (SR), partial oxidation (POX) and autothermal reforming (ATR) [2].

Reformation of diesel and kinetic modeling of the process is challenging. This is because diesel fuel is a complex mixture of around 400 hydrocarbon species, some 20 organic compounds of sulfur, and additives. The distribution of carbon number of hydrocarbon molecules peaks in the range of 15 to 25 carbon atoms per molecule [3]. Diesel fuel contain mainly iso-paraffins, but also n-paraffins, mono-, di-, tri-, tetra cycloparaffins, alkylbenzenes, naphthalenes and phenanthrenes and even pyrenes [4]. Paraffins are the major constituents of diesel with predominant species being $C_{16}H_{34}$ (38.7 wt.%) [5, 6]. The overall composition and heat of combustion of typical diesel fuel are more closely represented by dodecane [6, 7]. In order to design and optimize a diesel reformer, a better understanding of reforming of different hydrocarbons which constitute the diesel is required. Recent work in this area is mainly focused on experimental study of commercial diesel, and diesel surrogates [5-12].

Studies reporting kinetics of diesel reforming in heterogeneous environment are scarce. Dorazio *et al.* [13] proposed a gas-phase mechanistic study on tetradecane reforming. The proposed mechanism could qualitatively capture some of the behavior of the process but failed to quantitatively predict the experimental data. Sotelo-Boyas and Froment [14] presented a methodology for the generation of reaction network and kinetic model for catalytic reforming of low-octane straight run naphtha into gasoline. Elementary reaction steps for the transformation of each constituent hydrocarbon of gasoline were modeled according to a defined sequence of reaction. They considered that, for bifunctional catalysts (metal/acid), the transformations on the metal sites proceeds via a molecule as a whole whereas the transformations on acidic sites occurs via a ion intermediate and follows carbenium ion chemistry. It is important to point out that their study was focused on hydrocarbon-to-hydrocarbon transformation and not hydrocarbon-to-hydrogen reformation. However, the initial reaction steps for both hydrocarbon-to-hydrocarbon and hydrocarbon-to-hydrogen transformations may be expected to be similar. Berry *et al.* [15, 16] developed a simple power law expression based on experimental findings for diesel autothermal reforming. They found ATR kinetics to exhibit low reaction rate order with respect to O_2 concentration (*i.e.*, almost independent of O_2 concentration) and implied that water strongly inhibits the reaction rate because of negative reaction rate order. Pacheco *et al.* [17] developed and validated mathematical model for ATR of i-C_8 using published reaction network kinetic model and equilibrium parameters of methane reforming proposed by Xu and Froment [18]. A different approach based on Langmuir-Hinshelwood-Hougen-Watson (LHHW) type kinetic model was proposed by Rostrup-Nielsen initially for ethane steam reforming [19] and subsequently extended the generalized reaction mechanism for higher hydrocarbon steam reforming [20]. However, no work has reported for the estimation of kinetic parameters using Rostrup-Nielsel mechanism for higher hydrocarbons reforming.

The objective of the present work is to develop a LHHW type kinetic model for ATR of tetradecane. Experimental data of tetradecane reforming supplied by NETL [12, 21] is used to estimate the model parameters and to validate the model. Two approaches are used in developing surface reaction mechanisms. In the first approach, a mechanism similar to that proposed by Rostrup-Nielsen [20] is assumed. In this approach, dual site hydrocarbon adsorption and carbon–carbon breakage step is considered irreversible. In the second approach, as reported by Zaera [22], it is assumed that hydrocarbon (saturated hydrocarbons which are quite stable) is chemisorbed with scission of one of the C–H bonds. Parameters of kinetic rate expressions based on both approaches are obtained by maximizing the coefficient of determination (*R*-squared coefficient). The obtained parameters are then tested for thermodynamic consistency.

2. Model Development

Reforming has a complex reaction mechanism consisting of thousands of gas-phase and surface reactions. Reforming may comprise different reactions including cracking, isomerization, dehydrogenation/hydrogenation, hydrogenolysis and hydrocyclisation; with possibility of all reactions occurring simultaneously. In reforming hydrocarbon for hydrogen generation, a hydrocarbon molecule may undergo cracking or thermolysis when it comes in contact with high temperature reactor wall before reaching catalyst. As such the hydrocarbon molecule fed will not be the only molecule that undergoes the reforming but a whole spectrum of lighter hydrocarbons that formed due to thermolysis. To simplify such a complex problem, the presence of thermolysis product is usually ignored in the reforming analysis. Since ATR is a combination of both POX and SR reactions, it is essential to take both reactions in the reaction scheme. Kinetics of POX reforming of lighter hydrocarbons such as methane has been subject to many studies [23] but the published kinetic data for the heavier hydrocarbons is scant because of the difficulty in operations at high temperature and short contact time [24]. Pacheco *et al.* [17] studied the kinetics of ATR of isooctane by using combustion approach as described by Jin *et al.* [23] for lighter (methane) hydrocarbon. They assumed that hydrocarbon undergoes combustion followed by both steam and dry reforming. Recently, Ibrahim *et al.* [25] proposed the kinetics of the POX of gasoline over Ni–CeO_2 catalyst as a function of gasoline and oxygen molar flow rates as well as reaction temperature in a tubular fixed-bed reactor. In the present work, an approach similar to Pacheco *et al.* [17] is used. It is also assumed that the hydrocarbon molecule (tetradecane) undergoes total oxidation and produced water is utilized in steam reforming along with the water fed into the reactor and the produced CO_2 takes part in the reaction through water-gas-shift (WGS) reaction scheme. In the case of ATR in which steam is supplied in excess, the total oxidation reaction could be thought of as a summation of three more independent reactions such as partial oxidation, water-gas-shift and hydrogen oxidation. So as soon as small amounts of CO and H_2 form due to partial oxidation at the initial section of reactor bed, CO gets consumed by reaction with water, which is fed in excess, via the WGS reaction and H_2 gets oxidized to water. In the present analysis, these three gas-phase reactions are modeled as combustion reaction. The dry reforming step is not taken into account because dry reforming reaction is summation of steam reforming and reverse WGS reaction. For steam reforming it is assumed that hydrocarbon produce CO and H_2, and CO reacts with water to form CO_2 as per water-gas-shift reaction (WGS). Hence, steam reforming forming direct CO_2 step is avoided. So three independent reactions used for kinetic modeling of ATR of tetradecane are:

$$C_{14}H_{30} + 21.5O_2 \rightarrow 14CO_2 + 15H_2O \qquad \Delta H^{\circ}_{298} = -8850\,kJ/mol \tag{1}$$

$$C_{14}H_{30} + 14H_2O \rightarrow 14CO + 29H_2 \qquad \Delta H^{\circ}_{298} = 2170\,kJ/mol \tag{2}$$

$$CO + H_2O \leftrightarrows CO_2 + H_2 \qquad \Delta H^{\circ}_{298} = -41\,kJ/mol \tag{3}$$

2.1. Kinetic rate expression for tetradecane total oxidation

In this study, for total oxidation reaction, the rate expressions similar to that reported by Jin *et al.* [23] for methane oxidation is used. Pacheco *et al.* [17] used same activation energy as Jin *et al.* in their simulations and only changed the pre-exponential factor to fit the model to data. However, we have estimated all kinetic parameters.

$$r_1 = k_1 p_{C_{14}H_{30}} p_{O_2} \tag{4}$$

where rate constant can be given as

$$k_1 = A_1 \exp\left(-E_1/RT\right) \tag{5}$$

where A_1 is pre-exponential factor (mol/g_{cat}·s·atm^2), E_1 is the activation energy in (kJ/mol), R is the gas constant (kJ/mol·K), and T is the temperature (K)

2.2. Kinetic rate expression for tetradecane steam reforming and WGS reaction

In order to develop the rate expressions for steam reforming and WGS, two approaches are considered and discussed as below.

2.2.1. Reaction scheme 1

In the first approach, the kinetic model developed from the general mechanism provided by Rostrup-Nielsen [20] for hydrocarbon reforming is adopted. It is assumed that hydrocarbon is chemisorbed on dual sites involving dehydrogenation followed by rupture of carbon–carbon bond and formation of surface radical CH_2. Surface reaction is considered as irreversible and surface species. CH_2–L_1 and O–L_1 are assumed to be most abundant surface intermediates. In the case of platinum catalyst, CO can be sufficiently adsorbed on platinum catalyst, so CO adsorption on surface of active catalyst L_1 is assumed [26]. Since CO_2 is weekly adsorbed on the platinum catalyst it is considered negligibly adsorbed [27]. The developed rate expressions for reaction (2) and (3) are:

$$r_2 = \frac{k_2 p_{C_{14}H_{30}}}{DEN^2} \tag{6}$$

$$r_3 = \frac{\dfrac{k_3}{p_{H_2}}\left(p_{CO} p_{H_2O} - \dfrac{p_{CO_2} p_{H_2}}{K_{eq,WGS}} \right)}{DEN^2} \tag{7}$$

where

$$DEN = \left\{ 1 + 2\frac{k_2}{k_{18} K_w}\left(\frac{p_{C_{14}H_{30}} p_{H_2}}{p_{H_2O}} \right) + K_w \frac{p_{H_2O}}{p_{H_2}} + K_{CO} p_{CO} \right\} \tag{8}$$

and the rate constants k_2 and k_3 are considered to follow Arrhenius type dependency on temperature as per Equation (5), K_w is given by $K_w = \exp\left(\Delta S_w^o / R\right)\exp\left(-\Delta H_w^o / RT\right)$, and K_{CO}

is given by $K_{CO} = \exp\left(\Delta S^o_{CO}/R\right)\exp\left(-\Delta H^o_{CO}/RT\right)$, the parameter k_2/k_{18} is lumped into as a constant rather than a function of temperature, ΔH^o and ΔS^o is the standard enthalpy change (kJ/mol) and standard entropy change (kJ/mol·K) respectively. $K_{eq,WGS}$ is the equilibrium constant for water-gas-shift reaction and can be given as $\ln\left(K_{eq,WGS}\right) = \left(4306.6/T\right) - 3.93$, where T is temperature in Kelvin. The reaction mechanism is similar to that given in Rostrup-Nielsen [20], however it is important to point out that denominator do not contain dissociative hydrogen adsorption term as per original Rostrup-Neilsen's ethane reforming model [19] in order to have complete site balance. In summary, reaction scheme 1 includes three rate laws – Equations (4)–(7) with 11 parameters (*i.e.*, A_1, E_1, A_2, E_2, A_3, E_3, $\Delta H^o_{H_2O}$, $\Delta S^o_{H_2O}$, ΔH^o_{CO}, ΔS^o_{CO}, and k_2/k_{18}) that are estimated by fitting to the experimental data provided by NETL.

2.2.2. Reaction scheme 2

The second approach is based on a more fundamental understanding of reaction mechanisms of hydrocarbon reforming processes as provided by Zaera [22]. Using model single-crystal metals and modern surface analytical techniques, Zaera provided a brief but deeper understanding on reaction mechanisms of hydrocarbon reforming processes. It is considered that the hydrocarbon adsorption is accompanied by C-H bond scission forming surface alkyl species. Alkyl surface species can then follow a number of subsequent reactions, hydride, alkyl, and reductive eliminations, insertions, and hemolytic bond scissions, among others (Figure 4.1). Reforming catalyst shows the bifunctional character with rapid hydrogenation-dehydrogenation steps taking place on the hydrocarbon covered surface and more demanding skeletal rearrangement steps

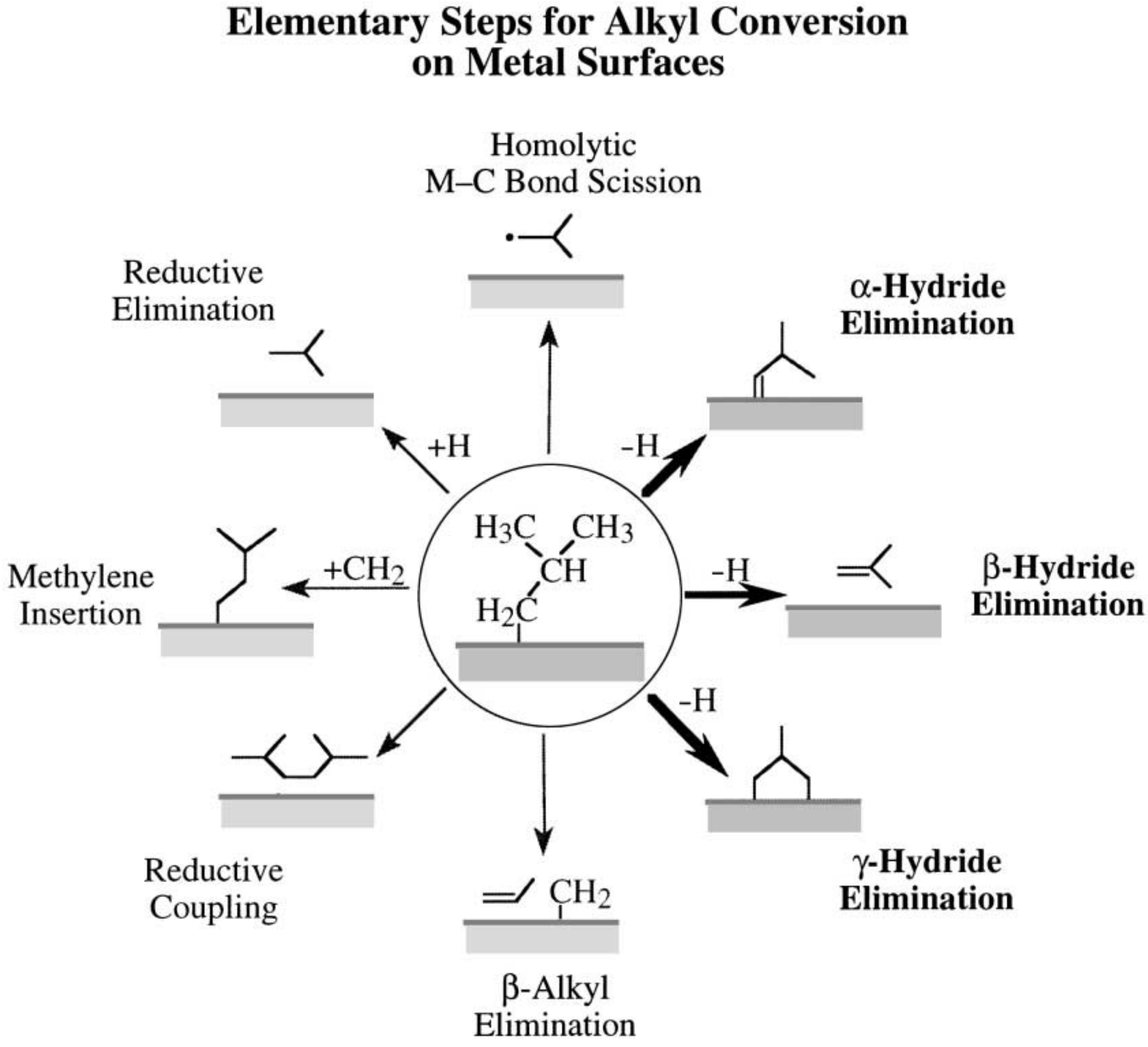

Figure 4.1: Potential elementary steps available to alkyl moeties when chemisorbed on metal surfaces. Adapted from [22].

occurring on patches of bare metal. It is mostly the regioselectivity of the hydride elimination steps that defines the selectivity in reforming. So the nature of the final product is typically determined by competition between hydrogenation and dehydrogenation steps. Zaera demonstrated that β-hydride elimination is responsible for alkene formation, dehydrogenation at α-position leads to eventual C-C bond scissions, and reactivity at γ-carbon is responsible for isomerization or cyclization steps. However, the thermal chemistry of alkyl groups on transition metal surfaces is dominated by the elimination of a hydrogen atom from the β–position, that is, the carbon adjacent to that bonded to the surface. Hence the hydride elimination from the α– and γ–position is much less favourable than from β–carbon. Based on Zaera's [22] reported different reaction steps, experimental observations and information reported in literatures, the following assumptions are made and reaction mechanism shown in Figure 4.2 is developed.

1. There is only single active metal site (support has no effect).
2. Hydrocarbons are assumed to be adsorbed by C–H bond scission.
3. β–hydride elimination, which is more facile reaction, forms alkenes.
4. β–alkyl elimination leads to surface CH_2 species.
5. Very small amount of C_6H_6 and negligible amount of isoparaffins and branched olefins are observed in the experiments, so reactivity at γ–position which is responsible for isomerization and cyclization is assumed negligible.
6. No cracking reaction in gas-phase or on the high temperature catalyst support and reactor wall.
7. Hydrogen is assumed to be dissociatively chemisorbed on the platinum (Pt) surface [28-31]. Since hydrogen adsorption on pure Al_2O_3 is weak and reversible [31], it is assumed that hydrogen is chemisorbed on Pt sites only. Some recent studies have found that H_2 is both physically adsorbed and chemically adsorbed, or initially physically adsorbed and then dissociate to form Pt–H bond [32].
8. Carbon monoxide is assumed chemisorbed on Pt active site [26].

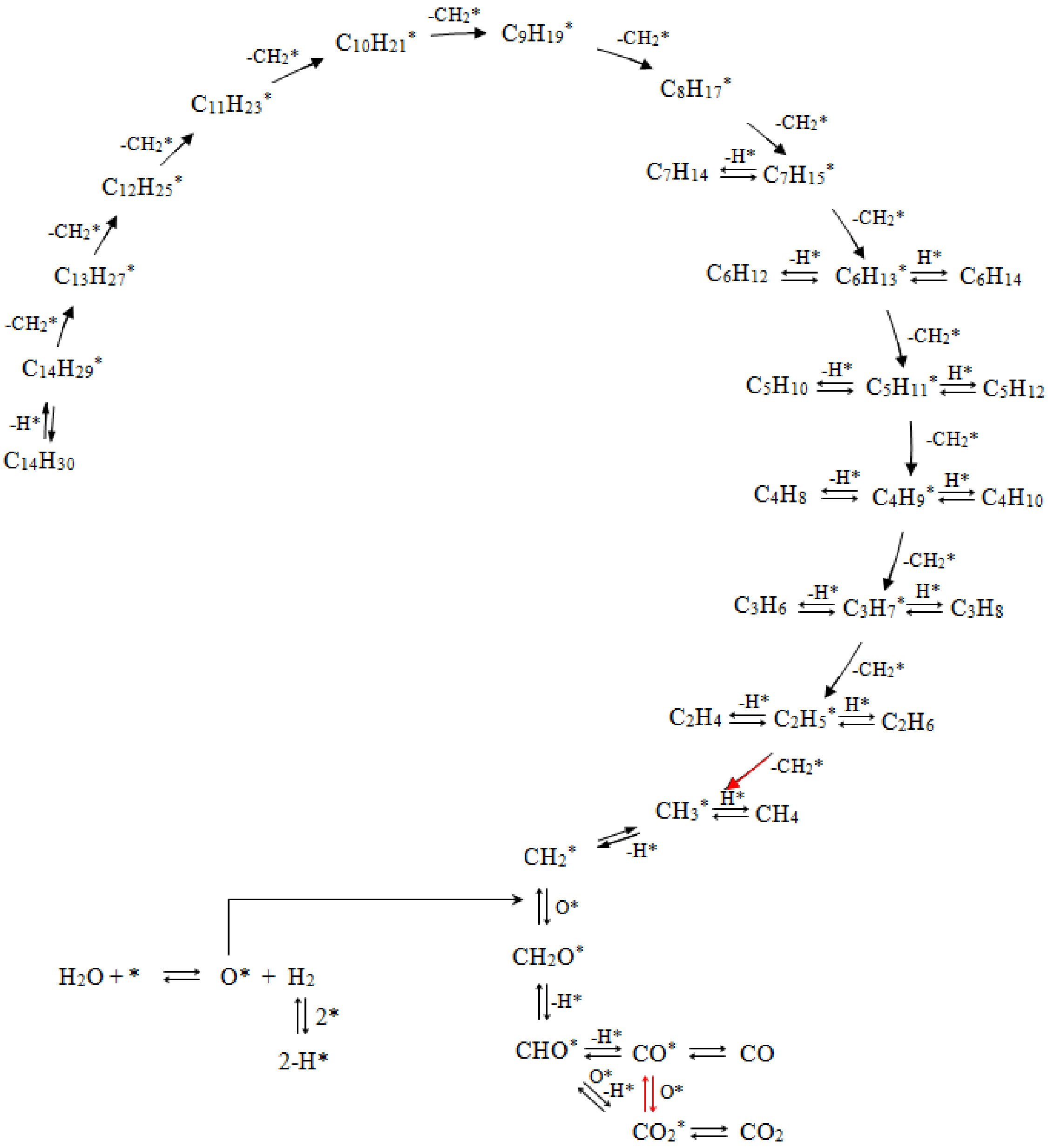

Figure 4.2: Proposed reaction mechanism (Rate determining steps are shown in red).

9. CO_2 is weakly adsorbed on the platinum catalyst hence considered negligibly adsorbed [27].

10. Although some of the studies suggest that water is dissociated on platinum active sites to form H and OH surface species [33], as reported by Xu and Froment [18] for nickel catalyst, it is assumed that water reacts with Pt atoms yielding adsorbed oxygen and gaseous hydrogen as bond strength of Pt–O is strong [33].
11. It is assumed that all reactions ultimately give CH_2 surface adsorbed species, which then reacts with adsorbed surface oxygen species. This is same as Xu and Froment [18] reaction mechanism.
12. Major adsorbed species on the surface of the catalyst are CH_2*, H*, O*, CO*.
13. Although in actual mechanism all the species produced during the reforming are included, only steam reforming and water-gas-shift part of the reaction scheme is used. So CH_4 and other all high hydrocarbon species are considered as unreacted C_{14}.
14. For steam reforming reactions, C-C bond breakage is considered irreversible and rate determining step. Rate determining step is shown in Figure 4.2.
15. For water-gas-shift reaction, a reaction similar to Xu and Froment [18] is considered as rate determining step. Rate determining step is shown in Figure 4.2.
16. For the experiments, the reactor bed temperature was controlled but only a single point bed temperature was measured. Thus, it was assumed that the entire bed was at the measured temperature. Thus, the assumption of isothermal and isobaric reactor conditions was applied.

By adopting above simplifying assumptions, steam reforming and water-gas-shift reaction rate expressions are developed following the steps given in Appendix–A.

$$r_2 = k_2 \frac{p_{C_{14}H_{30}}}{\sqrt{p_{H_2}}} \Bigg/ DEN_1^2 \qquad (9)$$

$$r_3 = \frac{k_3}{P_{H_2}}\left(p_{CO} p_{H_2O} - \frac{P_{H_2} p_{CO_2}}{K_{eq,WGS}} \right) \Big/ DEN_1^2 \tag{10}$$

where

$$DEN_1 = 1 + a\frac{p_{H_2}^2 p_{CO}}{P_{H_2O}} + K_{H_2O}\frac{p_{H_2O}}{P_{H_2}} + K_{CO} p_{CO} + \sqrt{K_{H_2} p_{H_2}} \tag{11}$$

where K_i can be given as $K_i = \exp\left(\Delta S_i^o / R\right)\exp\left(-\Delta H_i^o / RT\right)$, ΔH^o and ΔS^o is the standard enthalpy change (kJ/mol) and standard entropy change in (kJ/mol·K) respectively. $K_{eq,WGS}$ is the equilibrium constant for water-gas-shift reaction. In summary, reaction scheme 2 includes three rate laws – Equations (4), (9)–(10) with 13 parameters (*i.e.*, A_1, E_1, A_2, E_2, A_3, E_3, $\Delta H_{H_2O}^o$, $\Delta S_{H_2O}^o$, ΔH_{CO}^o, ΔS_{CO}^o, $\Delta H_{H_2}^o$, $\Delta S_{H_2}^o$ and a) that are estimated by fitting to the experimental data provided by NETL.

3. Experimental Data

For parameter estimation of the kinetic model, experimental data were obtained from NETL's (US-DOE) kinetic study for tetradecane autothermal reforming on Pt/Al_2O_3 catalyst in a fixed-bed reactor [12,21]. The reactor was operated continuously at steady state and about 0.9 g of Pt/alumina catalyst was used for these runs. Pt loading was 0.611 wt% and BET surface area was 103 m^2/g. The temperature was varied between 750 °C – 900 °C and Gas Hourly Space Velocity (GHSV) was in the range of 43,000 – 200,000 1/h. The data comprised of a set of 13 experiments with O_2/C ratio 0.3 and steam/carbon ratio 1.5 [13]. Prior to gas analysis, the reactor effluent gas was passed through the condenser to remove water and any other unreacted or heavy hydrocarbons. Dry effluent analysis included H_2, CO, CO_2, CH_4, C_2H_6, C_2H_4, C_3H_8, C_4H_{10}, C_5H_{10}, C_5H_{12}, C_6H_{12}, C_6H_{14}, C_7H_{14}, C_6H_6, and unconverted O_2. Concentration of water is obtained by O atom balance.

4. Model Parameter Estimation

Experimental data are used to obtain the parameters of developed kinetic models and discriminate between the models. The packed bed reactor represents a distributed system, an integral analysis of the reactor data was necessary for parameter estimation, which is based on minimization of SSE (squared sum of residuals) of outlet flow of components. Assuming isothermal and isobaric operations, the following set of differential equations are solved:

$$\frac{dF_i}{dW} = \frac{dF_i}{\rho A dZ} = \sum_{j=1}^{j=M} \upsilon_{i,j} r_j \quad for\, i = 1....n \tag{12}$$

where ρ is bulk density of catalyst, which is 0.83 gm/cc, A is the cross section area, which is 0.866 cm^2, F is flow rate of species i in mol/min, W is weight of catalyst in gms, $\upsilon_{i,j}$ is stoichiometric coefficient matrix, j is reaction number. The calculated outlet flow rates of H_2 and O_2 for all 13 experiments is compared with experimental flow rates. Ratio of SSE/TSS (total squared sum) is minimized, that is coefficient of determination (R^2) is maximized, by using spreadsheet solver function and Matlab fmincon function. Initially the spreadsheet solver function is used to estimate the parameters by maximizing the objective function coefficient of determination (R^2). The spreadsheet uses Euler method with sufficiently low step size so that the ODE45 function in Matlab generate approximately the same value as predicted by the Euler method having maximum of 5–10% error. The estimated parameters from spreadsheet solver are used as an initial guess to obtain refined parameters in Matlab using Runge–Kutta 4^{th}–5^{th} order algorithm and sequential quadratic programming (SQP) *i.e.* ODE45 and fmincon functions, respectively. Objective function SSE/TSS is minimized to estimate the refined parameters. Further, parameter estimation using Matlab lsqnonlin function did not result in any change in estimated parameters. In order to guide the minimization routine to some logical point, the parameters like standard heat of adsorption and standard entropy change are subjected to thermodynamic consistency constraints [18, 31, 34] as follows:

$$\Delta H_{ad}^{o} < 0 \tag{13}$$

$$0 < -\Delta S_{ad}^{o} < S_{g}^{o} \tag{14}$$

A constraint is also applied on activation energy ($E > 0$) and preexponential factors ($A > 0$) so that the solutions do not converge to any negative value which is physically meaningless. It should be noted that when estimating the kinetic parameters, first all parameters are estimated by comparing the outlet hydrogen flow rates and then the parameters are refined by comparing the outlet O_2 flow rate.

For predicted outlet molar flow of H_2, CO, CO_2, H_2O, and O_2, mean square regression ratio test is applied to check whether model has picked up significant trend.

$$Test\ Ratio = \frac{MSR}{MSE} \tag{15}$$

where MSR is mean square regression and MSE is mean square error.

5. Results and Discussion

5.1. Model Discrimination

The two kinetic models described in section 2.2 were subjected to parameter estimation. The estimated parameters for second kinetic model are reported in Table 4.1.

For the first kinetic model, which is based on Rosentrup-Nielsen [20] mechanism, the ratio k_2/k_{18}, which represents the ratio of tetradecane adsorption rate constant (k_2) to the rate constant of adsorbed methylene reaction with adsorbed oxygen (k_{18}) and is set as a constant in Equation (8), always ended up in a negative value. By introducing the constraint of non-negative constant value, the spreadsheet solver function could not maximize coefficient of determination (R^2) value. Without applying any constraint, model predictions are good however the model parameters are not thermodynamically consistent and ratio of k_2/k_{18} is negative. Physically the ratio of k_2/k_{18} should always be positive, hence the model was abandoned.

The second kinetic model, which is based on a more fundamental mechanism, is found to give thermodynamically consistent and physically meaningful estimated parameters (discussed in detail in section 5.3). As discussed in section 4, the obtained parameters from spreadsheet are fed as an initial guess into Matlab optimization function and more refined parameters are obtained using Runge-Kutta 4th-5th order algorithm and sequential quadratic programming (SQP). Computations for 13 experimental runs in the data set each comprising molar flow of 5 species (H_2, CO, CO_2, H_2O, and O_2) were carried out. That is, a total of 65 data points (*i.e.*, $n = 65$) were used. Thirteen parameters are estimated (*i.e.*, $p = 13$). The calculated ratio of MSR/MSE is 358.7, which is much greater than $F_{(p-1),(n-p),0.05}$. Hence, the null hypothesis that MSR and MSE are equal was rejected and it was concluded that model was able to pick up significant trend.

Table 4.1: Estimated parameters

Parameter	Units	Value
k_1	A_1 (mol/g_{cat}·min·atm^2)	100
	E_1 (kJ/mol)	47.28
k_2	A_2 (mol/$atm^{1/2}$·g_{cat}·min)	560
	E_2 (kJ/mol)	102.66
k_3	A_3 (mol/atm·g_{cat}·min)	273
	E_3 (kJ/mol)	141.14
$\Delta S^o_{H_2O}$	kJ/mol·K	0.011
$\Delta H^o_{H_2O}$	kJ/mol	63.62
ΔS^o_{CO}	kJ/mol·K	-0.151
ΔH^o_{CO}	kJ/mol	-90.01
$\Delta S^o_{H_2}$	kJ/mol·K	-0.125
$\Delta H^o_{H_2}$	kJ/mol	-80.17
a		0.56

5.2. Comparison of Model Predictions with Experimental Data

The predictions from second kinetic model are compared with experimental data for molar flow rates of key species at reactor exit. These results are presented in Figures 4.3−4.7. It can be seen from Figures 4.3−4.7 that the model is able to capture the general trends over a wide range of GHSV or residence time. Figures 4.3 and 4.4 show a peak in hydrogen and CO production at the residence time of about 5–6 ms. The model could capture the peak for both components and model prediction at 825 °C is close to that of experimental ones. There is some discrepancy between observed and predicted results at 750 °C and 900 °C. These discrepancies could be attributed to the experimental/measurement errors and limitation of kinetic model. Again for CO_2 (Figure 4.5) the model could capture the behavior of high amount of CO_2 at low residence time *i.e.*, high GHSV. At low residence time a considerable difference between observed and predicted results is obtained which could be attributed to the limitation of kinetic model and at least partially to measurement errors at low concentration. A very good agreement between predicted and experimental results of water is obtained at all temperatures and GHSV (Figure 4.6). In Figure 4.7, the predicted outlet oxygen flow rate is compared with experimental data. It should be noted the outlet oxygen concentration is low, which indicates that the measurements made

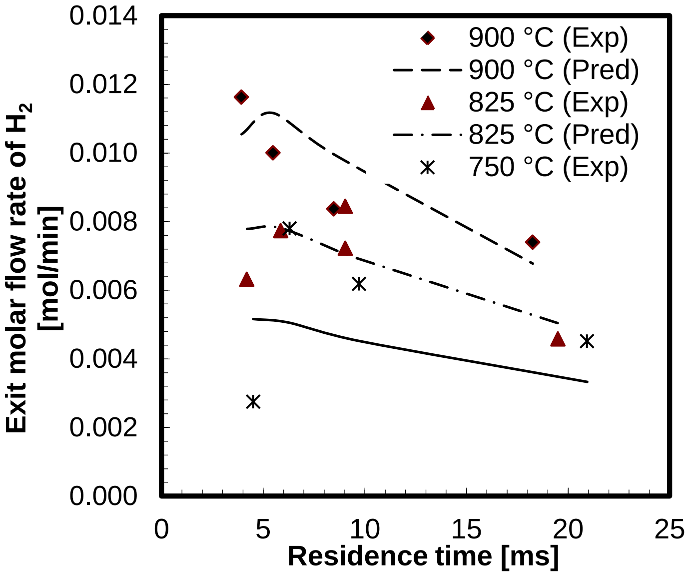

Figure 4.3: Experimental vs. predicted molar flow rate of hydrogen.

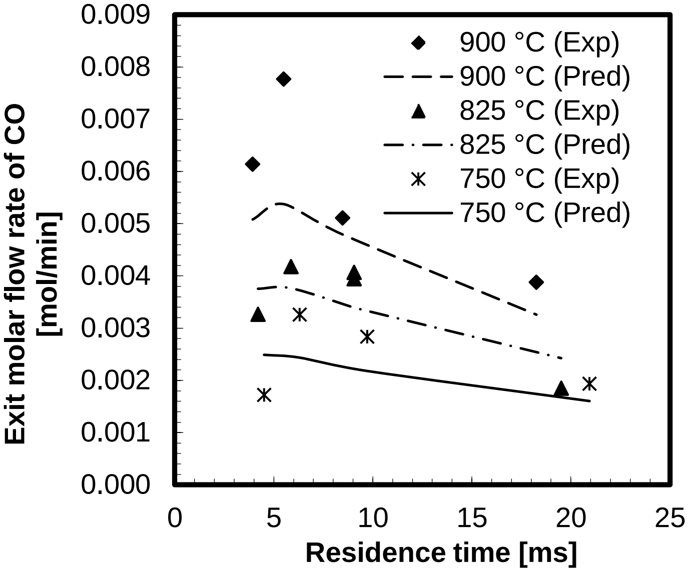

Figure 4.4: Experimental vs. predicted molar flow rate of CO.

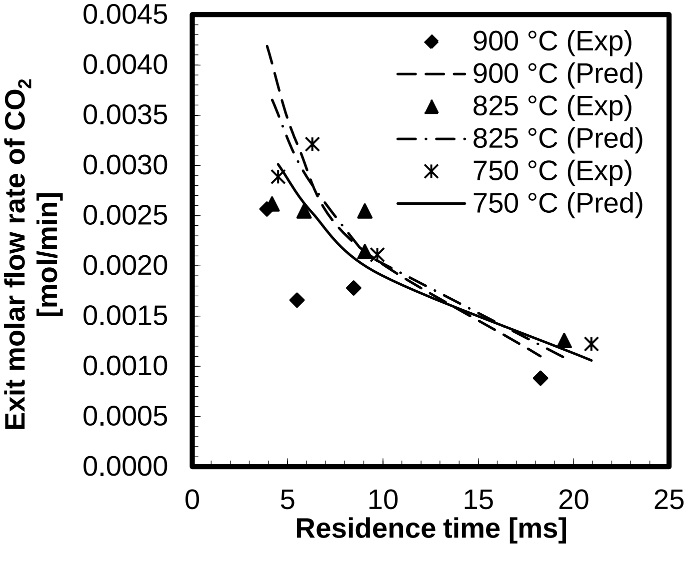

Figure 4.5: Experimental vs. predicted molar flow rate of CO_2.

may have errors associated. Experimentally, it is observed that as the residence time is increased, the O_2 flow rate decreases and then increases again. It is difficult to provide an intuitive explanation of this phenomenon. The kinetic model was also unable to capture this trend. At 900 °C, experimental data shows oxygen conversion increases and then decreases with lowering GHSV, which indicates some experimental or measurement error. The model predicts smooth decrease in oxygen concentration (*i.e.*, high conversion) with a decrease in GHSV and the predicted results do not capture the unexpected experimentally observed behavior of an increase in oxygen conversion after an expected initial decrease with increasing residence time.

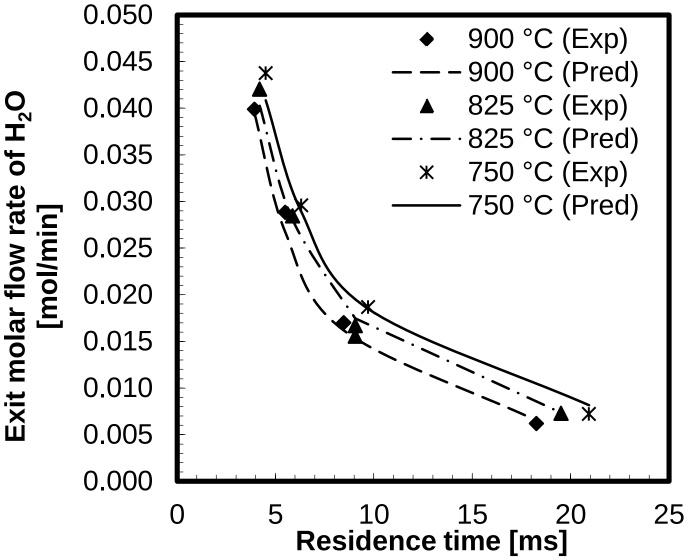

Figure 4.6: Experimental vs. predicted molar flow rate of H_2O.

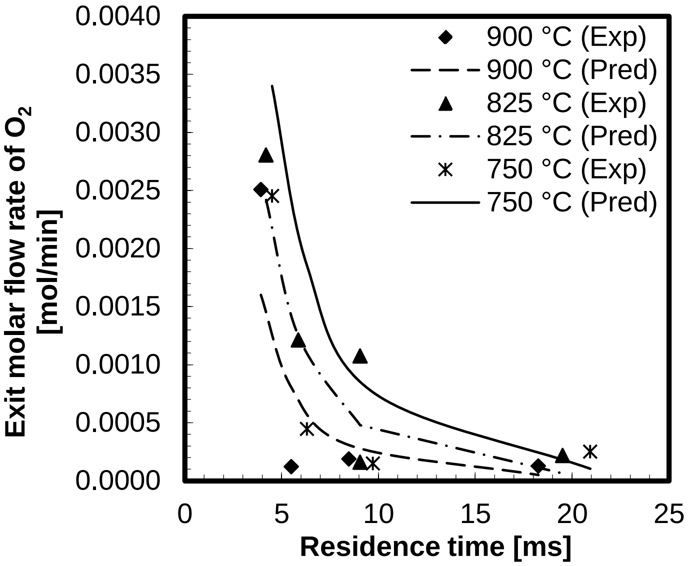

Figure 4.7: Experimental vs. predicted molar flow rate of O_2.

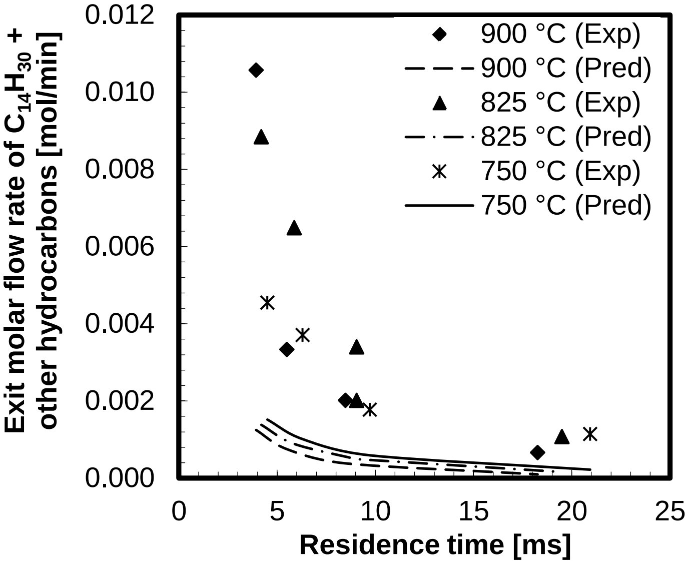

Figure 4.8: Experimental molar flow rate of C_{14} + hydrocarbons vs. predicted molar flow rate of C_{14}.

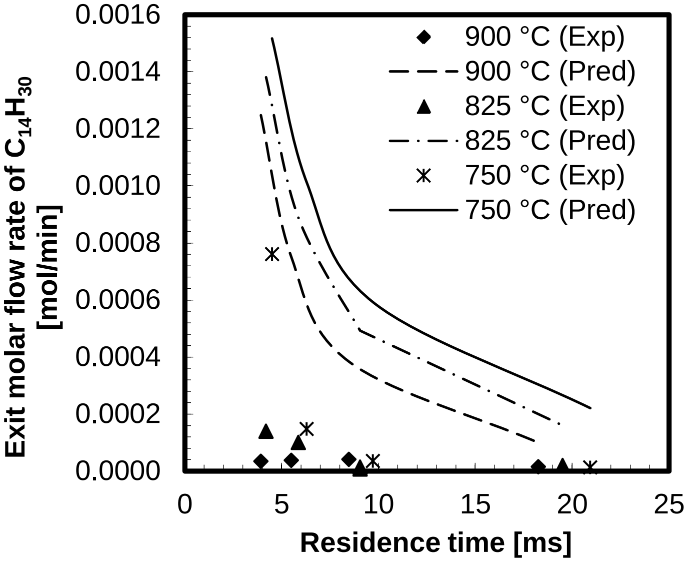

Figure 4.9: Experimental vs. predicted molar flow rate of C_{14}.

In Figure 4.8, it is observed that total experimental hydrocarbon molar flow (including C_{14}) is higher than the predicted C_{14} molar flow and Figure 4.9 indicates that experimental C_{14} molar flow is lower than the predicted C_{14} molar flow. This result is not surprising and simply points to the deficiency of not considering the formation of all hydrocarbons (for example, CH_4 and higher hydrocarbons) from overall reaction mechanism. Inclusion of all these hydrocarbons would result into high moles of hydrocarbon products (as per mechanism one mole of C_{14} forms more moles of hydrocarbons) and would have predicted higher molar flow than the current values. Even the inclusion of formation of other hydrocarbons resulted into lower value of C_{14} predicted as more C_{14} would have consumed. This is further confirmed by comparing the experimental and predicted volumetric flow as shown in Figure 4.10. The predicted volumetric flow is lower than the experimental volumetric flow. This indicates the effect of not considering other hydrocarbons in the calculation. Hence, inclusion of all hydrocarbons by providing some rate expression which describes formation of all hydrocarbons from C_{14} could result in better prediction for all hydrocarbons. However, it should be emphasized that the predicted molar flow of all components as shown in Figures 4.3–4.6 could alter after including all hydrocarbons. But since the molar flow is very low, the change in predicted molar flow would be minor.

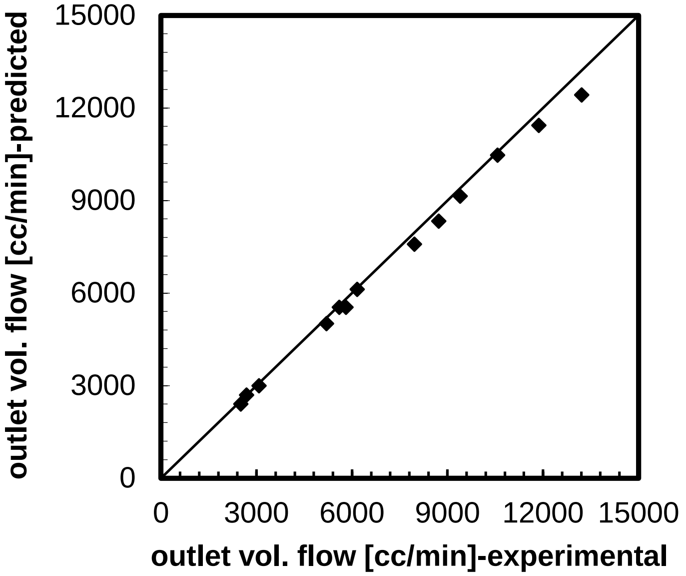

Figure 4.10: Experimental vs. predicted total volumetric flow at the reactor exit.

It is useful to mention that the current study reports initial results of our research on the development of kinetic model for diesel reforming processes. It must be noted that simplifications made in this study – such as neglecting gas-phase cracking reactions, exclusion of higher hydrocarbons and considering only three global reactions with six components with proposed steam reforming mechanism – must be relaxed to improve model prediction and description of the reforming operation. Nonetheless, the six component kinetic model presented in this study, although simple, is able to predict both qualitatively the experimental observed behavior of major components and quantitatively the molar flow within 25% as shown in Figure 4.11. For very low concentrations, *i.e.*, the molar flow rates lower than 0.0025 mol/min at the outlet of the reactor, the differences between the experimental data and the model predictions are higher than 25%. The difference can be attributed, at least partially, to the measurement errors at such a low concentration. In addition, the limitations of a three reaction, six components reaction scheme as pointed out above contribute to the differences.

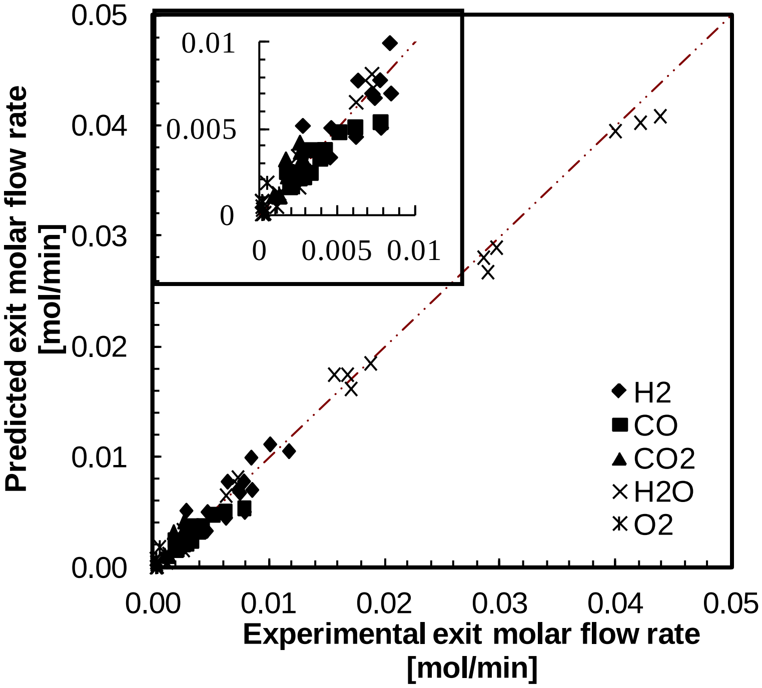

Figure 4.11: Experimental vs. predicted molar flow rates.

For high GHSV experimental runs, it is also observed that tetradecane undergoes oxidation reaction and produces water and CO_2 in the initial 15–20 % bed length and then steam reforming and water-gas-shift reactions controls the product composition. Around 50 % of the oxygen is consumed in initial 15 to 20 % of the reactor bed length (Figure 4.12). In the case of low GHSV, the oxidation reaction is dominant in the initial 5% of the bed length (not shown). It should be noted here that the bed temperature is considered constant as a single point bed temperature was measured and controlled in the experiments.

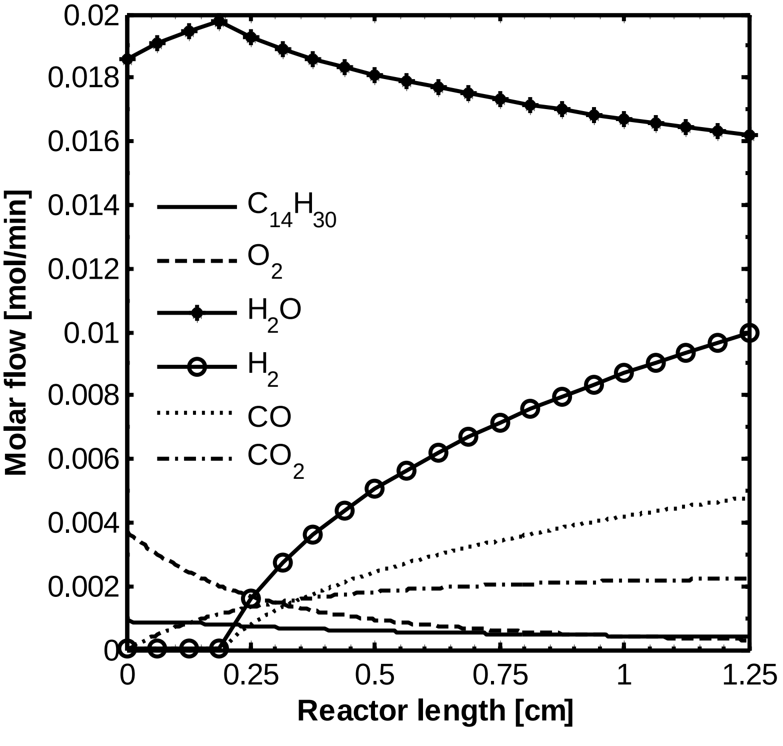

Figure 4.12: Predicted molar flow rates of species along the length of the reactor, GHSV 92,778 1/h and 900 °C.

5.3. Thermodynamic consistency of estimated parameters

The estimated parameters are reported in Table 4.1. Jin *et al.* [23] reported the activation energy for total oxidation of methane as 162 kJ/mol. The same value of activation energy is used by Pacheco *et al.* [17] for isooctane oxidation. However, the current analysis estimated lower activation energy (47.28 kJ/mol) for tetradecane. This could be attributed to the lower auto-ignition temperature of tetradecane (200 °C) than methane (630 °C) [35]. For steam reforming of tetradecane the activation energy is 102.66 kJ/mol. In general, it is said that the activation energy should be greater than heat of reaction (*i.e.*, $E > \Delta H$). In the case of steam reforming of tetradecane, this argument is not applied as rate constant is a lumped parameter.

Since steam adsorption step ($H_2O + * \leftrightarrows O^* + H_2$) is not actually any dissociative or non-dissociative chemical or physical adsorption step, its estimated parameters are not subjected to thermodynamic consistency. However, Xu and Froment [18] estimated $\Delta S^o_{H_2O}$ and $\Delta H^o_{H_2O}$ for nickel catalyst 0.100 kJ/mol·K and 88.68 kJ/mol, respectively. In this study, parameter estimation for Pt catalyst resulted in 0.01058 kJ/mol·K and 63.62 kJ/mol respectively.

While estimating the parameters like ΔH^o_{ad} and ΔS^o_{ad} for dissociative chemisorption of H_2 and chemisorption of CO, thermodynamic consistency constraints as shown in Equations (13)–(14) are applied. The estimated parameters are then passed though the major consistency test as given by Vannice *et al.* [34].

$$10 \le -\Delta S^o_{ad} \le 12.2 - 0.0014\Delta H^o_{ad} \quad (\text{in cal/mol}) \tag{16}$$

Theoretically hydrogen bond energy is 436 kJ/mol and Pt-H bond energy [36] is 261.5 kJ/mol. This gives -87 kJ/mol heat of dissociative chemisorption of H_2 on Pt metal atom. The estimated value (-80.16 kJ/mol) is close to the theoretical value. Guerrero-Ruiz [28] reported that heat of chemisoption of CO (approximately -140 kJ/mol on Pt/activated carbon catalyst) is higher than that of hydrogen. Podkolzin *et al.* [37] reported that heat of chemisorption of CO decreases with coverage from initial value of -190/-180 kJ/mol to -75 kJ/mol at saturation CO coverage on Pt/SiO_2. Estimated heat of chemisorption of CO (-90 kJ/mol) on Pt/alumina catalyst is higher than that of hydrogen and is within the range predicted by Podkolzin *et al*. [37].

For CO and H_2, the S_g^o values at 298 K are 0.198 and 0.13 kJ/mol·K, respectively. The estimated $-\Delta S_{ad}^o$ values for CO and H_2 are 0.151 kJ/mol·K and 0.125 kJ/mol·K, respectively, which are less than S_g^o as per thermodynamic consistency constraint.

Third criterion suggests that the minimum entropy change during dissociative or non-dissociative adsorption should be a minimum of 10 e.u. (cal/mol·K) and should be less or equal to $12.2-0.0014\Delta H_{ad}^o$, where ΔH_{ad}^o is in cal/mol. For CO and H_2, estimated $-\Delta S_{ad}^o$ values are 36.09 cal/mol·K and 29.88 cal/mol·K respectively and the value of the term $12.2-0.0014\Delta H_{ad}^o$ are 42.31 and 39.02 respectively. Hence, the consistency criterion (Equation (16)) is satisfied.

6. Conclusions

Kinetics of tetradecane reforming on Pt–Al_2O_3 catalyst is investigated using three independent global reactions with six model components such as $C_{14}H_{30}$, O_2, H_2O, H_2, CO, and

CO_2. For ATR, total combustion route is selected and since excess water is fed to the ATR the total oxidation reaction could be assumed to be summation of partial oxidation, WGS and hydrogen oxidation. The global total oxidation reaction is modeled by power law rate expression. For steam reforming and WGS reactions, model equations are derived from the reaction mechanism proposed by Rostrup-Neilson and developed reaction mechanism. The parameters of all three rate expressions are estimated by using the experimental data provided by NETL. The kinetic parameters for the model are estimated by using generalized reduced gradient method in spreadsheet and sequential quadratic programming in Matlab. The models are then subjected to model discrimination. The second fundamental LHHW model in which hydrocarbon is adsorbed on the catalyst surface as alkyl intermediate species by scission of C–H bond is found to give physically meaningful parameters. The estimated parameters for the selected model are thermodynamically consistent. The developed reaction scheme model could predict the behavior of the process reasonably well and also predicts the major components outlet flow rates within 25%. Some discrepancy for C_{14} concentration is observed due to exclusion of high hydrocarbons in the mechanism. The derived model also shows that, for the given operating conditions *i.e.*, at a given experimental bed temperature and pressure, the total oxidation reaction is dominant at initial 15–20 % of the total reactor bed length for high GHSV and at initial 5% of the reactor length at low GHSV.

References

[1] Reducing Vehicle Idling, Argonne National Laboratory: Transportation Technology R&D Center, http://www.transportation.anl.gov/engines/idling.html, Accessed - 25-Oct-2008.

[2] R.D. Parmar, A. Kundu, K. Karan, Thermodynamic analysis of diesel reforming process: Mapping of carbon formation boundary and representative independent reactions, Journal of Power Sources, 194 (2009) 1007-1020.

[3] G.A. Olah, A. Molnar, Hydrocarbon Chemistry, Wiley-Interscience, New Jersey, 2003.

[4] G. Kolb, Fuel processing: for fuel cells, Wiley-VCH, Weinheim, 2008.

[5] M. Nilsson, X. Karatzas, B. Lindström, L.J. Pettersson, Assessing the adaptability to varying fuel supply of an autothermal reformer, Chemical Engineering Journal, 142 (2008) 309-317.

[6] I. Kang, J. Bae, G. Bae, Performance comparison of autothermal reforming for liquid hydrocarbons, gasoline and diesel for fuel cell applications, Journal of Power Sources, 163 (2006) 538-546.

[7] D.-J. Liu, T.D. Kaun, H.-K. Liao, S. Ahmed, Characterization of kilowatt-scale autothermal reformer for production of hydrogen from heavy hydrocarbons, International Journal of Hydrogen Energy, 29 (2004) 1035-1046.

[8] I. Kang, J. Bae, Autothermal reforming study of diesel for fuel cell application, Journal of Power Sources, 159 (2006) 1283-1290.

[9] A. Lindermeir, S. Kah, S. Kavurucu, M. Mühlner, On-board diesel fuel processing for an SOFC–APU—Technical challenges for catalysis and reactor design, Applied Catalysis B: Environmental, 70 (2007) 488-497.

[10] R. Kaila, A. Krause, Autothermal reforming of simulated gasoline and diesel fuels, International Journal of Hydrogen Energy, 31 (2006) 1934-1941.

[11] J. Kopasz, D. Applegate, L. Miller, H. Liao, S. Ahmed, Unraveling the maze: understanding of diesel reforming through the use of simplified fuel blends, International Journal of Hydrogen Energy, 30 (2005) 1243-1250.

[12] D. Berry, D. Shekhawat, T. Gardner, Development of reaction kinetics for diesel-based fuel cell reformers Hydrogen, Fuel Cells, and Infrastructure Technologies Program, (2003) 1-6.

[13] L. Dorazio, M.J. Castaldi, Autothermal reforming of tetradecane (C14H30): A mechanistic approach, Catalysis Today, 136 (2008) 273-280.

[14] R. Sotelo-Boyás, G.F. Froment, Fundamental kinetic modeling of catalytic reforming, Industrial & Engineering Chemistry Research, 48 (2008) 1107-1119.

[15] D. Berry, D. Shekhawat, T. Gardner, Hydrogen, Fuel Cells, and Infrastructure Technologies Program, (2003) 147-152.

[16] D. Shekhawat, D.A. Berry, T.H. Gardner, J.J. Spivey, Catalytic reforming of liquid hydrocarbon fuels for fuel cell applications, Catalysis, 19 (2006) 184-254.

[17] M. Pacheco, J. Sira, J. Kopasz, Reaction kinetics and reactor modeling for fuel processing of liquid hydrocarbons to produce hydrogen: isooctane reforming, Applied Catalysis A: General, 250 (2003) 161-175.

[18] J. Xu, G.F. Froment, Methane steam reforming, methanation and water-gas shift: I. Intrinsic kinetics, AIChE Journal, 35 (1989) 88-96.

[19] J.R. Rostrup-Nielsen, Activity of nickel catalysts for steam reforming of hydrocarbons, Journal of Catalysis, 31 (1973) 173-199.

[20] J.R. Rostrup-Nielsen, Catalytic steam reforming, Catalysis, Science and Technology, 5 (1984) 1-117.

[21] D. Shekhawat, D.A. Berry, D.J. Haynes, J.J. Spivey, Fuel constituent effects on fuel reforming properties for fuel cell applications, Fuel, 88 (2009) 817-825.

[22] F. Zaera, Selectivity in hydrocarbon catalytic reforming: a surface chemistry perspective, Applied Catalysis A: General, 229 (2002) 75-91.

[23] W. Jin, X. Gu, S. Li, P. Huang, N. Xu, J. Shi, Experimental and simulation study on a catalyst packed tubular dense membrane reactor for partial oxidation of methane to syngas, Chemical Engineering Science, 55 (2000) 2617-2625.

[24] S. Springmann, G. Friedrich, M. Himmen, M. Sommer, G. Eigenberger, Isothermal kinetic measurements for hydrogen production from hydrocarbon fuels using a novel kinetic reactor concept, Applied Catalysis A: General, 235 (2002) 101-111.

[25] H.H. Ibrahim, R.O. Idem, Kinetic studies of the partial oxidation of gasoline (POXG) over a Ni-CeO2 catalyst in a fixed-bed flow reactor, Chemical Engineering Science, 62 (2007) 6582-6594.

[26] K. Kawasaki, Coadsorption of carbon monoxide and hydrogen on polycrystalline platinum, Surface Science, 64 (1977) 349-354.

[27] C.H. Nam, H.D. Shin, Inhibition effect of carbon dioxide on the oxidation of hydrogen over a platinum foil catalyst, Catalysis Today, 83 (2003) 257-264.

[28] A. Guerrero-Ruiz, Some aspects of reversible chemisorption on supported platinum catalysts, Reaction Kinetics and Catalysis Letters, 49 (1993) 53-60.

[29] J.P. Candy, P. Fouilloux, A.J. Renouprez, Hydrogen adsorption on platinum catalysts. Quantitative determination of the various species population, J. Chem. Soc., Faraday Trans. 1, 76 (1980) 616-629.

[30] P. Ferreira-Aparicio, A. Guerrero-Ruiz, I. Rodriguez-Ramos, Hydrogen adsorbed species at the metal/support interface on a Pt/Al2O3 catalyst, Journal of the Chemical Society, Faraday Transactions, 93 (1997) 3563-3567.

[31] M.A. Vannice, Kinetics of Catalytic Reactions, Springer Verlag, New York, 2005.

[32] J. Pacheco, A. Bravo, O. Novara, An ab initio study of platinum hydrogen interaction, Revista Mexicana De Física, 52 (2006) 394-397.

[33] S. Seong, A.B. Anderson, Water dissociation on Pt (111) and (100) anodes: Molecular orbital theory, The Journal of Physical Chemistry, 100 (1996) 11744-11747.

[34] M. Vannice, S. Hyun, B. Kalpakci, W. Liauh, Entropies of adsorption in heterogeneous catalytic reactions, Journal of Catalysis, 56 (1979) 358-362.

[35] Physical Properties of Chemicals, http://www.faqs.org/faqs/sci/chem-faq/part5/section-1, Accessed - 31-Jan-2009.

[36] E. Miyazaki, The heat of chemisorption of hydrogen on transition d-metals(correlation with bond energies), Surface Science, 71 (1978) 741-747.

[37] S.G. Podkolzin, J. Shen, J.J. de Pablo, J.A. Dumesic, Equilibrated adsorption of CO on silica-supported Pt catalysts, The Journal of Physical Chemistry B, 104 (2000) 4169-4180.

Chapter 5

Stable Diesel or Heavy Hydrocarbon Reforming Catalyst: Properties and Performance

5.1 **Preface**

Neglecting gas-phase reactions during high temperature reforming of tetradecane was a gross assumption made while developing a LHHW type of kinetic model in Chapter 4. However, understanding of both the gas-phase and surface reactions occurring in the autothermal reactor is essential for the development of a mechanistic kinetic model for this system. An experimental gas-phase and surface kinetic study was undertaken with an objective to explain the importance of both gas-phase and surface reactions and to validate the generated detailed kinetic models in Chapter 6 and Chapter 7.

This chapter discusses, in detail, the experimental methods used for catalyst synthesis, catalyst characterization, and kinetic studies. It presents the accelerated test to screen the catalysts for reforming of commercial-diesel fuel and also discusses results from a long term activity test for the screened catalyst. Under real operational scenario, the catalyst experiences both cyclic temperature changes as well as undergoes reducing and oxidizing (redox) cycles. From stability considerations, a desirable catalyst is the one that maintains its structural integrity with minimal changes in the accessible active metal sites for the reactions during cyclic temperature changes and under the redox environment. It presents a redox study test that highlights the importance of essential properties for the design of stable diesel reforming catalyst. Also the chemisorption test performed for catalyst characterization provided the surface site density of active rhodium metal catalyst that is the most important parameter for surface kinetic study discussed in Chapter 7. Kinetic studies with catalyst and without catalyst in a packed bed are presented to explain the importance of gas-phase reactions that form pyrolysis products at elevated reforming temperatures. Kinetic data collected for gas-phase reactions and surface reactions at different operating conditions are used for gas-phase and surface kinetic model validation in Chapter 6 and Chapter 7 respectively.

5.2 **Abstract**

The use of diesel as a fuel for Solid Oxide Fuel Cell (SOFC) application presents several challenges including the need to partially/fully reform it prior to being fed to SOFCs. A major issue in the design and optimization of a catalyst for commercial systems is that the catalyst must retain high activity and exhibit stable performance over long operational period. In present experimental study, two diesel reforming catalysts were synthesized – optimized Rh/pyrochlore (PY-1) and Pt supported on gadolinium-doped ceria (Pt-CGO). In an accelerated test for reforming of commercial-diesel fuel, the PY-1 catalyst showed stable performance, in terms of H_2 yield, for 24 hrs, whereas the Pt-CGO catalyst deactivated within 4 hrs of reaction. Also, the PY-1 catalyst showed long-term stability for pump diesel reforming. Fresh powders of catalysts were characterized by N_2-BET, XRD, H_2-chemisorption, and redox (TPR-TPO cycle) tests. In redox test, the PY-1 catalyst showed an initial structural change and in subsequent tests accessible rhodium remained unchanged which is further confirmed using chemisorption study. However, the Pt-CGO catalyst lost its platinum peak after first oxidation cycle suggesting loss of an accessible active metal in the actual reforming environment. The kinetic experiments with only quartz sand (*i.e.*, non-catalytic packed bed reactor) showed < 100 ppm oxygen at the reactor outlet with CO and CO_2, ethylene, propylene, and methane as major products. Incoloy-800 HT reactor showed high wall activity above 800 °C. Kinetic study experiments confirmed that the PY-1 catalyst is highly active and stable above 775 °C. 20-26 moles of hydrogen per mole of n-tetradecane and 2.5-2.7 moles of hydrogen per mole of carbon monoxide are obtained at temperatures higher than 775 °C. No mass-transfer limitations were observed.

Keywords: Diesel Autothermal Reforming; Solid Oxide Fuel Cell; Pyrochlore Catalyst; Catalyst Characterization; Catalyst Activity

1. Introduction

Global warming, depletion of fossil fuels, fuel economy and emission abatement issues are the major challenges facing automotive and energy industries. Stricter environmental norms are guiding the industry to search for an alternative sustainable technical solution. Fuel-cell based Auxiliary Power Units (FC-APUs) are considered as one such option that has a potential to deliver the electricity at high efficiency [1]. However, limited hydrogen infrastructure and durability issues have restricted the growth of the fuel cell industries. At present, fuel reforming is considered as a short-term alternative to supply high purity hydrogen [2]. In fuel reforming, the hydrocarbon fuels are subjected to steam reforming (SR), partial oxidation (POX), or autothermal reforming (ATR) to extract the maximum amount of hydrogen. Diesel, gasoline, and jet fuels are considered as potential candidates of hydrogen carrier for the FC-APU system because of their high energy density and existing infrastructure. Due to its high efficiency at high temperature, and ability to handle both CO, H_2, and light hydrocarbons as a feed stock [3], Solid Oxide Fuel Cell (SOFC) based APUs are considered to have early commercialization potential in transport sector (specifically for heavy-duty trucks and ships to provide power during stand-still) and in stationary power system (specifically for remote areas where the generating the electricity using diesel generator is very costly and highly polluting).

Methane reforming has been studied extensively as it is the major species in natural gas. Also, consistent efforts have been put by various research groups [4-8] in developing diesel, gasoline, JP8 fuel reformer systems to address the many challenges associated with the development of fuel reformer system including homogeneous mixing of fuel with steam and oxygen, design of stable and highly active catalyst, and heat integration for the system. The technical target set by the U.S. Department of Energy requires a reformer/catalyst durability of 5000 hrs [7]. Several experimental studies on catalysts have been reported for generating hydrogen from gasoline, diesel fuel and its surrogates [4-8]. Based on the progress made so far, none of the non-noble metal catalysts have shown acceptable long-term activity and stability for heavy hydrocarbon reforming. Platinum group metals such as Pt and Rh are found to be an excellent candidate for heavy hydrocarbon reforming. Krumpelt and coworkers at Argonne National Laboratory (ANL) developed Pt on doped ceria catalyst that gave promising results for autothermal reforming of isooctane for 47 days [9, 10]. Based on ANL's study, Bae and coworkers used 0.5 wt% Pt – on 20 mol% Gd doped ceria (CGO) for gasoline and diesel autothermal reforming [11, 12]. They observed that homogeneous mixing of the reactants lead to long term stability as generation of carbon precursor (*i.e.*, ethylene) was suppressed [13]. Further, Pt was reported to show better performance over Rh and Ru when CGO was used as the catalyst support. In later studies, they recommended a post-reforming stage (3 wt% Ru/CGO) to remove light hydrocarbons (over C_1) to get stable operation for synthetic diesel reforming [14, 15]. Schmidt and coworkers used Rh-α-Alumina coated monoliths for n-decane, n-hexadecane, JP-8, and isooctane autothermal reforming [16]. However, they observed carbon, ethylene and propylene and attributed this to gas-phase cracking. Roychoudhary and coworkers used Pt on La-Al_2O_3 and Rh on Ce-Zr microlith short-contact time reactor for isooctane autothermal reforming [17]. Later they used their proprietary catalyst for 50 hrs autothermal reforming of JP8 fuel. The catalyst activity was found to decrease initially and the performance was recovered when the catalyst was exposed to air after 45 hrs [18]. Kolb and coworkers reported declining of catalytic activity for iso-octane autothermal reforming in 1wt% Rh/Al_2O_3 coated micro-structured reactor [19]. The activity recovered to initial level after short oxidation. Thormann *et al.* [20, 21] reported

15 hrs stable operation for steam reforming of diesel surrogate (hexadecane) in microchannel reactor coated with Rh/CeO_2. They observed that activity declined at 645 °C, but remained constant at 700 °C. Pettersson and coworkers used two layers of monometallic Rh and bimetallic (Rh-Pt) washcoats (*i.e.*, Ce and La doped alumina) for diesel autothermal reforming [22]. In their XPS analysis, they observed lower amount of Rh/Al, Pt/Al and La/Al ratio at the entrance of reactor possibly sintering effect due to oxidation reactions at the entrance of the catalyst. The review of literature indicates that Pt/CGO catalyst has shown stable and better performance for long-term operation of a diesel reformer. However, none of the studies so far have examined the effect of reducing and oxidizing environment on the catalyst.

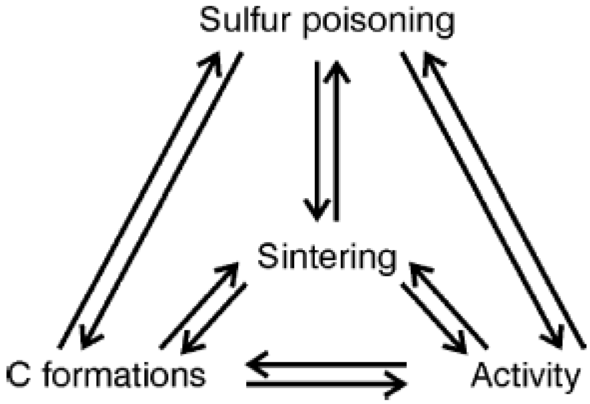

Figure 5.1: Four Major challenges for reforming catalyst [23]

Sehested [23] reported four major challenges for reforming catalysts (Figure 5.1). These challenges are strongly interconnected. Apart from carbon formation and sulfur poisoning, the sintering of the catalyst is the major concern, which particularly happens in redox environment.

Better catalysts are those whose structure as well as properties show minimum change with time, age, particularly at high temperature of exposure and under redox cycles during actual operating conditions. The objective of the present work is to test and characterize Pt-CGO and optimized lanthanum zirconate pyrochlore catalyst [24, 25] and investigate the effect of redox environment on the catalyst. Also, experiments were carried out in non-catalytic and catalytic reactors over a range of operating conditions to examine the importance of gas-phase reactions and wall effects and to identify a suitable operating regime for catalytic autothermal reforming.

2. Experimental

2.1. Catalyst preparation

Lanthanum zirconate pyrochlore catalysts, as shown in Table 5.1, were prepared by using Pechini method, a synthesis route to produce metal oxide compounds through a sol-gel intermediate phase [26-29]. An optimized pyrochlore catalyst ($La_{2-w}A_wZr_{2-y-z}Rh_yB'_zO_{7-\delta}$) formulation developed by NETL was used for this study. In this formulation the A site is substituted with an alkaline earth metal (*e.g.*, Mg, Ca, Sr, Ba) at the level '*w*' and the B site is substituted with Rhodium (2 wt%) and metal ions (B') of either Ti, Ce, Y, or Ba at the level of '*z*'[24, 25]. Metal nitrates and chloride precursors (*e.g.*, $La(NO_3)_3{\cdot}6H_2O$, $ZrO(NO_3)_2$, $RhCl_3{\cdot}2H_2O$) were dissolved in deionized water separately and then combined into a beaker. The solution was mixed with citric acid (CA) solution in a 1:1 molar ratio of CA:metal. The solution was then heated on a magnetic stirrer to bring the temperature up to 75 °C to ensure complete metal complexation. At 75 °C, 40:60 molar ratio of ethylene glycol (EG) to CA was added. The solution was continuously stirred at 75 °C until all liquid water was evaporated and a transparent, viscous gel remained. Further supply of heat resulted in violent bubbling with release of large plumes of NOx due to decomposition of nitrates. This promoted the poly-esterification reaction between EG and CA that ultimately formed an organic polymer network. The foam like mass was then dried at 110 °C overnight. Organic precursors were oxidized at 1000 °C for 8 hrs during calcination in the furnace. Three catalysts, lanthanum zirconate pyrochlore with B site doped with active Rh (LZ-Rh), optimized lanthanum zirconate pyrochlore with A site doped with alkaline earth metal and B site doped with Rh (PY-1), and optimized lanthanum zirconate pyrochlore with without active metal Rh (PY-2), were synthesized.

Table 5.1: Active metal percentage in pyrochlore and Pt-CGO catalyst

Catalyst	**$Ce_{0.8}Gd_{0.2}O_{1.9}$ (CGO)**	**$Pt/Ce_{0.8}Gd_{0.2}O_{1.9}$ (Pt-CGO)**	**$La_2Rh_{0.11}Zr_{1.89}O_{7-y}$ (LZ-Rh)**	**Optimized pyrochlore with Rh (PY-1)**	**Optimized pyrochlore without Rh (PY-2)**
Pt or Rh content (wt%)	0	0.5	2.0	2.0	0

0.5 wt% $Pt/Ce_{0.8}Gd_{0.2}O_{1.9}$ (Pt-CGO) and Gadolinium doped ceria (CGO- $Ce_{0.8}Gd_{0.2}O_{1.9}$) was prepared by glycine-nitrate process (GNP), in which all precursors (*e.g.*, $Ce(NO_3)_3 \cdot 6H_2O$, $Gd(NO_3)_3 \cdot 6H_2O$, $H_2PtCl_6 \cdot 6H_2O$) were dissolved in distilled water and the stoichiometric proportion of glycine was added [30]. The contents were heated at 100 °C on a hot plate while stirring. As the water evaporated, the content became sufficiently concentrated and combustion occurred between 100 °C to 150 °C. The obtained catalyst was then ground and calcined at 1000 °C for 8 hrs.

2.2. Characterization

The fresh calcined catalyst powder (-80+100 mesh) was characterized by several techniques as described below.

BET surface area: The BET specific surface area measurements were carried out on an Autosorb-1 instrument at liquid nitrogen temperature (77 K). Prior to the analysis, the sample was degassed at 110 °C for overnight and BET multipoint method was applied to calculate the surface area.

X-ray Diffraction (XRD): Phase analysis of calcined powder samples was examined using PanAnalytical X'pert Pro X-ray diffraction system, model number PW 3040 pro. Power requirements during the operation was 45kV and 40 mA and powder scan programs were set at 2θ scanning range 10-90° at a scan speed of 0.0164 °/s. Peak identification of X-ray data was done by comparing the scan with X'pert High Score Plus software, version 2.1 data. A similar analysis was repeated on Scintag X1 powder diffractometer without any noticeable differences in scan.

Temperature programmed reduction and oxidation: Temperature-programmed reduction (TPR) and temperature programmed oxidation (TPO) measurements were carried out in Micromeritics Autochem 2910 unit. TPR and TPO runs were repeated (redox cycles) to measure any changes related to active metals that were not detected using XRD spectra. 150 mg of the catalyst was loaded in a quartz tube and held between two quartz wool plugs. Before starting the experiments, the sample was dried using 30 ml/min argon flow by ramping the temperature to 200 °C at 5 °C/min rate and holding it at 200 °C for 30 minutes. For TPR, the sample temperature was ramped from ambient to 950 °C by 5 °C/min in 5% H_2/Ar mixture flow set at 30 ml/min and held isothermally at 950 °C for 30 minutes. After 30 minutes of holding time, gas was changed to 30 ml/min argon flow, and held at 950 °C for 15 minutes. The temperature of the sample was ramped back to ambient in the argon flow. For TPO, the sample temperature was ramped from ambient to 950 °C by 5 °C/min in 2% O_2/He mixture flow set at 30 ml/min and held isothermally at 950 °C for 30 minutes. As described before, the sample was ramped back to ambient temperature in the argon flow. The process was repeated for the redox property analysis of the sample.

Pulse chemisorption: Pulse chemisorption experiments were performed using Micromeritics Autochem 2910 unit. The sample was purged with 5% H_2/Ar contained in the sample loop volume of 0.5377 cm^3. Before chemisorption, TPR was conducted to remove any surface oxygen. The catalyst temperature was maintained at 950 °C for 30 minutes under the argon flow to remove any surface hydrogen. The sample was then cooled to 50 °C under argon to begin H_2 chemisorption. In analyzing the data 1:1 stoichiometric ratio of H:Rh was used [31, 32].

2.3. Reaction studies

Catalysts activity tests and kinetic study experiments were performed in a fixed bed continuous flow reactor (Autoclave Engineers, Model BTRS Jr.) shown in Figure 5.2. All inlet and outlet flow lines were inside the hot box for complete evaporation of the reactants and to avoid product condensation. Programmable temperature controller (Eurotherm, Model no. 2416) was used to control the hot box temperature at 375 °C. Nitrogen and air were delivered by mass flow controllers (Brooks, Model no. 5890E) with reported error of ± 1% of full scale. Liquid hydrocarbon fuel and water were delivered by highly accurate (± 1%) HPLC pump (Dionex Corp., Model no. P680A HPG). The liquid hydrocarbon was vaporized in a preheated nitrogen stream in a specially designed mixing unit. Water was evaporated in a coil and then mixed with the heated air. The air-steam mixture was then passed through a coil for complete mixing before it was mixed with hydrocarbon-N_2 mixture at the reactor inlet. For the kinetic study, 0.181 gm (-80 +100 mesh and -100 mesh) of catalyst was diluted with 4.536 gm (-20+60 mesh) of quartz sand. The catalyst was placed inside the 8 mm I.D., 27.94 mm long, Incoloy 800HT (approximate composition: 30-35% Ni, 39.5% min Fe, 19-23% Cr) tubular reactor tube. Quartz

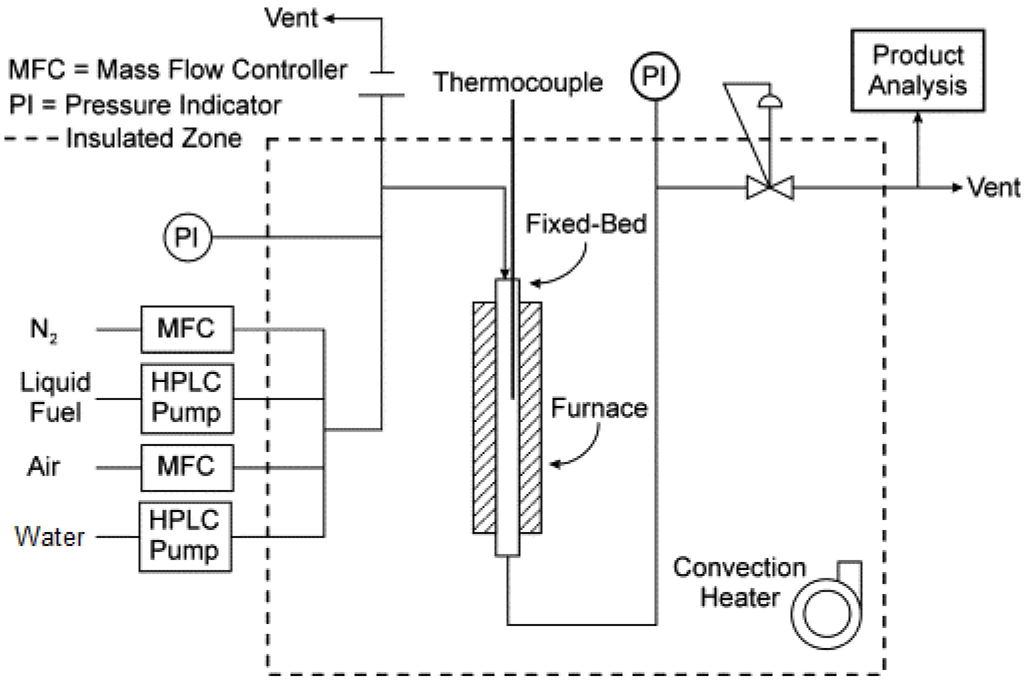

Figure 5.2: Experimental system for activity and kinetic study [33]

sand particles of the same size were used to pack the pre- and post-catalytic bed zones. One of the key purposes of the pre-catalytic bed zone was to promote good mixing of the reactants before they reach the catalyst surface. Hence, the overall reactor was divided into three segments with a 5.8 cm long diluted catalyst bed at the center of the reactor and 11 cm long quartz sand beds before and after the catalyst bed. The reactor was heated by the split tube furnace (Series 3210, Applied Test Systems, Inc.) controlled by a programmable controller (Eurotherm, Model no. 2416). The heat input to the furnace was determined by the difference in set-point temperature and thermocouple temperature at the center of the catalyst bed (T_{bed}). A sample conditioner (Universal Analyzers Inc., Model no. 1050S) at the reactor outlet was used to condense steam and any unconverted liquid hydrocarbons from the product gas stream.

2.4. Reactants and product analyses

N-tetradecane was used as a surrogate of diesel for the kinetic study. The long term activity tests and accelerated activity tests were carried out using commercial pump diesel. The product gas (N_2, H_2, O_2, CO, CO_2, and methane) was analyzed continuously using a Thermo Onix mass spectrometer (MS) (Model no. Prima δb, with a 200 a.m.u. scanning magnetic sector) with standard ±2% analytical error in gas concentrations. The gaseous hydrocarbon products were analyzed using a HP5890 gas chromatograph (GC) equipped with a flame ionization detector (FID).

2.4. Operating conditions for kinetic study

Three level factorial design experiments, as shown in Figure 5.3, at H_2O/C (S/C) ratio 1.5 and at following conditions were carried out.

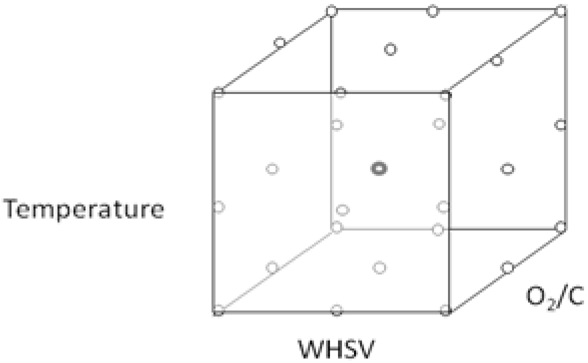

Figure 5.3: 3-level factorial design of experiments for kinetic study.

The three set-points for the three variables were as follows.

Temperature (T_{bed}): 700 °C; 775 °C; 850 °C

WHSV(Weight Hourly Space Velocity): 100,000 SCC/h·g; 160,000 SCC/h·g; 220,000 SCC/h·g

O_2/C ratio: 0.2; 0.35; 0.5

The above defined WHSV is equivalent to GHSV (Gas Hourly Space Velocity) 1,281 1/h, 2,050 1/h, and 2,819 1/h respectively. The following equation is used to calculate GHSV

$$GHSV = \frac{Volumetric\ flow(SCCM) \times 60}{Volume\ of\ blank\ reactor} \tag{1}$$

The measured reactor pressure was 20 psig. The product gas composition was analyzed for N_2, H_2, O_2, CO, CO_2, and methane concentration every 1 minute using the MS. After 5 to 10 minutes the concentration profiles reached at steady state. GC analysis of higher hydrocarbon was performed once the steady-state was reached. After each run, the carbon was burned out by passing air and increasing the temperature to 900 °C until no CO and CO_2 was detected in the outlet. For gas-phase kinetic study, similar set of kinetic data were collected with only quartz sand particles inside the reactor. Inlet flow rates, operating conditions, and measured outlet composition are given in Appendix B.

The following Equations (2)–(5) were used in the analysis of experimental data. The yield of gas products was calculated by

$$Yield\,of\ H_2\,[\%] = \frac{moles\,of\ H_2}{\left(15 \times moles\,of\ tetradecane\ fed + moles\,of\ water\ fed\right)} \times 100 \tag{2}$$

$$Yield\,of\ C_nH_m\,[\%] = \frac{n \times moles\,of\ C_nH_m}{\left(14 \times moles\,of\ tetradecane\ fed\right)} \times 100 \tag{3}$$

$$Yield\,of\ CO/CO_2[\%] = \frac{moles\,of\ CO/CO_2}{14 \times moles\,of\ tetradecane\ fed} \times 100 \tag{4}$$

where ‘*n*’ is the number of moles of carbon per mole of hydrocarbon in the product. Hydrogen yield is based on number of moles of hydrogen fed into the reactor as specified by Shekhawat *et al.* [6].

The conversion was calculated by

$$X\,[\%] = \frac{moles\,of\ carbon\,in\,outlet\ product\ gas}{14 \times moles\,of\ tetradecane\ fed} \times 100 \tag{5}$$

Carbon balances for all experiments were ± 7%.

3. Results and discussion

Before characterizing the catalysts, activity tests were performed to identify the stable catalyst for pump diesel autothermal reforming. Based on the results of the activity test for commercial diesel, a detailed characterization of stable catalyst was performed.

3.1. Activity/stability test

The activities of Pt/CGO and PY-1 catalysts were compared by using an accelerated test method developed by NETL for commercial catalyst screening. Pump diesel was used for the accelerated test. The experiments were performed at Weight Hourly Space Velocity (WHSV) 50,000 SCC/h·g , O_2/C ratio 0.55 and temperature 900 °C. These conditions are favourable for the carbon formation on the catalyst as per thermodynamic analysis [34], however the rate of carbon formation and/or deactivation is slow for the stable catalyst compared to the unstable catalyst. The test results shown in Figure 5.4 clearly indicate that the PY-1 catalyst deactivates very slowly compared to Pt/CGO catalyst. In the case of Pt/CGO catalyst, the high carbon formation increased the back pressure and tripped the furnace eventually. Long term activity test on PY-1 catalyst was conducted for 87 hrs for commercial diesel reforming at conditions that are not favourable for carbon formation. The test was performed at WHSV 25,000 SCC/h·g, O_2/C ratio 0.5, H_2O/C (S/C) ratio 0.5, and temperature 900 °C. Figure 5.5 shows the stability of the catalyst for long term. Hence the PY-1 catalyst was selected for further kinetic study. Recently, Bae and co-workers used Pt-CGO (ATR catalyst) and Ru-CGO (post reformer catalyst) for autothermal reforming of synthetic diesel for 2500 h with 5-10% degradation of the catalyst [15]. The failure of Pt-CGO catalyst in our test could be due to catalyst preparation method. The

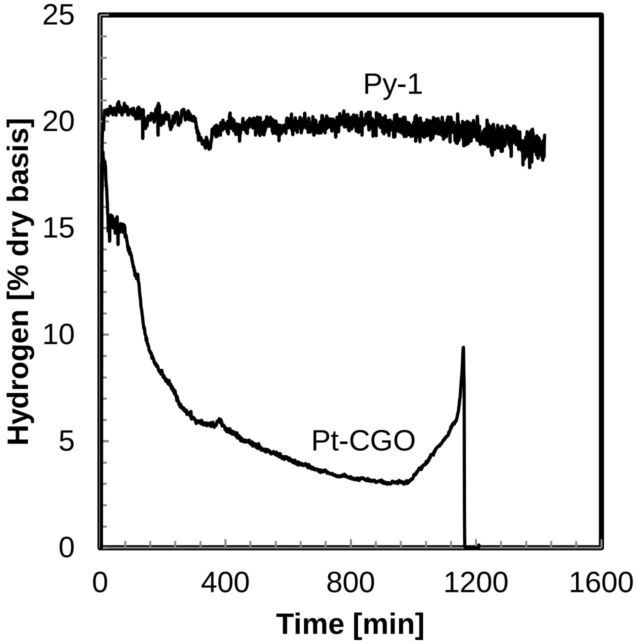

Figure 5.4: Accelerated activity tests for PY-1 and Pt-CGO.

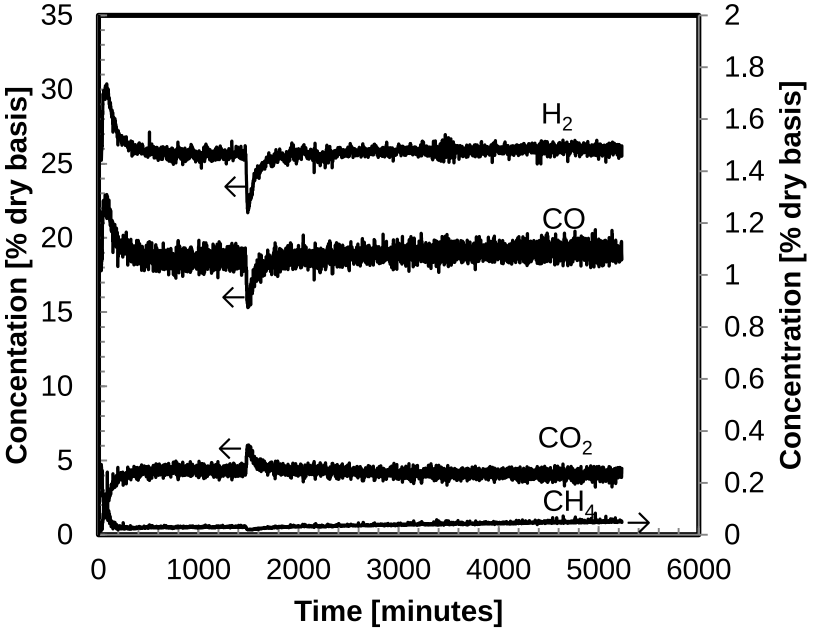

Figure 5.5: Long term activity test for PY-1 catalyst.

catalyst employed by Bae *et al.* was synthesized by Praxair via combustion spray pyrolysis. Since the PY-1 catalyst was found to be stable for long term operation, kinetic study and/or performance evaluation for PY-1 catalyst was carried out at different operating conditions.

3.2. Catalyst characterization

The complete characterization of Pt-CGO catalyst was not performed because it did not perform well in the accelerated test. Thus, catalyst characterization for PY-1 is reported here with only redox test results from Pt-CGO catalyst.

3.2.1 BET specific surface area

The surface area of Rh-based pyrochlore catalyst is presented in Table 5.2. The surface area of the catalysts is similar to that of Lanthanum Zirconate catalyst that indicates little effect of substitution of Rh and other ions into the catalyst structure [28].

Table 5.2: BET surface area for pyrochlore catalysts

Catalyst	**$La_2Rh_{0.11}Zr_{1.89}O_{7-y}$ (LZ-Rh)**	**Optimized Pyrochlore with Rh (PY-1)**
Specific surface area [m^2/g]	11.69	10.38

3.2.2 X-ray diffraction

The X-ray diffraction patterns of calcined powder samples are shown in Figure 5.6. The LZ-Rh peaks resembled the peaks of Lanthanum Zirconate pyrochlore (LZ) in the database as well as literature [28, 35, 36]. It is a single phase material having Face Centered Cubic (FCC) structure.

Substitution of rhodium at the B site does not result in any peak shift and phase change. It is attributed to the low percentage of the rhodium. Similar results were obtained by substituting A-site and B-site for PY-1 and PY-2 catalysts. Unidentified small intensity peak is observed at 31°, whereas other peaks in the PY-1 and PY-2 catalyst can be assigned to the doping of A and B site with proprietary dopants [37]. However these peaks disappeared when the catalyst was subjected to redox cycles as shown in Figure 5.10.

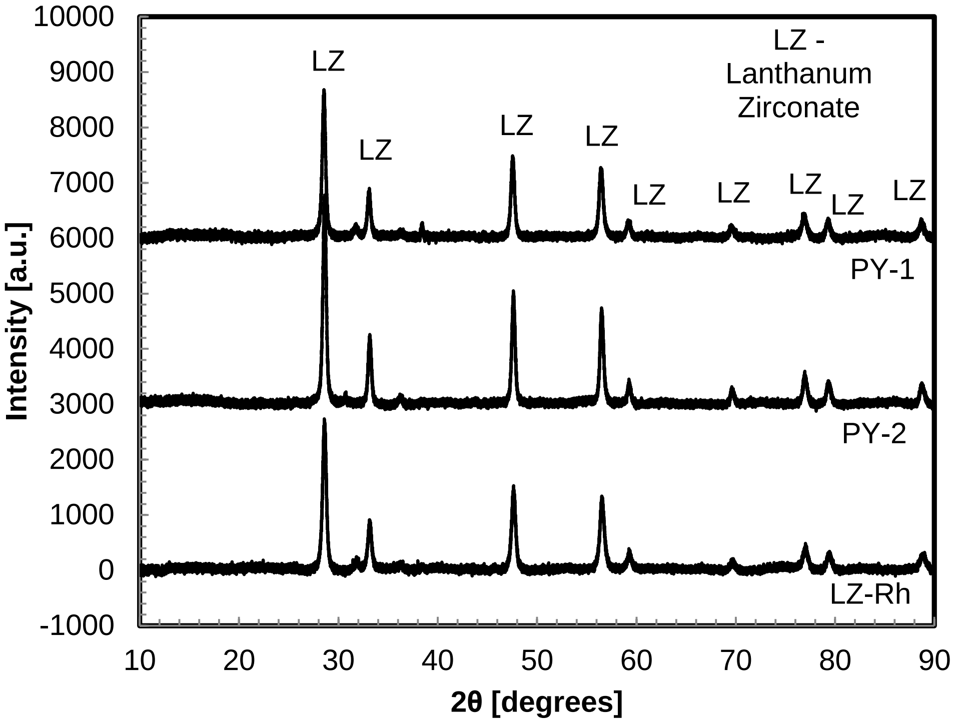

Figure 5.6: X-ray diffraction spectra of LZ-Rh, PY-1, and PY-2 calcined powder.

3.2.3 Temperature programmed reduction and oxidation (Redox)

TPR profiles of fresh calcinated pyrochlore catalysts are shown in Figure 5.7. TPR profiles after oxidation at temperatures of up to 950 °C for all pyrochlores are shown in Figure 5.8. No hydrogen consumption was observed during TPR of the PY-2 catalyst. This was expected due to the absence of any reducible metal substitution into the lattice. Multiple forms of rhodium oxide on oxide supports have been reported. Wong and McCabe [38] observed two forms of rhodium oxide in Rh/SiO_2 catalyst, whereas Hwang *et al.* [39] [36] observed five different forms of oxidation products on Rh/Al_2O_3 catalysts. Similar observation has been made in other studies, however, different peaks are not only because of interaction with different supports but also

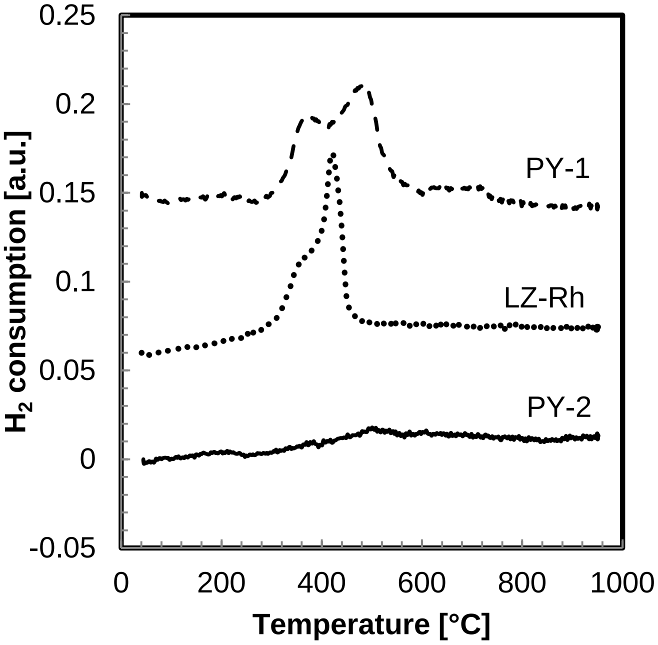

Figure 5.7: TPR profiles of fresh pyrochlore catalysts.

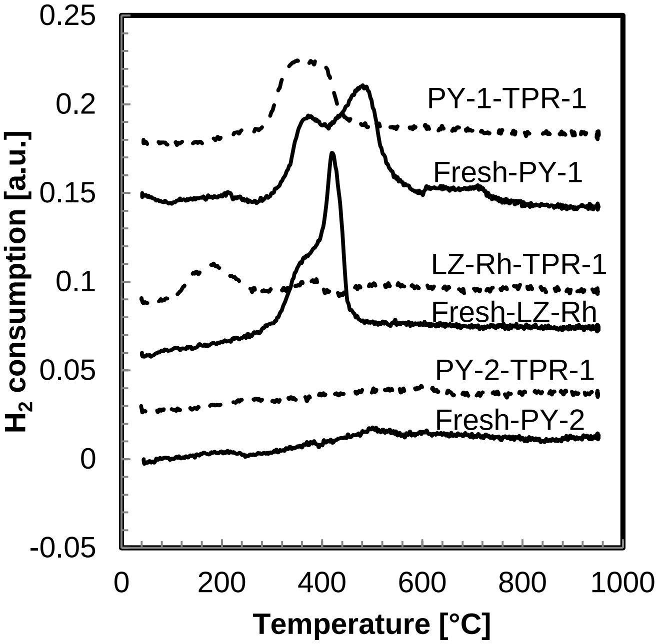

Figure 5.8: Redox cycle TPR profiles of pyrochlore.

due to different oxidation temperatures [40-43]. It has been reported that Rh/Al_2O_3 catalyst calcined above 900 °C resulted in the formation of 81% rhodium species that is irreducible by hydrogen below 600 °C because of strong Rh-O bond [42]. However, in the case of pyrochlore catalysts wherein Rh is part of the structure and not present as a dispersed crystallite, even at 1000 °C calcination temperature and 950 °C oxidation temperature, most of the accessible rhodium is reduced below 600 °C and no high temperature peak is observed (Figures 5.7 and 5.8). Freshly calcined LZ-Rh catalyst showed two clear peaks, a smaller one at 345 °C and a larger one at 420 °C. These peaks can be assigned to the presence of two kinds of RhOx species [26, 37]. The peaks can be due to the weak and strong interaction of rhodium with lattice oxygen, and the presence of small shoulder on 420 °C peak suggest a range of strong interaction of rhodium with the lattice oxygen [37]. However, after oxidation (Figure 5.8), both peaks are shifted to lower temperature. A distinctive large peak is observed at lower temperature (169 °C) and a very small peak at higher temperature (345 °C), indicative of the strong interaction, is observed. This observation suggests that the LZ-Rh catalyst can undergo major change in catalytic activity in the redox environment.

In the case of fresh, optimized-pyrochlore catalyst (PY-1), similar peaks at that reported for LZ-Rh catalyst are observed but both peaks are shifted to the higher temperature. The low and high temperature peaks appear at 357 °C and 466 °C, respectively (Figure 5.8). Peak shifting can be attributed to the substitution of A and B site with dopants. After first oxidation, both peaks of PY-1 are shifted to the lower temperature. However, in subsequent redox cycles the peaks shift is

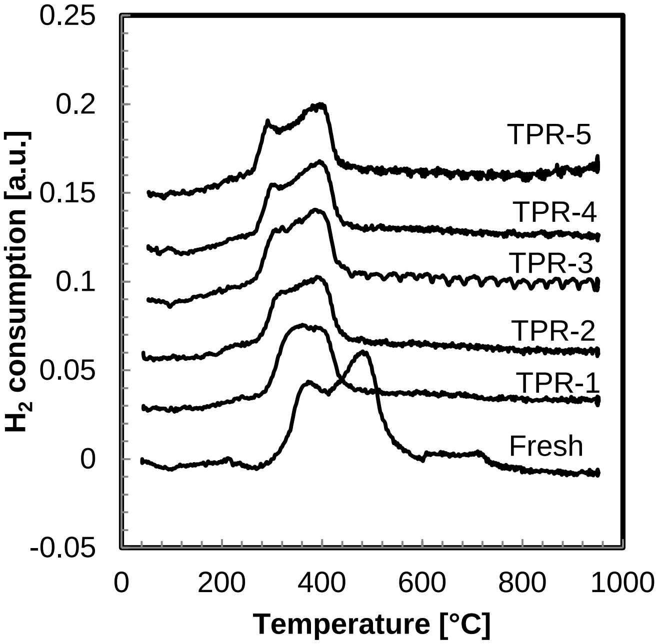

Figure 5.9: Redox cycle TPR profiles of PY-1 catalyst.

not major as shown in Figure 5.9. Unlike the LZ-Rh catalyst, both peaks do not show much change in their size indicating that the catalyst activity may not change much either. The redox cycle test confirmed that after the first initial change the catalyst does not change substantially in redox environment. In Figure 5.10 the XRD spectra of PY-1 catalyst after each redox cycle is shown. As argued before, Rh or RhOx peaks are not observed because of low concentration of rhodium. Also negligible shift in diffraction angles during redox cycling confirmed no major change in catalyst structure, which further supports the similar argument made in analyzing TPR results in Figure 5.9.

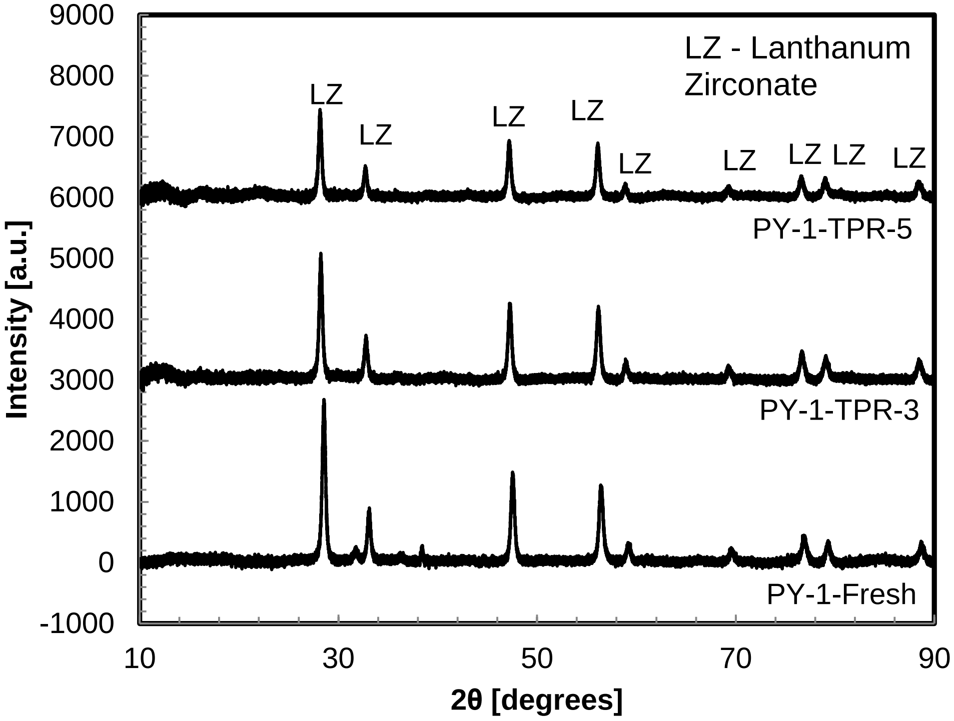

Figure 5.10: Phase analysis of PY-1 catalyst after redox cycles. TPR-3 and TPR-5 refer to samples obtained after third and fifth TPR cycles, respectively.

TPR spectra of redox cycles for Pt-CGO and CGO catalysts are shown in Figure 5.11. For fresh CGO, a very small peak at 539 °C and large broad peak above 600 °C is observed. The first peak at low temperature can be attributed to the reduction of oxygen adsorbed at the surface of the ceria, whereas the second large broad peak can be assigned to the bulk oxygen within the ceria lattice [44, 45]. After oxidation, no major change in TPR profile of CGO was noted. This confirmed the reversible bulk phase reduction [44]. By adding 0.5 wt% platinum to the support (*i.e.*, Pt-CGO catalyst), a large peak at lower temperature 215 °C is observed. This peak is assigned to PtOx [46, 47]. A second peak at 341 °C can be attributed to the weak surface oxygen

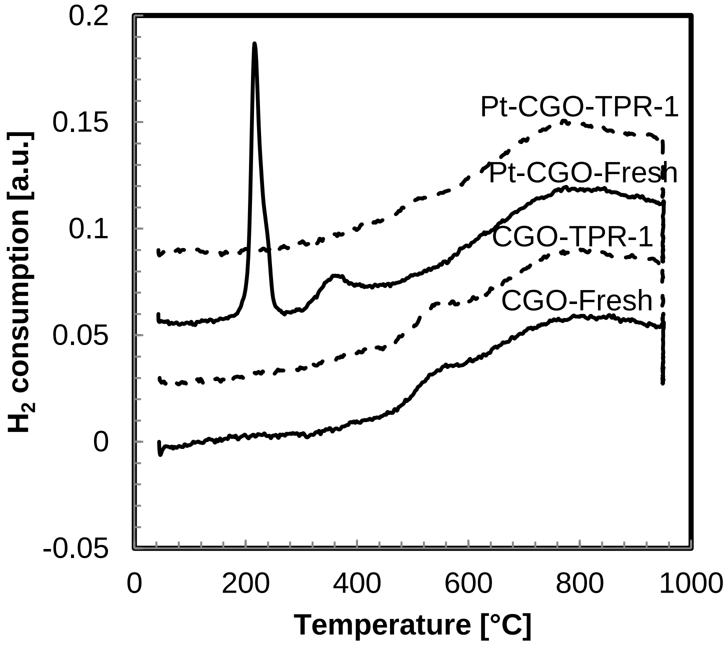

Figure 5.11: Redox cycle TPR profiles of Pt-CGO and CGO catalysts.

because of the spill over of hydrogen from platinum onto the support [48] . As discussed earlier, the third broad peak above 600 °C is assigned to the bulk oxygen within ceria. After oxidation, disappearance of first two peaks shows a major structural change in the catalyst and loss of the catalytic activity in the redox environment. Since no platinum is accessible to hydrogen, there is no spill over of hydrogen onto the support to oxidize surface oxygen. However very small peak appearing at about 500 °C indicates surface oxygen reduction due to direct interaction of hydrogen with surface oxygen same as that of the CGO catalyst. Bulk oxygen within ceria observed again above 600 °C indicating reversible bulk reaction.

3.2.4 Pulse chemisorption

Dispersion and active metal surface area of PY-1 catalyst was determined by pulse chemisorption. The data for catalyst subjected to 1, 3 and 5 redox cycles are presented in Table 5.3. The results confirmed that after major initial change a much smaller change is observed in the structure of the PY-1 catalyst compared to other catalysts in redox environment. The gain in dispersion after the first redox cycle suggests that the structural changes in the catalyst increases the accessible rhodium that ultimately results in higher activity.

Table 5.3: Dispersion and active metal surface area of PY-1 catalyst

Redox run number	Dispersion [%]	Metal surface area [m^2/g]
TPR-1	5.245	0.462
TPR-3	9.315	0.820
TPR-5	8.385	0.738

3.3. Gas-phase reactions and reactor wall activity

To identify the importance of gas-phase reactions in autothermal reforming, relative comparison of products with and without catalyst at the outlet of the reactor is made. Experiments were performed without catalyst (but with quartz sand bed) at the same conditions as that for the experiments with catalyst. Previous studies on methane combustion have shown that quartz sand does not have any activity for methane combustion at 850 °C [49, 50]. Similarly, experimental study on combustion of hydrocarbons in a bubbling sand bed has shown dominance of gas-phase reactions at and above 850 °C [51]. Further, water-gas-shift reaction study by Bustamante *et al.* [52] in a quartz reactor has shown that quartz reactor has minimal activity (conversion < 0.2%) at 900 °C for low residence time (time on-stream < 15 hrs). For experiments without catalyst (but with sand bed), negligible oxygen concentration (< 100 ppm) at the outlet of the reactor was observed. Although the sand bed activity can not be completely neglected, it can be concluded from previous studies that the homogeneous gas phase reactions are dominant inside the reactor. The product composition did not change much by varying the space velocity for gas-phase reactions. However, significant differences in the product composition were observed upon varying the O_2/C ratio and bed temperature (T_{bed}).

Comparison of product distribution with and without catalyst in a quartz sand bed for experiments conducted at 700 °C is shown in Figure 5.12. By adding the catalyst, hydrogen yield increases significantly. This indicates that most of the hydrogen in the reactor is produced by catalytic surface reactions at 700 °C. Also, the addition of catalyst results in a significantly higher amount of CO and CO_2 products. This suggests that the catalytic steam reforming, water-gas-shift reaction, and partial oxidation reactions are dominant on the surface of the catalyst. On the other

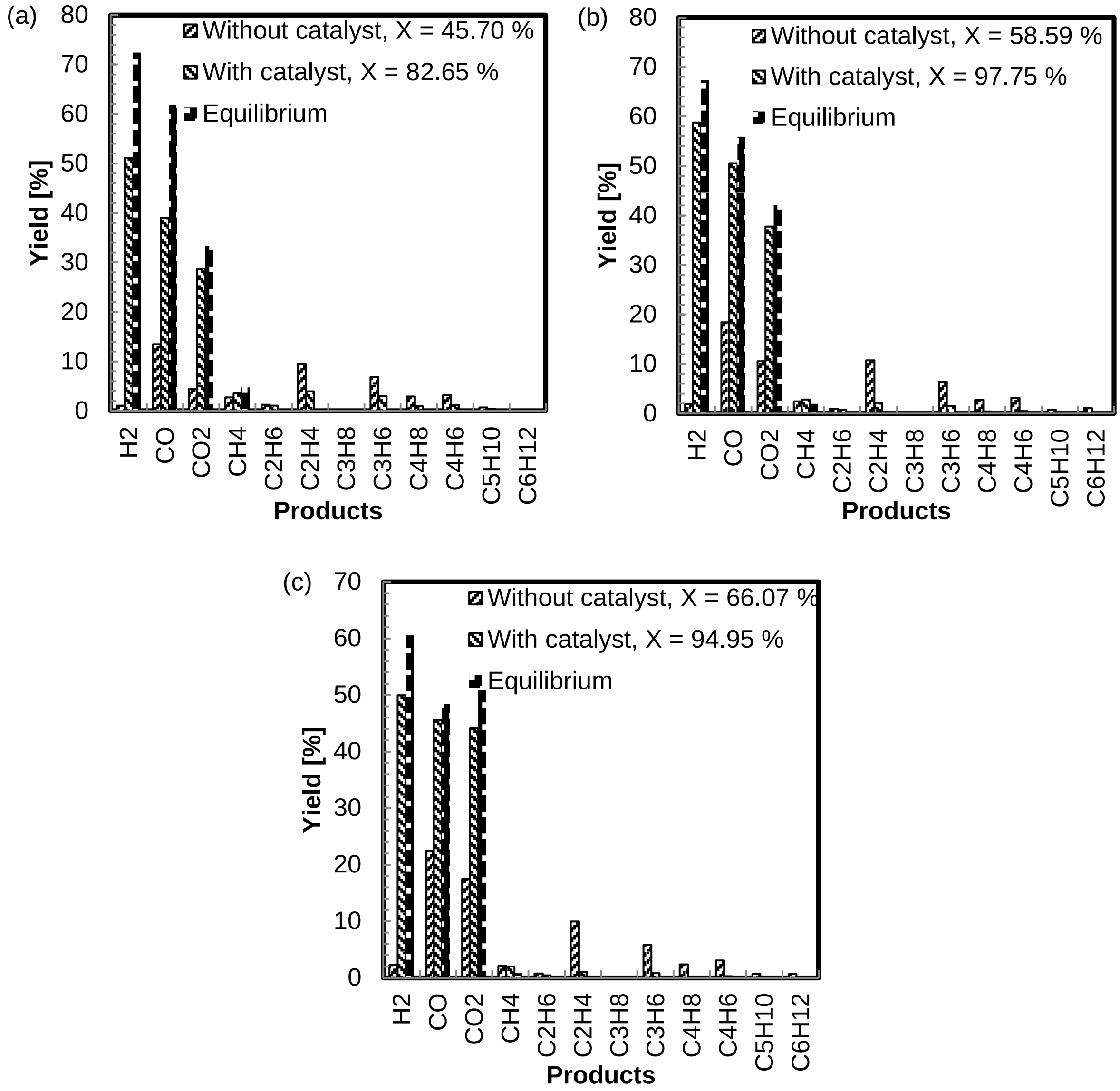

Figure 5.12: Observed exit gas product distribution with and without catalyst at WHSV = 100,000 SCC/h·g (GHSV = 1,281 1/h), T_{bed} = 700 °C, and (a) $O_2/C = 0.2$, (b) $O_2/C = 0.35$, (c) $O_2/C = 0.5$.

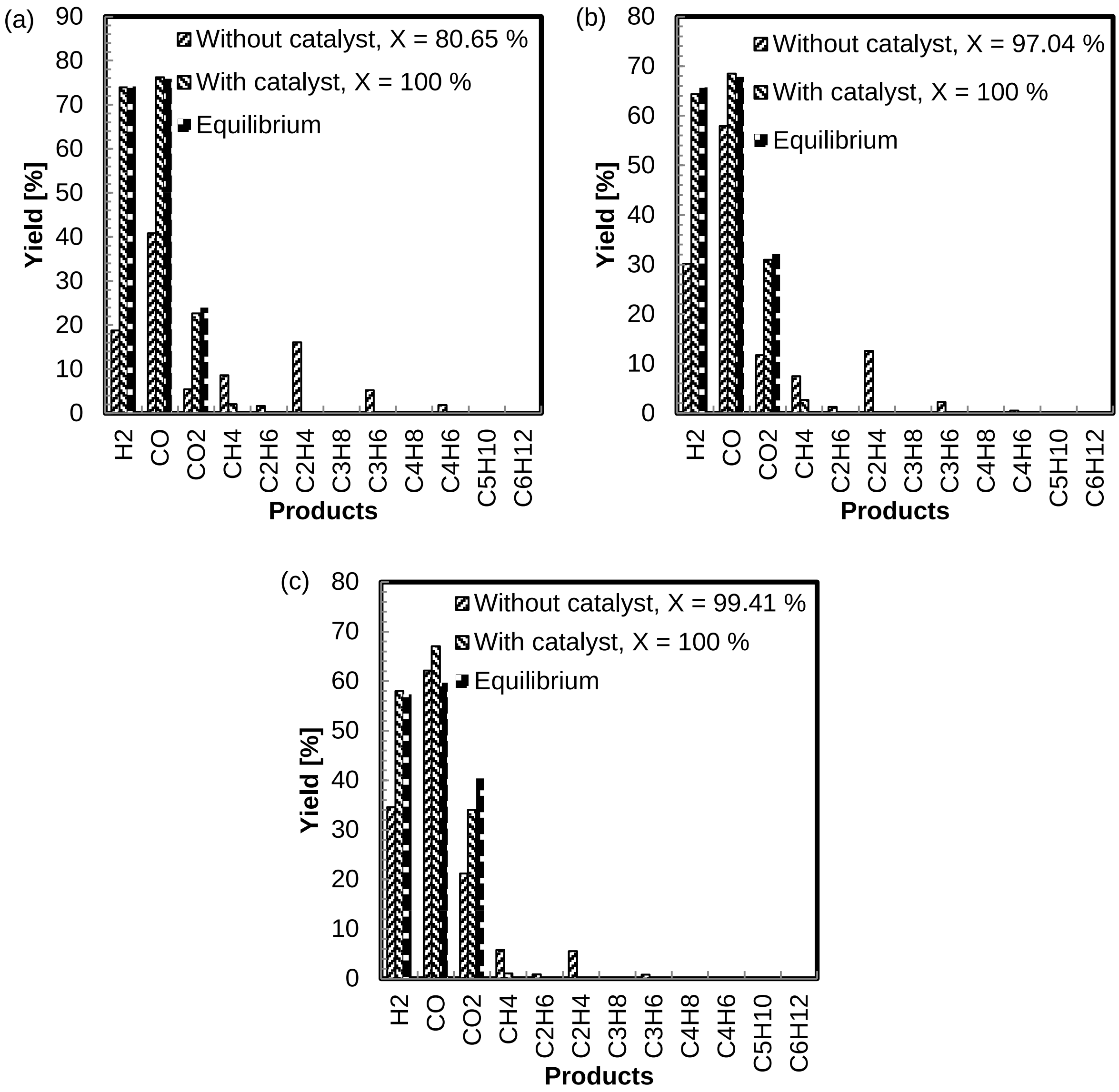

Figure 5.13: Observed exit gas product distribution with and without catalyst at WHSV = 100,000 SCC/h·g (GHSV = 1,281 1/h), T_{bed} = 850 °C, and (a) O_2/C = 0.2, (b) O_2/C = 0.35, (c) O_2/C = 0.5.

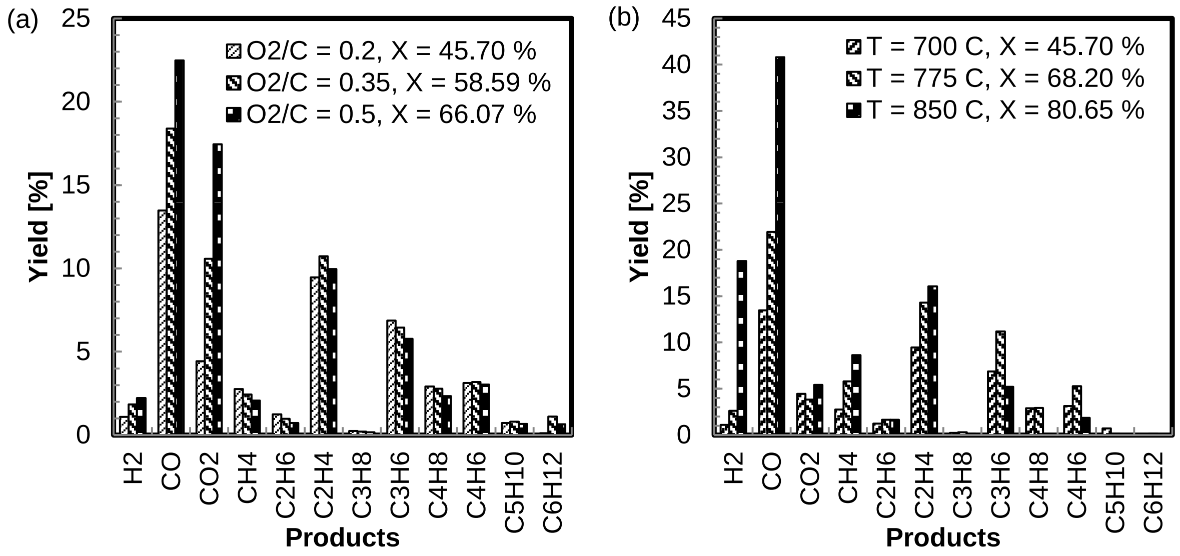

Figure 5.14: Observed exit gas product distribution without catalyst at GHSV = 1,281 1/h, (WHSV = 100,000 SCC/h·g) and (a) T_{bed} = 700 °C, (b) O_2/C = 0.2.

hand, gas-phase reactions favour ethylene and propylene formation by pyrolysis chemistry. In pyrolysis, the major ethylene formation pathway is decomposition of 1-alkyl molecule by the β-scission reaction. However, the addition of catalyst reduces ethylene and propylene yields. This could be due either to competition between gas-phase pyrolysis chemistry and surface reactions or to the consumption of ethylene by surface reactions. Conversion of greater than 45% at 700 °C without catalyst also indicates that the gas-phase reactions are significant.

At high temperature (850 °C), high amounts of CO and H_2 yield are observed without catalyst (Figure 5.13). This could be attributed to the reactor wall activity discussed later. At high temperature, alkanes and alkenes which are formed due to gas-phase reactions are found to be consumed by catalytic surface reactions. High temperature leads to more gas-phase reactions with increase in conversion to about 80% and higher.

In Figure 5.14(a), the variation of gas product composition from reactor without catalyst for changing O_2/C ratio is shown. As expected, an increase in O_2/C ratio results in an increase in CO and CO_2 yields. All alkanes and alkenes were found to decrease with increase in O_2/C ratio, except for ethylene at O_2/C equal to 0.2. Because the differences in ethylene yields are small, it is difficult to identify the reason for low ethylene yield at O_2/C ratio 0.2. An interesting observation is shown in Figure 5.14(b). A sharp jump in H_2 and CO yield at 850 °C is observed. This indicates some surface activity happening inside the reactor. This activity is attributed to catalytic reactor wall, which contains 30-35% of nickel. In one study, highly dispersed metal alloy was observed after oxidation in stainless steel reactor wall [53]. The oxidized reactor wall was found highly active for production of hydrogen by partial oxidation of n-tetradecane at 730 °C. In another study, a SS310S reactor containing 19-22% Ni for thermo-catalytic decomposition of methane was employed [54]. The reactor wall significantly affected the decomposition of methane when at temperatures higher than 850 °C. In yet another study, Incoloy 800 reactor was used for steam cracking and steam reforming of waste cooking oil [55]. It was reported that the formation of active metallic coke containing Fe and Ni particles on the wall of the reactor during gas-phase steam reforming at 800 °C. Our results are also consistent with the literature. In our study Incoloy 800 HT reactor is found to be highly active above 800 °C.

Figure 5.14 (a) and (b), clearly shows the ethylene and propylene are one of the major products from gas-phase reactions. These molecules are considered as the precursor to carbon formation on the surface of the catalyst. Hence the study of gas-phase chemistry and avoiding the formation of ethylene and propylene due to gas-phase reactions are important for better catalyst and reactor design.

3.4. Surface reactions with catalyst

The performance of the PY-1 catalyst at different operating conditions has been evaluated. As shown in Figures 5.12 and 5.13, product distribution is far from equilibrium at 700 °C, however it attains equilibrium composition at high temperature (850 °C). Figure 5.15 shows the effect of varying O_2/C ratio and space velocity on major products yield. At 700 °C and low space velocity, H_2 and CO yield is found to increase and then decrease with increasing O_2/C ratio. And at high space velocity yields of H_2 and CO were found to increase with increase in O_2/C ratio. Such behavior is unexpected in normal practical condition when the conversion is 100%. However, at 700 °C the conversion increases with increase in O_2/C (Figure 5.16). So at low O_2/C, conversion is low which ultimately results in low CO and H_2 yield. At high temperature, complete conversion of n-tetradecane is reached (not shown), and hence the expected behavior of reduction of hydrogen yield with increase in O_2/C ratio is observed (Figure 5.17). As expected, CO_2 yield is increased with increase in O_2/C ratio. CO_2 yield due to catalytic reactions is always higher than gas-phase (non-catalytic) reactions (Figure 5.12). This shows that CO_2 is not only produced by gas-phase kinetics but also by surface kinetics, such as water-gas-shift reaction. However, CO_2 yield is observed to decrease with increase in temperature, particularly at high temperature. It should be noted here that the equilibrium composition is reached at high temperature. So a decrease in CO_2 yield can be attributed to reverse water-gas-shift reaction, which also hampers the hydrogen production rate. As shown in Figure 5.18, hydrogen production is decreasing with time at 700 °C, where as hydrogen production remains stable at 775 °C and

850 °C. This suggests that the PY-1 catalyst is highly active and stable at and above temperature 775 °C.

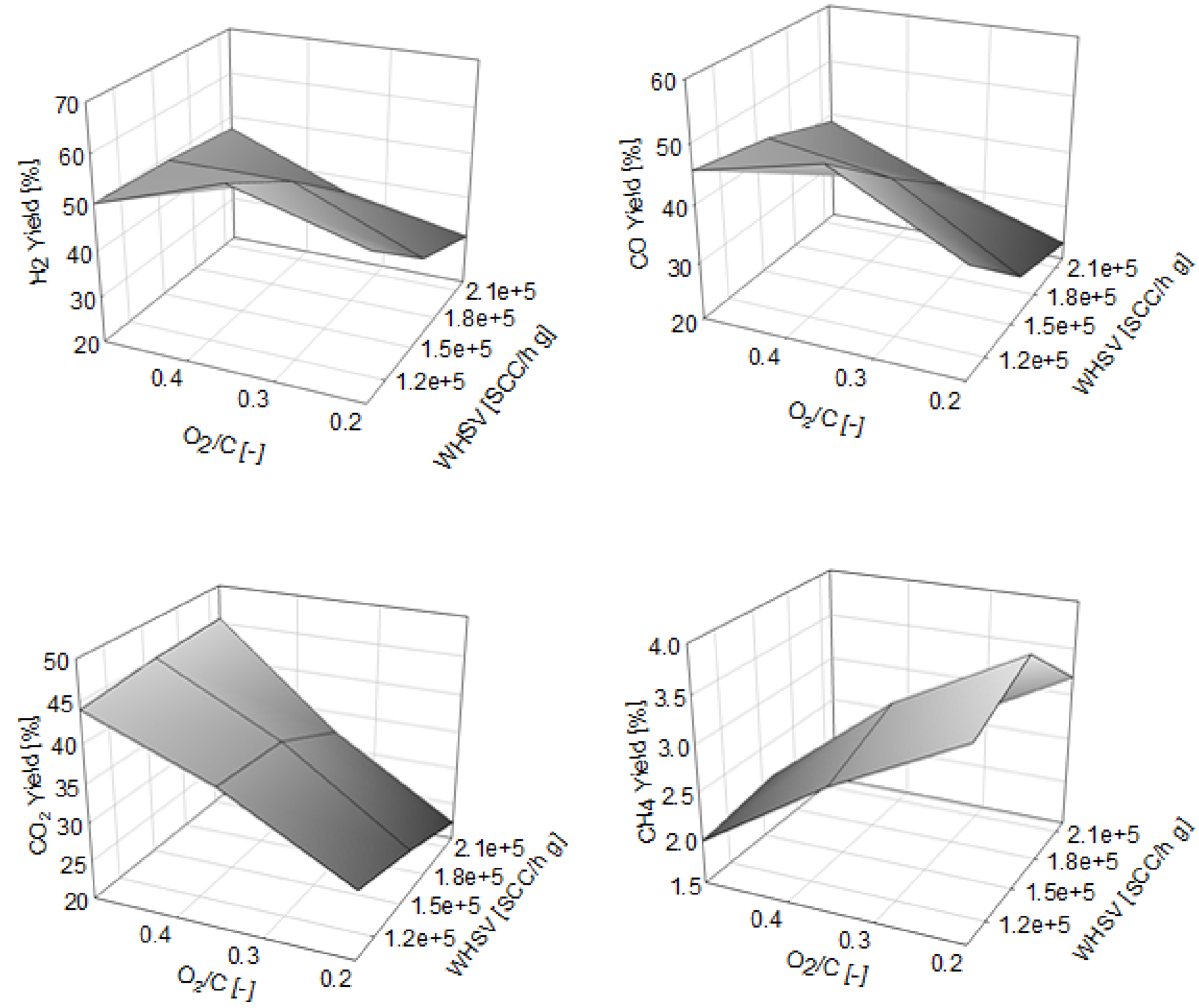

Figure 5.15: Major products yield at T_{bed}=700 °C and S/C = 1.5 (with PY-1 catalyst).

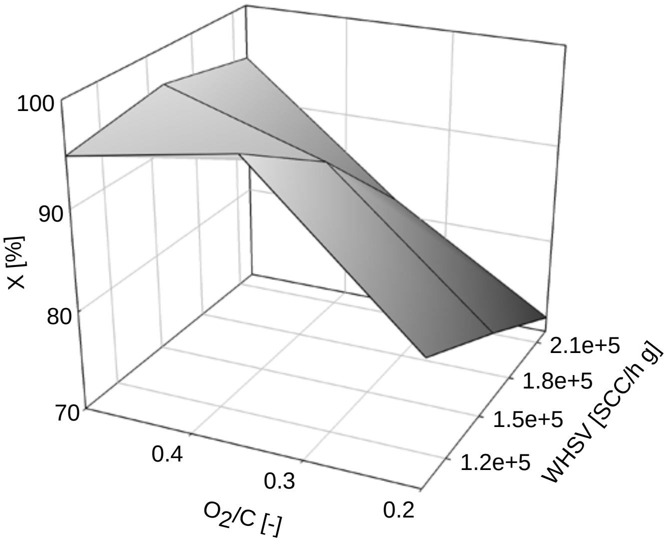

Figure 5.16: % conversion at T_{bed} = 700 °C and S/C = 1.5 (with PY-1 catalyst).

The production of methane decreases with an increase in O_2/C ratio. This was expected as a high O_2/C ratio favours combustion pathway than pyrolysis reactions. Increase in space velocity results in slight increase and then decrease in CH_4 yield. Since the change is small, it could be an experimental error (Figure 5.15). Similar behavior is observed for increase in temperature (Figure 5.17). At low O_2/C, CH_4 yield increased from 700 °C to 775 °C. This is attributed to low conversion at 700 °C.

In a reactor with only quartz sand bed, ethylene yield is observed to increase with an increase in temperature as shown in Figure 5.14(b)) due to increased rate of gas-phase reactions. However, in the reactor packed with PY-1 catalyst, negligible amount of ethylene is observed with stable hydrogen production (Figures 5.13 and 5.18) at a higher temperature (*i.e.*, at 850 °C) . This suggests that ethylene is consumed by catalytic surface reactions.

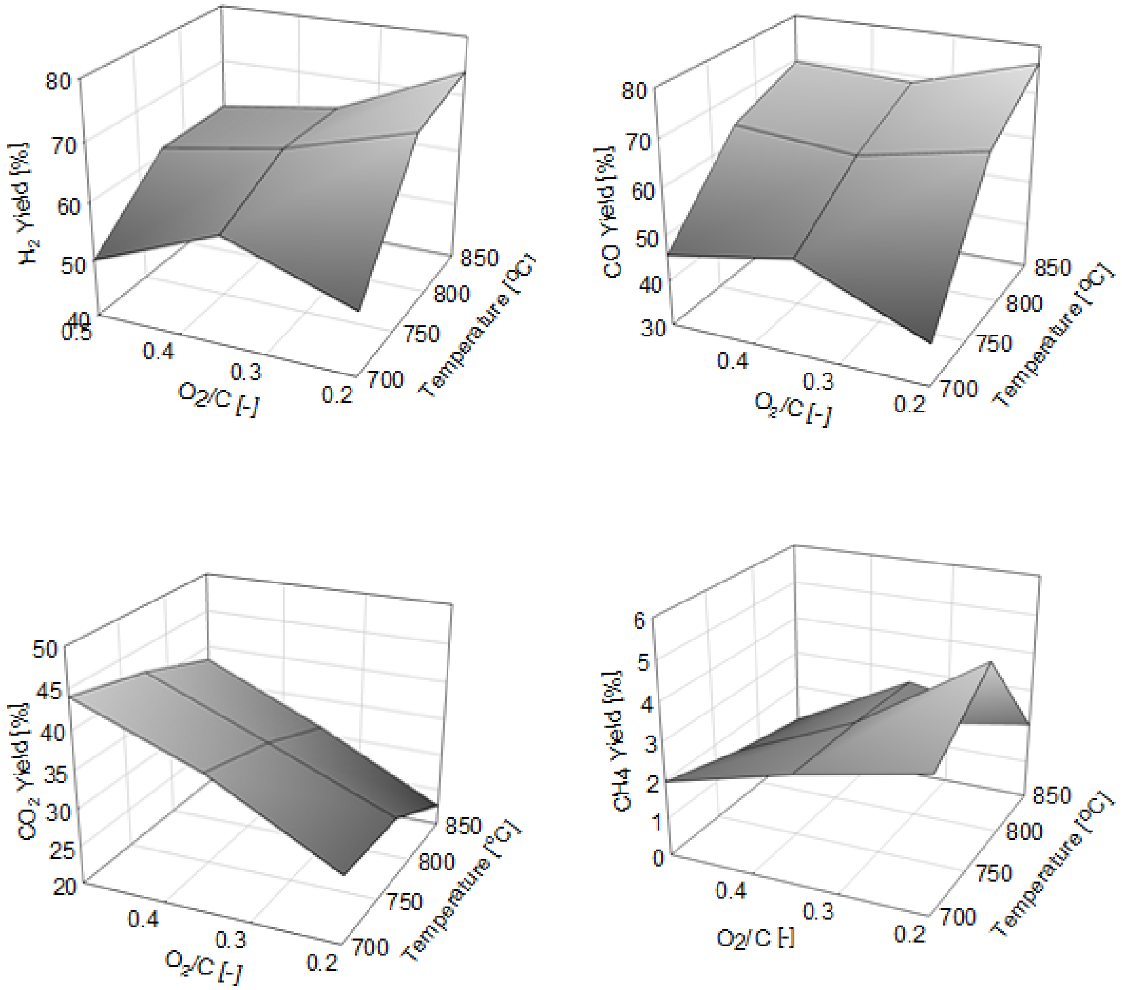

Figure 5.17: Major product yield at WHSV = 100,000 SCC/h·g, and S/C = 1.5 (with PY-1 catalyst).

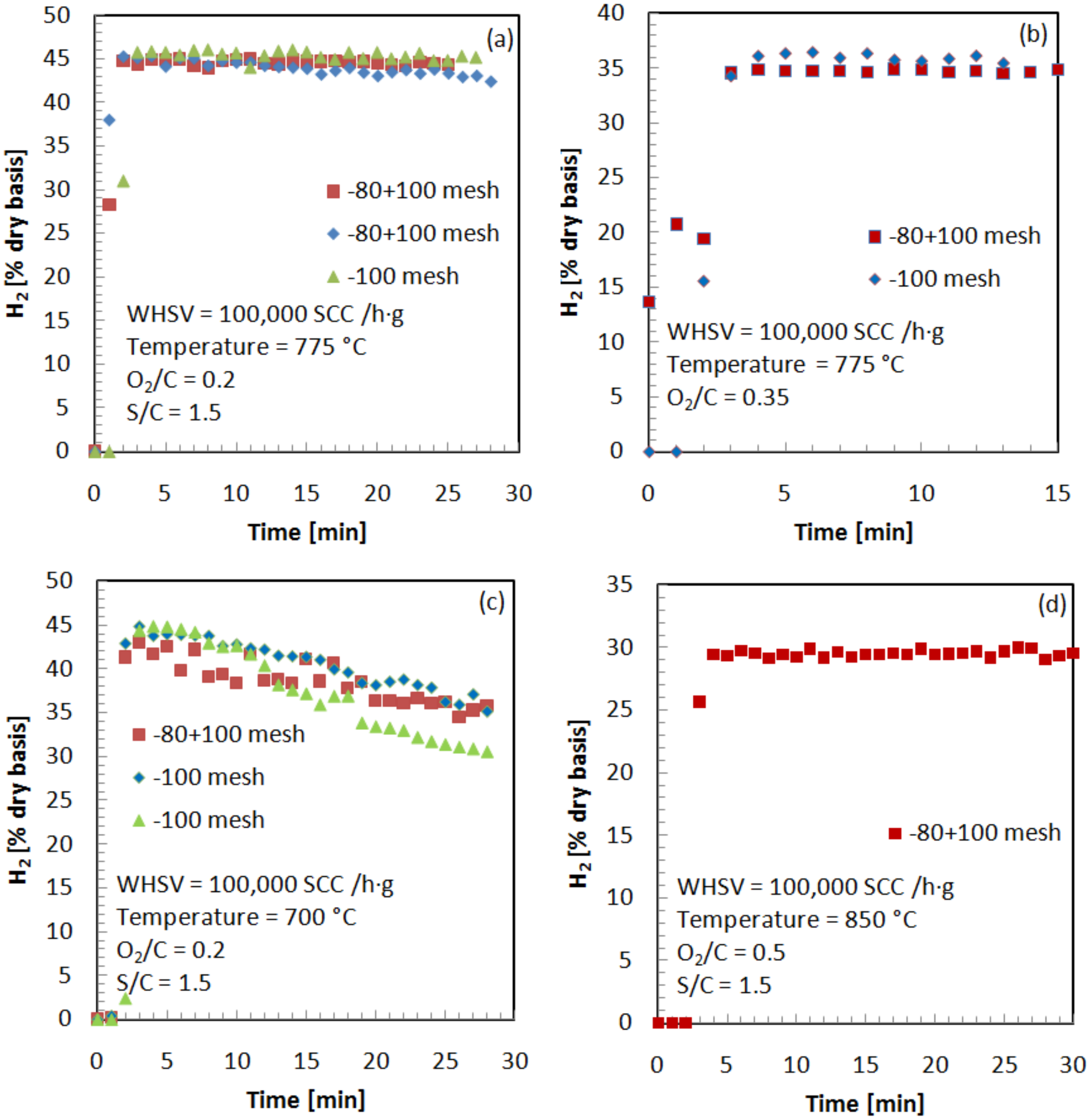

Figure 5.18: Hydrogen production at different operating conditions and with time (with PY-1 catalyst).

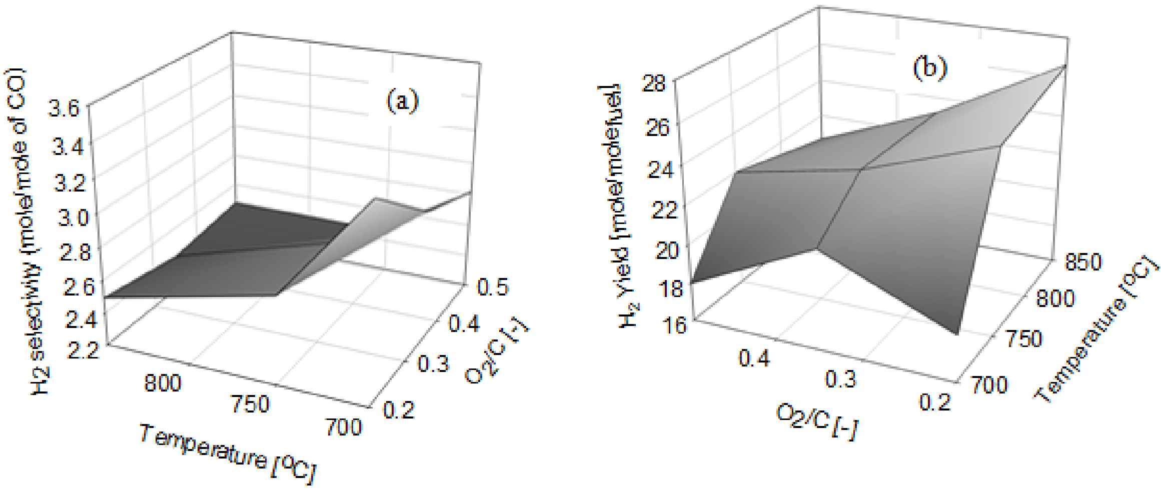

Figure 5.19: Performance of the catalyst (a) H_2 selectivity (mole of H_2/ mole of CO); (b) H_2 yield (mole of H_2/mole of n-tetradecane) at WHSV = 100,000 SCC/h·g.

Two important reformer performance characteristics H_2 selectivity (moles of hydrogen per mole of CO) and H_2 yield (moles of hydrogen per mole of n-tetradecane) are shown in Figure 5.19. As discussed earlier, due to the low conversion at 700 °C, hydrogen yield is found to increase and then decrease with increase in O_2/C ratio. We observed the stable performance at 750 °C and 850 °C. This suggests that hydrogen yield of 20 - 26 mole/mole of n-tetradecane can be obtained depending on the temperature and O_2/C ratio (Figure 5.19(a)). Hydrogen selectivity (defined as moles of hydrogen per mole of CO) is found in the range of $2.5 - 2.7$ at high temperature and various O_2/C ratios (Figure 5.19(b)).

3.5. Mass-transfer limitations

For developing an intrinsic kinetic model or validating the kinetic model, the experimental data should be free of any internal and external mass transfer limitations. To test whether the performance of the reactor was affected by diffusion (mass transfer) limitations, further experimental investigation was carried out. There have been many relationships developed to test intraparticle (intraphase or internal) and interparticle (interphase or external) mass transfer limitations [31, 56, 57]. However for packed bed reactor, the concentration profile, and thereby the reaction rate, varies along the length of the reactor making it non-trivial to apply these criteria in a straight-forward manner. The most effective way to check the internal and external mass transfer limitations is to use the experimental techniques to determine whether the rate is influenced by mass transport.

For external mass transfer limitations the criterion analogous to Weisz-Prater criterion can be used.

$$\frac{r''' r_p^2}{C_b k_c} < \frac{0.15}{n} \tag{6}$$

where r''' is the reaction rate per catalyst volume, r_p is the catalyst particle radius, C_b is the bulk phase reactant concentration, k_c is the mass transfer coefficient between the catalyst and bulk phase, and n is the reaction order.

In the above equation (6) the mass transfer coefficient is related to other variables as per the following expression [31]:

$$k_c \approx \frac{(D_{AB})^{2/3} u^{1/2} \rho^{1/6}}{(r_p)^{1/2} (\mu)^{1/6}} \tag{7}$$

where D_{AB} is the diffusivity, u is the velocity, ρ is the density, μ is the viscosity of surrounding reaction medium. Equation (6) shows that decreasing the catalyst particle size and increasing the fluid velocity can significantly increase the mass-transfer coefficient and hence decrease the external mass transfer limitations. Haynes [28] tested the external mass transfer limitations for n-tetradecane reforming on same reactor by varying the linear velocity while keeping the WHSV constant. Above 630 cm/min, the external mass transfer limitations were found to be negligible. For the current kinetic study, the minimum value of the velocity was 1562 cm/min and very fine particle (-80+100 mesh, and -100 mesh) diameter was used. Hence, this confirmed that the collected kinetic data are not affected by external mass transfer resistance.

To test the internal mass transfer limitations, the catalyst particle diameter was changed under similar operating conditions and hydrogen concentration was compared to see any difference in hydrogen concentration due to changes in particle diameter. The high temperature and high O_2/C ratio data were not used as at these conditions the outlet concentration reached the equilibrium concentration and high reactor wall activity was reported from a gas-phase kinetic study. The next choice was to use the data at 775 °C and 700 °C to test the internal diffusion limitations of the catalyst particles at high residence time. Figure 5.18 (a-c) shows the actual experimental data results on two catalyst particles diameter at 700 °C, 775 °C, and at low space velocity. The outlet hydrogen concentration at different time of the experiments and for different catalyst size particles does not vary significantly and the difference in concentration is well within experimental error. This set of data clearly shows that there is no significant internal mass transfer limitation.

4. Conclusions

The present experimental study demonstrates the characteristics and performance of stable diesel reforming catalyst. The catalyst characterization study provides a better understanding of the required criteria for stable operation in redox environment.

Two catalysts (Pt-CGO and PY-1) used in this study were subject of an accelerated test protocol that determines the rate of deactivation in a shorter duration. The Pt-CGO catalyst lost its reforming activity within 4 hrs whereas no significant changes in reforming performance were observed with the PY-1 catalyst for reforming of commercial-diesel. Also, the PY-1 catalyst was found stable at normal operating conditions for 87 hrs.

Substitution of Rh and other dopants into the lanthanum zirconate pyrochlore structure results in no major change in surface area. XRD results showed lanthanum zirconate peaks. Loss of platinum peak after the oxidation was observed in redox test for Pt/CGO catalyst. However, after the initial change, accessible rhodium didn’t significantly change in redox cycle test for the PY-1 catalyst. Further chemisorption tests confirmed the observations made by redox test.

Kinetic experiments with only quartz sand showed a significant amount of gas-phase reactions. Apart from CO and CO_2, the major products due to gas-phase reaction were ethylene and propylene, which are considered precursors for coke formation. For Incoloy 800 HT reactor, high reactor wall activity was observed above 800 °C.

Kinetic experiments using PY-1 catalyst were performed at different operating conditions. A complete conversion along with stable catalytic performance was observed at and above 775 °C. Negligible ethylene and propylene yields were observed at high temperatures and equilibrium product composition was achieved at 850 °C. 20-26 moles of hydrogen per mole of n-tetradecane, and 2.5-2.7 moles of hydrogen per mole of carbon monoxide were achieved at high temperature (*i.e.*, 850 °C).

Experimental studies showed no internal and external mass transfer resistances. Hence the collected kinetic data can further be used for kinetic study.

References

[1] B.C.H. Steele, A. Heinzel, Materials for fuel-cell technologies, Nature, 414 (2001) 345-352.

[2] C. Song, Fuel processing for low-temperature and high-temperature fuel cells: Challenges, and opportunities for sustainable development in the 21st century, Catalysis Today, 77 (2002) 17-49.

[3] S.C. Singhal, K. Kendall, High Temperature Solid Oxide Fuel Cells: Fundamentals, Design, and Applications, Elsevier Science, New York, 2003.

[4] D. Shekhawat, D.A. Berry, T.H. Gardner, J.J. Spivey, Catalytic reforming of liquid hydrocarbon fuels for fuel cell applications, Catalysis, 19 (2006) 184-254.

[5] D. Shekhawat, D.A. Berry, D.J. Haynes, J.J. Spivey, Fuel constituent effects on fuel reforming properties for fuel cell applications, Fuel, 88 (2009) 817-825.

[6] D. Shekhawat, J.J. Spivey, D. Berry, Fuel Cells: Technologies for Fuel Processing, Elsevier Science, Oxford, 2011.

[7] G. Kolb, Fuel processing: for fuel cells, Wiley-VCH, Weinheim, 2008.

[8] R.M. Navarro Yerga, M.C. Álvarez-Galván, N. Mota, J.A. Villoria de la Mano, S.M. Al-Zahrani, J.L.G. Fierro, Catalysts for hydrogen production from heavy hydrocarbons, ChemCatChem, 3 (2011) 440-457.

[9] M. Krumpelt, R. Wilkenhoener, D.J. Carter, J.M. Bae, J.P. Kopasz, T. Krause, S. Ahmed, Catalytic autothermal reforming, US DOE Annual Progress Report, 2000.

[10] M. Krumpelt, T. Krause, D.J. Carter, J.M. Mawdsley, J.M. Bae, S. Ahmed, C. Rossignol, Catalytic autothermal reforming, US DOE Annual Progress Report, 2001.

[11] I. Kang, J. Bae, G. Bae, Performance comparison of autothermal reforming for liquid hydrocarbons, gasoline and diesel for fuel cell applications, Journal of Power Sources, 163 (2006) 538-546.

[12] I. Kang, J. Bae, S. Yoon, Y. Yoo, Performance improvement of diesel autothermal reformer by applying ultrasonic injector for effective fuel delivery, Journal of Power Sources, 172 (2007) 845-852.

[13] I. Kang, S. Yoon, G. Bae, J.H. Kim, J. Bae, D. Lee, Y. Song, The micro-reactor testing of catalysts and fuel delivery apparatuses for diesel autothermal reforming, Catalysis Today, 136 (2008) 249-257.

[14] S. Yoon, J. Bae, A diesel fuel processor for stable operation of solid oxide fuel cells system: I. Introduction to post-reforming for the diesel fuel processor, Catalysis Today, 156 (2010) 49-57.

[15] S. Yoon, J. Bae, S. Lee, T.V. Pham, S.P. Katikaneni, A diesel fuel processor for stable operation of solid oxide fuel cells system: II. Integrated diesel fuel processor for the operation of solid oxide fuel cells, International Journal of Hydrogen Energy, 37 (2012) 9228-9236.

[16] B. Dreyer, I. Lee, J. Krummenacher, L. Schmidt, Autothermal steam reforming of higher hydrocarbons: n-Decane, n-hexadecane, and JP-8, Applied Catalysis A: General, 307 (2006) 184-194.

[17] S. Roychoudhury, M. Castaldi, M. Lyubovsky, R. LaPierre, S. Ahmed, Microlith catalytic reactors for reforming iso-octane-based fuels into hydrogen, Journal of Power Sources, 152 (2005) 75-86.

[18] S. Roychoudhury, M. Lyubovsky, D. Walsh, D. Chu, E. Kallio, Design and development of a diesel and JP-8 logistic fuel processor, Journal of Power Sources, 160 (2006) 510-513.

[19] G. Kolb, T. Baier, J. Schürer, D. Tiemann, A. Ziogas, E. Hermann, P. Alphonse, A micro-structured 5kW complete fuel processor for iso-octane as hydrogen supply system for mobile auxiliary power units: Part I—Development of water–gas shift and preferential oxidation catalysts reactors and assembly of the fuel processor, Chemical Engineering Journal, 137 (2008) 653-663.

[20] J. Thormann, P. Pfeifer, U. Kunz, K. Schubert, Reforming of diesel fuel in a micro reactor, International Journal of Chemical Reactor Engineering, 6 (2008) 1-18.

[21] J. Thormann, P. Pfeifer, K. Schubert, U. Kunz, Reforming of diesel fuel in a micro reactor for APU systems, Chemical Engineering Journal, 135 (2008) S74-S81.

[22] X. Karatzas, J. Dawody, A. Grant, E.E. Svensson, L.J. Pettersson, Zone-coated Rh-based monolithic catalyst for autothermal reforming of diesel, Applied Catalysis B: Environmental, 101 (2011) 226-238.

[23] J. Sehested, Four challenges for nickel steam-reforming catalysts, Catalysis Today, 111 (2006) 103-110.

[24] D.A. Berry, D. Shekhawat, D. Haynes, M. Smith, J.J. Spivey, Pyrochlore-type catalysts for the reforming of hydrocarbon fuels, U.S. Patent 8,133,463, March 2012.

[25] D.A. Berry, D. Shekhawat, D. Haynes, M. Smith, J.J. Spivey, Pyrochlore catalysts for hydrocarbon fuel reforming, U.S. Patent 8,241,600, Aug 2012.

[26] D.J. Haynes, D.A. Berry, D. Shekhawat, J.J. Spivey, Catalytic partial oxidation of n-tetradecane using pyrochlores: Effect of Rh and Sr substitution, Catalysis Today, 136 (2008) 206-213.

[27] D.J. Haynes, A. Campos, D.A. Berry, D. Shekhawat, A. Roy, J.J. Spivey, Catalytic partial oxidation of a diesel surrogate fuel using an Ru-substituted pyrochlore, Catalysis Today, 155 (2010) 84-91.

[28] D. Haynes, The Catalytic Partial Oxidation of N-tetradecane on Rh and Sr Substituted Pyrochlores. M.S. Thesis, Louisiana State University, 2007.

[29] M. Pechini, Method of preparing lead and alkaline earth titanates and niobates and coating methods using the same to form a capacitor, U.S. Patent 3, 330, 697, 1967.

[30] R.R. Kondakindi, A. Kundu, K. Karan, B.A. Peppley, A. Qi, C. Thurgood, P. Schurer, Characterization and activity of perovskite catalysts for autothermal reforming of dodecane, Applied Catalysis A: General, 390 (2010) 271-280.

[31] M.E. Davis, R.J. Davis, Fundamentals of Chemical Reaction Engineering, McGraw-Hill, New York, 2003.

[32] M. Ojeda, M. López Granados, S. Rojas, P. Terreros, J.L.G. Fierro, Influence of residual chloride ions in the CO hydrogenation over Rh/SiO_2 catalysts, Journal of Molecular Catalysis A: Chemical, 202 (2003) 179-186.

[33] D. Shekhawat, T.H. Gardner, D.A. Berry, M. Salazar, D.J. Haynes, J.J. Spivey, Catalytic partial oxidation of n-tetradecane in the presence of sulfur or polynuclear aromatics: Effects of support and metal, Applied Catalysis A: General, 311 (2006) 8-16.

[34] R.D. Parmar, A. Kundu, K. Karan, Thermodynamic analysis of diesel reforming process: Mapping of carbon formation boundary and representative independent reactions, Journal of Power Sources, 194 (2009) 1007-1020.

[35] K. Koteswara Rao, T. Banu, M. Vithal, G.Y.S.K. Swamy, K. Ravi Kumar, Preparation and characterization of bulk and nano particles of La2Zr2O7 and Nd2Zr2O7 by sol–gel method, Materials Letters, 54 (2002) 205-210.

[36] S. Yugeswaran, V. Selvarajan, P. Ananthapadmanabhan, L. Lusvarghi, Twin step synthesis of lanthanum zirconate through transferred arc plasma processing. In *23rd National Symposium on Plasma Science & Technology (PLASMA-2008),* India, 2010; 1-4

[37] S. Gaur, Dry Reforming of Methane on Rhodium and Nickel Substituted Pyrochlore Catalysts. M.S. Thesis, Louisiana State University, 2011.

[38] C. Wong, R.W. McCabe, Effects of oxidation/reduction treatments on the morphology of silica-supported rhodium catalysts, Journal of Catalysis, 107 (1987) 535-547.

[39] C.-P. Hwang, C.-T. Yeh, Q. Zhu, Rhodium-oxide species formed on progressive oxidation of rhodium clusters dispersed on alumina, Catalysis Today, 51 (1999) 93-101.

[40] Z.-r. Li, Y.-l. Fu, M. Jiang, Structures and performance of Rh–Mo–K/Al2O3 catalysts used for mixed alcohol synthesis from synthesis gas, Applied Catalysis A: General, 187 (1999) 187-198.

[41] H.Y. Wang, E. Ruckenstein, Partial Oxidation of Methane to Synthesis Gas over MgO- and SiO_2-Supported Rhodium Catalysts, Journal of Catalysis, 186 (1999) 181-187.

[42] W.-Z. Weng, X.-Q. Pei, J.-M. Li, C.-R. Luo, Y. Liu, H.-Q. Lin, C.-J. Huang, H.-L. Wan, Effects of calcination temperatures on the catalytic performance of Rh/Al_2O_3 for methane partial oxidation to synthesis gas, Catalysis Today, 117 (2006) 53-61.

[43] J.J. Strohm, J. Zheng, C. Song, Low-temperature steam reforming of jet fuel in the absence and presence of sulfur over Rh and Rh–Ni catalysts for fuel cells, Journal of Catalysis, 238 (2006) 309-320.

[44] U. Hennings, R. Reimert, Stability of rhodium catalysts supported on gadolinium doped ceria under steam reforming conditions, Applied Catalysis A: General, 337 (2008) 1-9.

[45] M. Salazar, D.A. Berry, T.H. Gardner, D. Shekhawat, D. Floyd, Catalytic partial oxidation of methane over Pt/ceria-doped catalysts: Effect of ionic conductivity, Applied Catalysis A: General, 310 (2006) 54-60.

[46] E. Rogemond, R. Fréty, V. Perrichon, M. Primet, M. Chevrier, C. Gauthier, F. Mathis, Evolution of the ceria surface area of Pt-Rh ceria-alumina catalysts submitted to hydrothermal aging at 1273 K, Applied Catalysis A: General, 156 (1997) 253-265.

[47] L.F. Liotta, A. Longo, A. Macaluso, A. Martorana, G. Pantaleo, A.M. Venezia, G. Deganello, Influence of the SMSI effect on the catalytic activity of a Pt(1%)/$Ce_{0.6}Zr_{0.4}O_2$ catalyst: SAXS, XRD, XPS and TPR investigations, Applied Catalysis B: Environmental, 48 (2004) 133-149.

[48] J. Kašpar, P. Fornasiero, M. Graziani, Use of CeO2-based oxides in the three-way catalysis, Catalysis Today, 50 (1999) 285-298.

[49] K. Tomishige, S. Kanazawa, K. Suzuki, M. Asadullah, M. Sato, K. Ikushima, K. Kunimori, Effective heat supply from combustion to reforming in methane reforming with CO_2 and

O_2: comparison between Ni and Pt catalysts, Applied Catalysis A: General, 233 (2002) 35-44.

[50] K. Tomishige, M. Nurunnabi, K. Maruyama, K. Kunimori, Effect of oxygen addition to steam and dry reforming of methane on bed temperature profile over Pt and Ni catalysts, Fuel Processing Technology, 85 (2004) 1103-1120.

[51] J. Baron, E.M. Bulewicz, W. Żukowski, S. Kandefer, M. Pilawska, Combustion of hydrocarbon fuels in a bubbling fluidized bed, Combustion and Flame, 128 (2002) 410-421.

[52] F. Bustamante, R. Enick, R. Killmeyer, B. Howard, K. Rothenberger, A. Cugini, B. Morreale, M. Ciocco, Uncatalyzed and wall-catalyzed forward water–gas shift reaction kinetics, AIChE Journal, 51 (2005) 1440-1454.

[53] H. Yamada, S. Kawai, T. Tomohiko, Tetradecane reforming with stainless-steel based catalyst. In *The 13th Asia Pacific Confederation of Chemical Engineering Congress*, Taipei, Taiwan, 2010.

[54] H.F. Abbas, W. Daud, Influence of reactor material and activated carbon on the thermocatalytic decomposition of methane for hydrogen production, Applied Catalysis A: General, 388 (2010) 232-239.

[55] J. Gornay, L. Coniglio, F. Billaud, G. Wild, Steam cracking and steam reforming of waste cooking oil in a tubular stainless steel reactor with wall effects, Energy & Fuels, 23 (2009) 5663-5676.

[56] J.A. Dumesic, D.F. Rudd, L.M. Aparicio, J.E. Rekoske, A.A. Treviño, The Microkinetics of Heterogeneous Catalysis, American Chemical Society Washington, DC, 1993.

[57] G.F. Froment, K.B. Bischoff, J. De Wilde, Chemical Reactor Analysis and Design, Wiley, New York, 1990.

Chapter 6

Development of a Mechanistic Model for Gas-phase Reactions Occurring in Autothermal Reforming of Diesel Surrogate (N-tetradecane)

6.1 Preface

High temperature catalytic reforming processes also favour gas-phase reactions. Experimental studies for ATR in a reactor without active metal catalyst, discussed in Chapter 5, showed that gas-phase reactions are dominant in autothermal reforming of n-tetradecane. The generalized kinetic modeling approach used in Chapter 4 is not sufficient as it assumes heavier hydrocarbon molecules reach the catalyst surface without any gas-phase reactions in the pre-catalytic region. This chapter describes the detailed gas-phase kinetic model generated using automatic “Reaction Mechanism Generator” (RMG) software. Also the validation of the model using literature data on combustion and pyrolysis, and current study experimental data on autothermal reforming is presented. A packed bed reactor model including all modes of heat transfer, mass transfer and momentum transfer is given and a hybrid approach of coupling large chemistry and complex heat transfer in a packed bed reactor system is presented. The importance of gas-phase reactions in the pre-catalytic zone of the packed bed reactor is explained based on fundamental understanding of oxidation and pyrolysis chemistry. Important reaction paths for major product formation are elucidated based on sensitivity analysis and rate of production analysis.

The conclusions drawn from this chapter not only helped in gaining detailed insight into the reaction chemistry in the pre-catalytic reactor zone but also highlighted that the steam reforming reactions are dominant on the surface of the catalyst. Gas-phase reaction kinetic model generated in this chapter along with modeled temperature profiles inside the reactor are used for surface kinetic study discussed in Chapter 7.

6.2 **Abstract**

Modeling an autothermal reformer (ATR) is a multi-scale problem, which requires detailed gas-phase and surface kinetics coupled with mass, momentum and heat transfer. Such models offer mechanistic insight and are useful tools in design and optimization. This study presents a multi-scale approach to modeling autothermal reforming of n-tetradecane in an inert packed-bed reactor. Kinetics for gas-phase reactions under ATR operating conditions were generated using the open-source Reaction Mechanism Generator (RMG) software package. The generated model was benchmarked against shock-tube ignition delays and the model was extended for high-pressure pyrolysis experiments to access its predictive ability in the oxidation and pyrolysis regimes. An iterative approach was used to couple the mass/heat transfer (solved in COMSOL^{TM}) with detailed kinetics (solved using Chemkin-Pro). The overall packed-bed ATR model performs well at temperatures below 700 °C but not so at higher temperatures most likely due to reactor wall activity. The current simulations suggest the presence of two oxidation regions inside the reactor. The first occurs near the inlet where degradation and oxidation of the parent fuel leads to the temperature jump of ~200K. The second stage involves oxidation of degradation products and occurs near the middle of the reactor. Rapid consumption of the inlet hydrocarbons suggests that the organic feed undergoing catalytic reforming depends heavily on the residence time in the upstream region. Sensitivity and flux analysis are used to analyze important pathways for CO, CO_2, C_2H_4 and C_3H_6 production.

Keywords: Diesel Autothermal Reforming; Solid Oxide Fuel Cell; Pyrochlore Catalyst; Catalyst Characterization; Catalyst Activity

1. Introduction

Reforming of liquid hydrocarbons to generate hydrogen-rich reformate, for use as fuel for solid oxide fuel cells, is being pursued by various groups. One of primary issues has been the development of a high activity catalyst that is also coke-tolerant/coke-suppressant. The catalyst is designed with idea that it “sees” gaseous hydrocarbons. Volatization or vaporization of the heavy hydrocarbons requires high temperatures, which can and does promote gas-phase reaction of the hydrocarbons. The nature of these gas-phase reactions occurring in the pre-catalytic, catalytic and post-catalytic zones of a reformer may significantly influence the product composition. For example, the extent and type of gas-phase reaction occurring in the pre-catalytic zone will dictate the composition of the reaction mixture entering the catalytic zone. Gas-phase chemistry in the upstream mixing region is often cited as a major source of ethylene, a precursor for carbonaceous deposits [1-5]. This in turn, will have an impact on the efficacy of the catalyst and also influence the pathway through which reaction proceeds in the catalytic zone. All of the aforementioned factors then also have implications on the reformer operation/performance and sizing.

Of the three major types of reforming processes – autothermal reforming, partial oxidation, and steam reforming – gas-phase reactions in the autothermal reforming is perhaps the most interesting and complicated. This is because under autothermal reforming conditions both combustion and pyrolysis chemistry contributes to the overall chemical transformations in the gas-phase. Gas-phase reactions also contribute to catalytic partial oxidation of light hydrocarbons in short contact time millisecond reactors [6-8]. An optimal reformer should provide homogeneous mixing of diesel with steam and air, and sufficiently high temperatures before the gas-phase products reach the catalyst surface. Many mixing zone designs have been proposed by various groups using both experimental and Computational Fluid Dynamic (CFD) studies of mixing of reactants in diesel and gasoline reforming reactors [5, 9-12]. Although there are continuous improvements in diesel reformer designs based on CFD simulations, the understanding and incorporation of gas-phase kinetics in the mixing region upstream of the catalyst zone in these models has been very limited. Recently, Dean and co-workers pointed out the importance of modeling the upstream mixing region using n-hexane and n-dodecane as diesel surrogates [13]. They reported a kinetic model based on the combustion modeling work of Westbrook and co-workers at the Lawrence Livermore National Laboratory (LLNL). It should be noted that these models were used to predict the gas-phase concentrations and temperature profiles at high equivalence ratios (equivalence ratio is defined as the ratio of the fuel-to-oxidizer ratio to the stoichiometric fuel-to-oxidizer ratio) whereas the kinetic models were originally developed for low equivalence ratio systems. Based on their simulation, Dean *et al.* proposed that reformer must be designed such that the reaction mixture must reach the catalyst surface in less than 0.1 sec to avoid formation of troublesome quantities of ethylene (1000 ppm), assuming that the reactants are perfectly mixed at 800 K. In a related study, Deutschmann and co-workers used kinetic models from the literature for gas-phase partial oxidation of iso-octane [14, 15]. They used a 10 mm heat-shield (non-catalytic monolith) before and after the catalyst zone and assumed that no isooctane conversion occurs before the heat-shield. Their main conclusion was that the homogeneous and heterogeneous chemistry was an important element in modeling CPOX (Catalytic Partial Oxidation). However, most alkane chemistry models in the literature are not developed specifically for autothermal reforming (ATR) conditions. The aim of the present study is to develop a mechanistic model for gas-phase reaction of n-tetradecane undergoing autothermal reforming. The Reaction Mechanism Generator (RMG) computer code is employed for mechanism generation. The model development and validation involved comparison of simulation results with experimental data for oxidation and pyrolysis reported in literature as well experimental data generated in this study from a non-catalytic reactor.

2. Diesel Surrogate

Actual commercial diesel is comprised of thousands of hydrocarbon species [16] with the composition varying with geographical region. Typical North-American (USA and Canada) diesel fuel composition and properties are shown in Table 6.1 [17]. More detailed analysis of pump diesel shows that normal paraffins are around 15 wt%, isoparaffins ~17 wt%, naphthenes ~48 wt%, monoaromatics ~15-25 wt%, diaromatics ~5-15 wt%, and polyaromatics ~0-5 wt% [18, 19]. North-American diesel contains higher aromatic and sulphur content than European diesel [12]. Experiments with surrogate fuels are always useful because they avoid the complexity

Table 6.1: Chemical and physical properties of typical North American diesel fuel [17]

Property	Value
Cetane Number	40-56
Carbon Number Range	C_{10}-C_{24}
Boiling Range (°C)	190-360
Composition (wt%):	
% normal and branched alkanes	25-40
% cyclo-alkanes	20-40
% aromatics	15-40

of real diesel while providing an understanding of the underlying physical as well as chemical processes such as ignition chemistry, pathways to pollutant formation, vaporization, and mixing of reactants. Heptane is commonly selected as a diesel surrogate as it has a cetane number of ~55, comparable to European and Japanese diesel fuel. However, the oxidation and pyrolysis kinetics of n-heptane do not correspond to the behaviour of real diesel [17]. Farrel *et al.* [17] have proposed different target surrogate molecules for advanced research in diesel combustion for efficient diesel combustion engine design. N-decane, n-dodecane, n-tetradecane, and n-hexadecane fall within the diesel boiling range and are considered more suitable representatives of paraffins in diesel surrogates. The National Energy Technology Laboratory's (NETL) recently proposed a mixture of n-tetradecane, 1-methylnaphathelene and decalin as a next-generation diesel surrogate to represent the paraffinic, aromatic and naphthenic components of diesel [18]. A comprehensive understanding of diesel reforming should ideally include representative components from all species classes but this is beyond the scope of a single study. As a result, n-tetradecane was selected as a surrogate fuel in the present work. Consequently, the results and conclusions shown below are representative of the fate of the paraffinic component of real diesel. Analysis of other species classes would definitely be useful for developing reformer models that better represent the processing of actual diesel fuel.

3. Experimental

Gas-phase kinetic experiments were performed in a fixed bed continuous flow reactor (Autoclave Engineers, Model. BTRS Jr.) without catalyst, but with quartz sand bed, as shown in Figure 6.1. All inlet and outlet flow lines were inside the hot box for complete evaporation of the reactants and to avoid product condensation. Programmable temperature controller (Eurotherm, Model no. 2416) was used to control the hot box temperature at 375 °C. Nitrogen and air were delivered by mass flow controllers (Brooks, Model no. 5890E) with a reported error of ± 1% of full scale. Liquid hydrocarbon fuel and water were delivered by highly accurate (± 1%) HPLC pump (Dionex Corp., Model no. P680A HPG). The liquid hydrocarbon was vaporized in a pre-heated nitrogen stream in a specially designed mixing unit. Water was evaporated in a coil and then mixed with the heated air. The air-steam mixture was then passed through a coil for complete mixing before it was mixed with hydrocarbon-N_2 mixture at the reactor inlet. For the

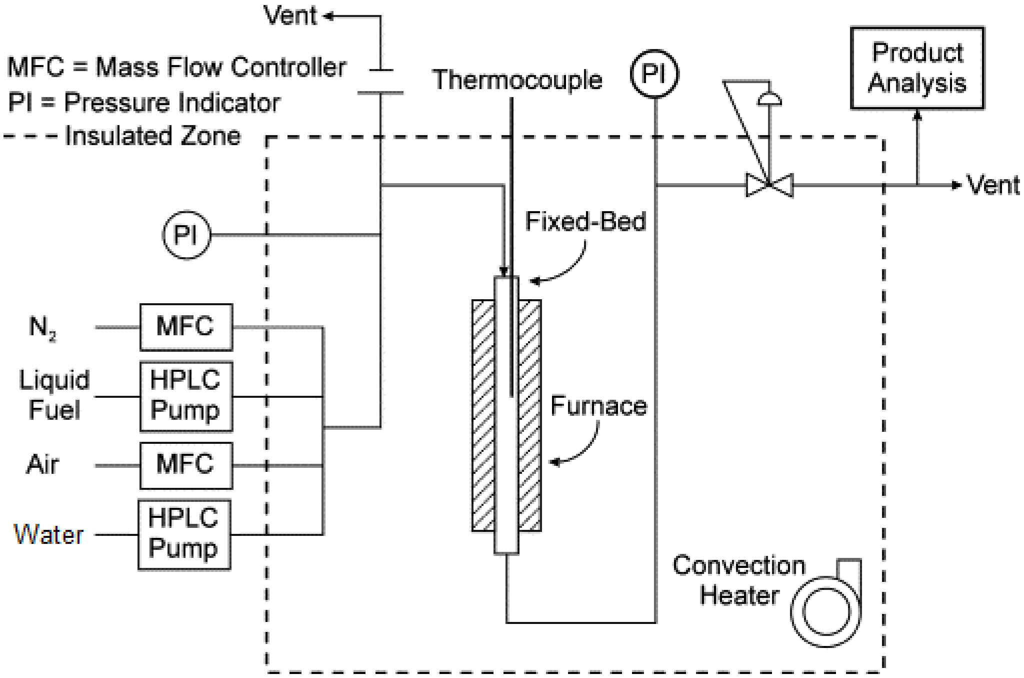

Figure 6.1: Experimental system for activity and kinetic study [20]

gas-phase kinetic study, -20+60 mesh quartz sand particles were placed inside the 8 mm i.d., 27.94 mm long, Incoloy 800HT (approximate composition: 30-35% Ni, 39.5% min Fe, 19-23% Cr) tubular reactor tube. The reactor was heated by the split tube furnace (Series 3210, Applied Test Systems, Inc.) controlled by a programmable controller (Eurotherm, Model no. 2416). The heat input to the furnace was determined by the difference in set-point temperature and thermocouple temperature at the center of the catalyst bed (T_{bed}). A sample conditioner (Universal Analyzers Inc., Model no. 1050S) at the reactor outlet was used to condense steam and any unconverted hydrocarbons from the product gas stream.

The product gas (N_2, H_2, O_2, CO, CO_2, and methane) was analyzed continuously using a Thermo Onix mass spectrometer (MS) (Model no. Prima δb, with a 200 a.m.u. scanning magnetic sector) with standard ±2% analytical error in gas concentrations. The gaseous hydrocarbon products were analyzed using a HP5890 gas chromatograph (GC) equipped with a flame ionization detector (FID).

A detailed schematic of the packed bed reactor system used in the experiments at NETL is shown in Figure 6.2. The reactor was filled with silica particles of average diameter 550 μm. The experimental set-up involves conductive, convective and radiation heat transfer. It is important to model the processes accurately to obtain an accurate temperature profile as this directly affects the rate of reaction. Because of safety and design issues, it was not possible to directly measure the temperature profile inside the reactor during the autothermal reforming experiments. The alternative was to validate the heat transfer model by measuring the temperature profile without reaction by moving a thermocouple along the axis of the reactor in nitrogen flow. The heat transfer model could then be used to predict the temperature profile in the reactor during reaction experiments.

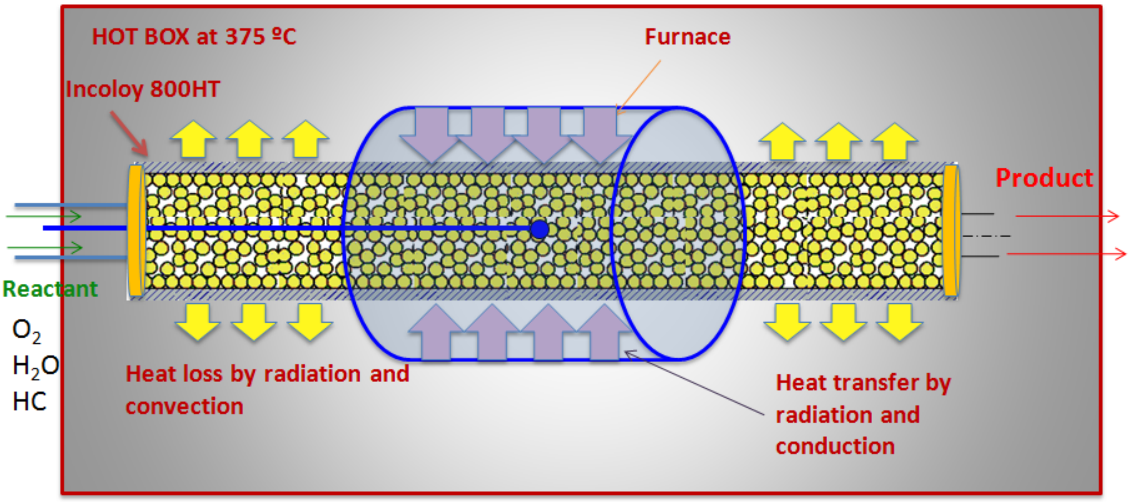

Figure 6.2: Experimental packed bed reactor system

4. A Packed Bed Reactor Model and Governing Equations

In addition to detailed kinetics, adequate treatment of the transport and heat transfer within the packed-bed reactor is necessary for modeling purposes. For this purpose, a two-dimensional (2-D) packed bed reactor model with heat and momentum transfer was developed. The software package, COMSOL^{TM}, was used including the heat transfer and fluid flow modules [21]. A detailed schematic of the packed bed reactor system used in the experiments at NETL is shown in Figure 6.2. The governing equations used to calculate the bed properties and to solve for the temperature and the velocity profiles within the reactor are presented in Appendix–C.1.

4.1. Iterative approach to solve for temperature profile within the reactor:

As the apparatus was not instrumented to measure the temperature profile inside the reactor, an iterative numerical approach was adopted instead. Coupling the fluid dynamics and heat transfer effects defined above with the large number of reactions and species was challenging using currently available Computational Fluid Dynamics (CFD) software even with the plug flow and isobaric assumptions. The Chemkin software package (Chemkin-Pro, 15112) allows the user to work with large detailed kinetic models; however, it does not allow a sophisticated description of heat transfer effects. The solution was to develop a hybrid approach in which the simplified packed-bed isobaric plug-flow reactor model with heat transfer was solved using a finite element CFD solver while the kinetic equations were solved using the Chemkin. The temperature profiles obtained without reaction were used as the initial guess that was provided as input to Chemkin which in turn calculates the heat of reaction along the length of the reactor. This heat of reaction profile was then fed back to the finite element plug flow solver to get the resulting temperature profile. This procedure was repeated until a convergent temperature profile was obtained. A proof-of-concept for this approach (shown in Appendix–C.2) was performed using a simple reactor system with a kinetic model simple enough to be handled by CFD software. Results from the iterative solution were found to be in excellent agreement with the exact solution. Although this does not prove the method is application to the more complex model it does provide some confidence that the method is viable.

5. Kinetic modeling using Reaction Mechanism Generator (RMG)

Mechanistic model for gas-phase reactions can be comprised of thousands of species and elementary reactions as is commonly seen in the combustion and pyrolysis literature. Traditionally, these models have been developed using chemical intuition to guide the choice of reactions and species to be included [22]. The models are validated against experimental measurements performed over a range of temperatures and pressures in different reactor configurations including shock-tubes and rapid compression machines. These validation tests provide data on the most sensitive kinetic and thermochemical parameters, which can then be refined with quantum chemistry calculations or elementary kinetics measurements.

The models, based on heuristics, are suitable for smaller systems, but quickly become cumbersome and tedious, especially for long chain alkanes where the number of reactions and species can quickly become intractable. An approach to overcome this problem is to use automated algorithms to select the most important reactions and species. Even though this approach has many attractive features, existing tools are not “black-box” in nature. The gas-phase kinetic models used in this work were obtained using the Reaction Mechanism Generation (RMG) software developed at the Green group in MIT [23, 24]. RMG offers an automated platform to build reaction mechanisms for systems of the size and complexity as those involved in the current problem.

The basic structure of RMG is shown in Figure 6.3. RMG uses a species-flux based criterion [25] to determine which species to include in the model (“core” species) and which ones to keep out (“edge” species). At any point in the simulation, all possible self and cross reactions of the species in the core are used to discover potential edge species. This is performed using twenty three elementary reaction classes such as H-abstraction, beta-scission, and bond-breaking. The most important edge species are incorporated into the core and the process is repeated till a user-specified termination criterion (typically reaction time or conversion of a particular species) is met. Whether a species ends up in the core or not depends on its net flux and the user-specified species tolerance. Edge species whose flux exceeds the critical flux (defined as the product of the species tolerance and the RMS flux of species in the current model core) are incorporated into the model core. The resulting model at the end of the iterative solution is self-consistent at the specified user-tolerance.

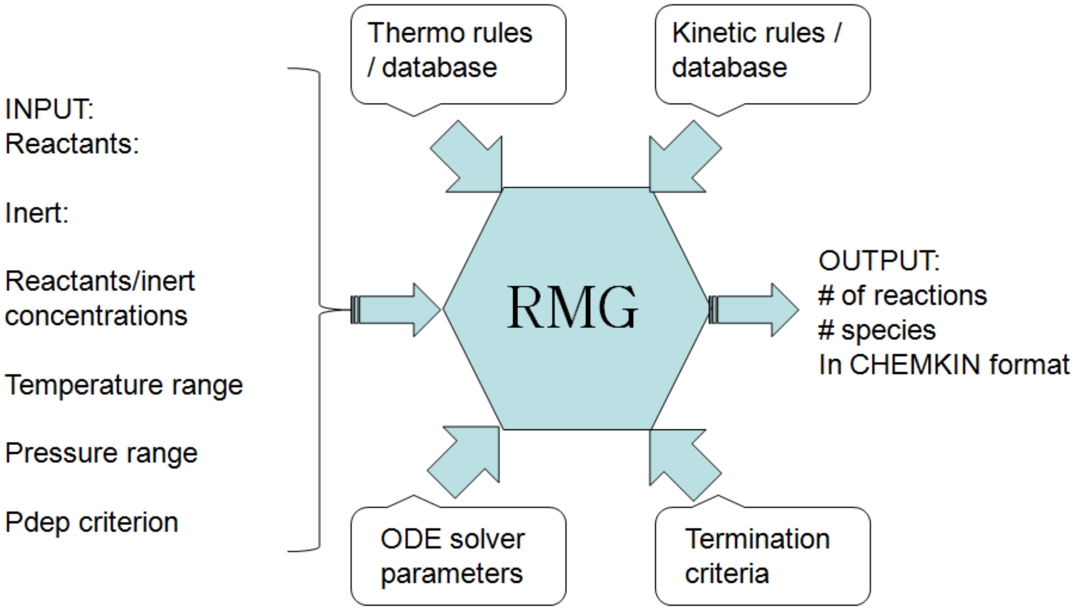

Figure 6.3: Structure of “Reaction Mechanism Generator” (RMG) software

The input to RMG consists of the temperature, pressure, initial concentration of the reacting mixture (n-tetradecane, steam and oxygen for the present case) and the termination criterion. RMG offers features that allow users to provide their own thermochemistry estimates and rate parameters using kinetic and thermochemistry libraries. If no libraries are used, RMG uses group additivity to estimate thermochemical parameters with HBI (Hydrogen Atom bond Increments) corrections of Bozzelli and co-workers [26] for radical species. The RMG kinetics database provides estimates of high-pressure limit rates for reactions based using rate-rules developed using quantum calculations and experimental data. Fall-off effects and chemical activation can also be estimated on-the-fly using methods described by Allen *et al.*[27] using either the steady-state master equation method (also referred to as the ‘‘Reservoir State” method) of Green and Bhatti or the ‘‘Modified Strong Collision” approach of Chang *et al.*[28]. The obtained $k(T,P)$ can be reported using either the pressure-dependent Arrhenius format (PLOG) or Chebyshev polynomials (CHEB). For this study, all pressure-dependent rates generated by RMG are reported in the PLOG format.

The output files of a RMG simulation include a CHEMKIN compatible reaction mechanism, species concentration profiles and reaction flux profiles. Models generated by RMG have previously been shown to be in good agreement with experimental data for the pyrolysis, combustion and steam cracking of other hydrocarbons [29, 30].

The input specifications used for mechanism generation are shown in Table 6.2. The species tolerance parameter in RMG is used to determine the relative importance of a given species and whether it should be included in the model. Tighter tolerances lead to larger models with all possible pathways but also capture many reaction channels that do not play any significant part in the overall reaction. For larger molecules like n-tetradecane, any tolerance less than 0.1 was found to be challenging in terms of model generation time and computer memory requirements because of exponentially large number of reactions and species. With the tolerance of 0.1, the generated model had nine thousand three hundred and forty-seven reactions and four hundred and fifty-nine species under ATR conditions. The generated model with given tolerances didn't capture any reaction channels for formation of higher alkanes (above C_3) at given input conditions (Table 6.2). This is consistent with the literature and current experimental studies discussed in detail later. In pyrolysis, available n-tetradecane pyrolysis experiments were performed at high pressure and low temperature conditions, and at these conditions alkanes higher than C_3 hydrocarbons were observed. So more alkane formation paths were added to the model beyond those included in the RMG generated model.

Table 6.2: List of input conditions used for mechanism generation with RMG

Parameters/keyword	Values	Remarks
Inlet concentration	$O_2/C^* = 0.2$; $H_2O/C^* = 1.5$ N_2 = diluents	ATR condition used in experiments
Temperature Range	400 °C – 1000 °C	Range of operation of ATR
Pressure	2.36 atm	Pressure in ATR
Species tolerance	0.1	See text
N-tetradecane conversion	99.99%	See text

*O_2/C and H_2O/C are molar ratios

GRI-Mech 3.0 model and species thermochemistry was used as a seed mechanism to capture the small molecule chemistry in the current model. In addition, a seed mechanism for n-tetradecane was used to capture the first and second O_2 addition pathways which are known to be important in low temperature ignition chemistry [31]. The developed model has been refined further by replacing the rate constants of several important reactions with more accurate recently measured or calculated rates. One of the most important reaction families in alkane pyrolysis and oxidation are the β-scission reactions of alkyl radicals derived from the parent fuel molecule. In the present study, these rates were obtained from the experimental work of Tsang and coworkers for long chain alkyl radicals [32]. The complete list of rate coefficients that were updated with recently published rates is given in Appendix–C.3. A few of most important are discussed here.

For the reaction $H + CH_2O \leftrightarrows HCO + H_2$ we used the Baulch *et al.* [33] recommendation. Recently, Friedrichs *et al.* [34] measured the rates for this reaction in the temperature range 1510 - 1960 K. However this temperature range is not of interest to the present study and as a result these rates were not used. High pressure rates for allyl + HO_2 and allyloxy decomposition were obtained from Goldsmith *et al.* [35]. Similarly high pressure rates for acetyl + O_2 system were obtained from recent work of Allen *et al.* [27] These high pressure rates were combined with modified strong collision approach to obtain pressure dependent rates in PLOG format. Pressure dependence calculations were performed with a stand-alone module of RMG package. Rates for propylene + $\cdot OH \leftrightarrows$ allyl + H_2O are obtained from Tsang [36] as discussed later. H-abstraction by methyl and H radicals from alkanes were obtained from Randolph *et al.* [37]. Rates for $HO_2+\cdot CH_3$ and O_2+CH_4 were taken from the recent measurements of Hong *et al.* [38]. These measurements are in agreement with the calculation of Jasper *et al.* [39]. The rest of the rate coefficients and species thermochemistry were default estimates by the RMG software, mostly based on group additivity calibrated by some quantum chemistry calculations [23].

6. Results and Discussion

6.1. Validation of n-tetradecane kinetic model

A summary of reaction conditions of interest for this study has been described in terms of equivalence ratio, excess air, and oxygen-to-carbon ratio in Figure 6.4. Autothermal reforming occurs under fuel-rich conditions with much higher equivalence ratios compared to those encountered during combustion process. Under the fuel-rich conditions, pyrolysis chemistry is expected to be dominant. However, the observation of CO and CO_2 and negligible quantities of O_2 (< 100 ppm) at reactor outlet suggests that oxidation chemistry is non-negligible and should be accounted for in the kinetic model. This underscores the need for validating a gas-phase kinetic model pertinent to autothermal reforming for both pyrolysis and partial oxidation regimes. In the following sections, we compare model predictions with available literature data on n-tetradecane combustion and pyrolysis. It must be noted that the model parameters are not adjusted to fit the

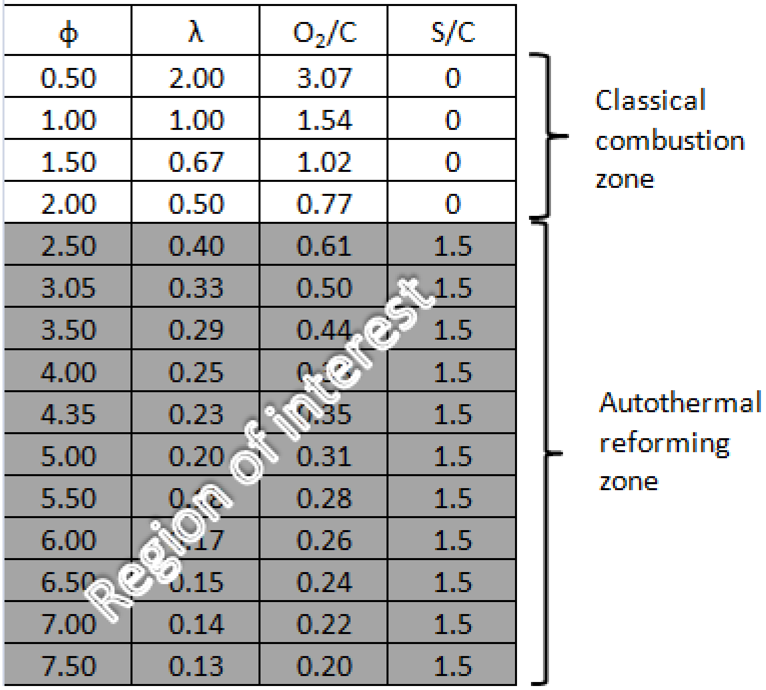

ϕ	λ	O_2/C	S/C
0.50	2.00	3.07	0
1.00	1.00	1.54	0
1.50	0.67	1.02	0
2.00	0.50	0.77	0
2.50	0.40	0.61	1.5
3.05	0.33	0.50	1.5
3.50	0.29	0.44	1.5
4.00	0.25	[illegible]	1.5
4.35	0.23	0.35	1.5
5.00	0.20	0.31	1.5
5.50	[illegible]	0.28	1.5
6.00	0.17	0.26	1.5
6.50	0.15	0.24	1.5
7.00	0.14	0.22	1.5
7.50	0.13	0.20	1.5

Figure 6.4: Reforming and combustion region, ϕ = equivalence ratio, γ = excess air = 1/ ϕ

experimental data used for validation, these are pure predictions.

6.2. Modeling ignition delay measurements

Modeling shock-tube ignition delays is commonly used for validating oxidation chemistry. The n-tetradecane reaction mechanism developed in this work was tested against shock tube ignition delays of long-chain alkanes reported by Shen *et al.* [40], Vasu *et al.* [41], and Zhukov *et al.* [42]. Shock tubes provide nearly ideal, constant volume, zero-dimensional reactor conditions up to the time of ignition, or longer in highly dilute mixture [43] and can be modeled with simple 0–D reactor models. In this study, shock tube ignition delays were modeled using the closed adiabatic homogeneous batch reactor module of Chemkin software package. The energy equation was solved by constraining the volume of the reactor. The ignition delay was calculated as time required to reach to ·OH peak or temperature inflection point, to be consistent with the definition used by the experimentalist. Shen *et al.* [40] compared their measurements with predictions from published models of Curran *et al.* [44], Westbrook *et al.* [22], Ranzi *et al.* [45], and Biet *et al.* [46] and found that the predictions from the LLNL model (six thousand four hundred and forty-nine reactions and one thousand six hundred and sixty-eight species) proposed by Westbrook *et al.* [22] was in good agreement with experimental data. Performance of the model developed in this study is compared with Shen's dataset in Figures 6.5 and 6.6. For stoichiometric mixture ($\phi=1$) and pressure of 14 atm (Figure 6.5(a)), the model predictions are in good agreement with experiment. At higher pressures, the model does well for temperatures greater than ~900 K (Figure 6.5(b)); at lower temperatures the predicted ignition delay can be up to a factor of 2.6 lower than experiment. The model also does well under fuel-lean condition ($\phi=0.5$) at both pressures reported by Shen *et al.* (Figure 6.6 (a) and (b)).

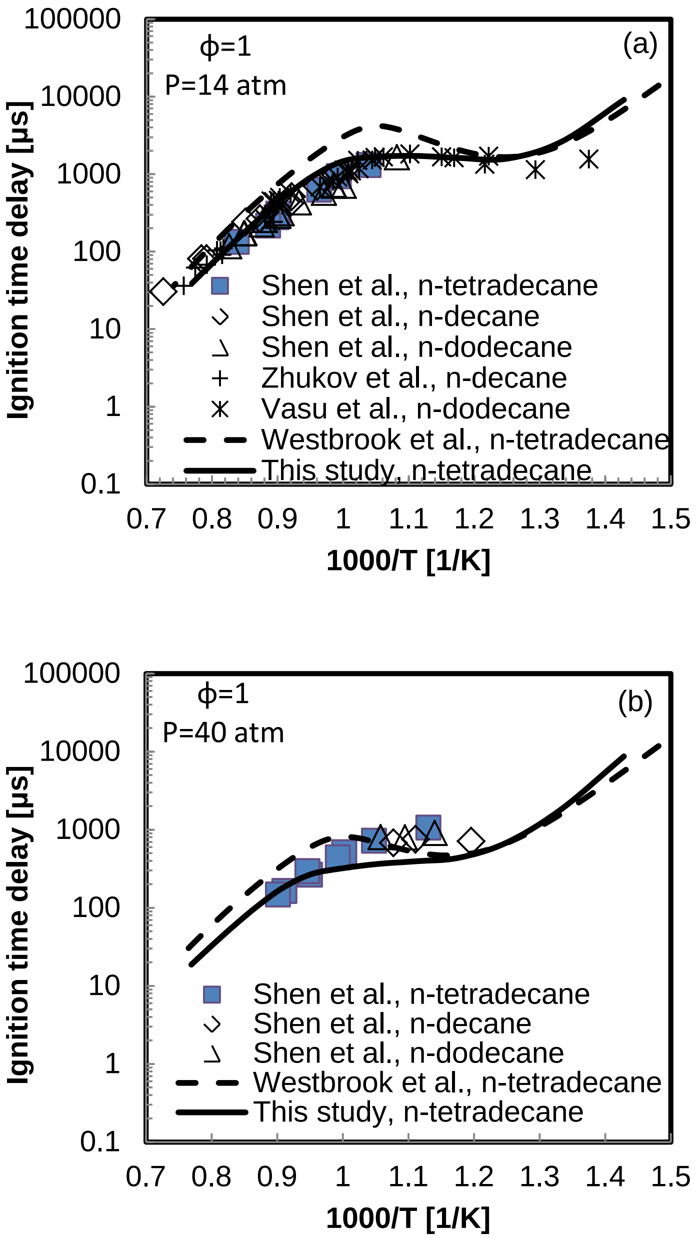

Figure 6.5: Comparison of ignition time for n-alkane/air mixtures at ϕ = 1 and *P* = 14 atm (a) and 40 atm (b) with model predictions. All literature data scaled to the listed pressures using $\tau = P^{-1}$ as used by Shen *et al.*

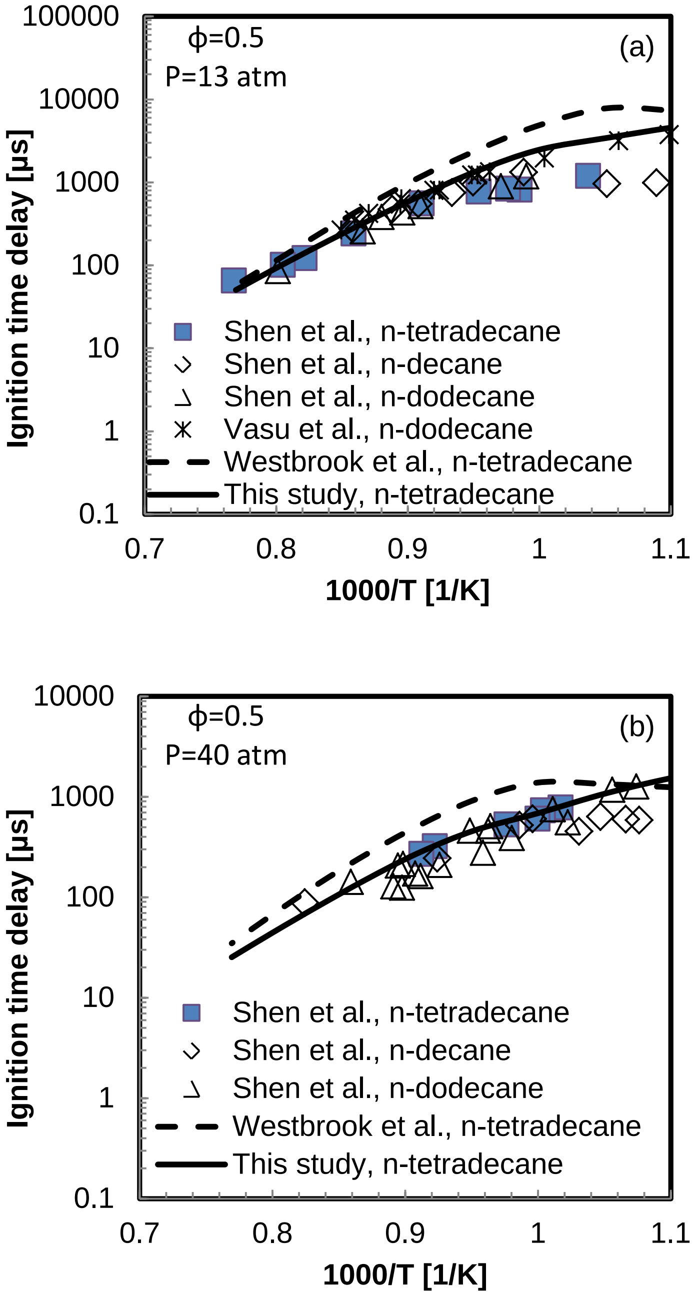

Figure 6.6: Comparison of ignition time for n-alkane/air mixtures at ϕ = 0.5 and *P* = 13 atm (a) and 40 atm (b) with model predictions. All literature data scaled to the listed pressures using $\tau = P^{-1}$ as used by Shen *et al.*

6.3. Sensitivity analysis and insights on reaction pathways

As mentioned earlier, detailed kinetic models often contain several thousand reactions and species and it is impossible to measure or calculate the large number of parameters associated with these models. The large parameter space also makes it easy to make good predictions for the wrong reasons. One approach for avoiding this common pitfall is to ensure that the reaction rates and equilibrium constants obey certain physical bounds (done to some extent in RMG itself). Another commonly used method is sensitivity analysis of model predictions. This not only reveals which pathways are dominant but also helps in model refinement by identifying which parameters need to be improved. Sensitivity analysis also helps identify spurious pathways, which may contaminate the model because of poor rate or thermochemical estimates.

Alkane oxidation pathways at different temperatures have been the subject of several investigations and are well documented in literature [31, 40, 47-51]. Sensitivity analysis was performed to gain insight into the alkane oxidation pathways predicted from our model. Details of the sensitivity analysis are presented in Appendix–C.5. At low temperatures (below 800 K), ·OH production from our model was found to be sensitive to alkyl+O_2 and hydroperoxyalkyl+O_2 reactions associated with peroxy chemistry. In this reaction sequence, alkyl radicals react with O_2 to form alkyl peroxy radicals (RO_2) that can dissociate back to alkyl radical and O_2 or isomerise (internal H-abstraction) to form hydroperoxy radicals (QOOH[1]). The QOOH radical reacts with O_2 to form hydroperoxy peroxy (OOQOOH), which isomerises and quickly decomposes to form ketohydroperoxide (HOOQ=O) and OH radicals. Ketohydroperoxide can decompose to form

---

[1] Terminology adoped from combustion literature (*e.g.*, QOOH is hydroperoxy radicals)

another radical (OQ=O) and ·OH radicals. This sequence of reactions produces two ·OH radicals and acts as a chain-branching step leading to ignition**.** Sensitivity analysis suggests that HOOQ=O dissociation reactions and other low temperature pathways are among the most sensitive reactions for ·OH production at T=700 K. At high temperatures (T > 1000 K), the alkyl radicals formed initially decompose to produce 1-olefins and smaller alkyl radicals. Sensitivity analysis for ·OH radicals at 1200 K at ignition suggests that C_1 and C_2 chemistry as well as alkyl decomposition (β-scission) reactions are important. This is consistent with current understanding which suggest that fuel decomposition reactions and small molecule chemistry is most sensitive at high temperature [48, 52-54].

6.4. Modeling pyrolysis experiments

Like alkane oxidation, alkane pyrolysis has been the subject of many previous modeling efforts and the basic chemistry is pretty well documented [13, 30, 37, 45, 55-58]. The free-radical mechanism for high temperature and low-pressure pyrolysis was first proposed by Rice-Herzfeld and Rice-Kossiakoff [59-61] and explained the formation of low molecular weight alkanes and alkenes as major products. It has been generally observed that no C_3+ alkanes are formed at low pressures (for examples, see the work of Voge and Good [62] and Depeyre *et al.* [63, 64] on n-hexadecane). Under high pressures employed by Song *et al.* [56], significant production of C_3+ alkanes was observed. This occurs because at higher concentration (*e.g.*, higher p) and lower temperature, H-abstraction to form alkanes is more competitive with β-scission. A basic schematic of pyrolysis chemistry under high and low pressure conditions is shown in Figure 6.7. At small residence times, the parent fuel is the main source of H-atoms in the system while at longer residence times most H-abstractions occur from primary pyrolysis products (secondary chemistry). Song *et al.* proposed that decrease in the yields of 1-akene (> C_3) at long residence time is mainly through H-abstraction reaction which leads to 1-alkenyl species and subsequently to cyclic / aromatic products.

To the best of our knowledge, the only experimental data on n-tetradecane pyrolysis is from the work of Song *et al.* [56] and De Witt *et al.* [55, 65]. Song *et al.* performed experiments at pressures between 2 and 9 MPa at 723.15 K. De Witt *et al.* used temperatures between 693.15 K and 723.15 K and high pressure (6.9 MPa). However, they do not report many important experimental details making it difficult to use their data for validation. Industrial scale pyrolysis

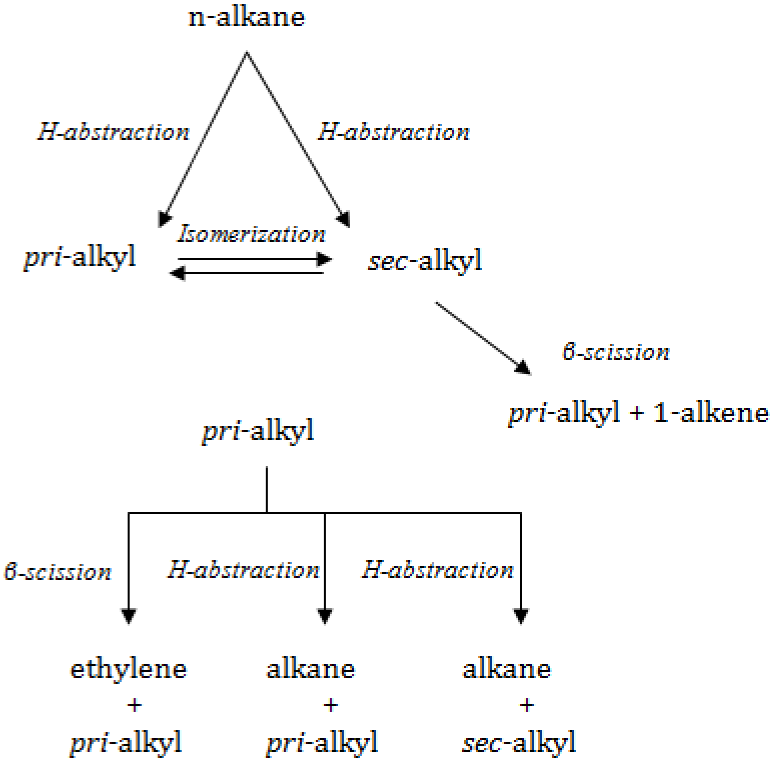

Figure 6.7: Major reaction paths for alkane pyrolysis

is normally performed at high temperatures (873 K−1173 K) and low pressures (1−5 atm) [66] which are also the conditions of interest in this study. However, due to the absence of experimental pyrolysis data under these conditions, we use the data from Song *et al.* for validation. Their batch experiments were performed under initial N_2 pressure of 0.69 MPa in 25 ml tubing bombs with 5 ml of n-tetradecane. The gaseous product concentrations were analyzed by gas chromatograph (GC) and liquid products were identified by capillary gas-chromatograph-mass spectrometry. The initial concentration was modeled used the approach of Burkl-Vitzthum *et al.* [67]. The experimental temperature profile for first six minutes (where the temperature rises from 198-723 K) was used directly in the simulation. In addition, the cooling rate was assumed to be fast.

A comparison between experimental data and predictions from different kinetic models is shown in Figure 6.8 (definition of yield is that adopted by Song *et al.*). Our model performs well for long chain alkenes but does poorly for ethylene and does not capture alkanes above C_3. Both discrepancies are related to the competition between uni-molecular beta-scission and bimolecular H-abstraction reactions of long chain alkyl radicals formed during pyrolysis. At high-pressures, H-abstraction reactions are expected to contribute significantly leading to the formation of long-chain products. However, the RMG model built under ATR conditions did not include these reactions in the model core hence enhancing the ethylene yield. Another source of error is the pressure dependence of beta-scission channels, which were not incorporated in the current model.

The missing H-abstraction channels were added to the model using the 'PopulateReactions' module of RMG, which generates a list of all possible reactions between a given set of reactants. In present study, H-abstraction, disproportionation, radical recombination, and β-scission

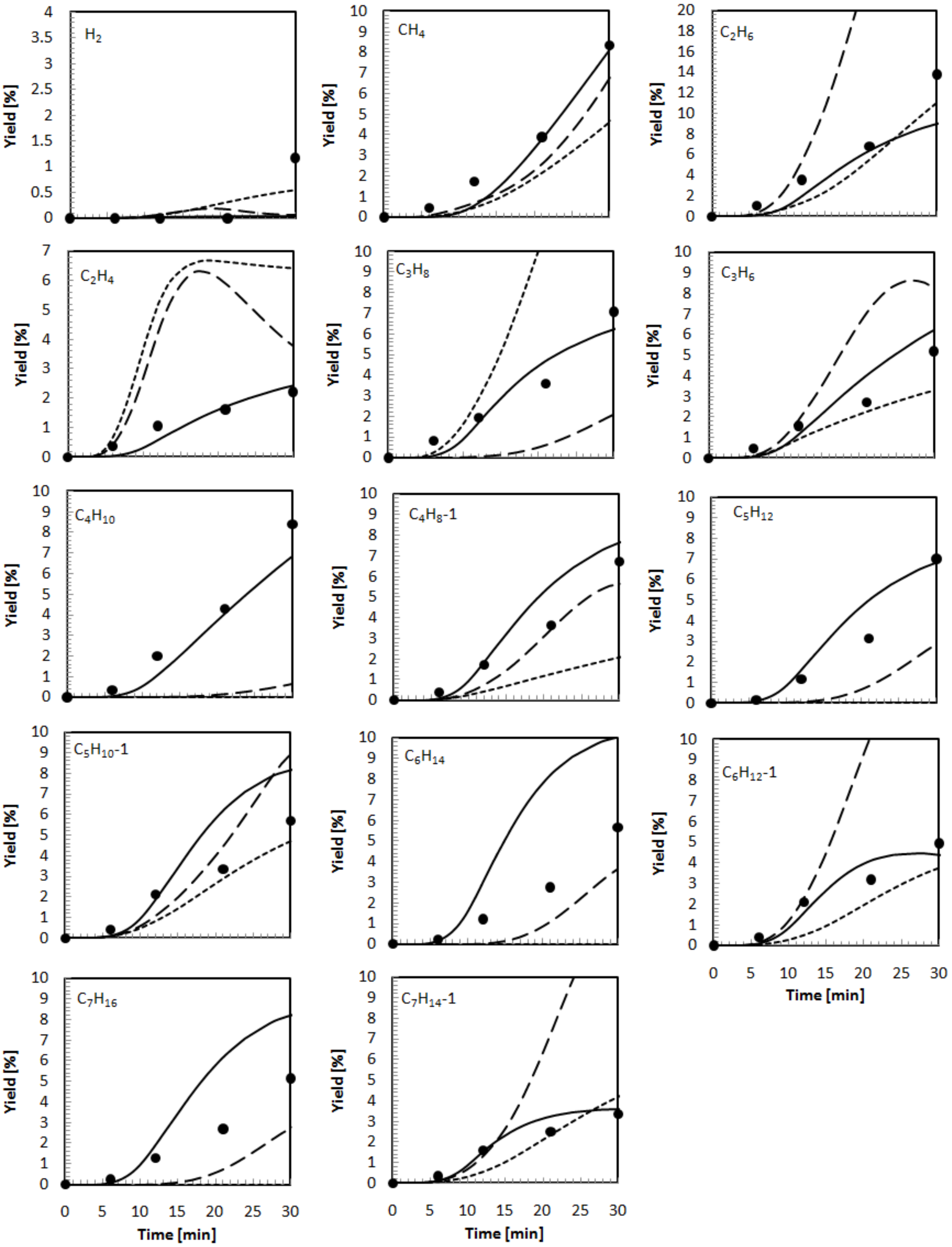

Figure 6.8: Comparison of fitted model lines and experimental results (symbols); — — LLNL model; - - - - -, this study (low *p* model); ——, this study-extended model.

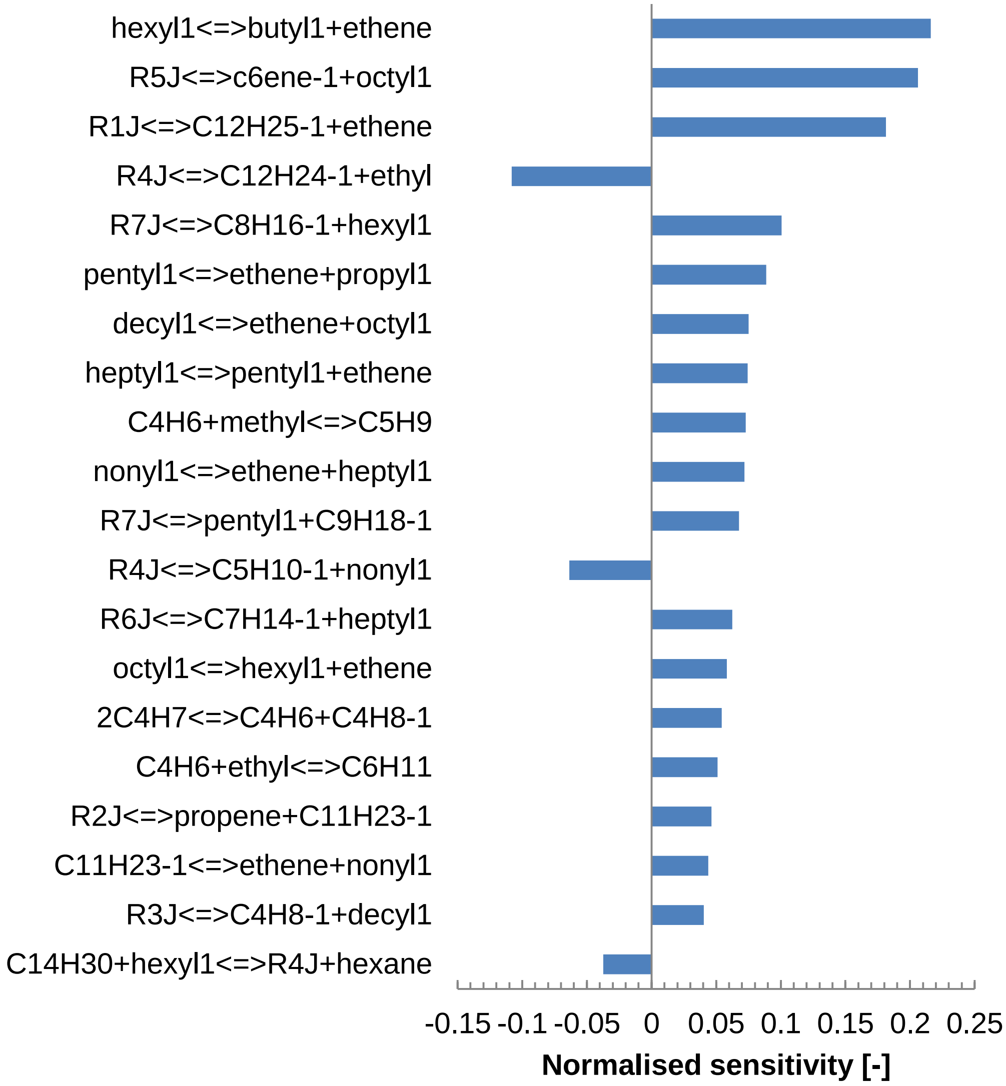

Figure 6.9: Top 20 reactions ranked by normalized sensitivity of ethylene at t=16 min, for extended model simulation of T = 723 K. "RNJ" is an acronym for tetradecan-N-yl radical. Note: <=> is a symbol used in Chemkin^{TM} to represent a reversible reaction.

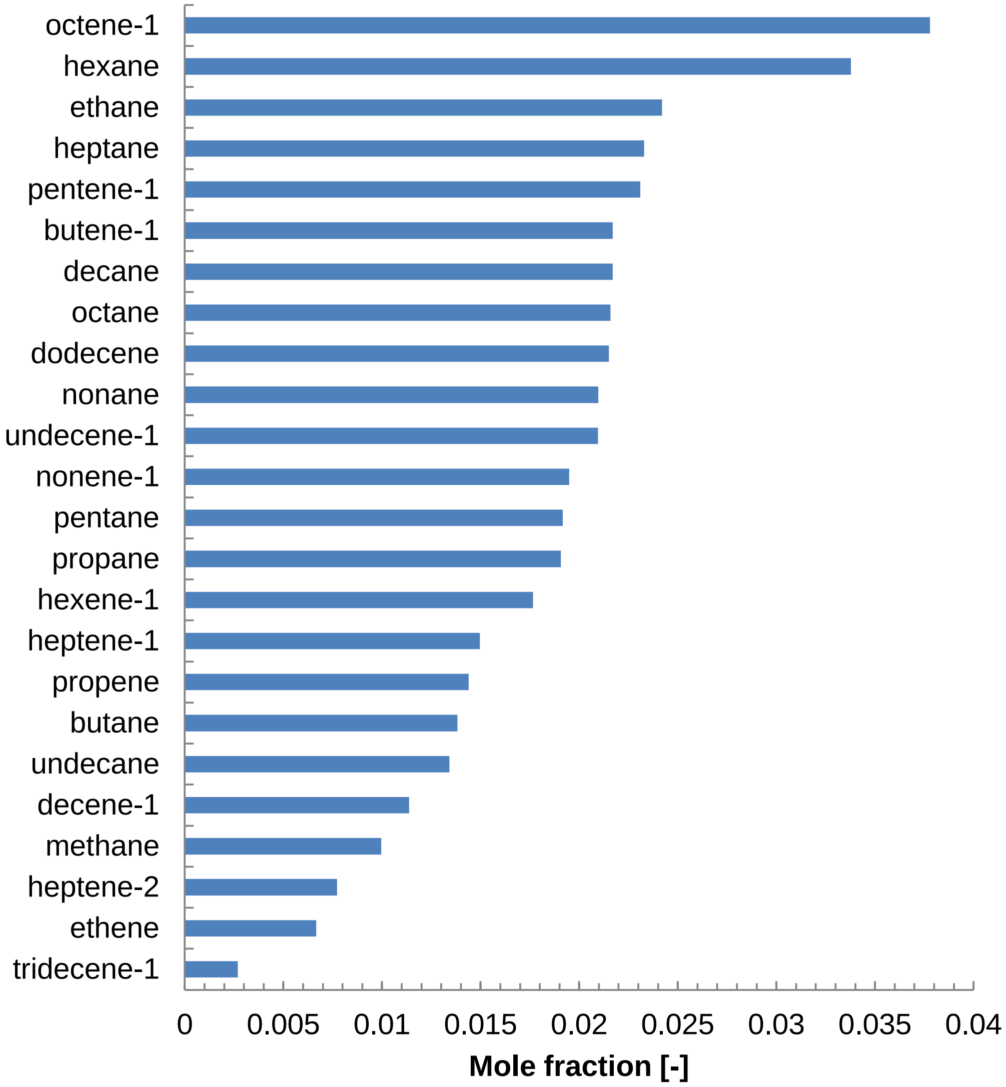

Figure 6.10: Major species formed in extended model pyrolysis simulation at *t* = 16 min.

reactions added manually using the populate reaction module of RMG. To keep the model size under control, only 1-alkyl isomers were considered for C_8-C_{13} radicals. The improved model, hereafter referred to as the extended model has 743 species and 11,388 reactions and the corresponding predictions are also shown in Figure 6.8. Both ethylene and long-chain alkane yields show significant improvement over the original model. Sensitivity analysis suggests that ethylene formation is most sensitive (positive) to β-scission and H-abstraction reactions (negative) of alkyl radicals (Figure 6.9) as expected. Hexyl-1 was found to be the most abundant alkyl-1 radicals which results in higher hexyl-1 β-scission sensitivity for ethylene formation. H-abstraction reaction has negative sensitivity as it competes with β-scission reaction. Negative sensitivity of R4J can be explained by relative competition of β-scission of R4J to form ethyl and nonyl radicals that subsequently forms ethylene by β-scission. Our own comparison suggests that ethylene formation by β-scission of ethyl radicals is very slow compared to analogous reactions for longer chain alkyl radicals. As a result, production of more ethyl radical (which also blocks the ethylene formation by nonyl-1 β-scission) impedes the ethylene yield. Under these conditions, 1-alkenes and high molecular weight (> C_3) alkanes were found to be the major products consistent with experiment (Figure 6.10).

6.3. Modeling of gas-phase ATR reactions in a non-catalytic packed bed reactor

A 3-level factorial design experimental study of n-tetradecane autothermal reforming with and without catalyst (but with quartz sand bed) was performed inside the packed bed reactor shown in Figures 6.1 and 6.2. The experimental gas-phase kinetic study data were obtained by varying O_2/C ratio, temperature, space velocity, all at constant S/C ratio. The following definitions were used to define and yield and conversion.

$$Yield\,of\;H_2\,[\%] = \frac{moles\,of\;H_2}{\left(15\times moles\,of\;tetradecane\;fed + moles\,of\;water\;fed\right)}\times 100 \qquad (1)$$

$$Yield\ of\ C_nH_m\,[\%] = \frac{n \times moles\ of\ C_nH_m}{(14 \times moles\ of\ tetradecane\ fed)} \times 100 \quad (2)$$

$$Yield\ of\ CO/CO_2\,[\%] = \frac{moles\ of\ CO/CO_2}{14 \times moles\ of\ tetradecane\ fed} \times 100$$

(3)

where ‘*n*’ is number of moles of carbon per mole of hydrocarbon in the product.Hydrogen yield is based on number of moles of hydrogen fed into the reactor as specified by Shekhawat *et al.* [68].

The conversion and Gas Hourly Space Velocity (GHSV) was calculated by the following expressions:

$$X\,[\%] = \frac{moles\ of\ carbon\ in\ outlet\ product\ gas}{14 \times moles\ of\ tetradecane\ fed} \times 100 \quad (4)$$

$$GHSV = \frac{Volumetric\ flow\,(SCCM) \times 60}{Volume\ of\ blank\ reactor} \quad (5)$$

It should be noted here that the reactor was packed with quartz sand bed for gas-phase kinetic study. Previous studies on methane combustion in the quartz sand bed reactor have shown no activity catalytic activity of the sand bed for combustion at 850 °C [69, 70]. Also, experimental study on combustion of hydrocarbons in a bubbling sand bed reactor has shown dominance of gas-phase reactions at and above 850 °C [71]. Bustamante *et al.* [72] performed water-gas-shift reaction study in a quartz reactor and reported minimal activity (conversion < 0.2%) at 900 °C for low residence time (time on-stream < 15 hrs). In the experimental study less than 100 ppm oxygen was obtained in the outlet of the reactor. Hence although sand bed activity can not be completely neglected, it was concluded that gas phase reactions were dominant inside the reactor (discussed in Chapter 5 [73]). The product profile obtained without the catalyst (Figure 6.11) indicates that ~45% of the hydrocarbon feed breaks down in the gas-phase into low molecular weight products comprising mainly methane, ethane, ethylene, propylene, 1-butene, 1-3 butadiene, CO, CO_2, and H_2 indicative of the importance of gas-phase chemistry upstream of the catalyst. For comparison sake, data for reactor packed with Rh-Pyrochlore catalyst is also included in Figure 6.11. The data were collected on the same reactor and the results are discussed in Chapter 5 [73]. It can be noted from Figure 6.11 that the conversion of n-tetradecane increases

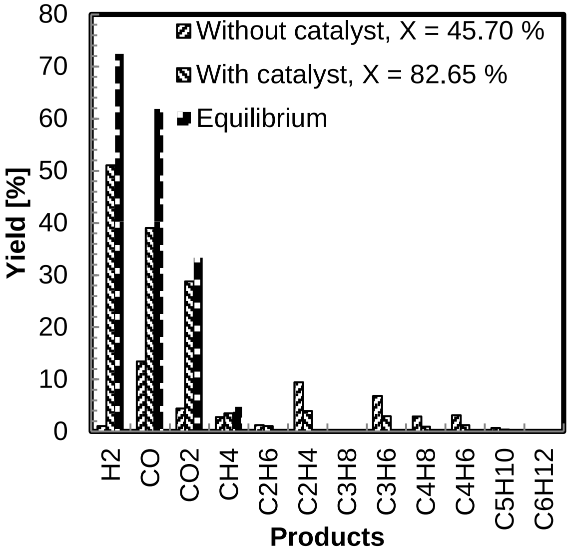

Figure 6.11: Experimental exit product concentration with and without catalyst with n-tetradecane passing through an ATR reactor ($H_2O/C = 1.5$, $O_2/C = 0.2$, $T_{bed} = 973.15$ K); conversion = moles of carbon in gas-phase at the exit x 100 / moles of carbon fed in the system.

significantly to ~83% and a simultaneous rise in H_2 production occurs due to catalytic reforming of the lower molecular weight products of n-tetradecane degradation. Formation of lower alkenes like ethylene and propylene due to gas-phase chemistry is a major concern as they are precursors to coke formation. The kinetic model developed and validated earlier was used to simulate the gas-phase reactions in the reactor and identify major reactions and paths for ethylene and propylene formation. As discussed, the generated model did not predict formation of any species heavier than C_3 alkanes, which is consistent with literature and current experimental observation.

While simulating the pyrolysis experiments, the model was extended to include higher alkanes, which are formed at high pressure and low temperature conditions. Developing a comprehensive model capturing combustion, pyrolysis and ATR/POX (Partial Oxidation) regimes across a wide range of temperatures and pressures was out of the scope of the present work. Instead, we use the model obtained from RMG at ATR conditions and discussed above. The capabilities of our original reforming kinetic model (nine thousand three hundred and forty-seven reactions and four hundred and fifty-nine species) in describing the gas-phase reactions occurring in the non-catalytic packed bed reactor fed with typical ATR reactant mixture was assessed. A schematic of the Chemkin-Pro packed-bed reactor model used in this study is shown in Figure 6.12. The reactor, modeled as a plug-flow reactor (PFR) is divided into three sections, inlet section (PFR-1) where there is no packing material, middle section (PFR-2) where the porosity is 0.486 (due to the presence of the thermocouple), and last section (PFR-3) where the porosity is 0.406. The heat transfer characteristics of the reactor were described by modeling the measured temperature profile of the reactor in the absence of any reactions (see the Appendix–C.4). For modeling the reactor in presence of reactions, an iterative approach discussed in section 4.1 was employed. The measured temperature profile without reaction was

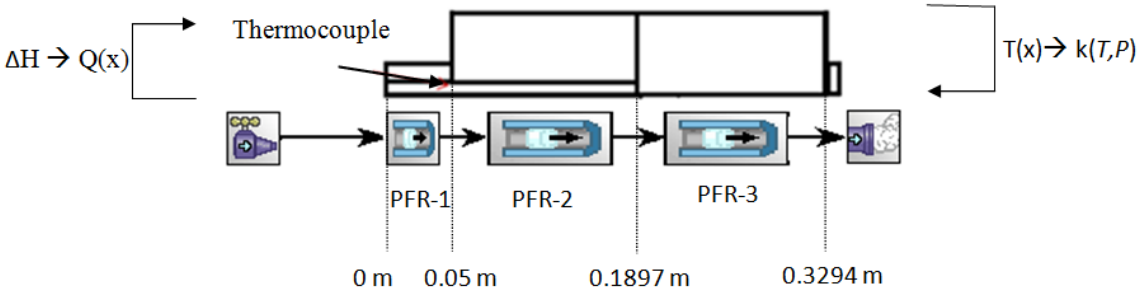

Figure 6.12: Chemkin packed bed reactor model

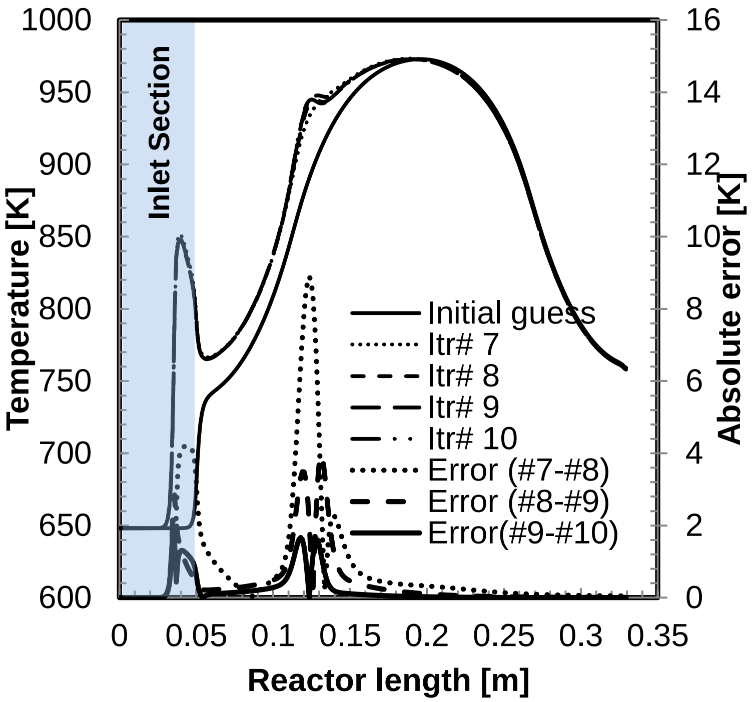

Figure 6.13: Temperature profile inside the reactor and error in temperature profile (right hand scale) after successive iteration: S/C = 1.5; O_2/C = 0.35, GHSV = 1,281 1/h, T_{bed} = 973.15 K.

used as an initial guess and the iterations performed till the absolute error between successive solutions below 2 K (usually within 10-15 steps). The converged temperature profiles from this approach were used in the Chemkin-Pro reactor model to simulate the reforming experiments. Figure 6.13 shows the variation of the estimated temperature profile at one set of conditions and convergence with successive iterations.

Temperature profiles inside the reactor at operating conditions studied experimentally are shown in Figure 6.14. At low space velocities (*i.e.*, high residence time), oxidation chemistry contributes significantly in the inlet section itself at different O_2/C ratios and T_{bed} (Figure 6.14 (a) and (c), respectively). Two stages of oxidation were observed in each case. In the first stage, oxidation of the parent fuel molecule (and radicals derived from it) results in sharp increase in temperature (very similar to that seen in ignition but lower in magnitude due to the large amount of steam and N_2 in the mixture) of about 200 K. The second stage involves the reactions of products derived from initial fuel decomposition and this controls the species produced during gas-phase reactions (discussed later). Increasing the space velocity (Figure 6.14(b)) moves the first stage oxidation front to the middle section (PFR-2). As the bed temperature is controlled at the centre of the reactor, the increase in space velocity results in more small hydrocarbons reaching high temperature zone which ultimately oxidizes in the second zone giving high temperature jump in the second stage. Such predictions in temperature profile are helpful in optimizing the reactor design and operating conditions, and to avoid the hot spot inside the reactor.

Comparisons of experimental and simulated yields of different products at the reactor exit are shown in Figures 6.15−6.17. At low space velocities, T_{bed} 973.15 K, and varying O_2/C ratio, the model predicts the yield of major products reasonably well, except for CO_2 and propylene which are under-predicted by factor of 3 (Figure 6.15). Experimental and simulated yields of important products are shown in Table 6.3. It is possible that lower prediction of CO_2 could be due to the occurrence of water-gas shift reaction arising from the activity of the reactor material which contains about 30-35 % Nickel. In fact, Bustamante *et al*. [72] has reported that Inconel reactor (72 % Ni) has very high water-gas-shift activity and equilibrates in less than 1 second at a reactor temperature of 950 K. At large O_2/C ratios, second stage oxidation results in a larger temperature jumps which ultimately results in higher water-gas-shift activity and could account for the discrepancy between the modeled and experimental CO and CO_2 yields. To

Table 6.3: Comparison of predicted and experimental product yield from ATR of n-tetradecane: T_{bed}= 973.15K, GHSV = 1,2811/h, and S/C = 1.5, and O_2/C = 0.2, *P* = 2.36 atm

	Experiment	**Model**
Hydrogen	1.09	0.45
Carbon Monoxide	13.48	11.79
Carbon Dioxide	4.44	1.51
Methane (CH_4)	2.76	2.34
Ethane (C_2H_6)	1.24	0.80
Ethylene (C_2H_4)	9.46	14.37
Propane (C_3H_8)	0.24	0.22
Propylene (C_3H_6)	6.87	1.89
1-Butene (C_4H_8)	2.91	1.58
1,3 Butadiene(C_4H_6)	3.13	3.25
1-Pentene (C_5H_{10})	0.72	0.45
1-Hexene (C_6H_{12})	0.11	0.20

examine this hypothesis, the experimental $CO+CO_2$ yield is compared with the predicted $CO+CO_2$ yield. The results show good agreement confirming the possibility of catalytic wall water-gas-shift activity (Figure 6.18). Moreover, from the model predictions we also conclude that the water-gas-shift equilibrium is not reached indicating that there is a driving force for the reaction on the wall of the reactor. Although thermodynamic analysis suggest that there is no carbon formation at $O_2/C = 0.2$, $S/C = 1.5$ and $T = 1073$ K [16], kinetic study results suggest large amount of ethylene formation at these conditions, which ultimately results in coke formation. As shown in Figure 6.16, varying space velocity does not result in major changes in the species profiles, although there is a significant change in the temperature profile and the location of the initial temperature jump.

Model predictions of species yields at different bed temperatures (T_{bed}) are shown in Figure 6.17. Experimental data shows sharp jump in H_2 and CO concentration from 1048.15 K to 1123.15 K and this could be due to high wall reforming activity at temperature above 800 °C. Several other studies in the literature have reported similar problems. Recently, Abbas and Wan Daud [74] studied influence of the reactor material on thermo-catalytic decomposition of methane. They used a SS310S reactor containing 19-22% Ni and reported that the reactor wall significantly affected the decomposition of methane when at temperatures higher than 1123 K. Gornay *et al.* [75] performed steam cracking and steam reforming of waste cooking oil in an Incoloy 800 reactor. They reported the formation of active metallic coke containing Fe and Ni particles on the wall of the reactor during gas-phase steam reforming at 1073 K. Yamada *et al.* [76] performed n-tetradecane steam reforming and partial oxidation in stainless steel based catalyst reactor wall (SUS 304). They reported that the metal alloy being highly dispersed after oxidation results in high hydrogen production rates in partial oxidation at 1003 K. We think this

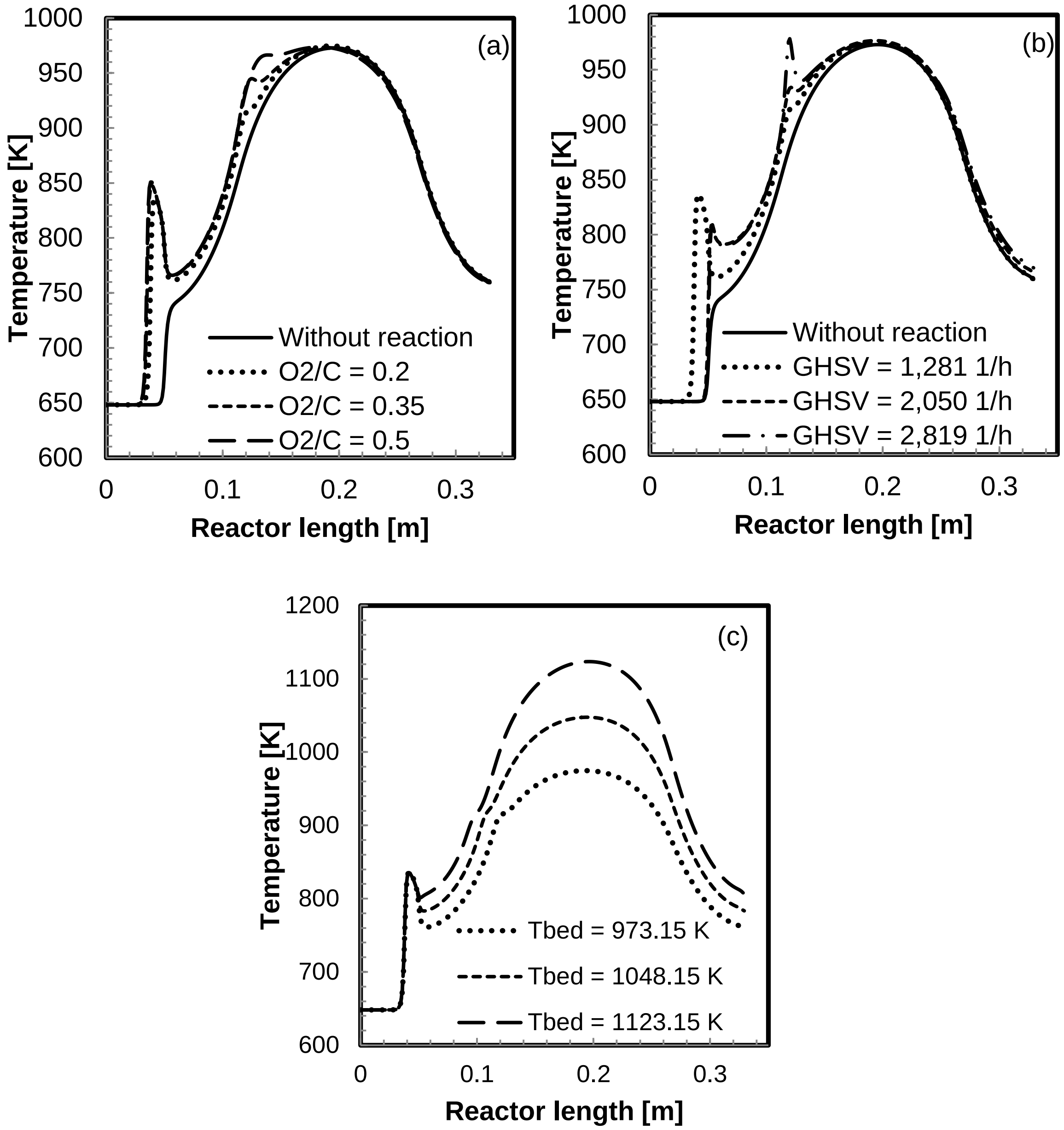

Figure 6.14: Simulated temperature profile inside the reactor: (a) S/C = 1.5, GHSV = 1,281 1/h, T_{bed} = 973.15 K; (b) S/C = 1.5, O_2/C = 0.2, T_{bed} = 973.15 K; (c) S/C = 1.5, GHSV = 1,281 1/h, O_2/C = 0.2.

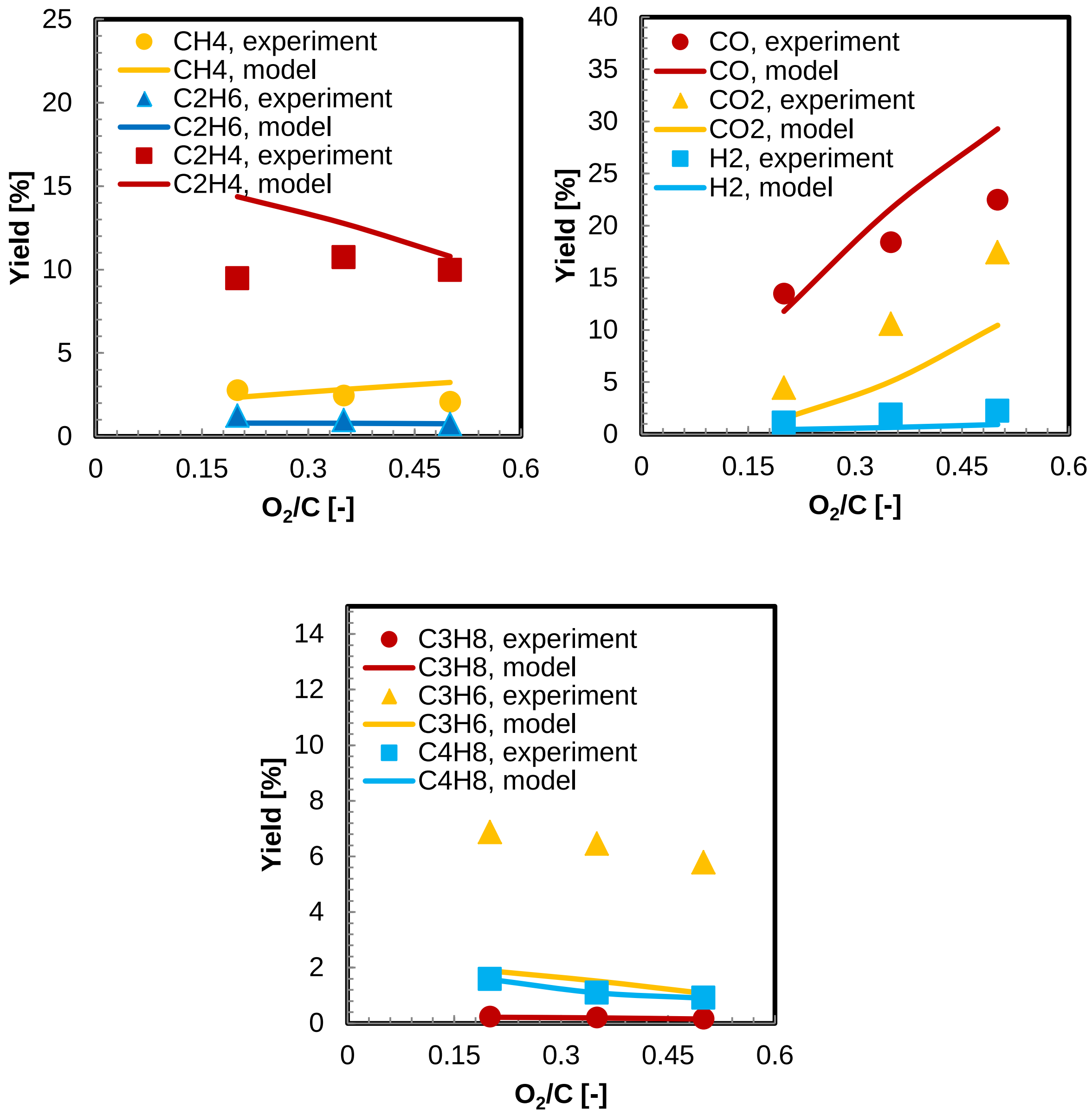

Figure 6.15: Comparison of experimental (symbol) and simulated (line) product composition profile at different O_2/C ratios, and at constant S/C = 1.5, GHSV = 1,281 1/h, T_{bed} = 973.15 K.

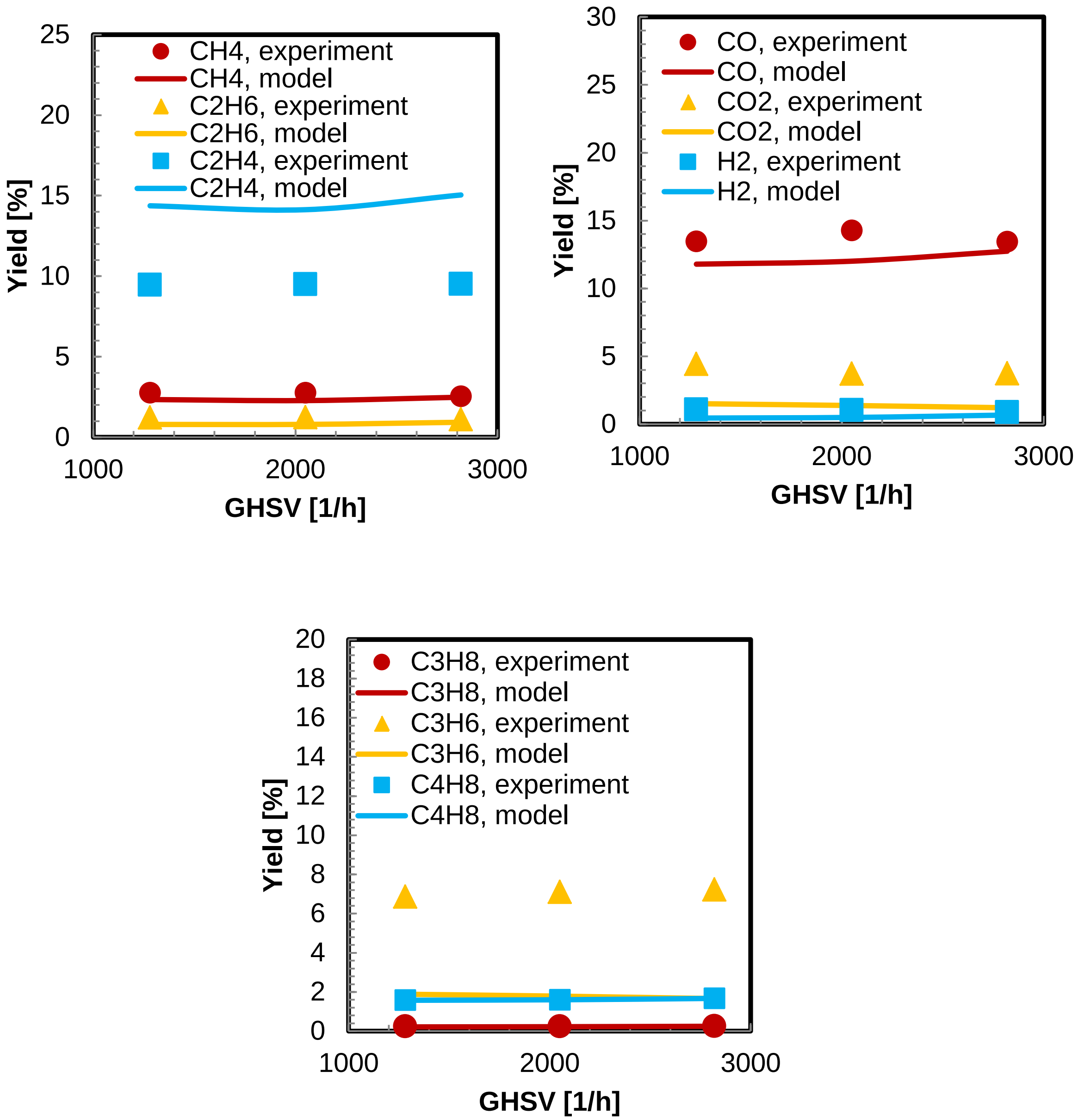

Figure 6.16: Comparison of experimental (symbol) and simulated (line) product composition from ATR at different space velocities, S/C = 1.5, O_2/C = 0.2, T_{bed} = 973.15 K.

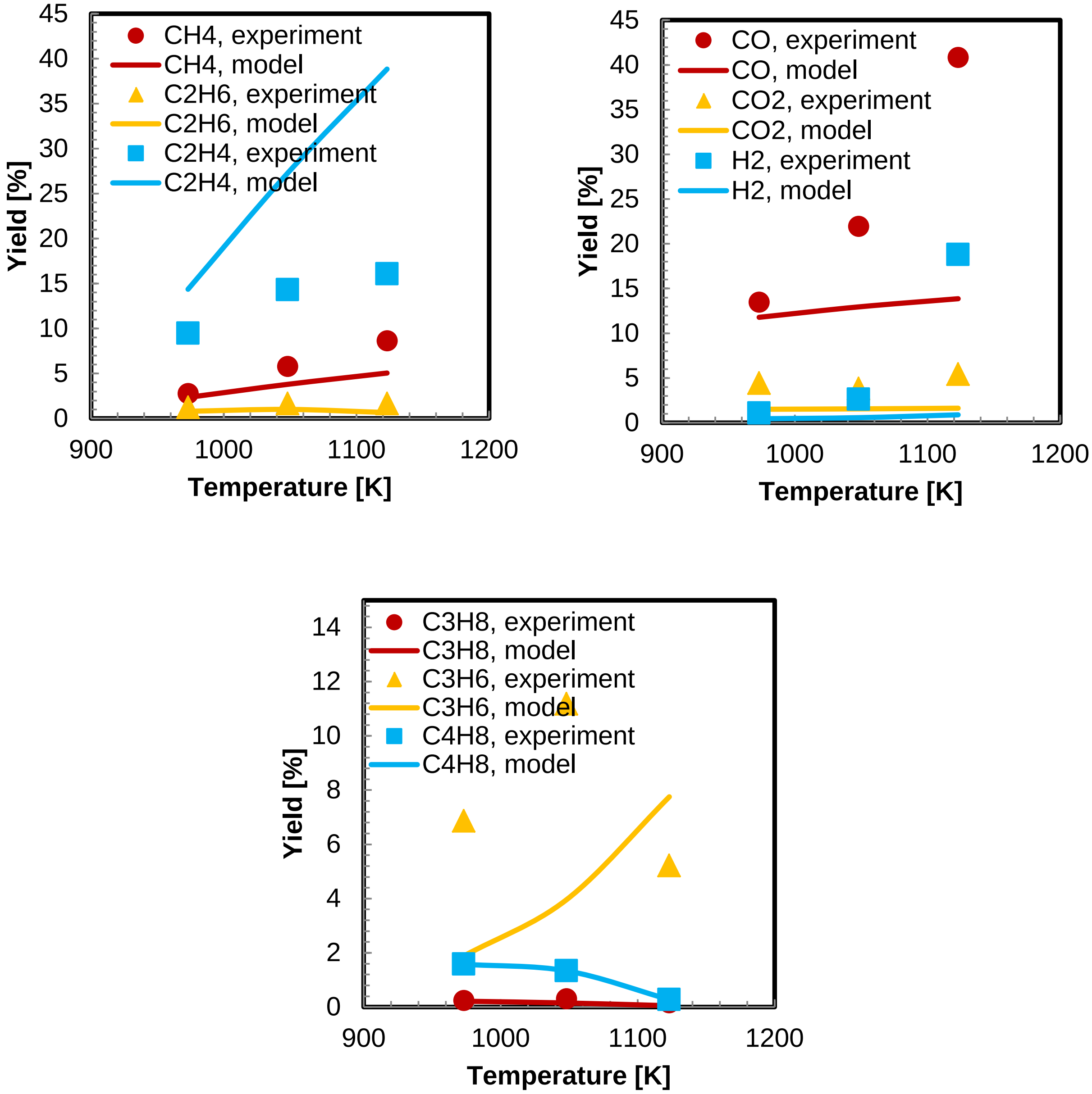

Figure 6.17: Comparison of experimental (symbol) and simulated (line) product composition from ATR at different bed temperatures, S/C = 1.5, O_2/C = 0.2, GHSV = 1,281 1/h.

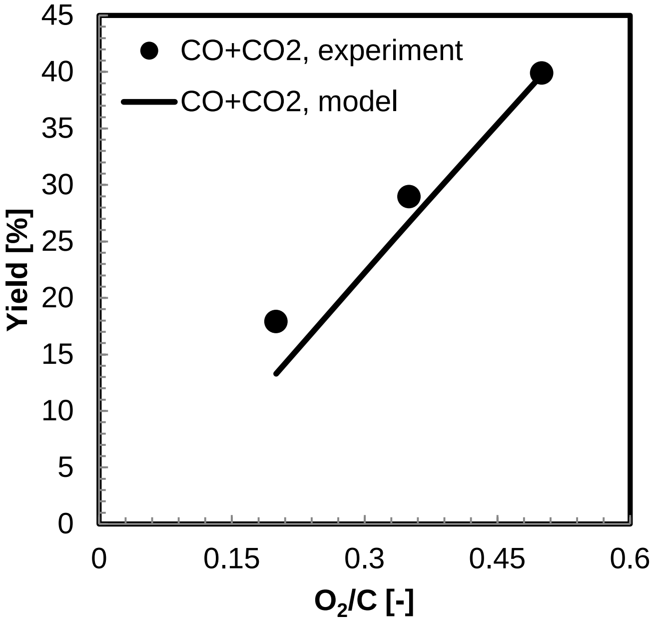

Figure 6.18: Comparison of experimental (symbol) and simulated (line) CO+CO_2 yield at different O_2/C ratios, and at constant S/C = 1.5, GHSV = 1,281 1/h, T_{bed} = 973.15 K.

could be the reason for poor predictions from the model at higher temperatures (particularly at 850 °C). The activity of reactor wall also results in decreased ethylene and propylene yields compared to gas-phase reactions if only gas-phase chemistry was occurring. This can also be observed in Figure 6.11 where adding the catalyst drastically reduces the outlet alkene concentrations. Such reactor wall activity could also lead to carbon formation on reactor wall as indicated by Yamada *et al.* [76].

Simulated composition profile for major species at O_2/C ratio 0.2, T_{bed} = 973.15 K and different space velocities is given in Figure 6.19. Our results suggest that most of the n-tetradecane is consumed in first stage oxidation *i.e.*, in less than 0.05 s (which corresponds to

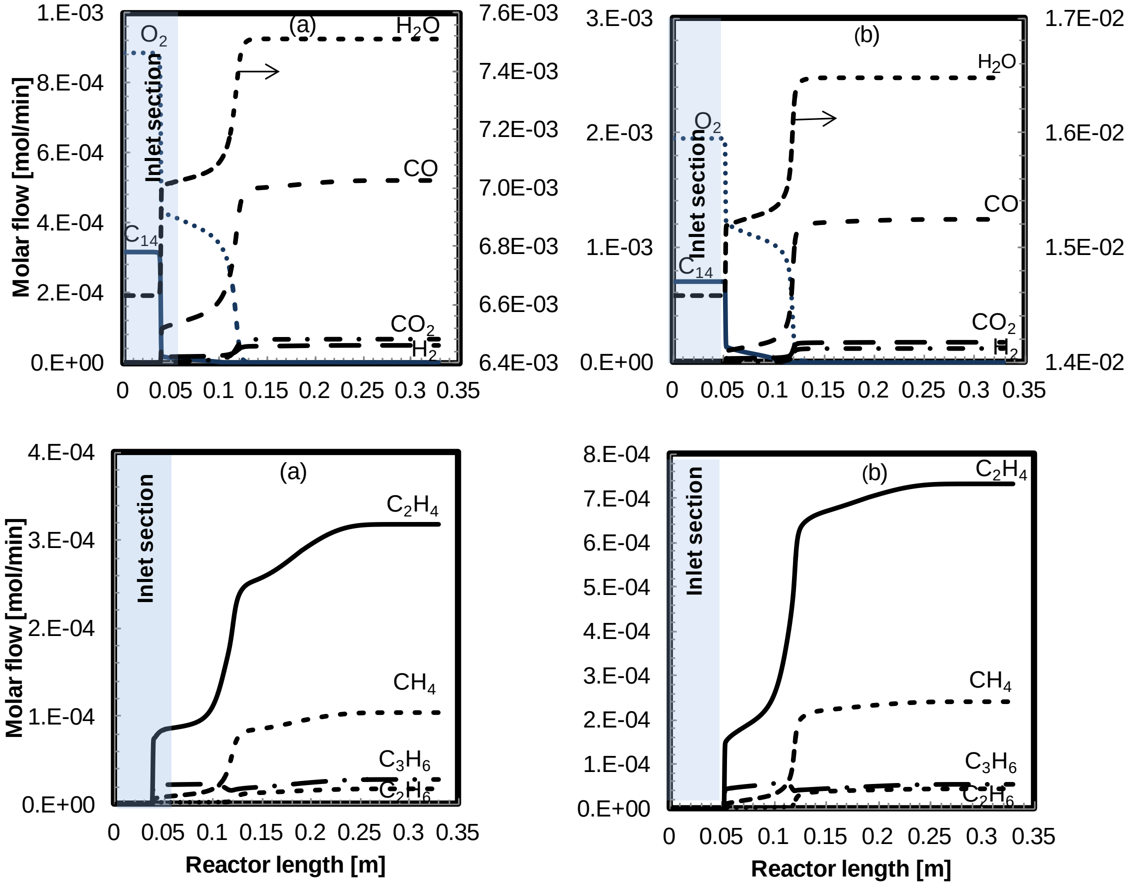

Figure 6.19: Simulated composition profile for major species at O_2/C = 0.2, T_{bed} = 973.15 K, and (a) GHSV = 1,281 1/h, (b) GHSV = 2,819 1/h.

axial distance of ~0.1 m in the current reactor). At the inlet of the reactor (*T* = 648 K), oxygen consumption is mainly driven by the oxygen to fuel ratio. This is due to the R·⇆ROO·⇆·QOOH⇆·OOQOOH⇆HOOQ=O+·OH sequence of reactions where two moles of oxygen are consumed for every mole of alkyl radicals created. In the present case, the oxygen to fuel ratio at the inlet is 2.8 and as a result, not all the oxygen is instantly consumed in the inlet of the reactor. The R· + O_2 ⇆ ROO· reaction (which leads to autocatalytic chain branching) creates large numbers of radicals, which catalyze the overall oxidation reaction RH + $O_2 \leftrightarrows$ alkene + H_2O_2, leading to the jump in H_2O_2 shown in Figure 6.20(b). However, once the exotherm due to this oxidation causes the temperature to exceed the ceiling temperature of the $R\cdot + O_2 \leftrightarrows ROO\cdot$ equilibrium, Figure 6.20(a), and the chain branching turns off, replaced by relative fast radical termination mediated by HOO· and allylic radicals formed from the alkene. The resulting sudden drop in chemical heat release rate due to the loss of the radicals catalyzing the oxidation and heat loss from the wall of the reactor causes the temperature to decline until the gas enters the furnace, and also explains the sudden change in O_2 consumption rate shown in Figure 6.19(a). This implies that if the catalyst is placed beyond $x = 0.1$ m, it is most likely to encounter low molecular weight products formed from fuel degradation. This is contrary to popular belief that chemistry upstream of the catalyst has negligible contributions to the reforming [15, 77-80]. We also observe that as the temperature in the furnace section gets high enough for H_2O_2 decomposition, the resulting ·OH radicals catalyze oxidation in the second stage. This is clearly seen in Figure 6.20(b) where H_2O_2 concentration plummets as temperature rises above 900 K around $x = 0.14$ m. This results in complete consumption of oxygen in less than 0.35 s (which corresponds to $x = 0.14$ m) in current reactor. In the current set-up for catalytic reforming the catalyst is normally placed at $x = 0.16$ m. So this suggests that both oxygen and n-tetradecane are completely consumed before the gas-phase reaction products reach the catalyst. A large jump in the concentrations of CO, CO_2, ethylene, methane, and H_2 is seen in the second stage of oxidation where small molecule chemistry is important. The two-stage oxidation seen in the current simulations is a direct result of homogeneous gas-phase chemistry upstream of the catalyst and highlights the importance of incorporating these effects in reformer design.

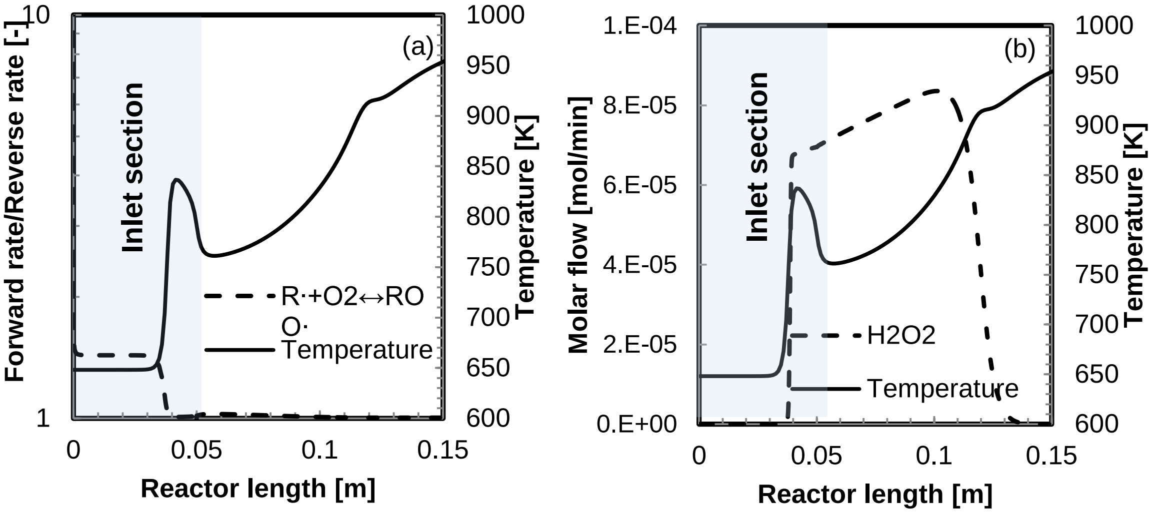

Figure 6.20: (a) Equilibrium for R·+O_2⇆ROO· and (b) H_2O_2 profile at O_2/C = 0.2, T_{bed} = 973.15 K, and GHSV = 1,281 1/h.

6.4. Reaction pathway analysis

As discussed earlier, the mechanism used to model the experiment consists of nine thousand three hundred and forty-seven reactions and four hundred and fifty-nine species. The PLUG suit in Chemkin-Pro was used to perform sensitivity analysis at O_2/C ratios of 0.2 and 0.5, and at S/C 1.5, WHSV 100,000SCC/h·g, and T_{bed} 973.15 K. In order to keep the discussion concise, the following discussion focuses on the formation of major products: CO, CO_2, ethylene and propylene mainly during the secondary oxidation phase (Figure 6.19). Since the analysis results are not very sensitive to the O_2/C ratio, the discussion here is mainly from results at O_2/C=0.2 and t > 0.05 s.

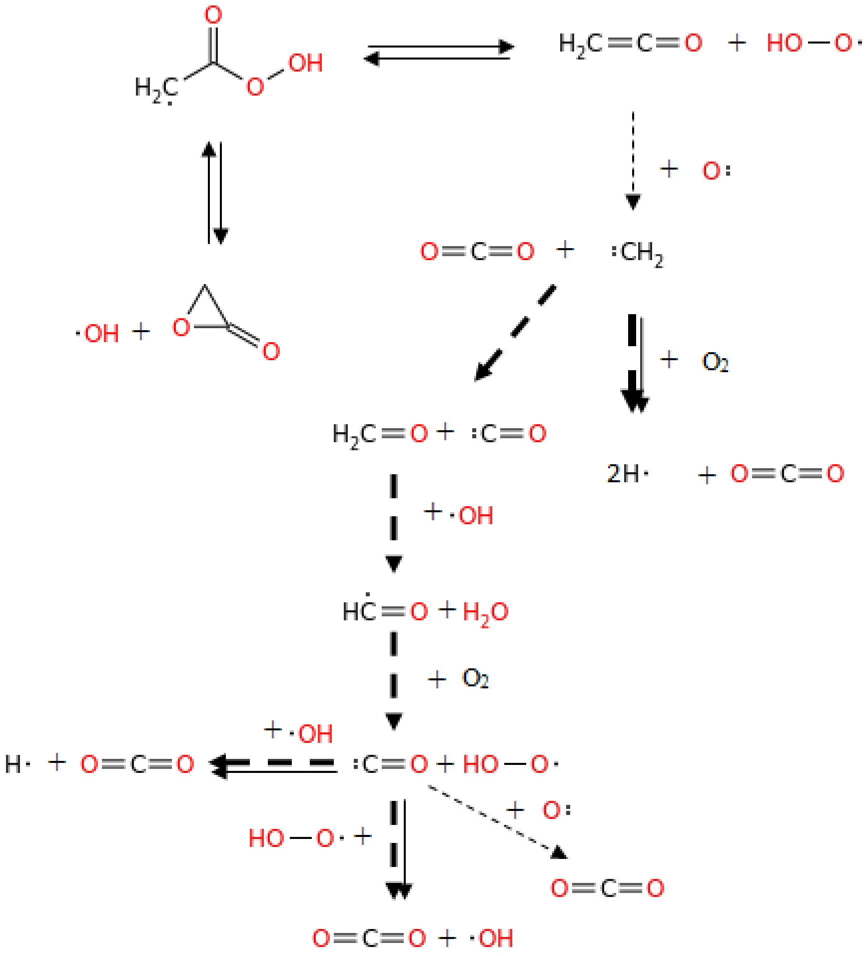

Figure 6.21: Reaction path for CO_2 formation based on sensitivity analysis and flux analysis of top 10 reactions in the middle section (PFR-2) of the reactor (t > 50 ms). Continuous line shows highly sensitive reaction path for CO_2 formation and dashed line shows high flux for CO_2 formation.

Based on sensitivity and flux analysis in the middle part of the reactor (PFR-2), the most important reactions that control CO_2 formation are shown in Figure 6.21. CO_2 formation was largely due to the: $CH_2 + O_2 \leftrightarrows CO_2 + 2H\cdot$ reaction which had the large positive sensitivity coefficient, consistent with the findings of Warnatz [48]. Other channel for CO_2 formation is from

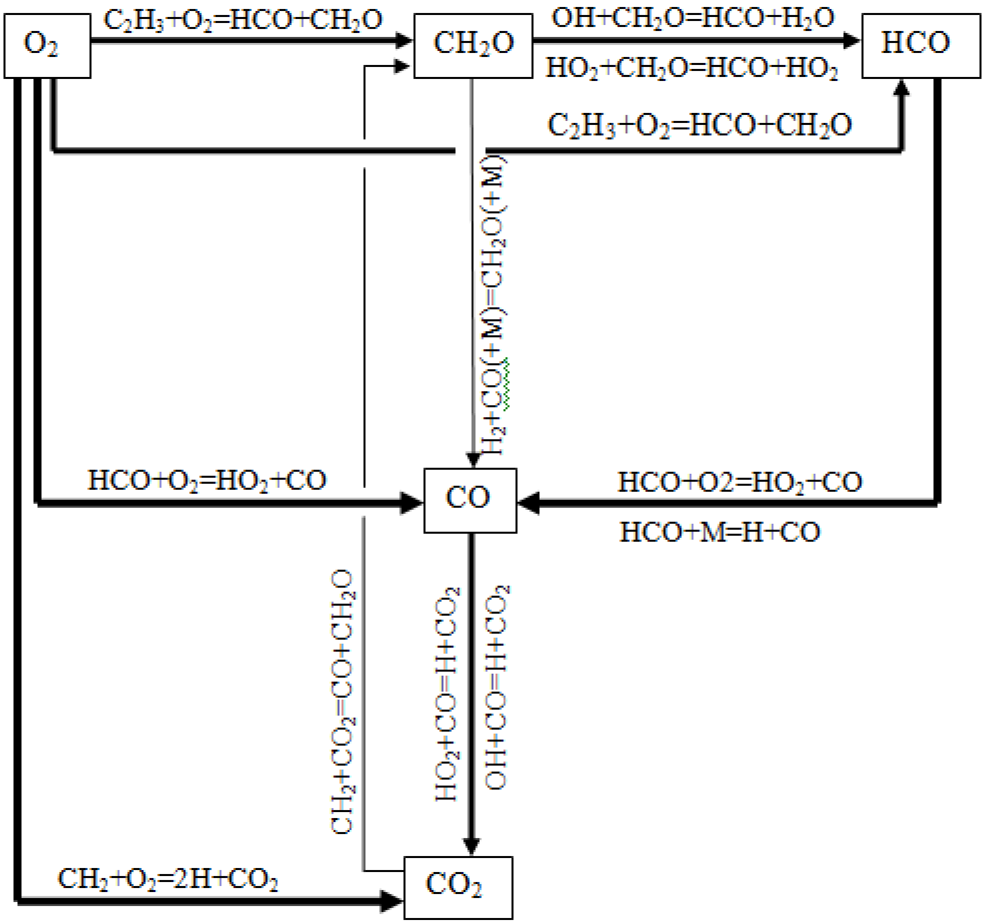

Figure 6.22: Major paths for formation of CO and CO_2; dark lines shows high flux.

CH_2O and HCO· (Figure 6.21). By sensitivity analysis, it is found that CO_2 formation is sensitive to reaction network containing hydroperoxyl-vinoxy, lactone, and CH_2CO species. . Rates for the reaction: hydroperoxyl-vinoxy ⇆ lactone + ·OH and hydroperoxyl-vinoxy ⇆ CH_2CO + HOO· were obtained from recently published work on acetyl + O_2 reaction [27]. Using species path analysis of Chemkin-pro, major pathways for CO and CO_2 formation are obtained (Figure 6.22) and it shows that CO and CO_2 are formed by CH_2O and HCO·, which are majorly produced by C_2H_3· + O_2 ⇆ HCO· + CH_2O reaction. Rates for this reaction are obtained from GRI-Mech 3.0 mechanism. Detailed analysis of the reaction paths shows reactions and species involved in CH_2O and HCO· formation. H-abstraction of ethylene by ·OH radical results in formation of vinyl radicals that are responsible for HCO· and CH_2O formation. Rates for the reaction: C_2H_4 + ·OH ⇆ C_2H_3 + H_2O reaction are obtained from recently published study of Vasu [81]. Other species responsible for CH_2O and HCO· formation are CH_2CHO and HCCO.

The most important pathways for ethylene formation and consumption are shown in Figure 6.23. A bulk of the ethylene is formed from β-scission of 1-alkyl radicals that is consistent with pyrolysis mechanism. Rates for the decomposition of C_2H_5· and its reaction with O_2 were found to be sensitive and were obtained from the GRI-Mech-3.0 mechanism. The most important source of ethylene was β-scission of propyl and other 1-alkyl radicals. The fastest destructive pathway was H-abstraction by ·OH to form the vinyl radical (C_2H_4 + ·OH ⇆ C_2H_3· + H_2O). Ethylene is also consumed by reaction with vinyl radicals to form C_4H_7·. Reaction between vinyl and O_2 leads to formation of large amounts of HCO· and CH_2O. HCO· is also formed from the reaction between ethylene and ·O. C_2H_3·, HCO· and formaldehyde are direct products of ethylene consumption and as a result reactions controlling the concentrations of these species also affect the concentration of ethylene. Rate coefficients for most of these small molecule reactions were obtained from the GRI-Mech 3.0 mechanism.

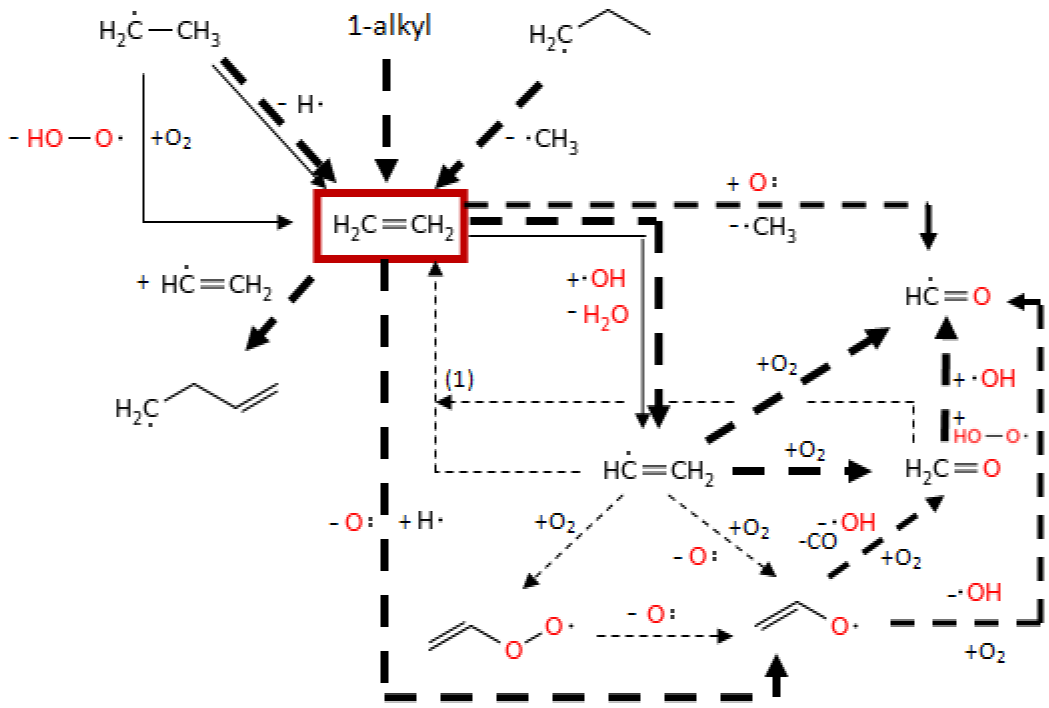

Figure 6.23: Major paths for formation and decomposition of ethylene based on sensitivity analysis and flux analysis; continuous line represents sensitive reaction, dashed line represents flux, line thickness represents high relative flux; (1) C_2H_3+CH_2O⇆C_2H_4+HCO and C_2H_3+H_2O_2⇆C_2H_4+HO_2

Figure 6.24 shows a similar analysis of the pathways for propylene formation. Most of the propylene in the current model comes from β-scission of 2-alkyl radicals (particularly 2-hexyl and 2-tetradecyl). The rates for these and other similar reactions were obtained from recently reported rates by Curran [82]. The primary consumption pathway for propylene is H-abstraction by ·OH to form allyl and H_2O. Kappler *et al.* [83] measured the rate constant for this reaction and found the branching ratio for the allyl formation channel to be ~85% in the 700-900 K range, while Smith *et al.* [84] reported measurements at higher temperatures. Recently, Zador *et al.*[85] presented calculated rates for this system. The measured and calculated rates agree below 950 K

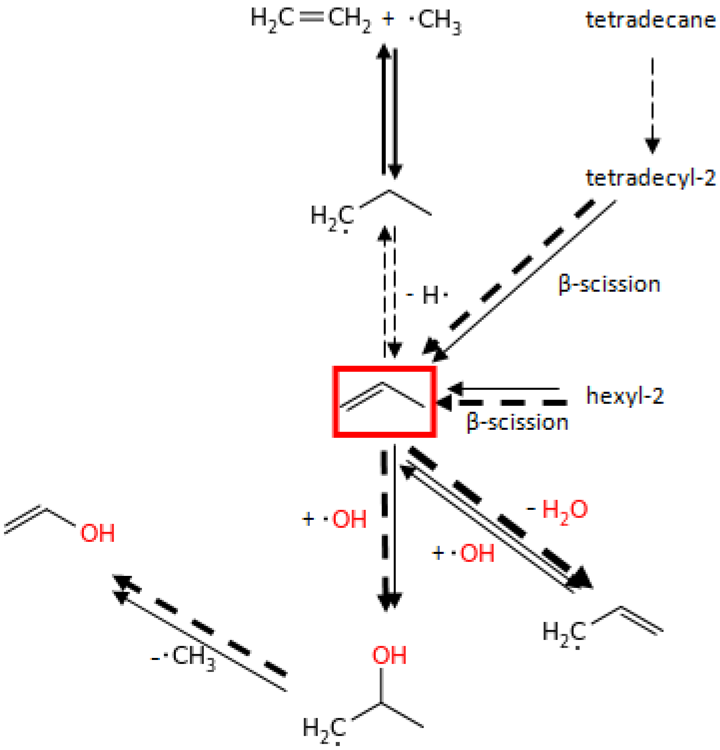

Figure 6.24: Major paths for formation and decomposition of propylene based on sensitivity analysis and flux analysis; continuous line represents sensitive reaction, dashed line represents flux, line thickness represents high relative flux.

but not with the high temperature data of Smith *et al.* However, the estimates of Tsang [36] agree well with the experiments at all temperatures reasonably well. These rates are approximately a factor of two lower than those of Kappler *et al.* [83] at 1000 K. The propylene consumption in second stage oxidation (Figure 6.19) is due to H-abstraction by ·OH and also by recombination reaction to form C_3H_6OH. The rates for propene recombination with ·OH are obtained the work of Kappler *et al.* [83].

7. Conclusions

Gas-phase kinetics for modeling gas-phase reactions pertinent to n-tetradecane reforming under autothermal conditions was developed. The kinetic model was generated using the RMG software package and key rates were refined with measured or calculated values. The resulting model was found to capture the oxidation regime very well compared to the existing LLNL model. The model was extended by adding certain missing reactions to predict the high pressure pyrolysis experiments.

The model suggests the presence of two oxidation zones within the non-catalytic ATR reactor. N-tetradecane is completely consumed in the first oxidation zone within 0.05 s and results in a temperature rise of ~200 K. Large amounts of ethylene, which is also responsible for carbon formation, are produced in the second oxidation zone which consumes the remaining oxygen and occurs in less than 0.35 s. This is consistent with experimental results where n-tetradecane and oxygen are found to be completely consumed in the region upstream of the catalyst. The hot spot and species profiles predicted by the current model could be useful in the optimization of reactor design and operating conditions.

Using sensitivity and flux analysis, major pathways responsible for CO, CO_2, ethylene and propylene were identified. The major channels for CO and CO_2 formation are through CH_2O and HCO· intermediates. CO_2 is also formed by: $CH_2+O_2 \leftrightarrows CO_2 + 2H\cdot$ reaction channel which is consistent with the literature. Major pathways to ethylene formation are 1-alkyl, propyl β-scission, ethyl decomposition. Consumption of ethylene leads primarily to CH_2O and HCO· (via vinyl). Propylene yield was found to be very sensitive to the H-abstraction by ·OH to form allyl radical. Refined rate estimates for this reaction would be very useful to better analyze propylene yields.

References

[1] S. Yoon, I. Kang, J. Bae, Suppression of ethylene-induced carbon deposition in diesel autothermal reforming, International Journal of Hydrogen Energy, 34 (2009) 1844-1851.

[2] B. Dreyer, I. Lee, J. Krummenacher, L. Schmidt, Autothermal steam reforming of higher hydrocarbons: n-Decane, n-hexadecane, and JP-8, Applied Catalysis A: General, 307 (2006) 184-194.

[3] S. Yoon, I. Kang, J. Bae, Effects of ethylene on carbon formation in diesel autothermal reforming, International Journal of Hydrogen Energy, 33 (2008) 4780-4788.

[4] I. Kang, J. Bae, S. Yoon, Y. Yoo, Performance improvement of diesel autothermal reformer by applying ultrasonic injector for effective fuel delivery, Journal of power sources, 172 (2007) 845-852.

[5] I. Kang, S. Yoon, G. Bae, J.H. Kim, J. Bae, D. Lee, Y. Song, The micro-reactor testing of catalysts and fuel delivery apparatuses for diesel autothermal reforming, Catalysis Today, 136 (2008) 249-257.

[6] D.K. Zerkle, M.D. Allendorf, M. Wolf, O. Deutschmann, Understanding homogeneous and heterogeneous contributions to the platinum-catalyzed partial oxidation of ethane in a short-contact-time reactor, Journal of Catalysis, 196 (2000) 18-39.

[7] A. Beretta, L. Piovesan, P. Forzatti, An investigation on the role of a Pt/Al2O3 catalyst in the oxidative dehydrogenation of propane in annular reactor, Journal of Catalysis, 184 (1999) 455-468.

[8] A. Beretta, E. Ranzi, P. Forzatti, Oxidative dehydrogenation of light paraffins in novel short contact time reactors. Experimental and theoretical investigation, Chemical Engineering Science, 56 (2001) 779-787.

[9] Z. Porš, J. Pasel, A. Tschauder, R. Dahl, R. Peters, D. Stolten, Optimised mixture formation for diesel fuel processing, Fuel Cells, 8 (2008) 129-137.

[10] M. O'Connell, G. Kolb, K. Schelhaas, J. Schuerer, D. Tiemann, A. Ziogas, V. Hessel, Development and evaluation of a microreactor for the reforming of diesel fuel in the kW range, International Journal of Hydrogen Energy, 34 (2009) 6290-6303.

[11] G. Kolb, T. Baier, J. Schürer, D. Tiemann, A. Ziogas, S. Specchia, C. Galletti, G. Germani, Y. Schuurman, A micro-structured 5kW complete fuel processor for iso-octane as hydrogen supply system for mobile auxiliary power units: Part II—Development of water–

gas shift and preferential oxidation catalysts reactors and assembly of the fuel processor, Chemical Engineering Journal, 138 (2008) 474-489.

[12] B. Lindström, J. Karlsson, P. Ekdunge, L. De Verdier, B. Häggendal, J. Dawody, M. Nilsson, L. Pettersson, Diesel fuel reformer for automotive fuel cell applications, International Journal of Hydrogen Energy, 34 (2009) 3367-3381.

[13] I. Kang, H.H. Carstensen, A.M. Dean, Impact of gas-phase reactions in the mixing region upstream of a diesel fuel autothermal reformer, Journal of Power Sources, 196 (2011) 2020-2026.

[14] M. Hartmann, L. Maier, H. Minh, O. Deutschmann, Catalytic partial oxidation of iso-octane over rhodium catalysts: An experimental, modeling, and simulation study, Combustion and Flame, 157 (2010) 1771-1782.

[15] L. Maier, M. Hartmann, S. Tischer, O. Deutschmann, Interaction of heterogeneous and homogeneous kinetics with mass and heat transfer in catalytic reforming of logistic fuels, Combustion and Flame, 158 (2011) 796-808.

[16] R.D. Parmar, A. Kundu, K. Karan, Thermodynamic analysis of diesel reforming process: Mapping of carbon formation boundary and representative independent reactions, Journal of power sources, 194 (2009) 1007-1020.

[17] J. Farrell, N. Cernansky, F. Dryer, D. Friend, C. Hergart, C. Law, R. McDavid, C. Mueller, A. Patel, H. Pitsch, Development of an experimental database and kinetic models for surrogate diesel fuels, SAE Paper, (2007) 1-27.

[18] D. Shekhawat, D.A. Berry, D.J. Haynes, J.J. Spivey, Fuel constituent effects on fuel reforming properties for fuel cell applications, Fuel, 88 (2009) 817-825.

[19] C. Song, C.S. Hsu, I. Mochida, Chemistry of Diesel Fuels, Taylor & Francis, New York, 2000.

[20] D. Shekhawat, T.H. Gardner, D.A. Berry, M. Salazar, D.J. Haynes, J.J. Spivey, Catalytic partial oxidation of n-tetradecane in the presence of sulfur or polynuclear aromatics: Effects of support and metal, Applied Catalysis A: General, 311 (2006) 8-16.

[21] COMSOL, in, Chemical Reaction Engineering User's Guide 4.2a, 2011.

[22] C.K. Westbrook, W.J. Pitz, O. Herbinet, H.J. Curran, E.J. Silke, A comprehensive detailed chemical kinetic reaction mechanism for combustion of n-alkane hydrocarbons from n-octane to n-hexadecane, Combustion and Flame, 156 (2009) 181-199.

[23] W.H. Green, J.W. Allen, R.W. Ashcraft, G.J. Beran, C.A. Class, C. Gao, C.F. Goldsmith, M.R. Harper, A. Jalan, G.R. Magoon, D.M. Matheu, S.S. Merchant, J.D. Mo, S. Petway, S.

Raman, S. Sharma, J. Song, K.M.V. Geem, J. Wen, R.H. West, A. Wong, H.-W. Wong, P.E. Yelvington, J. Yu, RMG - Reaction Mechanism Generator v3.3, in, 2011.

[24] A. Jalan, R.H. West, W.H. Green, An extensible framework for capturing solvent effects in computer generated kinetic models, The Journal of Physical Chemistry B, 117 (2013) 2955-2970.

[25] R.G. Susnow, A.M. Dean, W.H. Green, P. Peczak, L.J. Broadbelt, Rate-based construction of kinetic models for complex systems, The Journal of Physical Chemistry A, 101 (1997) 3731-3740.

[26] T.H. Lay, J.W. Bozzelli, A.M. Dean, E.R. Ritter, Hydrogen atom bond increments for calculation of thermodynamic properties of hydrocarbon radical species, The Journal of Physical Chemistry, 99 (1995) 14514-14527.

[27] J.W. Allen, C.F. Goldsmith, W.H. Green, Automatic estimation of pressure-dependent rate coefficients, Physical Chemistry Chemical Physics, 14 (2012) 1131-1155.

[28] A.Y. Chang, J.W. Bozzelli, A.M. Dean, Kinetic analysis of complex chemical activation and unimolecular dissociation reactions using QRRK theory and the modified strong collision approximation, The Journal of Physical Chemistry, 214 (2000) 1533-1568.

[29] N. Hansen, M.R. Harper, W.H. Green, High-temperature oxidation chemistry of n-butanol - experiments in low-pressure premixed flames and detailed kinetic modeling, Physical Chemistry Chemical Physics, 13 (2011) 20262-20274.

[30] K.M. Van Geem, M.F. Reyniers, G.B. Marin, J. Song, W.H. Green, D.M. Matheu, Automatic reaction network generation using RMG for steam cracking of n-hexane, AIChE Journal, 52 (2006) 718-730.

[31] J. Zádor, C.A. Taatjes, R.X. Fernandes, Kinetics of elementary reactions in low-temperature autoignition chemistry, Progress in Energy and Combustion Science, 37 (2011) 371-421.

[32] W. Tsang, W.S. McGivern, J.A. Manion, Multichannel decomposition and isomerization of octyl radicals, Proceedings of the Combustion Institute, 32 (2009) 131-138.

[33] D. Baulch, C. Cobos, R. Cox, P. Frank, G. Hayman, T. Just, J. Kerr, T. Murrells, M. Pilling, J. Troe, Evaluated kinetic data for combustion modeling. Supplement I, Journal of Physical and Chemical Reference Data, 23 (1994) 847.

[34] G. Friedrichs, D.F. Davidson, R.K. Hanson, Direct measurements of the reaction $H + CH_2O \rightarrow H_2 + HCO$ behind shock waves by means of Vis–UV detection of formaldehyde, International Journal of Chemical Kinetics, 34 (2002) 374-386.

[35] C.F. Goldsmith, S.J. Klippenstein, W.H. Green, Theoretical rate coefficients for allyl+ HO_2 and allyloxy decomposition, Proceedings of the Combustion Institute, 33 (2011) 273-282.

[36] W. Tsang, Chemical Kinetic Data Base for Combustion Chemistry Part V. Propene, Journal of Physical and Chemical Reference Data, 20 (1991) 221.

[37] K.L. Randolph, A.M. Dean, Hydrocarbon fuel effects in solid-oxide fuel cell operation: an experimental and modeling study of n-hexane pyrolysis, Physical Chemistry Chemical Physics, 9 (2007) 4245-4258.

[38] Z. Hong, D.F. Davidson, K.Y. Lam, R.K. Hanson, A shock tube study of the rate constants for the reaction of HO_2 and CH_3, Combustion and Flame, Submitted (2012).

[39] A.W. Jasper, S.J. Klippenstein, L.B. Harding, Theoretical rate coefficients for the reaction of methyl radical with hydroperoxyl radical and for methylhydroperoxide decomposition, Proceedings of the Combustion Institute, 32 (2009) 279-286.

[40] H.P.S. Shen, J. Steinberg, J. Vanderover, M.A. Oehlschlaeger, A shock tube study of the ignition of n-heptane, n-decane, n-dodecane, and n-tetradecane at elevated pressures, Energy & Fuels, 23 (2009) 2482-2489.

[41] S. Vasu, D. Davidson, Z. Hong, V. Vasudevan, R. Hanson, n-Dodecane oxidation at high-pressures: Measurements of ignition delay times and OH concentration time-histories, Proceedings of the Combustion Institute, 32 (2009) 173-180.

[42] V.P. Zhukov, V.A. Sechenov, A.Y. Starikovskii, Autoignition of n-decane at high pressure, Combustion and Flame, 153 (2008) 130-136.

[43] D. Davidson, R. Hanson, Interpreting shock tube ignition data, International Journal of Chemical Kinetics, 36 (2004) 510-523.

[44] H. Curran, P. Gaffuri, W.J. Pitz, C.K. Westbrook, A comprehensive modeling study of n-heptane oxidation, Combustion and Flame, 114 (1998) 149-177.

[45] E. Ranzi, A. Frassoldati, S. Granata, T. Faravelli, Wide-range kinetic modeling study of the pyrolysis, partial oxidation, and combustion of heavy n-alkanes, Industrial & Engineering Chemistry Research, 44 (2005) 5170-5183.

[46] J. Biet, M.H. Hakka, V. Warth, P.A. Glaude, F. Battin-Leclerc, Experimental and modeling study of the low-temperature oxidation of large alkanes, Energy & Fuels, 22 (2008) 2258-2269.

[47] R. Cox, J. Cole, Chemical aspects of the autoignition of hydrocarbon---air mixtures, Combustion and Flame, 60 (1985) 109-123.

[48] J. Warnatz, Chemistry of high temperature combustion of alkanes up to octane. In *Twentieth Symposium (International) on Combustion*, University of Michigan, Ann Arbor, Michigan, 1985; 845-856

[49] C. Morley, A fundamentally based correlation between alkane structure and octane number, Combustion Science and Technology, 55 (1987) 115-123.

[50] D.C. Horning, A study of the high-temperature autoignition and thermal decomposition of hydrocarbons. Ph.D. Thesis, Stanford University, 2001.

[51] F. Battin-Leclerc, Detailed chemical kinetic models for the low-temperature combustion of hydrocarbons with application to gasoline and diesel fuel surrogates, Progress in Energy and Combustion Science, 34 (2008) 440-498.

[52] C.K. Westbrook, F.L. Dryer, Chemical kinetic modeling of hydrocarbon combustion, Progress in Energy and Combustion Science, 10 (1984) 1-57.

[53] J. Warantz, The mechanism of high temperature combustion of propane and butane, Combustion Science and Technology, 34 (1983) 177-200.

[54] J.M. Simmie, Detailed chemical kinetic models for the combustion of hydrocarbon fuels, Progress in Energy and Combustion Science, 29 (2003) 599-634.

[55] M.J. De Witt, D.J. Dooling, L.J. Broadbelt, Computer generation of reaction mechanisms using quantitative rate information: Application to long-chain hydrocarbon pyrolysis, Industrial & Engineering Chemistry Research, 39 (2000) 2228-2237.

[56] C. Song, W.C. Lai, H.H. Schobert, Condensed-phase pyrolysis of n-tetradecane at elevated pressures for long duration. Product distribution and reaction mechanisms, Industrial & Engineering Chemistry Research, 33 (1994) 534-547.

[57] R. Bounaceur, V. Warth, P.M. Marquaire, G. Scacchi, F. Dominé, D. Dessort, B. Pradier, O. Brevart, Modeling of hydrocarbons pyrolysis at low temperature. Automatic generation of free radicals mechanisms, Journal of Analytical and Applied Pyrolysis, 64 (2002) 103-122.

[58] S. Pierucci, E. Ranzi, M. Dente, S. Barendregt, A kinetic generator of hydrocarbon pyrolysis mechanisms, Computer Aided Chemical Engineering, 20 (2005) 241-246.

[59] F. Rice, The thermal decomposition of organic compounds from the standpoint of free radicals. III. The calculation of the products formed from paraffin hydrocarbons, Journal of the American Chemical Society, 55 (1933) 3035-3040.

[60] F. Rice, K. Herzfeld, The thermal decomposition of organic compounds from the standpoint of free radicals. VI. The mechanism of some chain reactions, Journal of the American Chemical Society, 56 (1934) 284-289.

[61] A. Kossiakoff, F.O. Rice, Thermal Decomposition of Hydrocarbons, Resonance Stabilization and Isomerization of Free Radicals1, Journal of the American Chemical Society, 65 (1943) 590-595.

[62] H. Voge, G. Good, Thermal cracking of higher paraffins, Journal of the American Chemical Society, 71 (1949) 593-597.

[63] D. Depeyre, C. Flicoteaux, C. Chardaire, Pure n-hexadecane thermal steam cracking, Industrial & Engineering Chemistry Process Design and Development, 24 (1985) 1251-1258.

[64] D. Depeyre, C. Flicoteaux, Modeling of thermal steam cracking of n-hexadecane, Industrial & Engineering Chemistry Research, 30 (1991) 1116-1130.

[65] M.J. De Witt, L.J. Broadbelt, Binary interactions between tetradecane and 4-(1-naphthylmethyl) bibenzyl during low-and high-pressure pyrolysis, Energy & Fuels, 13 (1999) 969-983.

[66] P.A. Willems, G.F. Froment, Kinetic modeling of the thermal cracking of hydrocarbons. 1. Calculation of frequency factors, Industrial & Engineering Chemistry Research, 27 (1988) 1959-1966.

[67] V. Burkl-Vitzthum, R. Bounaceur, P.M. Marquaire, F. Montel, L. Fusetti, Thermal evolution of n-and iso-alkanes in oils. Part 1: Pyrolysis model for a mixture of 78 alkanes (C_1-C_{32}) including 13,206 free radical reactions, Organic Geochemistry, 42 (2011) 439-450.

[68] D. Shekhawat, J.J. Spivey, D. Berry, Fuel Cells: Technologies for Fuel Processing, Elsevier Science, Oxford, 2011.

[69] K. Tomishige, S. Kanazawa, K. Suzuki, M. Asadullah, M. Sato, K. Ikushima, K. Kunimori, Effective heat supply from combustion to reforming in methane reforming with CO_2 and O_2: comparison between Ni and Pt catalysts, Applied Catalysis A: General, 233 (2002) 35-44.

[70] K. Tomishige, M. Nurunnabi, K. Maruyama, K. Kunimori, Effect of oxygen addition to steam and dry reforming of methane on bed temperature profile over Pt and Ni catalysts, Fuel Processing Technology, 85 (2004) 1103-1120.

[71] J. Baron, E.M. Bulewicz, W. Żukowski, S. Kandefer, M. Pilawska, Combustion of hydrocarbon fuels in a bubbling fluidized bed, Combustion and Flame, 128 (2002) 410-421.

[72] F. Bustamante, R. Enick, R. Killmeyer, B. Howard, K. Rothenberger, A. Cugini, B. Morreale, M. Ciocco, Uncatalyzed and wall-catalyzed forward water–gas shift reaction kinetics, AIChE Journal, 51 (2005) 1440-1454.

[73] R.D. Parmar, D. Shekhawat, B.A. Peppley, K. Karan, Stable diesel or heavy hydrocarbon reforming catalyst: properties and performance, Manuscript included as Chapter-5, (2013).

[74] H.F. Abbas, W. Daud, Influence of reactor material and activated carbon on the thermocatalytic decomposition of methane for hydrogen production, Applied Catalysis A: General, 388 (2010) 232-239.

[75] J. Gornay, L. Coniglio, F. Billaud, G. Wild, Steam cracking and steam reforming of waste cooking oil in a tubular stainless steel reactor with wall effects, Energy & Fuels, 23 (2009) 5663-5676.

[76] H. Yamada, S. Kawai, T. Tomohiko, Tetradecane reforming with stainless-steel based catalyst. In *The 13th Asia Pacific Confederation of Chemical Engineering Congress*, Taipei, Taiwan, 2010.

[77] R.D. Parmar, A. Kundu, C. Thurgood, B.A. Peppley, K. Karan, Kinetic studies of the autothermal reforming of tetradecane over Pt/Al_2O_3 catalyst in a fixed-bed reactor, Fuel, 89 (2010) 1212-1220.

[78] J. Thormann, L. Maier, P. Pfeifer, U. Kunz, O. Deutschmann, K. Schubert, Steam reforming of hexadecane over a Rh/CeO_2 catalyst in microchannels: Experimental and numerical investigation, International Journal of Hydrogen Energy, 34 (2009) 5108-5120.

[79] D. Creaser, X. Karatzas, B. Lundberg, L.J. Pettersson, J. Dawody, Modeling study of 5 kWe-scale autothermal diesel fuel reformer, Applied Catalysis A: General, 404 (2011) 129-140.

[80] L. Shi, D.J. Bayless, M.E. Prudich, A CFD model of autothermal reforming, International Journal of Hydrogen Energy, 34 (2009) 7666-7675.

[81] S.S. Vasu, Measurements of Ignition Times, OH Time-histories, and Reaction Rates in Jet Fuel and Surrogate Oxidation Systems. Ph.D. Thesis, Stanford University, 2010.

[82] H. Curran, Rate constant estimation for C1 to C4 alkyl and alkoxyl radical decomposition, International Journal of Chemical Kinetics, 38 (2006) 250-275.

[83] C. Kappler, J. Zádor, O. Welz, R.X. Fernandez, M. Olzmann, C.A. Taatjes, Competing Channels in the Propene+ OH Reaction: Experiment and Validated Modeling over a Broad Temperature and Pressure Range, Zeitschrift für Physikalische Chemie, 225 (2011) 1271-1291.

[84] G.P. Smith, P.W. Fairchild, J.B. Jeffries, D.R. Crosley, Laser pyrolysis/laser fluorescence studies of high-temperature reaction rates: description of the method and results for hydroxyl+ methane, propane, and propylene, The Journal of Physical Chemistry, 89 (1985) 1269-1278.

[85] J. Zádor, A.W. Jasper, J.A. Miller, The reaction between propene and hydroxyl, Physical Chemistry Chemical Physics, 11 (2009) 11040-11053.

Chapter 7

Multi-Component, Micro-Kinetic Model for Diesel Surrogate Autothermal Reforming

7.1 Preface

A clean and sustainable future energy is mainly governed by the science behind the catalysis. Future for energy and transition towards more cost-effective newer energy technologies is completely dependent on uses of catalysis. Although the prospect of designing a catalyst from first principle is still far away, a significant progress is made in describing the reaction pathways on a well-defined single crystal of metal in simplified conditions. However, the real world catalyst is far more complicated in which the same reaction is carried out on the supported catalyst. Also understanding the complex reaction system using ab-initio quantum chemistry methods is computationally costly.

This chapter describes the development of multi-component, surface micro-kinetic model using hybrid approach in which the binding energy or heat of chemisorption of most of the adsorbed species is obtained from literature reported values (either from DFT study or from experimental study) and the energetic (activation energy) is obtained using semi-empirical techniques, such as unity bond index-quadratic exponential potential (UBI-QEP). The methodology adopted to get the energetic of kinetic model is not computationally costly and describes the energetic of the reaction path on the surface of the catalyst reasonably well. Simple Transition State Theory (TST) rules are used for catalytic reactions to estimate the pre-exponential factors instead of performing computationally expensive calculations. The packed bed reactor simulation using gas-phase reaction kinetic model, discussed in Chapter 6, and surface micro-kinetic model is described and model predictions are compared with experimental data from Chapter 5. Dominant reactions for hydrogen generation and reaction pathways for reforming reactions on the catalyst are discussed. The chapter also highlights the importance of gas-phase reactions in the post-catalytic zone of the reactor and discusses the possible reaction sequence that lead to ethylene formation.

7.2 **Abstract**

A multi-component, micro-kinetic model for gas-phase species reaching catalyst surface during autothermal reforming of diesel surrogate (n-tetradecane) was developed using hybrid approach in which the binding energy or heat of chemisorption of most of the adsorbed species was obtained from literature reported values (either from DFT study or from experimental study) and the energetic (activation energy) was obtained using semi-empirical techniques, such as unity bond index-quadratic exponential potential (UBI-QEP). Pre-exponential factors were set based on Transition State Theory (TST) rule. The gas-phase kinetic model developed by using the Reaction Mechanism Generator (RMG) was used to simulate the gas-phase reactions (Chapter 6 [1]). The overall model simulation (*i.e.*, gas-phase reactions in entire reactor and surface reactions in the catalyst zone) could predict the experimental species profiles reasonably well at different operating conditions. Using sensitivity analysis (SA) and rate of production analysis (ROP), reaction path for alkanes and alkenes reforming on the surface of the catalyst was identified. Model simulations indicated that the CO generated due to gas-phase reactions in the pre-catalytic zone of the reactor was consumed by water-gas-shift (WGS) reaction within first millimeter of the catalyst due to high WGS activity. After the first millimeter of the catalyst, steam reforming of smaller hydrocarbons was found to be responsible for H_2 and CO generation. The study also identified that slippage of 1,3- butadiene through the catalyst could lead to ethylene formation due to gas-phase reactions at high temperature in the post-catalytic zone of the reactor.

Keywords: Surface micro-kinetic model, Autothermal reforming, Diesel surrogate-n-tetradecane, gas-phase reactions

1. Introduction

Solid Oxide Fuel Cell (SOFC) fed with diesel is a promising technology that has potential to replace existing low efficiency and high polluting diesel generators/engines for low power, distributed power applications. The application of such technology is envisaged in remote communities such as the Northern part of Canada where there is no electric grid [2] and in long-haul trucks to meet the electric demand while the truck is idle [3, 4]. Apart from Northern-America, there are still large communities around the world that rely on highly polluting diesel generators. Overall integrated Auxiliary Power Unit (APU) offers certain challenges both in fuel cell design and reformer design. The optimized reformer design needs highly active diesel reforming catalyst with proper understanding of gas-phase and surface kinetics. The present work, which is also one of the sub-themes of SOFC Canada, is more focused towards understanding and developing the gas-phase kinetics and surface kinetics and validating the developed models against experimental data. This research article presents the development of multi-step, multi-component, surface micro-kinetic model, validating the model against experimental data, and elucidating the influence of gas-phase reactions.

Very few studies have been done to include gas-phase kinetics while simulating or modeling the reforming experiments. Widely used approach for modeling the surface kinetics of higher hydrocarbon (*i.e.*, diesel or gasoline surrogate) reforming assumes no gas-phase reactions. The majority of the studies used experimental data of diesel or gasoline surrogate reforming to fit either power law type of model [5-10] or Langmuir-Hinshelwood-Hougen-Watson (LHHW) type of model [11-22] by estimating the model parameters. Assuming no gas-phase reactions, Deutschmann and co-workers proposed a micro-kinetic model for hexadecane reforming on

Rh/CeO_2 catalyst. The model used was basically a detailed C_1 reaction mechanism developed for Rh/Al_2O_3 catalyst and a global reaction mechanism for dissociative adsorption of hexadecane over Rh catalyst was proposed [23]. It could predict the outlet composition very well qualitatively. Later, using similar approach, they also proposed a micro-kinetic mechanism for ethane, propane, and butane reforming on Rh catalyst [24]. Along similar line of work, Rickenbach *et al.* [25] used Hickman and Schmidt's [26] methane oxidation mechanism, added more parameters (*i.e.*, reactions), replaced methane adsorption step with butane adsorption, and proposed a simple 23 step mechanism for butane reforming over Rhodium catalyst. None of these micro-kinetic modeling works used gas-phase reactions, and they are all based on one step decomposition of heavy hydrocarbons on the surface of the catalyst. Recently Dean and co-workers identified the importance of gas-phase reactions in the up-steam mixing regime for n-hexane and n-dodecane autothermal reforming [27]. They reported to have used a kinetic model developed by Westbrook and co-workers [28] at Lawrence Livermore National Laboratory (LLNL). Using isothermal and adiabatic reactors, they modeled the gas-phase concentrations and temperature profiles at equivalence ratios (or O_2/C ratio) where gas-phase kinetic model validity is unclear. However, using their modeling study they concluded that gas-phase reactions plays significant role in the up-steam mixing zone during autothermal reforming of diesel fuel. To study the importance of homogeneous gas-phase reactions and heterogeneous surface reaction kinetics for partial oxidation of isooctane, Deutschmann and co-workers used the available kinetic models from literature for gas-phase reactions and modeled surface micro-kinetic mechanism using few important reaction steps for partial oxidation of C_1-C_3 species coupled with lumped reactions for adsorption of iso-octane [29, 30]. They reported that both homogenous gas-phase chemistry and surface reaction chemistry plays a significant role while reforming of isooctane. They emphasized the need for detailed chemistry models to understand the complex interaction of catalytic and gas-phase reactions. Recently they also reported that high temperatures in the down-stream of the catalyst lead to significant gas-phase homogeneous reactions that are responsible for coke formation [31].

The present literature study suggests that no gas-phase reaction model validated for high equivalence ratio (*i.e.*, low O_2/C ratio) and no detailed surface kinetic model are available in the literature. In Chapter 6 [1], a detailed and validated gas-phase kinetic model for autothermal reforming of n-tetradecane is discussed. We have identified two stage oxidation in the upstream region, and all of the n-tetradecane and oxygen are consumed before they reach the catalyst bed suggesting steam reforming on the catalyst surface. Also major ethylene production, a precursor to carbon formation, was observed in the second oxidation stage where it is majorly formed by alkyl-1 beta-scission reaction. In this paper, we are presenting a detailed surface micro-kinetic model for the species reaching the catalyst bed and validating the model against experimental data. Also the effect of gas-phase reactions in the post-catalytic bed of the reactor is discussed in detail.

2. Experimental

N-tetradecane was selected as a diesel surrogate in the present work. A 3-level factorial design experiments with and without catalyst were performed in a fixed bed reactor experimental system as shown in Figure 7.1. For surface kinetic study 0.181 gm (-80+100 mesh and -100 mesh) of catalyst was diluted with 4.536 gm (-20+60 mesh) of quartz sand. The catalyst was placed inside the 8 mm I.D., 27.94 mm long, Incoloy 800HT (approximate composition : 30-35%

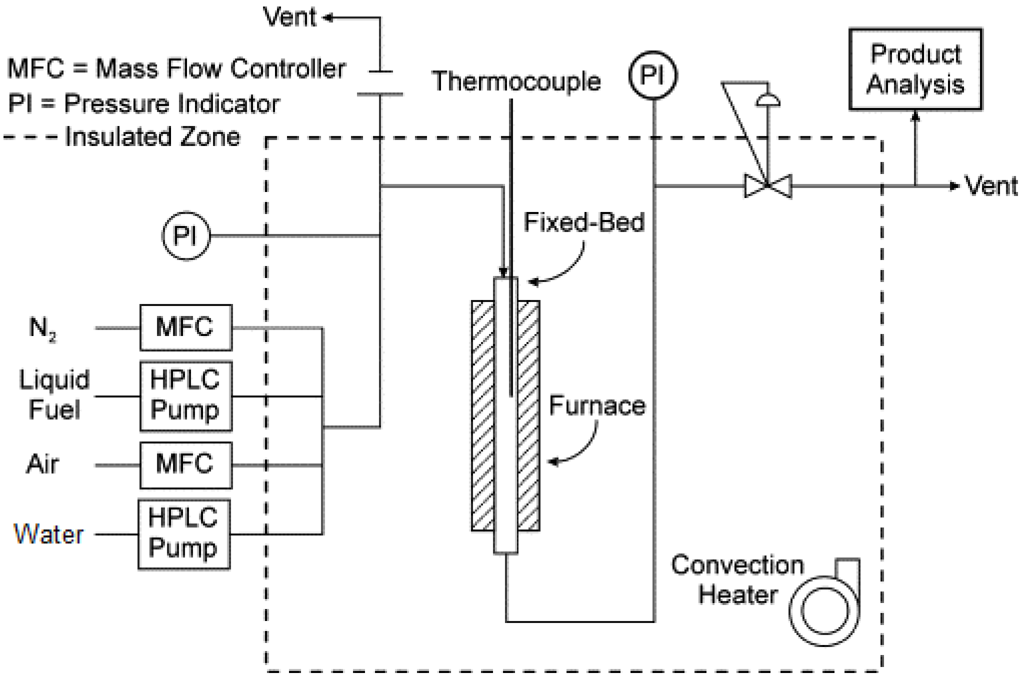

Figure 7.1: Experimental system for activity and kinetic study [32]

Ni, 39.5% min Fe, 19-23% Cr) tubular reactor tube. Quartz sand particles of the same size were used above and below the catalyst bed, which enhances the mixing of the reactants before they reach the catalyst surface. The product gas (N_2, H_2, O_2, CO, CO_2, and methane) was analyzed continuously using a Thermo Onix mass spectrometer (MS) (Model no. Prima δb, with a 200 a.m.u. scanning magnetic sector) with standard ±2% analytical error in gas concentrations. The gaseous hydrocarbon products were analyzed using a HP5890 gas chromatograph (GC) equipped with a flame ionization detector (FID). The experimental data for surface as well as gas-phase kinetic study (*i.e.*, with and without catalyst respectively) were obtained by varying O_2/C ratio, temperature and space velocity, all at constant S/C ratio. Complete experimental details and results are discussed in Chapter 5 [33]. The following definitions were used to define the yield of products.

$$Yield\,of\;H_2\,[\%] = \frac{moles\,of\;H_2}{(15 \times moles\,of\;tetradecane\;fed + moles\,of\;water\;fed)} \times 100 \tag{1}$$

$$Yield\,of\;C_nH_m\,[\%] = \frac{n \times moles\,of\;C_nH_m}{(14 \times moles\,of\;tetradecane\;fed)} \times 100 \tag{2}$$

$$Yield\,of\;CO/CO_2[\%] = \frac{moles\,of\;CO/CO_2}{14 \times moles\,of\;tetradecane\;fed} \times 100 \tag{3}$$

where '*n*' is the number of moles of carbon per mole of hydrocarbon in the product. Hydrogen yield is based on number of moles of hydrogen fed into the reactor as specified by Shekhawat *et al.* [34].

The conversion was calculated by

$$X\,[\%] = \frac{moles\,of\;carbon\,in\,outlet\;product\;gas}{14 \times moles\,of\;tetradecane\;fed} \times 100 \tag{4}$$

Carbon balances for experiments were ± 7%.

3. Reactor Model

A schematic diagram of the packed bed reactor system used in the experiments at NETL is shown in Figure 7.2. A two dimensional packed bed reactor model with heat transfer (considering all modes of heat transfer *i.e.*, conduction, convection and radiation) and momemtum transfer

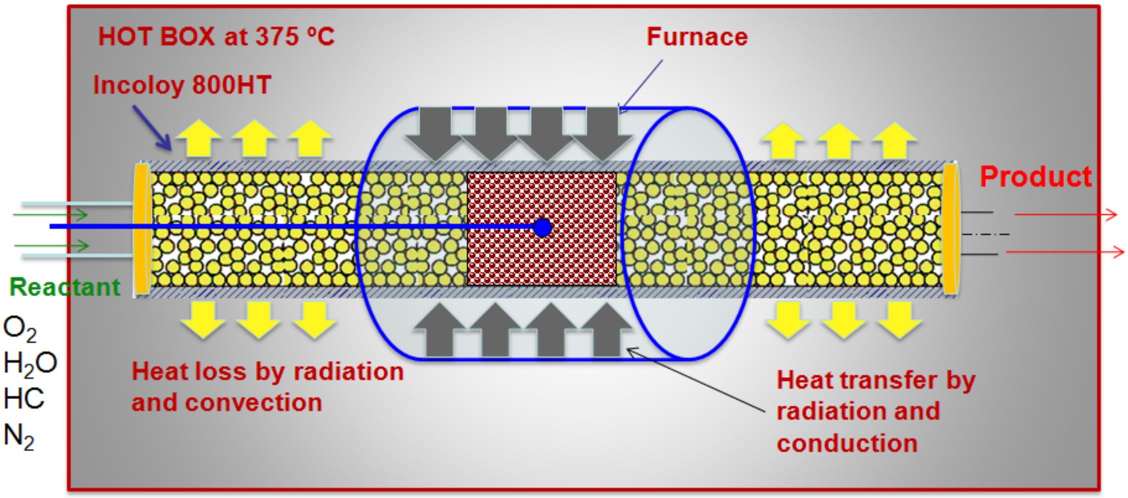

Figure 7.2: Experimental packed bed reactor system

(considering modified Navier-Stokes equation which takes into account the radial void distribution) was made using COMSOL^{TM} and temperature profile inside the reactor without reaction (*i.e.*, with N_2 flow) was validated against experimental data. Simultaneous solution of detailed chemistry coupled with mass transfer, momentum transfer, and heat transfer within the packed bed reactor was not possible with available computational resources. The reactor model was then simplified as the plug flow isobaric reactor as it satisfied plug flow isobaric reactor assumption criteria [35, 36] as shown below:

(1) Ratio of catalyst bed height to catalyst particle size $(L/d_p) = 508 > 50$

(2) Ratio of catalyst bed diameter to the catalyst particle size $(d/d_p) = 14.4 > 10$

(3) Maximum pressure drop inside the reactor < 5%

Above assumptions reduced the model as a one-dimensional problem for mass and momentum transfer and two-dimensional problem for heat transfer. Coupling of two-dimensional heat transfer with large number of reactions and species was challenging in available Computational Fluid Dynamic (CFD) software. Hence an iterative hybrid approach was used in which the simplified packed-bed isobaric plug-flow reactor model with heat transfer was solved using a finite element CFD solver while the kinetic equations were solved using the Chemkin. The temperature profiles obtained without reaction were used as the initial guess that was provided as input to Chemkin, which in turn calculates the heat of reaction along the length of the reactor. This heat of reaction profile was then fed back to the finite element plug flow solver to get the resulting temperature profile. This procedure was repeated until a convergent temperature profile was obtained. Details about the reactor modeling, iterative approach with proof-of-concept study is discussed in Chapter 6 [1]. The above-described procedure was done for gas-phase kinetic study. It was found that all of the oxygen is consumed before the catalyst leading to steam reforming of smaller hydrocarbons on the surface of the catalyst. Since heat is continuously supplied to maintain central bed temperature, the obtained temperature profile along the length of the reactor during the gas-phase kinetic study can be used to simulate the surface reactions.

For reactor simulation, Chemkin reactor model as shown in Figure 7.3 is used. The reactor is divided into five sections. The first section is an inlet zone (0 - 0.05m), Second section is zone before the catalyst surface (0.05 m – 0.16 m), the third section is a catalyst zone (0.16 m – 0.19 m), the fourth section is also a catalyst zone (0.19 m – 0.22 m), and fifth section is a downstream zone (0.19 m – 0.33 m). All sections except first section contain packing. The average porosity in the second and third section is equal to 0.483, whereas the average porosity in fourth and fifth section is equal to 0.406. The average porosity is high in second and third section compared to fourth and fifth section due to the thermocouple. The detailed explanation of the modeling is given in Chapter 6 [1].

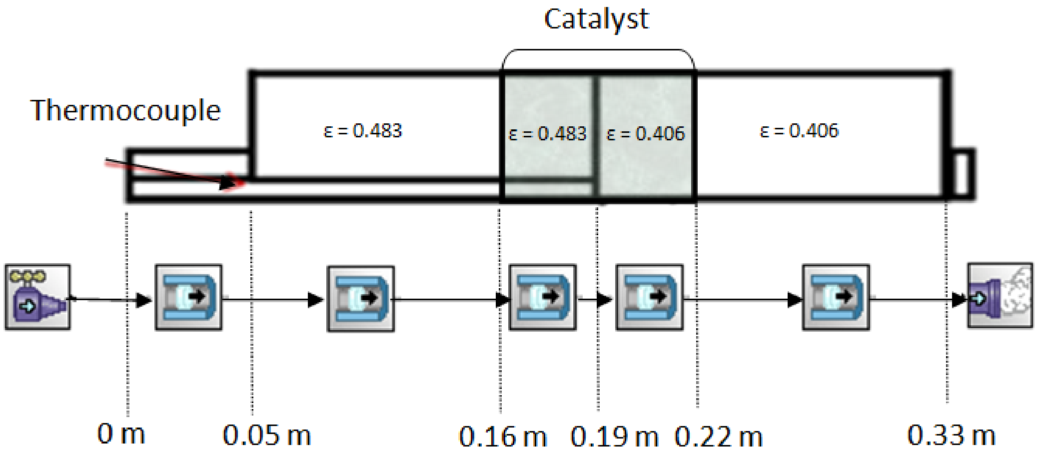

Figure 7.3: Chemkin packed bed reactor model

4. Kinetic Model Development

4.1. Approach

A micro-kinetic model approach has been adapted so that it can be applied over a wide range of operating conditions [37]. Major advantages of micro-kinetic approach over the classical approach are that it does not require a *priori* assumption about the rate-determining-step (RDS), most abundant reaction intermediates (MARI), quasi-steady state (QSS) *etc.* and it can capture the reacting system behavior under different operating conditions. It also aids in understanding the fundamental reaction pathways and determining the rate-limiting step at different operating conditions. Implementing the micro-kinetic model for practical process control and system analysis purpose or for computational fluid dynamic simulations could be a daunting task as it requires much longer computational time for simulation compared to the classical power law or

LHHW type of model. But the micro-kinetic model also offers an advantage of building hierarchical model in which the model could be converted into a simple power law type of model or LHHW type of model that is valid under certain operating conditions [38, 39].

Micro-kinetic model development involves the construction of elementary reaction scheme based on the literature on surface science study, quantum study on a particular reaction path, experimental evidence and experience. Another major task in model development is to get the parameters such as pre-exponential factor and activation energy for elementary reactions. Often the reaction is carried out at different temperatures and surface coverage of species changes with time and space. This poses a big challenge in estimating the activation energy as a function of temperature and surface coverage. Even if model parameters are calculated from the first principle techniques, such as Density Functional Theory (DFT), they are subject to intrinsic uncertainty of the calculation method used (*e.g.*, binding and activation energies calculated with DFT can have an accuracy of about 5 kcal/mol [40, 41]) . Uncertainty can also arise from estimating the parameters from experimental data, such as obtaining heat of chemisorption from temperature programmed desorption (TPD) data. Apart from aforementioned uncertainty, heterogeneity of real catalyst, such as point defects, steps, faces, edges, and corners of sites, can affect the activation energy significantly [42]. Also, the heat of chemisorption of real catalyst, either supported or substituted, may vary due to support effect, catalyst preparation methods (*i.e.*, interaction of catalyst with support). Considering all these uncertainties that could be present in developing a micro-kinetic model, a semi-empirical approach is used to obtain the approximate rate parameters. The approach similar to those proposed by Vlachos and coworkers for hierarchical multi-scale model development is used to develop a predictive surface reaction mechanism [43-45].

There are many challenges in the development of a surface kinetic model of diesel or diesel surrogate reforming. Heavier hydrocarbons such as diesel can decompose into smaller molecules in the hot pre-catalytic region. These smaller molecules may serve as the primary reactants through which the surface reactions proceed. The ability to identify the reaction intermediates and their surface coverage is non-trivial. These reactions proceed with thermal effects (endothermic or exothermic reactions) resulting in temperature gradients in a reactor. Gas-phase reactions can proceed in parallel to the surface reactions, even competing with it. Moreover, the data available for validation are typically limited to the composition of the stable species at the reactor exit.

4.2. Importance of gas-phase reactions

The data collected for packed bed, non-catalytic reactor shows that significant amounts of CO, CO_2 and lower hydrocarbons are generated even in the absence of the catalyst (Figure 7.4). An elementary kinetic model developed in Chapter 6 [1] for the gas-phase reactions was employed to investigate the extent of reaction occurring in the pre-catalytic (or heating) zone of the reformer and, more importantly, to simulate the composition of reaction mixture entering the catalytic bed. The model predicts that apart from CO, CO_2, H_2 and H_2O many other smaller hydrocarbons, such as alkanes, alkenes, ketenes, aldehydes, alcohols, ketones and furans, reach the catalyst surface. Subsequently, the fate of these hydrocarbons is decided by the type and design of the catalyst. Various hydrocarbons that reach the catalyst surface are shown in Table 7.1.

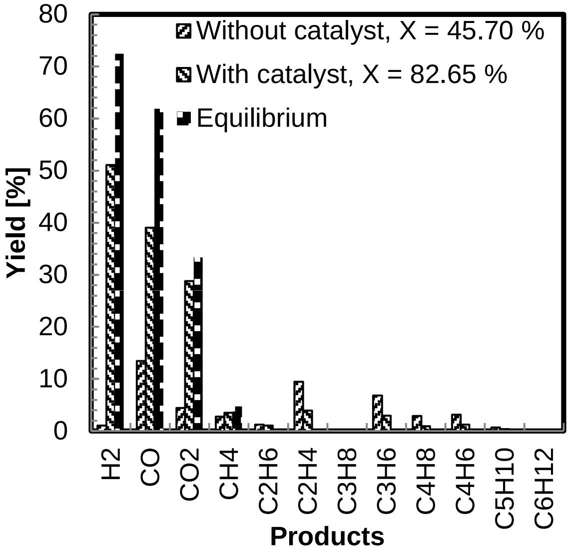

Figure 7.4: Experimental exit product concentration with and without catalyst with n-tetradecane passing through an ATR reactor ($H_2O/C = 1.5$, $O_2/C = 0.2$, $T_{bed} = 973.15$ K); conversion = moles of carbon in gas-phase at the exit x 100 / moles of carbon fed in the system

4.3. Kinetic scheme

The path taken and assumptions made for the kinetic scheme are as follows:

1. Rh(111) site (also denoted as *) is assumed to be active for catalytic reactions.
2. Reaction scheme for methane partial oxidation (POX), steam reforming (SR), WGS, and oxygenates (*e.g.,* formaldehyde and methanol) decomposition is adapted from the Mhadeshwar and Vlachos [44].

Table 7.1: Gas-phase species reaching catalyst surface

Species	**Example**
Alkanes: C_1 to C_3	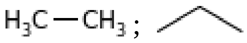
Alkenes: C_2 to C_{14}	
Dienes: C_4 to C_6	
Ketene	$H_2C=C=O$
Oxygenates (aldehydes, alcohols, ketones, furans)	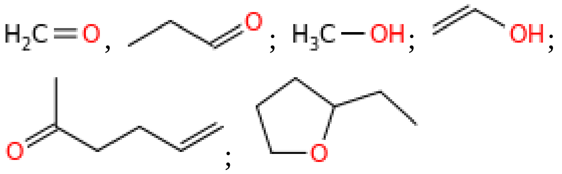

3. C_2 and C_3 species dehydrogenation and fragmentation reactions are taken from the work of Bhattacharjee [46].
4. All alkenes above C_3 are assumed to fragment on the surface of the catalyst into ethylene and other alkenes.
5. Ketones are assumed to decompose into CH_3, CH_2, CH, and CH_3CO (acetyl) species on the surface of the catalyst.
6. Reaction scheme for acetaldehyde (CH_3CHO) and acetyl (CH_3CO) species reactions is taken from Koehle and Mhadeshwar [47] work of ethanol partial oxidation and reforming on Pt catalyst.
7. Ketene (CH_2CO) surface reaction scheme is obtained from the work of Choi and Liu [48], and Li *et al.* [49] for ethanol decomposition on Rh(111).

8. Aldehydes (except formaldehyde), alcohols and furans are assumed to decompose into adsorbed C, H and O species.
9. C_{14} alkane is assumed to dissociate into adsorbed CH_3, CH_2 and H species as per the reaction mechanism proposed by Parmar *et al.* [50]

The identified reaction scheme has two hundred and seventy reactions and fifty-two adspecies.

4.4. Kinetic parameters

Having identified the reaction scheme, the second step in hierarchical model development is calculating model parameters while maintaining enthalpic and entropic consistency. The reaction rate constant is calculated by using modified Arrhenius form:

$$k = \frac{A}{\Gamma_{Rh}^{n-1}}\left(\frac{T}{T_o}\right)^{\beta} e^{-E/RT} \quad \text{or in CHEMKIN FORMAT} \quad k = A'T^{\beta}e^{-E/RT} \tag{5}$$

or

$$k = \frac{s}{\Gamma_{Rh}^{n}}\left(\frac{T}{T_o}\right)^{\beta}\sqrt{\frac{RT}{2\pi M}}e^{-E/RT} \tag{6}$$

where A is the preexponential factor (or prefactor) in 1/s, s is the sticking coefficient, n is the reaction order, Γ is the site density in mol/cm^2, β is the temperature exponent, E is the activation energy in kcal/mol, R is the ideal gas constant in kcal/mol·K, T is the temperature in K, and T_o is the reference temperature 300 K. Surface site density (2.2082×10^{-9} mol/cm^2) is obtained from chemisorption study on Rh/pyrochlore catalyst discussed in Chapter 5 [33]. Each elementary reaction in the mechanism is associated with kinetic parameters: pre-exponential factor *A* or sticking coefficient *s*, temperature exponent β, and activation energy *E*. To obtain activation energy of the reaction, the hybrid approach is used in which the binding energy or heat of chemisorption of most of the adsorbed species is obtained from literature reported values (either from DFT study or from experimental study) and the energetic (activation energy) is obtained using semi-empirical techniques, such as bond order conservation (BOC), generalized in 1998 to be known as unity bond index-quadratic exponential potential (UBI-QEP) [51-53]. Use of Transition state theory (TST) or molecular dynamics simulations [52] is computationally expensive to calculate the pre-exponential factor, hence the pre-exponential factors are taken from typical estimates based on TST (*e.g.*, 10^{13} 1/s for desorption and 10^{11} 1/s for Langmuir-Hinshelwood type surface reactions) [37]. Heat of adsorption values used for activation energy calculation for various adsorbed species is given in Table 7.2.

Table 7.2: Temperature and coverage dependent heat of chemisorption

Species	**Heat of chemisorption (kcal/mol)**	**Temperature dependence $(Q(T_0)-Q(T))/R_g\Delta T$**	**Reference**
O*	$100 - 26\theta_O$	1.5	[45]
CO*	$38.5 - 15\theta_{CO} - 3.7\theta_H$	2.0	[45]
CO_2*	5.20	2.0	[45]
H*	$62.3 - 3.7\theta_{CO} - 2.5\theta_H$	1.5	[45]
OH*	$70.0 - 33\theta_O - 25\theta_{H2O}$	2.0	[45]
H_2O*	$10.8 + 25\theta_H - 4.5\theta_{H2O}$	2.5	[45]
COOH*	62.20	2.5	[45]
HCOO**	69.20	3.0	[45]

Species	Heat of chemisorption (kcal/mol)	Temperature dependence $(Q(T_0)-Q(T))/R_g\Delta T$	Reference
C*	159.00	1.5	[45]
CH*	151.20	2.0	[45]
CH_2*	109.30	2.5	[45]
CH_3*	42.40	2.5	[45]
CH_4*	6.00	2.0	[45]
CH_3OH*	11.00	2.5	[44]
CH_2O*	22.00	2.5	[44]
HCO*	64.70	2.5	[44]
CH_2OH*	56.40	2.5	[44]
C_2H_6*	7.37	2.0	[46]
CH_3CH_2*	48.43	2.5	[46]
CH_3CH**	99.85	2.5	[46]
CH_3C***	146.21	2.5	[46]
C_2H_4**	23.98	2.5	[46]
CH_2CH***	70.11	3.0	[46]
CH_2C***	101.01	3.0	[46]
C_2H_2***	60.88	3.0	[46]
CHC***	110.23	3.0	[46]
CC****	136.06	2.5	[46]
C_3H_8*	8.00	2.5	Approx[53]
CH_3CHCH_3*	41.79	2.5	UBI-QEP
C_3H_6**	10.52	2.5	UBI-QEP
CH_3CCH_3**	79.23	2.5	UBI-QEP
CH_3CCH_2***	7.86	2.5	UBI-QEP
CH_3CHO*	11.20	3.0	Same as on Pt[47]
CH_3CO*	57.80	3.0	Same as on Pt[47]
CH_2CO*	30.40	3.0	[49]
CHCO*	74.10	3.0	[49]

Using UBI-QEP framework activation energy for various elementary reactions is calculated. The UBI-QEP method ensures the enthalpic consistency at only one temperature. To ensure the enthalpic consistency and to obtain the activation energy and heat of reaction at high temperature, the heat of chemisorption dependence on temperature is incorporated by using statistical mechanics as suggested by Mhadeshwar *et al*. [43, 44].

The assumptions used to calculate the temperature dependence are as follows:

(a) Translational, rotational, and vibrational degree of freedom (DOF) corresponds to 0.5RgT, $0.5R_gT$, and R_gT, respectively.

(b) When a species adsorbed on the surface of the catalyst, all translational, and rotational DOF are lost. In the case of weakly bound molecules (CO_2, CH_4 and C_2H_6) only one translational degree of freedom is lost (*i.e.,* molecule is able to move readily on the surface of the catalyst).

(c) Number of DOF lost is converted into vibrational DOF. For species, such as CH_2, H_2O *etc*., with vertical axis through adsorbed atom, one gained DOF can be assumed to be a free, internal rotor. DOF associated with rigid rotor approximation is $0.5R_gT$. Entropic consistency is applied by using the methodology as described by Mhadeshwar *et al*. [43].

The overall assumptions and methodology used in calculating and/or refining the rate constant parameters are as follows:

1. Since it was not possible to incorporate the thermodynamic consistency criteria in Surface-CHEMKIN format, all parameters are obtained at 1073 K. Initially all parameters activation energy is calculated using zero surface coverage. The model simulation at different conditions showed that θ_H values lie in the range of 0.2 to 0.35 and θ_{CO} values lie in the range of 0.05 to 0.24. For the reported study, all activation energies are calculated using $\theta_H = 0.35$

and θ_{CO} = 0.24. θ_H and θ_{CO} values in above defined range results in an activation energy change less than 5 Kcal/mol, which is inherent in the semi-empirical method used.

2. For the reactions for methane SR, POX and WGS, the pre-exponential factors, sticking coefficient, bond index and temperature exponent are obtained from Maestri *et al.* [45]. The bond-index for $CO_2* + H* \rightarrow CO* + OH*$ was changed back to 0.5 (instead of 0.7) and its pre-exponential factor was multiplied by factor 3 (which is within the uncertainty for pre-exponential factor) for better fit to the experimental data.
3. Oxygenates (formaldehyde and methanol) decomposition activation energy is calculated using UBI-QEP method and pre-exponential factor, sticking coefficient, bond index and temperature exponent are obtained from Mhadeshwar and Vlachos [44].
4. C_2 and C_3 species adsorption sticking coefficient was initially set to 0.5 and desorption pre-exponential factor was set to 10^{13} 1/s. Ethylene and propylene adsorption parameters (*i.e.*, sticking coefficient) was later adjusted based on sensitivity analysis (not shown) to get a better fit to the experimental data. A similar approach is reported by Deutschmann and co-workers [54] for ethane partial oxidation on Pt catalyst in which they adjusted the sticking coefficient parameters to fit the experimental data.
5. Ethane and propane dissociative adsorption pre-exponential factor was initially set same as that of methane dissociative adsorption. It was later reduced based on sensitivity analysis (not shown) to fit the experimental data.
6. All C_2 and C_3 species dehydrogenation and fragmentation activation energy is obtained by UBI-QEP method with bond index of 0.5. Pre-exponential factor for forward reaction was set to 10^{11} 1/s. Reverse reaction pre-exponential factor was calculated by using the entropic consistency approach as described by Mhadeshwar *et al.* [43]

7. Adsorption sticking coefficient for all alkenes (> C_3) was set in the range of 10^{-6} to 10^{-7}. Pre-exponential factor for alkenes dissociation into ethylene and subsequent alkenes was set to 10^{11} 1/s. From experimental study, at high temperature all carbon was observed in the gas-phase indicating the majority of smaller hydrocarbons are reformed or fragmented on Rhodium catalyst. Hence, the activation every for alkenes decomposition was set to 15 kcal/mol, which is approximately equal to the alkane dissociation into CH_3 and CH_2 species as given by Deutschmann and co-workers [23].
8. Rate parameters for ketones fragmentation into CHx and acetyl species, Dienes fragmentation into CHx, and furans, alcohols and aldehydes (except formaldehyde) fragmentation into C, H and O species were set equal to the ones given by Deutschmann and co-workers [23] for overall dissociation of alkanes into CHx species. The rate parameters were later tuned to fit the experimental data based on the analysis of composition profiles at different temperatures.
9. Pre-exponential factor, temperature exponent, bond index and sticking coefficient for acetyl species reaction is obtained from Koehle and Mhadeshwar [47]. The activation energy is calculated using UBI-QEP method.
10. For ketene fragmentation on Rh, activation energy was calculated using UBI-QEP method and sticking coefficient and desorption rate constant were set equal to those for acetyl reaction. The forward reaction rate parameter was set equal to 10^{11} 1/s. Reverse reaction pre-exponential factor was calculated by using the entropic consistency approach as described by Mhadeshwar *et al.* [43]
11. As discussed in section 3, all oxygen is consumed before the catalyst and endothermic steam reforming of smaller hydrocarbons is dominant on the surface of the catalyst. Since heat is

continuously supplied to furnace to maintain central bed temperature, the temperature profile obtained by the gas-phase reaction modeling study is used to simulate the surface kinetics.

12. It is assumed that no mass transfer limitations exist. This is supported by the experimental study (discussed in Chapter 5 [33]) showing no mass transfer limitations.
13. The active metal specific surface area (0.7380 m^2/gm of catalyst) was obtained from Chemisorption study. This leads to Rh specific surface 465 cm^2/cm^3. Maestri *et al.* [45], have shown that the Rh specific surface has major impact on model predictions as it is a multiplicative factor of the pre-exponentials.

5. Results and Discussion

As discussed in section 4.4, it should be noted here that few of the kinetic model parameters are tuned or refined based on sensitivity analysis to fit the experimental data at different temperatures and at a fixed space velocity (WHSV = 100,000 SCC/h·g), O_2/C ratio (O_2/C = 0.2), and S/C ratio (S/C =1. 5). No optimization or parameter estimation tool was employed for tuning the rate parameters. Rather, based on sensitivity analysis the kinetic rate parameters were changed until the best fit was obtained at all three temperatures. Also it should be noted here that the parameters for lower hydrocarbon chemistry, which is very important for the major product formation (discussed later), were not adjusted except for the reaction $CO_2^* + H^* \rightarrow CO^* + OH^*$ as discussed in section 4.4. The refined kinetic model was later used as it is to validate it against the experimental data at different space velocities and O_2/C ratios. The Chemkin reactor model as shown in Figure 7.3 simulates the gas-phase reactions in section one, two and five, whereas both gas-phase and surface reactions are simulated in section three and four. The predicted composition for the base case (*i.e.*, T_{bed}= 973.15 K, WHSV = 100,000 SCC/h·g, and S/C = 1.5, and O_2/C = 0.2, P = 2.36 atm) is verified with experimental data as shown in Table 7.3. The model could predict the major products, such as , CO and CO_2, as well as minor products, such as hydrocarbons from C_1 to C_6 reasonably well (*i.e.*, within +/- 20%).

Table 7.3: Comparison of predicted and experimental product yield from ATR of n-tetradecane: T_{bed}= 973.15 K, WHSV = 100,000 SCC/h·g, and S/C = 1.5, and O_2/C = 0.2, P = 2.36 atm

	Experiment (%)	**Model (%)**
Hydrogen	51.09	51.80
Carbon Monoxide	39.07	39.64
Carbon Dioxide	28.81	28.98
Methane (CH_4)	3.51	3.44
Ethane (C_2H_6)	1.09	0.95
Ethylene (C_2H_4)	3.97	4.52
Propane (C_3H_8)	0.16	0.22
Propylene (C_3H_6)	2.98	1.56
1-Butene (C_4H_8)	0.97	1.16
1,3 Butadiene(C_4H_6)	1.23	1.45
1-Pentene (C_5H_{10})	0.39	0.36
1-Hexene (C_6H_{12})	0.26	0.21

5.1. Analysis of kinetic model at different operating conditions

All major products yield is compared to modeled results at different operating conditions as shown in Figures 7.5, 7.7, and 7.9. In Figure 7.5, the model is capturing trends for major species and predicts their composition very well at different temperatures and fixed O_2/C = 0.2, S/C = 1.5 and WHSV = 100,000 SCC/h·g. High temperature leads to more H_2 and CO production due to more catalytic steam reforming of hydrocarbons that are produced by gas-phase reactions *i.e.* higher conversion. The model is able to predict the conversion within the experimental error limit as shown in Figure 7.6. Experimental data show that H_2 and CO yield increases with an increase in the O_2/C ratio from 0.2 to 0.35 but decreases with a further increase in O_2/C ratio from 0.35 to 0.5 (Figure 7.7). This is attributed to the increase and then decrease in conversion with increase in O_2/C as shown in Figure 7.8. The model predicts decrease in H_2 and CO yield (Figure 7.7) and decrease in conversion (Figure 7.8) with increase in O_2/C ratio. The model slightly under-predicts the H_2 and CO yield at high O_2/C ratio. This could be attributed to many factors such as uncertainty in model parameters, approximate heavy molecules surface chemistry, error associated with gas-phase chemistry for heavy hydrocarbons, and changes in dispersion of the catalyst. The model could predict the methane, ethylene, and CO_2 yield very well (Figure 7.7). At a high space velocity the model slightly over-predicts the H_2, CO and CO_2 yield (Figure 7.9). At a high space velocity more hydrocarbons slip through the catalyst surface resulting in low conversion. Since the model has approximate heavy molecules surface chemistry, it predicts little high conversion at high space velocity (Figure 7.10), which ultimately results in higher yields of major products. Figure 7.11 (a) and (b) shows parity plots for ethylene and all products yield respectively. The model is able to predict the ethylene yield (which is a pre-cursor to carbon formation) and all other products yields very well within 20% of the experimental yield with few outliers.

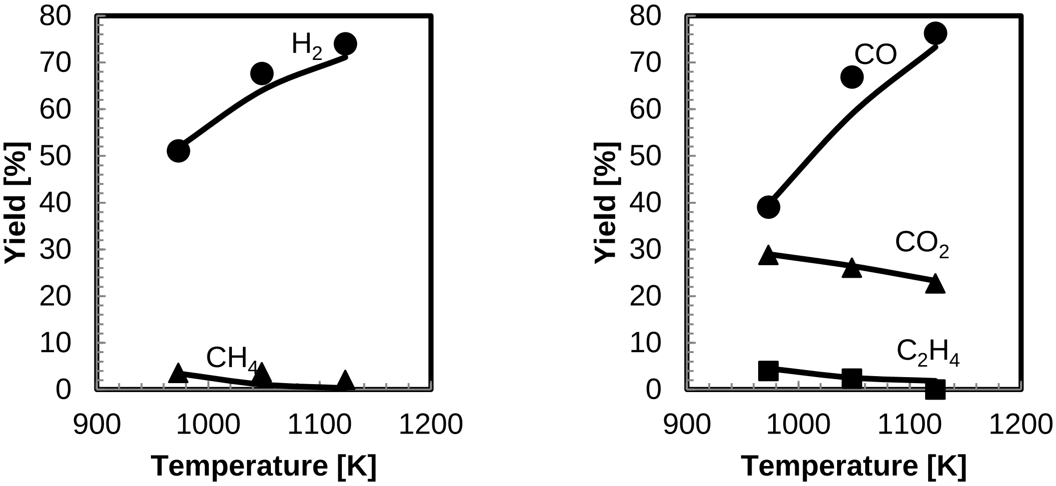

Figure 7.5: Comparison of experimental (symbol) and simulated (line) product composition from ATR at different bed temperatures, S/C = 1.5, O_2/C = 0.2, WHSV = 100,000 SCC/h·g.

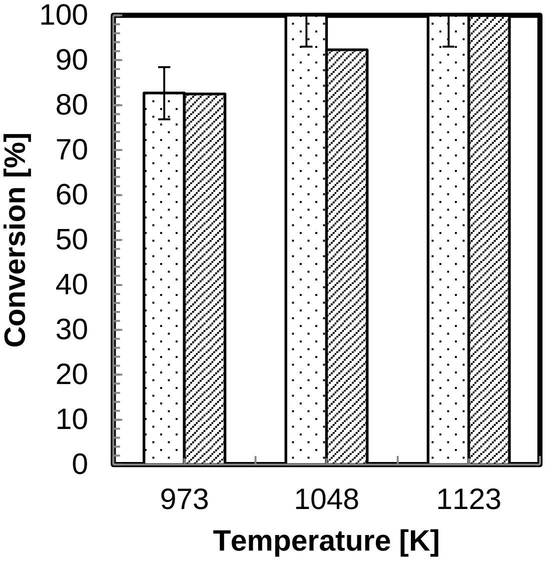

Figure 7.6: Comparison of experimental (dots) and simulated (lines) conversion from ATR at different bed temperatures, S/C = 1.5, O_2/C = 0.2, WHSV = 100,000 SCC/h·g. Error bars are +/- 7% error observed in carbon balance.

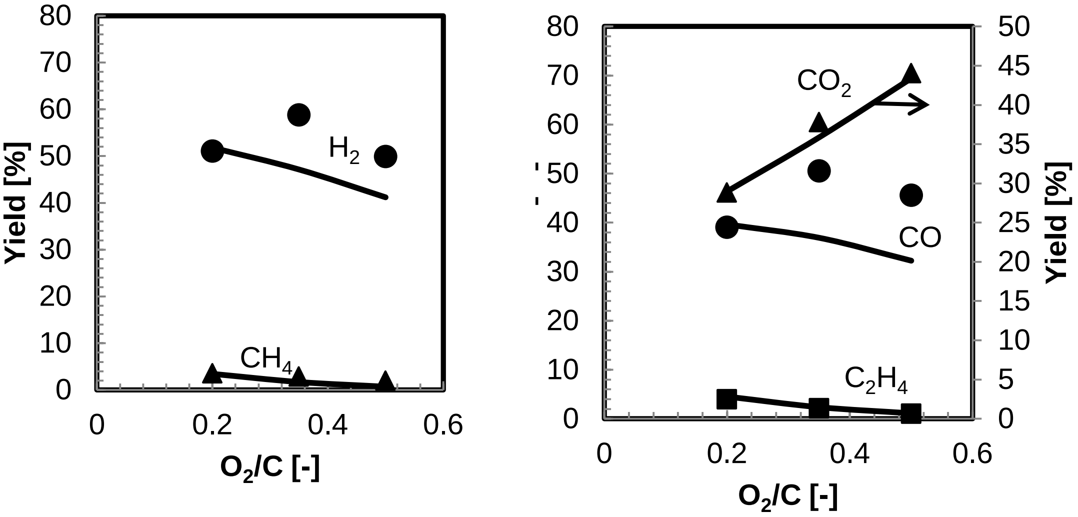

Figure 7.7: Comparison of experimental (symbol) and simulated (line) product composition profile at different O_2/C ratios, S/C = 1.5, WHSV = 100,000 SCC/h·g, T_{bed} = 973.15 K.

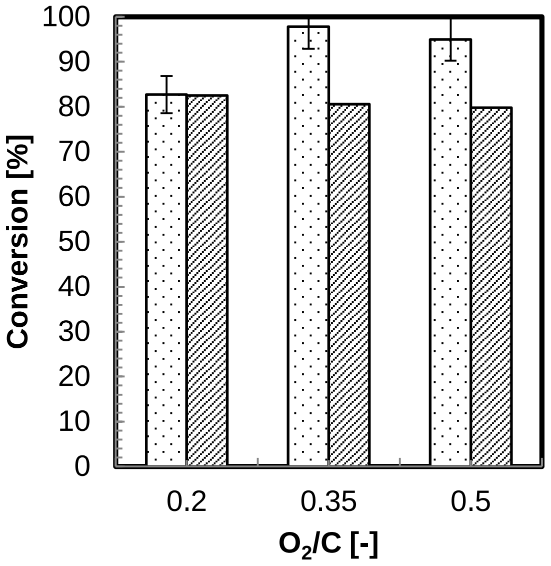

Figure 7.8: Comparison of experimental (dots) and simulated (lines) conversion at different O_2/C ratios, S/C = 1.5, WHSV = 100,000 SCC/h·g, T_{bed} = 973.15 K. Error bars are +/- 7% error observed in carbon balance.

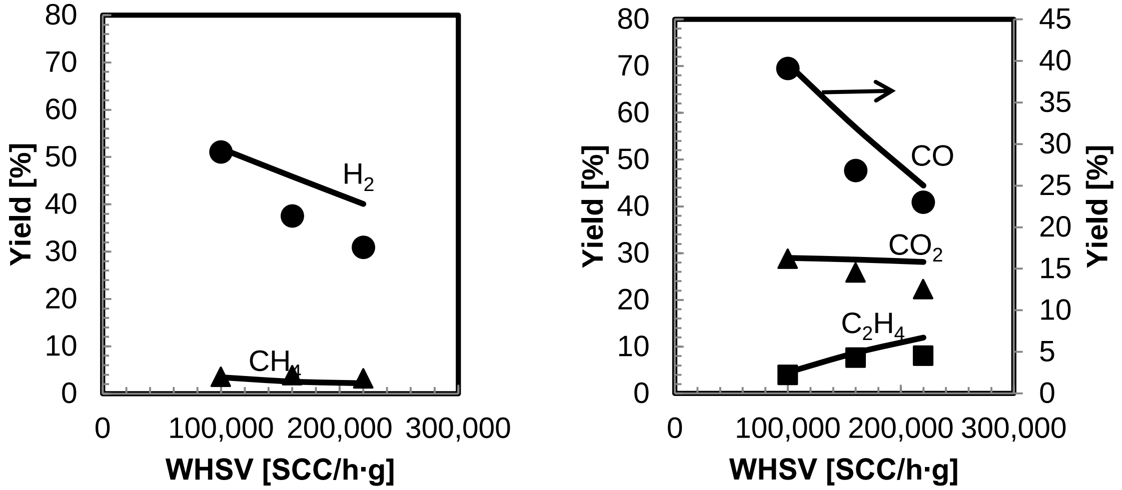

Figure 7.9: Comparison of experimental (symbol) and simulated (line) product composition from ATR at different space velocities, S/C = 1.5, O_2/C = 0.2, T_{bed} = 973.15 K.

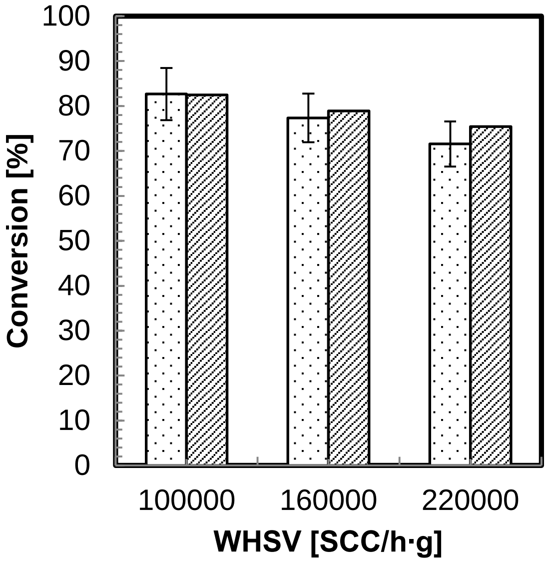

Figure 7.10: Comparison of experimental (dots) and simulated (lines) conversion at different space velocities, S/C = 1.5, O_2/C = 0.2, T_{bed} = 973.15 K. Error bars are +/- 7% error observed in carbon balance.

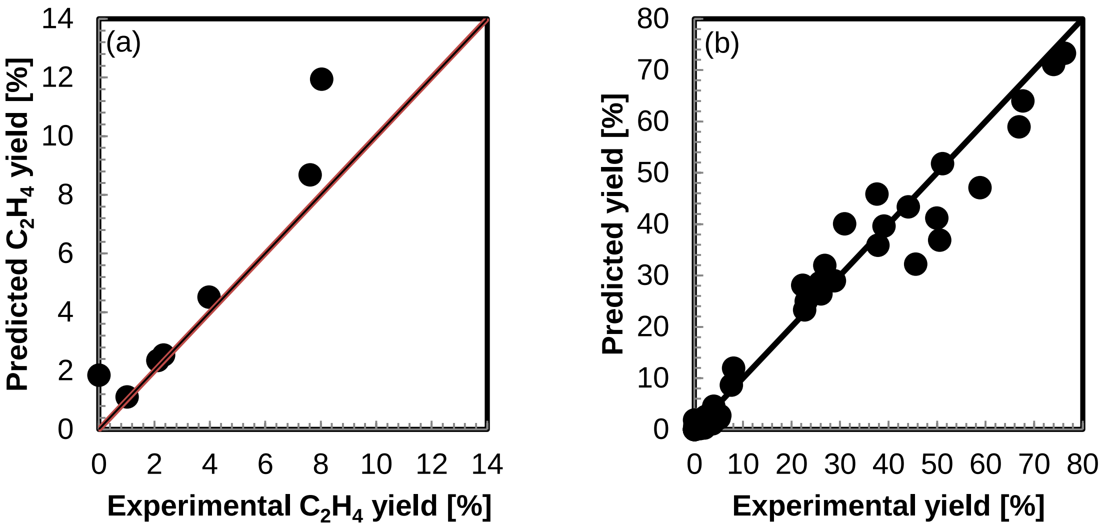

Figure 7.11: Parity plot for (a) ethylene and (b) all other product species.

5.2. Reaction pathways

Since the model is able to predict the outlet composition reasonably well, it becomes a useful tool to evaluate and understand what is happening along the length of the reactor. So it is essential to know major reaction paths from reactants to products inside the reactor. Based on sensitivity analysis (SA) and rate of production analysis (ROP) at different operating conditions, the reaction path for alkanes and alkenes is shown in Figure 7.12. It should be noted here that the methane reforming mechanism is similar to those initially proposed by Mhadeshwar and Vlachos [44], and later on optimized by Maestri *et al.* [45] Hence the model captures the small molecules chemistry (*i.e.*, CH_4 chemistry) exactly the same described by Maestri *et al.* [39]. Methane adsorbs dissociatively on the surface of the catalyst, and dehydrogenates to C* ($CH_4 \leftrightarrows CH_3^* \leftrightarrows CH_2^* \leftrightarrows CH^* \leftrightarrows C^*$). A H_2O molecule on the surface of the catalyst dissociates into OH* which then oxidizes C* to CO*. Part of the CO* is desorbed and other part is oxidized to CO_2* directly by OH* and considerably at slower rate by COOH* route (CO* + OH* $\leftrightarrows$ COOH* $\leftrightarrows$ CO_2* + H*). It is found that the methane reforming mechanism is the backbone for higher hydrocarbons reforming as all hydrocarbons ultimately dissociates into the CH_x* surface species. Ethane and propane dissociatively adsorb on the surface of the catalyst forming C_2H_5* surface C_3H_7* species respectively. Major reaction path for both adsorbed alkyl species is dehydrogenation to respective adsorbed alkene species. Also the gas-phase alkenes are adsorbed on the catalyst surface as a dicoordinated mode. C_2H_4** then fragments into CH_2* adsorbed species and C_3H_7** fragments into CH_2* and CH_3CH**, which ultimately dissociates to CH_3* and CH* adsorbed species. C_2H_4** also undergoes hydrogenation to form C_2H_5* which subsequently decomposes to CH_3* and CH_2*. All adsorbed higher alkenes (> C_3**) are assumed to fragment into adsorbed C_2H_4** and adsorbed small alkene** species. ROP analysis showed oxygenates (methanol and formaldehyde) decomposition path same as those proposed by Mhadeshwar and Vlachos [44] (CH_3OH $\leftrightarrows$ CH_3OH* $\leftrightarrows$ CH_2OH* $\leftrightarrows$ CH_2O* $\leftrightarrows$ HCO* $\leftrightarrows$ CO* $\leftrightarrows$ CO).

5.2. Simulation of ATR in a packed bed reactor

Composition of major species profiles and temperature profiles along the length of the reactor at a catalyst bed temperature 973 K, WHSV 100,000 SCC/h·g, O_2/C 0.2, and S/C = 1.5 is shown in Figure 7.13. As discussed in Chapter 6 [1], two stage gas-phase oxidation is observed before the catalyst that consume all the n-tetradecane, oxygen, and generate water before the catalyst ($x < 0.16$ m). Also the major amount of ethylene is found to be generated by gas-phase reactions in the mixing zone ($x < 0.16$ m) particularly during the second oxidation stage. Detailed

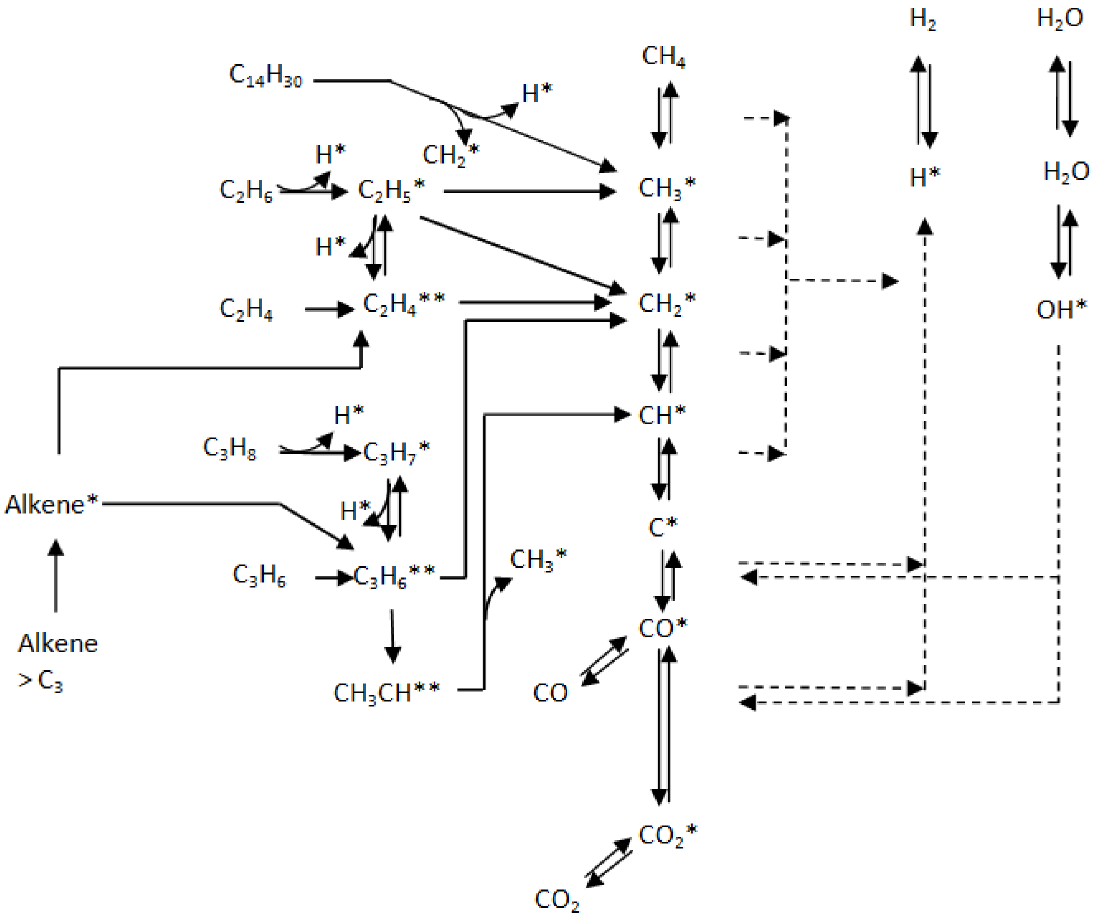

Figure 7.12: Reaction path for alkanes and alkenes reforming at different operating conditions.

discussion on gas-phase reactions is given in Chapter 6 [1]. As soon as the gas-phase species reach the catalyst surface, a sharp decline in CO and H_2O molar flow and jump in CO_2 and H_2 molar flow is observed. This is due to very high water-gas-shift activity of the catalyst. This can also be observed by a sharp increase OH* site fraction as shown in Figure 7.16(a). As soon as steam reforming of other hydrocarbons start, the CO and H_2 concentration again starts to build-

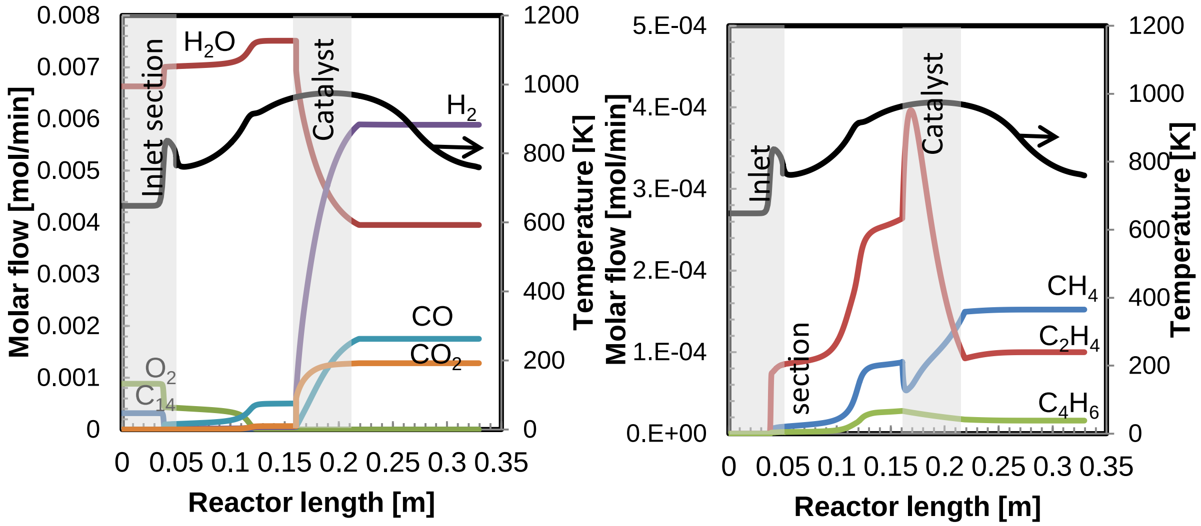

Figure 7.13: Simulated composition profile for major species at S/C = 1.5, O_2/C = 0.2, T_{bed} = 973 K, and WHSV = 100,000 SCC/h·g.

up. The maximum number of surface sites are occupied by H* and CO* adspecies along the length of the reactor (Figure 7.16(a)), which is same as those reported for methane steam reforming at 873 K by Maestri *et al.*[39]. Methane generated by gas-phase reactions before the catalyst, is consumed initially on the surface of the catalyst but later it is generated on the surface of the catalyst. Also at the inlet of the catalyst zone, increase in ethylene is found due to adsorption of all alkene species and subsequent fragmentation of it though ethylene consumption route (Figure 7.12). At low temperature, increased ethylene consumed through two competitive channels. The first channel is fragmentation of C_2H_4** to CH_2* ($C_2H_4^{**} \leftrightarrows CH_2^{*} + CH_2^{*}$) and the other channel is formation of CH_3* and CH_2* on the surface of the catalyst through $C_2H_4^{**} + H^{*} \leftrightarrow C_2H_5^{*} \leftrightarrows CH_3^{*} + CH_2^{*}$ route. Also at low temperature (973 K) the reaction rate for CH_3*

+ H* ⇆ CH_4 + 2* (k = 1.32E+19 cm^2/mol·s) and CH_3* + * ⇆ CH_2* + H* (k = 1.88E+19 cm^2/mol·s) are very close leading to formation of methane. These reactions rates are compared with rates reported by Deutschmann and coworkers [29]. It is observed that current reaction rates are a factor of 1.95 higher than those reported by Deutschmann and coworkers (k = 6.74E+18 cm^2/mol·s for CH_3* + H* ⇆ CH_4 + 2* and k = 1.10E+19 cm^2/mol·s for CH_3* + * ⇆ CH_2* + H*), which is within the uncertainty limit. 1,3 butadiene (C_4H_6) produced by gas-phase reactions in the pre-catalytic zone is slowly consumed on the catalyst. However, in the post-catalytic zone, gas-phase reactions lead to ethylene formation from 1,3 butadiene. This reaction is significant only at high temperatures as discussed later.

The species profiles at high temperature and other all similar conditions discussed above are shown in Figure 7.14. At the inlet of the catalyst (x = 0.16 m), high water-gas-shift activity leads to sharp decrease in CO and H_2O concentration and increase in H_2 and CO_2 concentration. After some distance along the catalyst zone CO_2 slowly decreases. This is due to reverse water-gas-shift activity of the catalyst. It can be explained by the plot of Φw along the length of the reactor (Figure 7.15). The Φ_w parameter represents the product composition relative to WGS equilibrium (K_w):

$$\Phi w = \left(\frac{p_{CO_2} p_{H_2}}{p_{CO} p_{H_2O}} \right) \frac{1}{K_w} \;\; ; \;\; K_w = \exp\left(-4.33 + \frac{4577.8}{T(K)} \right) \qquad (7)$$

Figure 7.15 shows that the reactant mixture entering the catalyst zone is far from the WGS equilibrium. As soon as it enters the catalyst zone, the high activity of the catalyst and driving

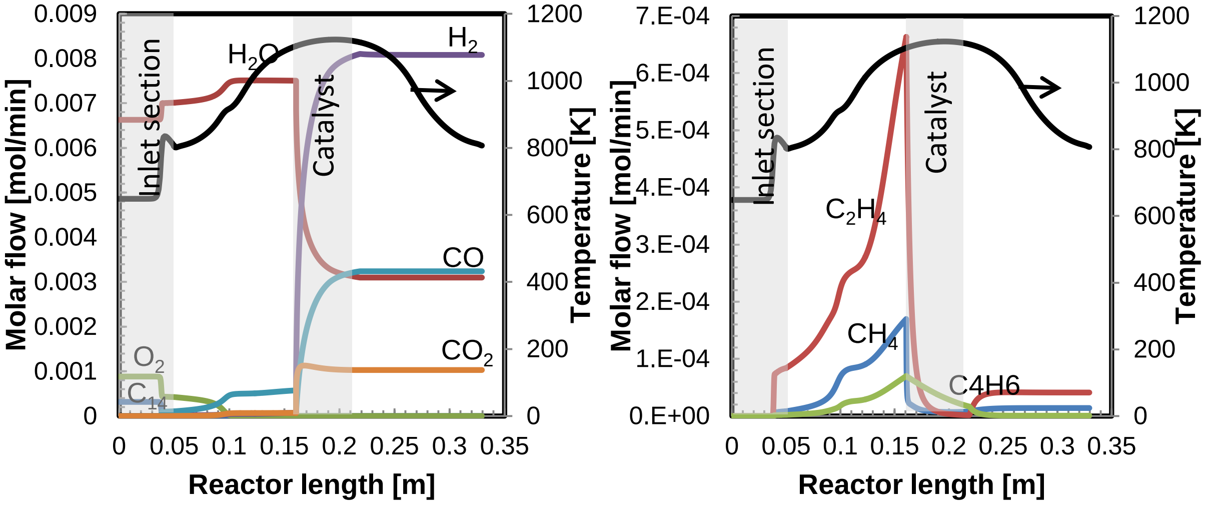

Figure 7.14: Simulated composition profile for major species at S/C = 1.5, O_2/C = 0.2, T_{bed} = 1123 K, and WHSV = 100,000 SCC/h·g.

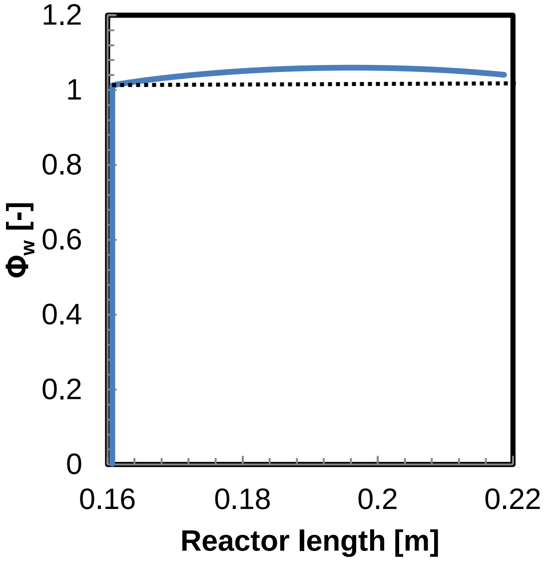

Figure 7.15: Φ_w along the length of reactor catalyst zone at S/C = 1.5, O_2/C = 0.2, T_{bed} = 1123 K, and WHSV = 100,000 SCC/h·g.

force to reach to equilibrium, leads to a sudden consumption of CO and H_2O to form H_2 and CO_2. This also leads to OH* peak at the inlet of the catalyst zone as shown in Figure 7.16(b). However within one mm distance it reaches equilibrium composition and further along the length of the catalyst Φ_w is slightly greater than one indicating reverse-WGS.

At high temperature, no ethylene build up was observed at the inlet of the catalyst due to the fast rate of hydrogenation and decomposition of C_2H_4** to C_2H_5* and $2CH_2$* respectively. However at high temperature the reaction rate for $CH_3^* + H^* \leftrightarrows CH_4 + 2^*$ (k = 1.18E+19 cm^2/mol·s) is four times slower than $CH_3^* + {}^* \leftrightarrows CH_2^* + H^*$ (k = 4.54E+19 cm^2/mol·s). That leads to consumption of methane at high temperature. 1,3 butadiene is consumed on the surface of the catalyst, but the small amount of 1,3-butadiene which slips through the catalyst bed is completely consumed by gas-phase reactions in the post-catalytic zone. Also, ethylene is formed after the catalyst zone due to gas-phase reactions. At high temperature, the major species on the surface of the catalyst is H* (Figure 7.16(b)). An increase in the O_2/C ratio at fixed T_{bed} of 973K, results in a similar profile behavior along the length of the reactor (not shown here) and no remarkable change in adspecies profile is noted (Figure 7.16(c)).

Coke formation in the post-catalytic zone is a major concern [31] due to high temperatures and hydrocarbon slip through the catalyst bed. In the current study, it is identified that at high temperature ethylene, which is a precursor to carbon formation, is formed by gas-phase reactions in the post-catalytic zone ($x > 0.22$ m). To identify the probable reaction pathways leading to ethylene formation SA and ROP of ethylene is performed. Figure 7.17 shows most sensitive reactions for ethylene formation and Figure 7.18 shows the major reactions for ethylene formation. Figure 7.14 shows that 1,3 butadiene (C_4H_6) is consumed by gas-phase reactions after

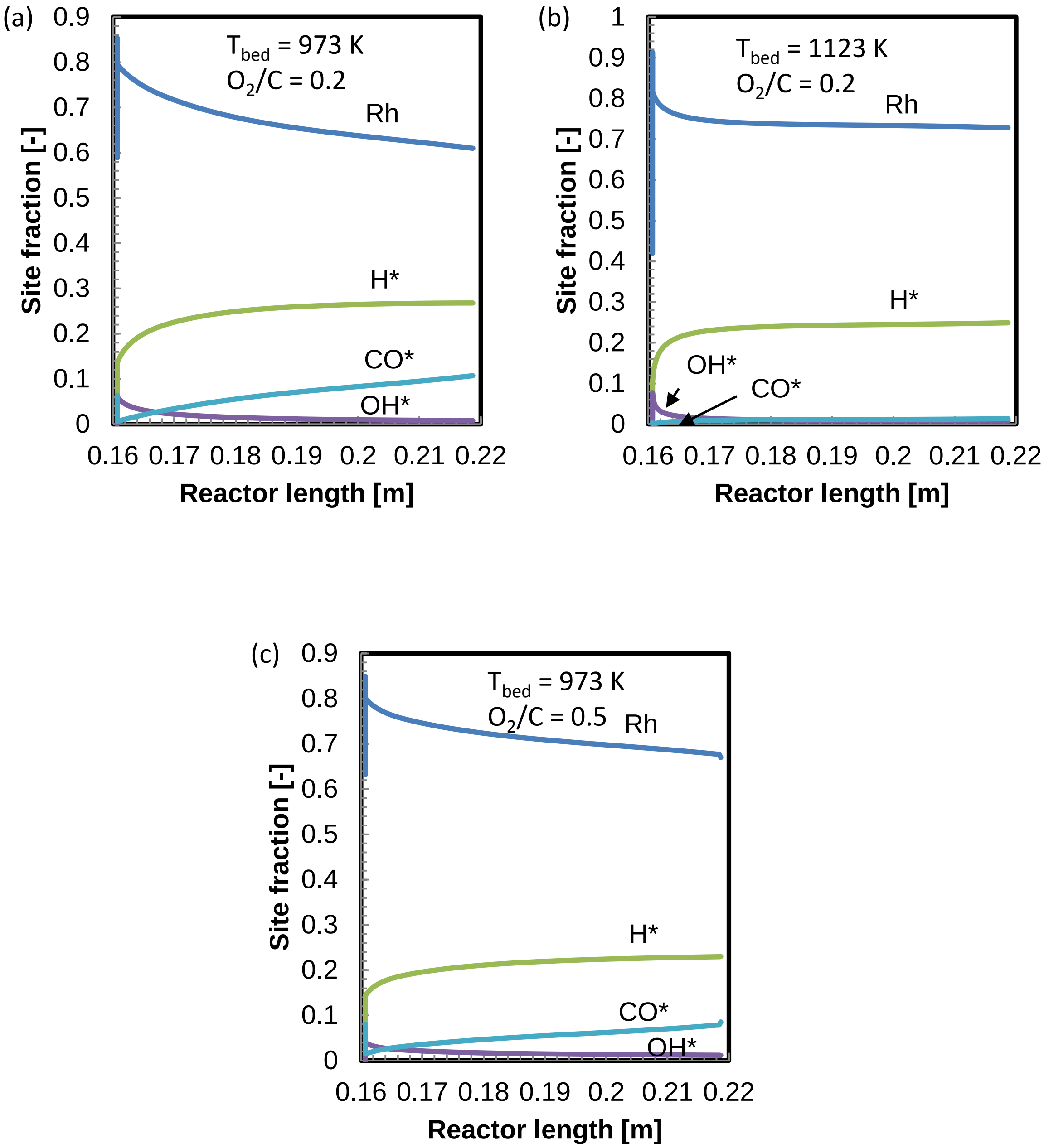

Figure 7.16: Major surface species at different temperatures and O_2/C ratios at fixed S/C = 1.5 and WHSV = 100,000 SCC/h·g.

the catalyst zone. From this analysis, the major reaction path for the formation of ethylene from 1,3-butadiene is identified as shown in Figure 7.19. So if 1,3-butadiene formed by gas-phase reactions before the catalyst zone is not consumed by surface reactions or it slips through the catalyst surface, then chain reaction sequence as shown in Figure 7.19 results in butadiene consumption and ethylene formation at high temperature. It should be noted that this reaction path also consumes small amount of hydrogen.

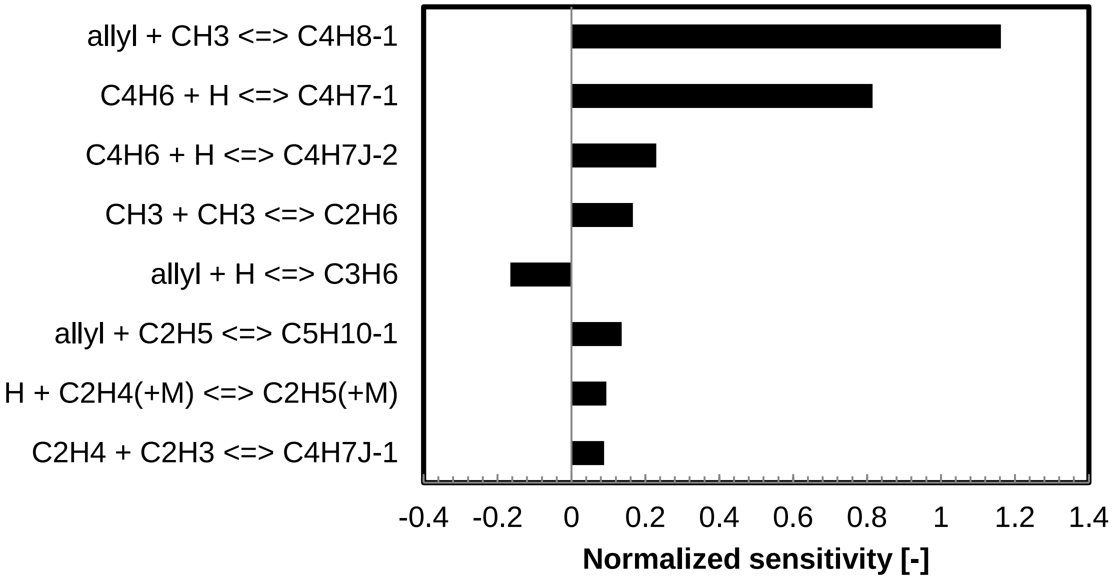

Figure 7.17: Sensitivity analysis of ethylene in fifth section of the reactor at S/C = 1.5, O_2/C = 0.2, T_{bed} = 1123 K, and WHSV = 100,000 SCC/h·g. Note: <=> is a symbol used in Chemkin^{TM} to represent a reversible reaction.

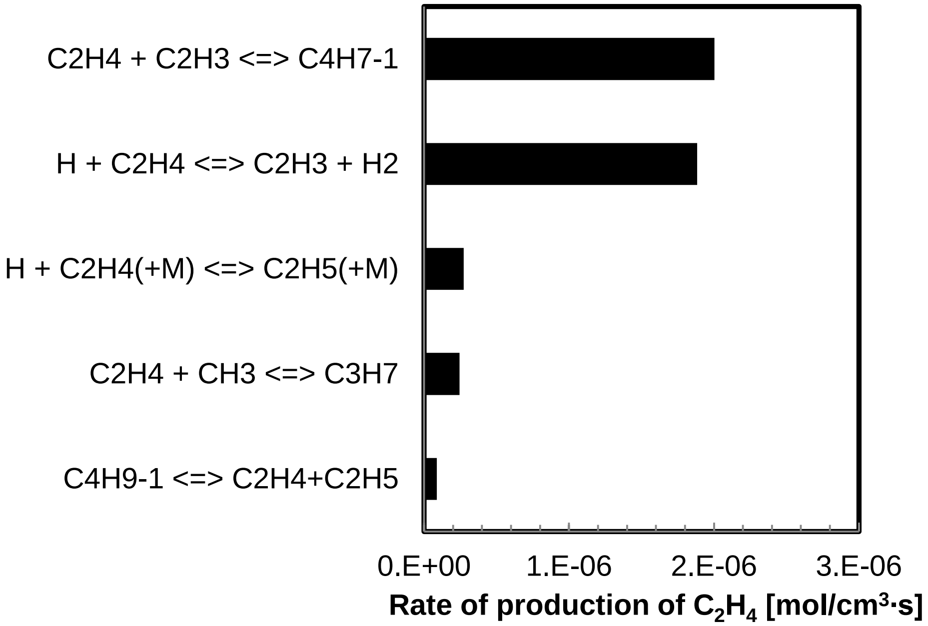

Figure 7.18: Rate of production (ROP) analysis of ethylene in fifth section of the reactor at S/C = 1.5, O_2/C = 0.2, T_{bed} = 1123 K, and WHSV = 100,000 SCC/h·g. Note: <=> is a symbol used in Chemkin™ to represent a reversible reaction.

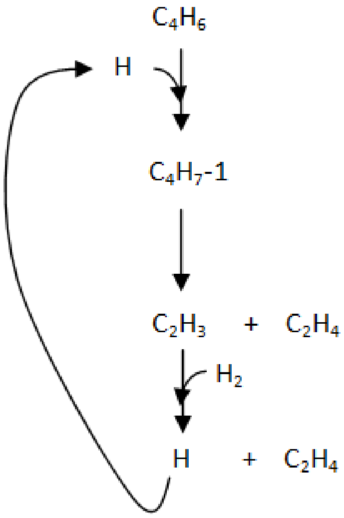

Figure 7.19: Major reaction path for formation of ethylene from 1,3, butadiene by gas-phase reactions.

6. Conclusions

A micro-kinetic model for catalytic reforming of n-tetradecane is reported. Unlike the majority of models that do not consider any reactions occurring in the pre-catalytic zone, this study considered the gas-phase reactions in the pre-catalytic zone to identify the prominent species entering the catalyst bed. From the elementary reactions based gas-phase kinetic model, it was determined that all of the n-tetradecane and oxygen is consumed before the reacting mixture reaches the catalyst surface. Based on simulation of the reactor using gas-phase kinetic model, the species reaching the catalyst surface were identified. A micro-kinetic model was developed that includes alkane species up to C_3, oxygenates, acetyl and ketene. Alkenes above C_3 species were assumed to fragment into ethylene and other alkenes, and all remaining species were assumed to fragment into CH_x*, C*, H*,and O* species on the surface of the catalyst. The model was developed using a hybrid approach in which the binding energy or heat of chemisorption of most of the adsorbed species was obtained from literature reported values (either from DFT study or from experimental study) and the energetic (activation energy) was obtained using semi-empirical techniques, such as unity bond index-quadratic exponential potential (UBI-QEP). Pre-exponential factors were set based on Transition State Theory (TST) rule.

Simulations of both homogeneous gas-phase reactions and surface reactions predict the outlet composition reasonably well (within 20% of the experimental yield) at different temperatures, O_2/C ratios, WHSV and constant S/C ratio. The model also captures the conversion of hydrocarbon very well except for the high O_2/C ratio. The study identifies the major paths for C_2 and C_3 reactions on the surface of the rhodium catalyst. Model simulations suggest that the CO generated by gas-phase reactions before the catalyst is consumed by water-gas-shift (WGS) reaction within first millimeter of the catalyst due to high WGS activity. Later, the H_2 and CO are produced by steam reforming of other hydrocarbons on the surface of the catalyst. Since it was assumed that all alkenes are fragmented into ethylene before it further breaks down, ethylene is found to generate initially due to surface reactions at low temperature. To validate such behavior a detailed kinetic model for higher alkenes is required with all experimental species composition measurements along the length of the catalyst. The model simulations also suggest that slippage of 1,3-butadiene through the catalyst could lead to cyclic reactions at high temperature that consume 1,3-butadiene and form ethylene in the post-catalytic zone of the reactor. This can eventually lead to coke formation.

Although the model predictions are good (within 20% of the experimental measurement) at different operating conditions, detailed surface chemistry for large alkenes ($> C_3$), dienes, aldehydes, alcohols and furans is required to understand the interaction of surface and gas-phase reactions along the length of the reactor. Despite the assumptions and limitations of the overall micro-kinetic modeling approach, the suggested mechanism provides a starting point to gain fundamental understanding of different component reforming kinetics, with which detailed reactor and catalyst design can be carried out. The overall gas-phase and surface kinetic model can also be useful to evaluate the effect of gas-phase reactions after the catalyst surface.

References

[1] R.D. Parmar, A. Jalan, D. Shekhawat, W.H. Green, K. Karan, B.A. Peppley, Development of a mechanistic model for gas-phase reactions occuring in autothermal reforming of diesel surrogate (n-tetradecane), Manuscript included as Chapter-6, (2013).

[2] T.M. Weis, A. Ilinca, J.P. Pinard, Stakeholders' perspectives on barriers to remote wind–diesel power plants in Canada, Energy Policy, 36 (2008) 1611-1621.

[3] C.J. Brodrick, T.E. Lipman, M. Farshchi, N.P. Lutsey, H.A. Dwyer, D. Sperling, S.W. Gouse, D.B. Harris, F.G. King, Evaluation of fuel cell auxiliary power units for heavy-duty diesel trucks, Transportation Research Part D: Transport and Environment, 7 (2002) 303-315.

[4] S. Jain, H.Y. Chen, J. Schwank, Techno-economic analysis of fuel cell auxiliary power units as alternative to idling, Journal of Power Sources, 160 (2006) 474-484.

[5] T. Phillips, J. Mulhall, G. Turner, The kinetics and mechanism of the reaction between steam and hydrocarbons over nickel catalysts in the temperature range 350–500° C, part 1, Journal of Catalysis, 15 (1969) 233-244.

[6] K. Sjostrom, Steam Reforming of n-Heptane at Low Concentration for Hydrogen Injection into Internal Combustion Engines, Industrial & Engineering Chemistry Process Design and Development, 19 (1980) 148-153.

[7] D. Shekhawat, D.A. Berry, T.H. Gardner, J.J. Spivey, Catalytic reforming of liquid hydrocarbon fuels for fuel cell applications, Catalysis, 19 (2006) 184-254.

[8] A.B. Shigarov, V.V. Kireenkov, V.A. Kuzmin, N.A. Kuzin, V.A. Kirillov, Autothermal reforming of diesel fuel in a structured porous metal catalyst: Both kinetically and transport controlled reaction, Catalysis Today, 144 (2009) 341-349.

[9] D. Creaser, X. Karatzas, B. Lundberg, L.J. Pettersson, J. Dawody, Modeling study of 5 kWe-scale autothermal diesel fuel reformer, Applied Catalysis A: General, 404 (2011) 129-140.

[10] F. Gökaliler, Z.I. Önsan, A.E. Aksoylu, Power-law type rate equation for propane ATR over Pt–Ni/Al2O3 catalyst, International Journal of Hydrogen Energy, 37 (2012) 10425-10429.

[11] M. Pacheco, J. Sira, J. Kopasz, Reaction kinetics and reactor modeling for fuel processing of liquid hydrocarbons to produce hydrogen: isooctane reforming, Applied Catalysis A: General, 250 (2003) 161-175.

[12] J.R. Lattner, M.P. Harold, Comparison of conventional and membrane reactor fuel processors for hydrocarbon-based PEM fuel cell systems, International Journal of Hydrogen Energy, 29 (2004) 393-417.

[13] L. Shi, D.J. Bayless, M.E. Prudich, A CFD model of autothermal reforming, International Journal of Hydrogen Energy, 34 (2009) 7666-7675.

[14] J.R. Rostrup-Nielsen, Activity of nickel catalysts for steam reforming of hydrocarbons, Journal of Catalysis, 31 (1973) 173-199.

[15] J.R. Rostrup-Nielsen, Catalytic steam reforming, Catalysis, Science and Technology, 5 (1984) 1-117.

[16] Z. Chen, Y. Yan, S.S.E.H. Elnashaie, Hydrogen production and carbon formation during the steam reformer of heptane in a novel circulating fluidized bed membrane reformer, Industrial & Engineering Chemistry Research, 43 (2004) 1323-1333.

[17] C.Y. Nah, S. Palanki, Analysis of heptane autothermal reformer to generate hydrogen for fuel cell applications, International Journal of Hydrogen Energy, 34 (2009) 8566-8573.

[18] H.H. Ibrahim, R.O. Idem, Kinetic studies of the partial oxidation of isooctane for hydrogen production over a nickel–alumina catalyst, Chemical Engineering Science, 61 (2006) 5912-5918.

[19] H.H. Ibrahim, R.O. Idem, Kinetic studies of the partial oxidation of gasoline (POXG) over a Ni-CeO_2 catalyst in a fixed-bed flow reactor, Chemical Engineering Science, 62 (2007) 6582-6594.

[20] M.F.A. Khan, A. Khan, H. Ibrahim, R. Idem, Kinetic Study of the Catalytic Partial Oxidation of Synthetic Diesel over 5 wt % Ni/$Ce_{0.5}Zr_{0.33}Ca_{0.085}Y_{0.085}O_{2-\delta}$ Catalyst for Hydrogen Production, Energy & Fuels, 26 (2012) 5421-5429.

[21] A.A.A. Praharso, D. Trimm, N. Cant, Kinetic study of iso-octane steam reforming over a nickel-based catalyst, Chemical Engineering Journal, 99 (2004) 131-136.

[22] H. Huang, Z. Wang, H. Liu, H. Sun, Y. Wei, X. Zhou, A kinetic model for analyzing partial oxidation reforming of heavy hydrocarbon over a novel self-sustained electrochemical promotion catalyst, International Journal of Hydrogen Energy, 37 (2012) 15125-15134.

[23] J. Thormann, L. Maier, P. Pfeifer, U. Kunz, O. Deutschmann, K. Schubert, Steam reforming of hexadecane over a Rh/CeO_2 catalyst in microchannels: Experimental and numerical investigation, International Journal of Hydrogen Energy, 34 (2009) 5108-5120.

[24] B.T. Schädel, M. Duisberg, O. Deutschmann, Steam reforming of methane, ethane, propane, butane, and natural gas over a rhodium-based catalyst, Catalysis Today, 142 (2009) 42-51.

[25] J.V. Rickenbach, M. Nabavi, I. Zinovik, N. Hotz, D. Poulikakos, A detailed surface reaction model for syngas production from butane over Rhodium catalyst, International Journal of Hydrogen Energy, 36 (2011) 12238-12248.

[26] D. Hickman, L. Schmidt, Steps in CH4 oxidation on Pt and Rh surfaces: High temperature reactor simulations, AIChE Journal, 39 (1993) 1164-1177.

[27] I. Kang, H.H. Carstensen, A.M. Dean, Impact of gas-phase reactions in the mixing region upstream of a diesel fuel autothermal reformer, Journal of Power Sources, 196 (2011) 2020-2026.

[28] C.K. Westbrook, W.J. Pitz, O. Herbinet, H.J. Curran, E.J. Silke, A comprehensive detailed chemical kinetic reaction mechanism for combustion of n-alkane hydrocarbons from n-octane to n-hexadecane, Combustion and Flame, 156 (2009) 181-199.

[29] M. Hartmann, L. Maier, H. Minh, O. Deutschmann, Catalytic partial oxidation of iso-octane over rhodium catalysts: An experimental, modeling, and simulation study, Combustion and Flame, 157 (2010) 1771-1782.

[30] L. Maier, M. Hartmann, S. Tischer, O. Deutschmann, Interaction of heterogeneous and homogeneous kinetics with mass and heat transfer in catalytic reforming of logistic fuels, Combustion and Flame, 158 (2011) 796-808.

[31] T. Kaltschmitt, L. Maier, M. Hartmann, C. Hauck, O. Deutschmann, Influence of gas-phase reactions on catalytic reforming of isooctane, Proceedings of the Combustion Institute, 33 (2011) 3177-3183.

[32] D. Shekhawat, T.H. Gardner, D.A. Berry, M. Salazar, D.J. Haynes, J.J. Spivey, Catalytic partial oxidation of n-tetradecane in the presence of sulfur or polynuclear aromatics: Effects of support and metal, Applied Catalysis A: General, 311 (2006) 8-16.

[33] R.D. Parmar, D. Shekhawat, B.A. Peppley, K. Karan, Stable diesel or heavy hydrocarbon reforming catalyst: properties and performance, Manuscript included as Chapter-5, (2013).

[34] D. Shekhawat, J.J. Spivey, D. Berry, Fuel Cells: Technologies for Fuel Processing, Elsevier Science, Oxford, 2011.

[35] G.F. Froment, K.B. Bischoff, J. De Wilde, Chemical Reactor Analysis and Design, Wiley, New York, 1990.

[36] H.F. Rase, J.R. Holmes, Chemical Reactor Design for Process Plants, John Wiley & Sons, New York, 1977.

[37] J.A. Dumesic, D.F. Rudd, L.M. Aparicio, J.E. Rekoske, A.A. Treviño, The Microkinetics of Heterogeneous Catalysis, American Chemical Society Washington, DC, 1993.

[38] S. Raimondeau, D. Vlachos, Recent developments on multiscale, hierarchical modeling of chemical reactors, Chemical Engineering Journal, 90 (2002) 3-23.

[39] M. Maestri, D.G. Vlachos, A. Beretta, G. Groppi, E. Tronconi, Steam and dry reforming of methane on Rh: Microkinetic analysis and hierarchy of kinetic models, Journal of Catalysis, 259 (2008) 211-222.

[40] R. Van Santen, M. Neurock, Concepts in theoretical heterogeneous catalytic reactivity, Catalysis Reviews. Engineering and Science, 37 (1995) 557-698.

[41] E.W. Hansen, M. Neurock, First-principles-based Monte Carlo methodology applied to O/Rh (100), Surface Science, 464 (2000) 91-107.

[42] Z.P. Liu, P. Hu, General rules for predicting where a catalytic reaction should occur on metal surfaces: A density functional theory study of CH and CO bond breaking/making on flat, stepped, and kinked metal surfaces, Journal of the American Chemical Society, 125 (2003) 1958-1967.

[43] A. Mhadeshwar, H. Wang, D. Vlachos, Thermodynamic consistency in microkinetic development of surface reaction mechanisms, The Journal of Physical Chemistry B, 107 (2003) 12721-12733.

[44] A. Mhadeshwar, D. Vlachos, Hierarchical multiscale mechanism development for methane partial oxidation and reforming and for thermal decomposition of oxygenates on Rh, The Journal of Physical Chemistry B, 109 (2005) 16819-16835.

[45] M. Maestri, D.G. Vlachos, A. Beretta, G. Groppi, E. Tronconi, A C1 microkinetic model for methane conversion to syngas on Rh/Al2O3, AIChE Journal, 55 (2009) 993-1008.

[46] T. Bhattacharjee, Towards Understanding Catalytic processes for the Reactivity of Hydrocarbons on Rh Surface: A Quantum Chemical Study. Ph.D. Thesis, University of Heidelberg, 2011.

[47] M. Koehle, A. Mhadeshwar, Microkinetic modeling and analysis of ethanol partial oxidation and reforming reaction pathways on platinum at short contact times, Chemical Engineering Science, 78 (2012) 209-225.

[48] Y.M. Choi, P. Liu, Understanding of ethanol decomposition on Rh (111) from density functional theory and kinetic Monte Carlo simulations, Catalysis Today, 165 (2011) 64-70.

[49] M. Li, W. Guo, R. Jiang, L. Zhao, X. Lu, H. Zhu, D. Fu, H. Shan, Density functional study of ethanol decomposition on Rh (111), The Journal of Physical Chemistry C, 114 (2010) 21493-21503.

[50] R.D. Parmar, A. Kundu, C. Thurgood, B.A. Peppley, K. Karan, Kinetic studies of the autothermal reforming of tetradecane over Pt/Al_2O_3 catalyst in a fixed-bed reactor, Fuel, 89 (2010) 1212-1220.

[51] E. Shustorovich, The bond-order conservation approach to chemisorption and heterogeneous catalysis: applications and implications, Advances in Catalysis, 37 (1990) 101-163.

[52] E. Shustorovich, H. Sellers, The UBI-QEP method: a practical theoretical approach to understanding chemistry on transition metal surfaces, Surface Science Reports, 31 (1998) 1-119.

[53] A.V. Zeigarnik, R.E. Valdes-Perez, O.N. Myatkovskaya, CC Bond Scission in Ethane Hydrogenolysis, The Journal of Physical Chemistry B, 104 (2000) 10578-10587.

[54] D.K. Zerkle, M.D. Allendorf, M. Wolf, O. Deutschmann, Understanding homogeneous and heterogeneous contributions to the platinum-catalyzed partial oxidation of ethane in a short-contact-time reactor, Journal of Catalysis, 196 (2000) 18-39.

Chapter 8

Conclusion

In this thesis, a combined experimental and modeling study of the n-tetradecane autothermal reforming was undertaken. Brief summaries of scientific observations and major contributions are presented as well as recommendations for future work.

8.1 **Summary of Scientific Observations and Findings**

Detailed thermodynamic analysis using Gibb's energy minimization revealed that steam reforming (SR) of diesel is an energy intensive process that could lead to overall lower efficiency of the system. The partial oxidation (POX) process was shown to be only feasible above 1000 °C thus limiting this process because of material of construction issues and sealing issues. Autothermal reforming (ATR) is the best choice for diesel reforming as it can be carried out at lower temperatures than POX process and can have a significantly higher yield of hydrogen than POX process. However, it is not possible to run the ATR process at thermo-neutral point and also avoid being in an operating regime where carbon formation occurs. The carbon formation boundary map provides essential information on the range of operating conditions that thermodynamically favour carbon formation.

Based on a surface science study of alkane molecule adsorption and dissociation on the catalyst surface, a simple mechanistic scheme was proposed and a LHHW type of kinetic model was derived for n-tetradecane reforming. This model, however, was based on the major assumption that no gas-phase reactions occurring inside the reactor. Thermodynamically consistent and physically meaningful parameters were estimated using experimental data on Pt/Al_2O_3 catalyst. The proposed model represented the overall behavior of the process reasonably well. The relative error of the predicted flow rate of major species was always within 25% of the experimental value. The study, however, identified the need for a mechanistic understanding of gas-phase processes as well as need for a more detailed surface reaction study and drived the future path of the research.

Based on a literature study, experiments were conducted to synthesize and characterize Pt/CGO and Rh/pyrochlore catalyst. The Rh-pyrochlore catalyst was found to give stable performance than the Pt-CGO catalyst for commercial diesel reforming. One of the most significant experimental observations, previously unreported, is the structural change of the stable (Rh-pyrochlore) and un-stable (Pt-CGO) catalyst under redox environment which is found in practical reformer systems. The accessible Rh didn't change significantly in Rh-pyrochlore catalyst in TPR-TPO cycle (redox cycle) whereas the Pt peak was lost after TPO in Pt-CGO catalyst. This study shows that characterization of reforming catalyst using a redox cycle test for predicting the stability of the catalyst under real operating conditions. The kinetic experiments with only quartz sand showed < 100 ppm oxygen in the outlet with CO, CO_2, ethylene, propylene, and methane as the major yield of the product. This kinetic study thus confirmed that gas-phase reactions that are normally neglected in studying reforming of the higher hydrocarbons at temperatures above 700 °C are significant and need to be considered in the overall reaction mechanism of heavy hydrocarbon reforming.

A detailed gas-phase kinetic model under autothermal reforming conditions was generated using the Reaction Mechanism Generator^{TM} software package. Key reaction rates were refined using experimental and calculated values. The generated kinetic model was found to predict published experimental data on combustion regime reasonably well and better than commonly used LLNL model. To predict the high pressure pyrolysis experiments that favour formation of alkanes above C_3, the model was extended by adding H-abstraction, disproportionation, radical recombination, and β-scission reactions manually. The model predicts the non-catalytic ATR experiments very well at low temperature. At high temperature, reactor wall activity played a significant role to produce hydrogen by reforming reactions which is consistent with the existing literature. The present kinetic model gives a mechanistic understanding of gas-phase reactions dominant before the catalyst. The model suggests the presence of two oxidation zones within the non-catalytic ATR reactor. N-tetradecane is completely consumed in the first oxidation zone within 0.05 s and results in temperature rise of ~ 200 K. Low temperature oxidation chemistry plays a significant role to consume most of the n-tetradecane and approximately half of the oxygen. The second oxidation that is catalyzed by ·OH radicals from H_2O_2 decomposition results in complete consumption of oxygen in less than 0.35 s. The model predicts that n-tetradecane and oxygen are completely consumed before the catalyst due to gas-phase reactions suggesting steam reforming of lower hydrocarbons on the surface of the catalyst. Major ethylene was found to produce during second stage oxidation due to pyrolysis reaction pathways such as 1-alkyl and propyl β-scission, and ethyl decomposition. Propylene yield was found to be very sensitive to the H-abstraction by ·OH to form allyl radicals.

Using detailed gas-phase reactions kinetic model in the pre-catalytic zone of the autothermal reformer, the species reaching the catalyst surface were identified. A micro-kinetic model was developed for different species using hybrid approach in which the binding energy or heat of chemisorption of most of the adsorbed species was obtained from literature reported values (either from DFT study or from experimental study) and the energetic (activation energy) was obtained using semi-empirical techniques, such as unity bond index-quadratic exponential potential (UBI-QEP). Pre-exponential factors were set based on Transition State Theory (TST) rule. Alkenes above C_3 were assumed to fragment into ethylene and other alkenes and remaining species were assumed to fragment into CH_x*, C*, H* and O* species. Simulation of experimental packed bed autothermal reformer using gas-phase reaction kinetic model and surface micro-kinetic model could predict the experimental data reasonably well (within 20% of the experimental value) at different operating conditions for autothermal reforming of n-tetradecane on Rh-pyrochlore catalyst. The species flow profiles along the length of the reactor bed showed that CO generated by gas-phase reactions in pre-catalytic zone is consumed rapidly over the catalyst bed by water-gas-shift reaction to produce CO_2 and H_2. After the first millimeter of the catalyst, majority of H_2 and CO were produced by steam reforming of hydrocarbons. The study also confirmed that at high temperature slippage of 1,3-butadiene over the catalyst could lead to cyclic reactions that consume 1,3-butadiene and form ethylene in the post-catalytic zone of the reactor. This can eventually lead to coke formation.

8.2 **Summary of Major Contributions**

The original research contributions of this thesis include:

1. Developed a map of carbon formation region for diesel reforming processes at various operating conditions.

2. Proposed a simple mechanistic scheme for n-tetradecane reforming based on the literature understanding of adsorption of hydrocarbon molecules and subsequent reaction of adsorbed alkyl species on the surface of the catalyst, and derived a LHHW type of kinetic model.
3. Demonstrated a method for evaluating a catalyst stability based on redox cycling.
4. Revealed the importance of gas-phase reaction kinetics during autothermal reforming of heavy hydrocarbons based on studies done using an inert packed-bed of silica.
5. Generated predictive gas-phase reaction kinetic model using "Reaction Mechanism Generator". The model was validated against n-tetradecane ignition delay from Shen *et al.* (2009) and inert bed autothermal reforming data collected as part of this work. The model was further extended and validated to predict high pressure pyrolysis kinetics from Song *et al.* (1994).
6. Developed a detailed understanding of important reaction chemistries in the pre-catalytic zone of the diesel reformer. It was also identified that n-tetradecane and oxygen are completely consumed in the pre-cataytic zone.
7. Developed a new surface micro-kinetic model based on the species that are predicted to reach the catalyst surface by the gas-phase reaction kinetic model described above.
8. Identified ethylene formation reaction path during gas-phase reactions in the post-catalytic zone of the reactor.

8.3 **Recommendations for Future Work**

Based on the current study observations, research in the following path could be useful in gaining insight for diesel reforming process.

1. Carry out gas-phase kinetic study experiments in a blank quartz tube reactor to minimize the wall/surface or heterogeneous reaction effect on collected kinetic data.
2. Use multi-point thermocouple to measure the temperature along the length of the reactor for both, gas-phase reactions and surface reactions, kinetic study.
3. Insert the thermocouple into the reactor from outlet of the reactor to minimize the thermocouple wall effect on collected kinetic data.
4. Perform shock tube ignition delay experimental study at high equivalence ratios to validate the gas-phase kinetic model at autothermal reforming conditions.
5. Collect the batch reactor or flow reactor pyrolysis experiments at low pressure and high temperature conditions to validate the gas-phase reaction kinetic model at these conditions.
6. In the current thesis an extended kinetic model is proposed for pyrolysis experiments at high pressure and low temperature conditions. These conditions favour certain reaction paths that form higher alkanes. 'PopulateReactions' module of RMG was used to generate these reactions. Ultimate target should be a single gas-phase kinetic model that has an ability to capture combustion, pyrolysis and autothermal reforming behavior at all operating conditions. This requires pressure dependent (pdep) rates for all reactions that are affected significantly by variation in pressure. So generating the kinetic model using pdep function in RMG would be an essential tool to go forward.
7. Propylene yield in gas-phase kinetic model is found to be very sensitive to the H-abstraction by ·OH to form allyl radical. Refined rate estimates for this reaction would be very useful to predict the propylene yield.

8. Adding the reaction paths for formation of benzene and aromatics in gas-phase kinetic model could lead to understanding of coke formation due to gas-phase reactions in the reforming process.
9. For surface reaction mechanism, few surface reaction kinetic parameters were adjusted based on sensitivity analysis. It is recommended to use an optimization tool to estimate the parameters of highly sensitive reactions.
10. Detailed reaction paths with all intermediate species heat of adsorption data for higher alkenes (> C_3), dienes, ester, aldehydes reactions on the surface of the Rh catalyst is essential to deconvolute the surface reaction mechanism.

Appendix A

Supplemental Material for Generalized Kinetic Model

A.1 Derivation of LHHW model

Reaction rate is given as

$$rate = k_2 C_{C_{14}H_{29}^*} C_* \tag{A.1-1}$$

Total site balance:

$$C_*^T = C_* + C_{CH_2^*} + C_{O^*} + C_{CO^*} + C_{H^*} \tag{A.1-2}$$

where C_* is vacant site concentration

$$C_{CH_2^*} = a \frac{p_{H_2}^2 p_{CO}}{P_{H_2O}} C_* \ , \tag{A.1-3}$$

where a is lumped parameter of equilibrium constants

$$C_{O^*} = K_{H_2O} \frac{p_{H_2O}}{P_{H_2}} C_* \tag{A.1-4}$$

$$C_{H^*} = \sqrt{K_{H_2} p_{H_2}} C_* \tag{A.1-5}$$

$$C_{CO^*} = K_{CO} p_{CO} C_* \tag{A.1-6}$$

Substitute Equations (A.1-3)-(A.1-6) into Eqquation (A.1-2), the vacant site concentration can be given as

$$C_* = \frac{C_*^T}{1 + a \frac{p_{H_2}^2 p_{CO}}{P_{H_2O}} + K_{H_2O} \frac{p_{H_2O}}{P_{H_2}} + K_{CO} p_{CO} + \sqrt{K_{H_2} p_{H_2}}} = \frac{C_*^T}{DEN_1} \tag{A.1-7}$$

At steady state, very first step of alkane adsorption,

$$K_1 = \frac{C_{C_{14}H_{29}{}^*} C_{H^*}}{p_{C_{14}H_{30}} C_*^2} \tag{A.1-8}$$

Substitute Equations (A.1-5) and (A.1-8) into Equation (A.1-1)

$$rate = \frac{k_2 K_1}{\sqrt{K_{H_2}}} \frac{p_{C_{14}H_{30}}}{\sqrt{p_{H_2}}} C_*^2 = k \frac{p_{C_{14}H_{30}}}{\sqrt{p_{H_2}}} C_*^2 \tag{A.1-9}$$

Substitute Equation (A.1-7) into Equation (A.1-9)

$$rate = \frac{k \frac{p_{C_{14}H_{30}}}{\sqrt{p_{H_2}}} \left(C_*^T\right)^2}{DEN_1^2} = \frac{k' \frac{p_{C_{14}H_{30}}}{\sqrt{p_{H_2}}}}{DEN_1^2} \tag{A.1-10}$$

Similarly the equation for water-Gas-shift reaction is derived.

Appendix B

Experimental Data

B.1 Inlet experimental conditions

Exp.No. Without catalyst	Exp.No. With catalyst	WHSV [SCC/h·g]	O_2/C	Temp [°C]	$C_{14}H_{30}$ [cc/min]	H_2O [cc/min]	Air [SCCM]	N_2 [SCCM]
BW	R	100000	0.20	700	0.0821	0.1194	94.3396	50
BX	V	160000	0.20	700	0.1313	0.1911	150.9434	80
BY	T	220000	0.20	700	0.1806	0.2627	207.5472	110
BZ	BO	100000	0.35	700	0.0640	0.0931	128.6765	50
CA	O	160000	0.35	700	0.1024	0.1489	205.8824	80
CB	AB	220000	0.35	700	0.1407	0.2048	283.0882	110
CC	BQ	100000	0.50	700	0.0524	0.0763	150.6024	50
CD	BS	160000	0.50	700	0.0839	0.1220	240.9639	80
CE	BI	220000	0.50	700	0.1153	0.1678	331.3253	110
CG	Z	100000	0.20	775	0.0821	0.1194	94.3396	50
CH	F	160000	0.20	775	0.1313	0.1911	150.9434	80
CI	Y	220000	0.20	775	0.1806	0.2627	207.5472	110
CK	BR	100000	0.35	775	0.0640	0.0931	128.6765	50
CL	N	160000	0.35	775	0.1024	0.1489	205.8824	80
CM	AA	220000	0.35	775	0.1407	0.2048	283.0882	110
CN	AZ	100000	0.50	775	0.0524	0.0763	150.6024	50
CP	BD	160000	0.50	775	0.0839	0.1220	240.9639	80
CQ	BJ	220000	0.50	775	0.1153	0.1678	331.3253	110
CT	E	100000	0.20	850	0.0821	0.1194	94.3396	50
CU	G	160000	0.20	850	0.1313	0.1911	150.9434	80
CV	J	220000	0.20	850	0.1806	0.2627	207.5472	110
CW	M	100000	0.35	850	0.0640	0.0931	128.6765	50
CX	Q	160000	0.35	850	0.1024	0.1489	205.8824	80
CY	AC	220000	0.35	850	0.1407	0.2048	283.0882	110
CZ	BA	100000	0.50	850	0.0524	0.0763	150.6024	50
DA	BE	160000	0.50	850	0.0839	0.1220	240.9639	80
DB	BK	220000	0.50	850	0.1153	0.1678	331.3253	110

B-2 Experimental results for kinetic study without catalyst

Exp. No.	Mass Spectrometer Measurement H_2 [%]	CO [%]	CO_2 [%]	O_2 [%]	N_2 [%]
BW	1.75	8.46	2.79	0.00	78.91
BX	1.64	8.92	2.33	0.00	78.61
BY	1.42	8.46	2.35	0.01	79.12
BZ	1.95	7.56	4.34	0.00	80.70
CA	1.15	7.93	3.79	0.00	81.44
CB	1.01	7.39	4.04	0.01	82.16
CC	1.76	6.92	5.38	0.00	82.30
CD	0.94	7.38	4.79	0.00	83.11
CE	0.93	7.23	5.03	0.01	83.33
CG	3.76	12.25	2.13	0.00	70.15
CH	3.50	12.66	1.84	0.00	70.04
CI	3.30	12.28	1.91	0.00	70.39
CK	3.99	10.55	3.64	0.00	74.27
CL	3.18	13.32	1.87	0.00	70.39
CM	3.10	10.43	3.43	0.00	75.24
CN	9.49	10.90	4.72	0.00	70.84
CP	2.94	9.55	4.33	0.00	77.78
CQ	2.70	8.50	5.06	0.00	78.37
CT	20.07	16.96	2.25	0.00	52.24
CU	13.04	15.48	2.12	0.00	59.18
CV	11.06	14.92	2.25	0.00	61.01
CW	21.55	16.10	3.26	0.00	54.59
CX	14.58	14.81	3.03	0.00	61.23
CY	11.35	13.32	3.63	0.00	64.81
CZ	19.80	13.82	4.71	0.00	59.45
DA	11.38	12.97	3.93	0.00	67.50
DB	11.65	12.50	4.28	0.00	67.27

Exp.	**Gas Chromatograph measurement**									
No.	**CH_4 [ppm]**	**C_2H_6 [ppm]**	**C_2H_4 [ppm]**	**C_3H_8 [ppm]**	**C_3H_6 [ppm]**	**C_4H_8-1 [ppm]**	**1,3-C_4H_6 [ppm]**	**C_5H_{10}-1 [ppm]**	**C_6H_{12}-1 [ppm]**	**C_6H_6 [ppm]**
BW	17354	3877	29701	498	14370	4560	4918	900	111	372
BX	17352	3920	29732	504	14808	5539	5118	1897	536	590
BY	16086	3497	29971	544	15170	6372	5370	2496	785	712
BZ	10039	2003	22031	282	8835	2857	3262	660	765	641
CA	10002	1949	22573	281	9374	3596	3395	1224	499	646
CB	8556	1687	21983	290	9003	3620	3139	1391	462	653
CC	6379	1133	15339	171	5939	1802	2333	410	336	380
CD	6155	1069	15918	169	6231	2340	2425	662	161	555
CE	4896	857	14622	160	5645	2367	2152	895	485	551
CG	32319	4600	39929	559	20785	4103	7347	171	145	641
CH	32097	4586	40434	575	21535	4377	8010	228	223	816
CI	31074	4451	40480	630	22071	5337	8438	314	289	1019
CK	19453	2527	29618	312	11845	2259	4460	103	128	971
CL	32030	4587	37534	564	19196	3642	7313	251	267	817
CM	18135	2378	30654	337	13201	3274	4980	208	218	338
CN	10786	1265	18208	155	5455	674	1863	50	50	558
CP	13827	1557	23135	190	7693	1250	3073	88	86	576
CQ	11031	1296	23910	192	8456	1991	3349	107	133	517
CT	35949	3432	33408	213	7228	121	1932	23	15	436
CU	38637	3817	39130	275	11212	462	4067	89	49	768
CV	37719	3644	41018	309	13079	768	5283	174	86	992
CW	20843	1802	17452	104	2099	34	397	12	15	1379
CX	25288	2092	27207	147	4938	116	1409	31	15	846
CY	24324	2047	29465	183	7076	218	2332	67	40	821
CZ	12894	977	6115	48	578	9	102	3	7	1066
DA	15851	1154	20057	82	3136	89	897	19	3	98
DB	14614	1150	20796	102	3770	96	1105	27	12	263

B.3 Experimental results for kinetic study with catalyst

Exp. No.	Mass Spectrometer Measurement				
	H_2 [%]	CO [%]	CO_2 [%]	O_2 [%]	N_2 [%]
R	39.45	11.73	8.65	0.00	37.75
V	33.64	9.34	9.01	0.00	43.78
T	30.28	8.76	8.49	0.00	47.86
BO	34.26	11.45	8.56	0.00	44.51
O	31.01	9.79	9.08	0.00	48.26
AB	25.90	8.33	8.92	0.00	54.37
BQ	26.29	9.33	9.02	0.00	54.69
BS	25.96	8.86	9.29	0.00	54.95
BI	25.37	8.09	9.55	0.00	55.98
Z	43.37	16.68	6.50	0.00	31.33
F	40.90	14.52	7.34	0.00	33.79
Y	37.37	14.23	6.91	0.00	36.86
BR	35.97	13.28	7.58	0.00	42.48
N	33.69	13.05	7.57	0.00	44.19
AA	31.62	12.81	7.30	0.00	45.81
AZ	29.52	11.97	7.84	0.00	50.22
BD	29.47	10.98	8.48	0.00	50.58
BJ	28.86	10.94	8.44	0.00	51.02
E	45.62	18.29	5.44	0.00	30.15
G	44.60	19.48	4.63	0.00	30.05
J	44.57	17.73	5.69	0.00	30.54
M	35.64	14.75	6.67	0.00	42.30
Q	34.96	15.69	5.93	0.00	42.46
AC	34.27	15.57	5.94	0.00	42.90
BA	29.57	13.02	7.14	0.00	50.04
BE	29.24	12.34	7.51	0.00	50.52
BK	28.35	12.24	7.53	0.00	51.40

Exp.	Gas Chromatograph measurement									
No.	CH_4 [ppm]	C_2H_6 [ppm]	C_2H_4 [ppm]	C_3H_8 [ppm]	C_3H_6 [ppm]	C_4H_8-1 [ppm]	1,3-C_4H_6 [ppm]	C_5H_{10}-1 [ppm]	C_6H_{12}-1 [ppm]	C_6H_6 [ppm]
R	10549	1633	5965	161	2983	727	921	233	129	110
V	13469	2814	13254	293	5873	1646	1791	668	393	385
T	12148	2551	15292	292	6575	2357	2161	1096	693	637
BO	6407	820	2412	83	1120	221	277	66	27	396
O	7770	1106	4608	118	2249	602	795	231	163	301
AB	6799	1150	8158	144	3698	1278	1371	445	195	423
BQ	4027	416	1042	48	553	111	143	36	10	141
BS	4343	548	2117	67	1030	270	357	99	48	137
BI	3633	446	2610	63	1261	444	485	197	166	366
Z	11617	1505	5060	126	1724	72	345	16	6	363
F	18113	2184	7989	201	3352	344	1011	38	31	405
Y	16497	2473	17054	235	5713	572	1789	64	50	408
BR	6059	396	160	35	72	0	7	0	7	189
N	8294	842	3678	77	1356	84	322	11	7	100
AA	9653	1240	8654	131	2948	284	801	27	20	238
AZ	2623	66	0	0	0	19	9	17	423	781
BD	4310	242	93	24	41	0	6	0	0	99
BJ	4724	385	1364	43	527	47	117	5	0	131
E	4872	79	0	0	0	0	56	0	0	101
G	11186	416	484	20	93	0	12	0	0	53
J	11627	896	1589	61	272	0	26	0	0	131
M	5773	324	165	16	20	0	0	0	0	51
Q	7765	552	951	34	142	0	7	0	0	98
AC	9860	787	1898	55	290	28	0	17	5	142
BA	1890	35	0	0	0	15	12	52	10	130
BE	3656	121	14	8	0	0	35	0	0	28
BK	4283	221	121	19	20	0	0	0	39	24

Appendix C

Supplemental Material for Gas-phase Kinetic Study

C.1 Governing equations for packed bed reactor model

Real sand consists mainly of quartz with some amount of other mineral content. The thermal conductivity of this mixture is typically modeled as:

$$K_p = K_{quartz}^{\theta} K_{\min}^{1-\theta} \tag{C.1-1}$$

where Kmin is the thermal conductivity of other minerals (usually about 2 W/m-K [1]) and θ is volumetric content of quartz. For the present study it was assumed that the sand bath has negligible mineral content (θ≈1) and can be modeled with the thermal properties of pure quartz. Thermal conductivity values parallel (*K₂*) and perpendicular to the optic axis of quartz (*K₁*) were obtained from the work of Clauser and Huenges [2]. The weighted geometric mean of these values was used as the particle thermal conductivity of randomly oriented quartz crystals as shown below.

$$K_p = K_2^{1/3} K_1^{2/3} \tag{C.1-2}$$

The thermal conductivity of the bed was calculated using a series-parallel model specifically developed and validated for sand [1, 3].

$$K_{bed} = K_g\left(\varepsilon - n_{wm}\right) + \frac{\left(1-\varepsilon+n_{wm}\right)^2}{\left(\dfrac{1-\varepsilon}{K_p}+\dfrac{n_{wm}}{K_g}\right)} \tag{C.1-3}$$

where, K_g is gas-phase thermal conductivity, ε is the average porosity of the bed, n_{WM} is the fluid fraction in a series path of heat flow. For sand, n_{WM} values lie netween 0.041 to 0.043 [1] and an estimated value of 0.0415 was used for this study.

For flow through a packed bed, the effective lateral thermal conductivity ($K_{b,flow}$) was calculated as shown below [4].

$$\frac{1}{P_{E,r}} = \frac{K_{bed}/K_g}{P_{E,o}} + \frac{1}{K_r} \tag{C.1-4}$$

where $P_{E,r}$ is the effective radial Peclet number defined as $P_{E,r} = \frac{u_x^s C_{P,g} \rho_g d_p}{K_{b,flow}}$ and $P_{E,o}$ is the molecular Peclet number defined as $P_{E,o} = \frac{u_x^s C_{P,g} \rho_g d_p}{K_g}$. Values of K_r were estimated using the following expression [4]:

$$K_r = 6.96\left(2 - \left(1 - \frac{2}{d_t/d_p}\right)^2\right) \tag{C.1-5}$$

where d_t is tube (reactor) diameter and d_p is particle diameter. The modified Navier-Stokes equations shown below were used to solve for the momentum transfer inside the packed bed [5].

$$\rho_g \frac{\partial u_x^l}{\partial t} + \rho_g u_x^l \frac{\partial u_x^l}{\partial x} = \rho g - \frac{\partial p}{\partial x} - \frac{\mu u_x^l \varepsilon}{K} - \frac{\mu \left(u_x^l\right)^2 \varepsilon^2}{K_z} + \mu_{eff} \frac{\partial^2 u_x^l}{\partial x^2} \tag{C.1-6}$$

$$K = \frac{d_p^2 \varepsilon^3}{150(1-\varepsilon)^2} \qquad K_z = \frac{d_p \varepsilon^3}{1.75(1-\varepsilon)}$$

The following boundary conditions were used: No slip at wall, fully developed laminar flow at the inlet, symmetry about the center line of the reactor, output pressure of 2.36 atm. At steady state (first term), no applied body forces (third term), no viscous dissipation (seventh term), and no variation in axial velocity with position (second term), the above equation turns into the Ergun equation. The values 150 and 1.75 are the constants of the Ergun equation. Application of an effective turbulent viscosity for calculating the flow distribution in a porous system, as reported in the literature [6], was employed in the present study. Effective turbulent viscosity increases with velocity and can be correlated with particle Reynolds number for spheres as shown below [6].

$$\frac{\mu_{eff}}{\mu} = 1 + \left(7\times10^{-6}\frac{d_t}{d_p} + 2\times10^{-5}\right)\left(\frac{d_p u_x^s \rho_g}{\mu}\right)^2 \tag{C.1-7}$$

Recently, Castillo-Araiza and Lopez-Isunza [7] were able to reproduce experimental observations with model predictions by fitting the Ergun constants and using the molecular viscosity as effective viscosity. However, their method was not pursued in the present study.

The equations proposed by Muller [8, 9] were used to calculate the radial porosity distribution inside the reactor as well as between the thermocouple and reactor wall. It should be noted that the resulting porosity distribution is symmetric between wall and thermocouple. However, recently Theuerkauf *et al.* [10] have shown, using discrete element modeling, that the porosity distribution is not symmetric due to differences in the curvature of the thermocouple compared to the reactor wall. Unfortunately, there is no model available for capturing these effects. Hence for the present study, the approximate symmetric model proposed by Muller was employed.

Heat transfer in the packed bed was modeled using the pseudo-homogeneous heat transfer equation shown below:

$$\left(\varepsilon\rho_g C_{P,g} + (1-\varepsilon)\rho_p C_{P,p}\right)\frac{\partial T}{\partial t} + \rho_g C_{P,g} u_x^s \frac{\partial T}{\partial x} = k_{eff}\left(\frac{\partial^2 T}{\partial r^2} + \frac{1}{r}\frac{\partial T}{\partial r} + \frac{\partial^2 T}{\partial x^2}\right) + \left(\sum_{j=1}^{M}(-\Delta H_r)_j r_j\right)\varepsilon \tag{C.1-8}$$

The furnace wall temperature, inlet temperature, heat flux continuity across different sections, and outflow boundary conditions were used to model the heat transfer. Radiation between the furnace and reactor walls was modeled using the surface to surface radiation module described in reference [11, 12]. Conductive heat transfer from furnace wall to the reactor wall was also included. Heat loss from the reactor wall to the hot box (maintained at 648 K) was assumed to occur primarily by convection and radiation. Since the convective heat transfer coefficient is a function of wall temperature, an average value of 5 W/m^2·K was used [13]. For radiative heat transfer calculations, Incoloy emissivity was assumed to be 0.2 [14] whereas furnace wall emissivity was taken as 0.9 [data obtained from manufacturer specifications].

Simplification of packed bed reactor model

The simultaneous solution of the full model including the detailed chemistry model coupled with mass, momentum and heat transfer within the packed-bed reactor was not possible with available computational resources. To simplify the problem, plug flow and constant pressure were assumed. The validity of these approximations (*i.e.*, radially uniform velocity and temperature profile, absence of back mixing and channeling) the following criteria recommended by Froment, Bischoff [15], and Rase [16] were used:

(1) ratio of catalyst bed height to catalyst particle size $(L/d_p) > 50$

(2) ratio of catalyst bed diameter to the catalyst particle size $(d/d_p) > 10$

For the current study, values of L/d_p and d/d_p were calculated to be 508 and 14.4 respectively justifying the plug-flow approximation. The maximum pressure drop inside the reactor was found to be less than 5%. The simplifying assumptions were therefore, deemed to be acceptable.

C.2 Proof of concept for iterative approach

Unfortunately standard computational fluid dynamic (CFD) tools, such as COMSOL and Fluent, have limitations in handling large chemistries and it is not possible to model complex heat transfer system in Chemkin. So to solve large chemistry in complex system with multiple modes of heat transfer, an iterative approach is used. To prove the logic, a proof of concept study is made in which a small and simple chemistry system is selected that could be easily modeled in any available CFD software package and compared to the iterative approach solutions. In present study, COMSOL^{TM} is used for direct modeling and iterative approach. Since the geometry is simple it could be directly modeled using Plug Flow Reactor tool of Chemkin-Pro.

Small and simple hydrogen oxidation kinetic model with 20 reactions and 9 species given in Chemkin tutorial is chosen and a packed bed reactor geometry as shown in Figure C.2-1 is selected.

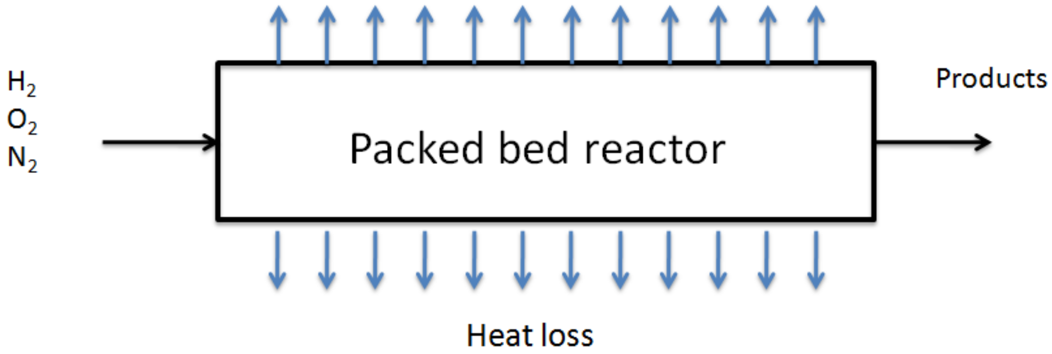

Figure C.2-1: Packed bed reactor for proof of concept study

Reactor dimensions and operating conditions are given below:

Diameter = 0.001 m; Length = 0.1 m; Porosity = 0.4

Inlet temperature = 1000 K; Inlet velocity = 100 m/s; Inlet H_2 mole fraction = 0.2958; Inlet O_2 mole fraction = 0.1479; Inlet N_2 mole fraction = 0.5562; heat loss = 5E+07 W/m^3.

The following governing equations were used to solve heat and mass transport in a packed bed with inert packing.

Continuity equation:

$$\rho_g \frac{\partial u_x^s}{\partial x} + u_x^s \frac{\partial \rho_g}{\partial x} = 0 \tag{C.2-1}$$

Species transfer equation:

$$\rho_g u_x^s \frac{\partial Y_i}{\partial x} = \left(\sum_{j=1}^{j=m} \upsilon_{i,j} r_j \right) M_i \varepsilon \qquad i = 1 \text{ to } n \tag{C.2-2}$$

Heat transfer equation:

$$\rho_g \overline{C}_p u_x^s \frac{\partial T}{\partial x} = \left(\sum_{j=1}^{j=m} \left(-\Delta H_r\right)_j r_j \right) \varepsilon + \dot{Q} \tag{C.2-3}$$

For iterative approach, a random guess of the initial temperature profile was made. After 21 iterations, the temperature difference between successive iterations was found to be less than 3 °C, as shown in Figure C.3-2(a), suggesting that the solution has converged. The converged temperature profile was compared to that obtained from direct solution of Chemkin-Pro and COMSOL simulations. As shown in (Figure C.2-2(b), the iterative approach converges to the exact solution. This simple study shows that the iterative approach can be used to predict the temperature profile inside reactors with complicated heat transfer mechanisms and large detailed kinetic models.

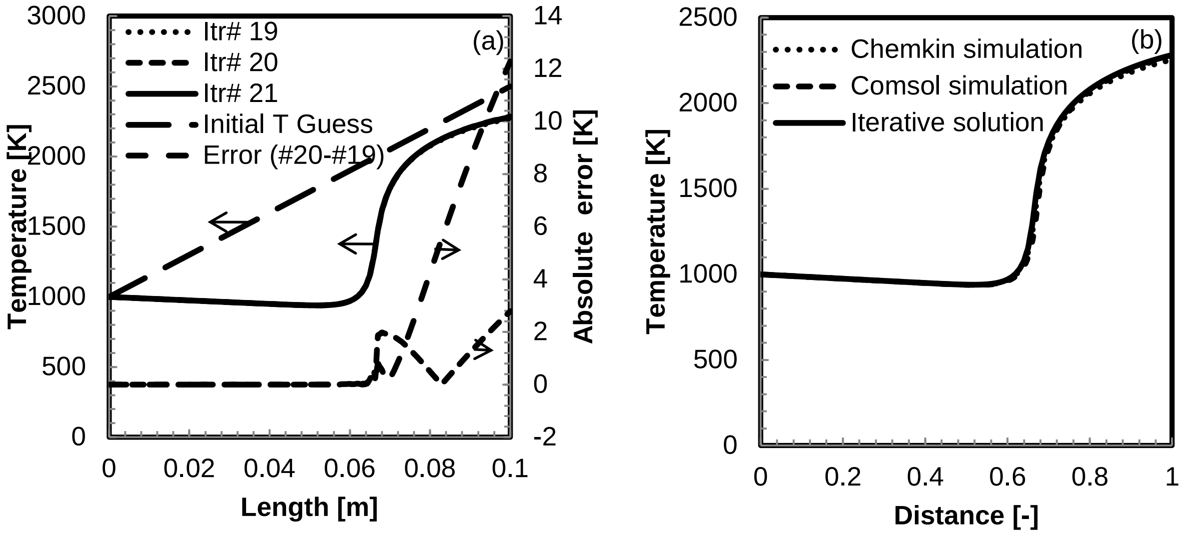

Figure C.2-2: (a) Temperature profile and absolute difference in temperature profile after each iteration; (b) comparison of temperature profile using iterative method against standard COMSOL and Chemkin-Pro models.

C.3 Rate parameters updated with measured or calculated rates in literatures

Reaction	A	n	E	Comments
$HO_2+CH_3 \leftrightarrows O_2+CH_4$	4.400e+12	0	0	[17]
$HO_2+CH_3 \leftrightarrows OH+CH_3O$	6.800e+12	0	0	[17]
$C_4H_6\text{-}1+OH \leftrightarrows C_4H_7\text{-}2+H_2O$	1.335e+01	3.41	-3.61	[18] rates are divided by factor 2
 + $HO_2 \leftrightarrows H_2O_2$ + 	1.490e+05	1.67	6.81	[19]
$OH+C_2H_4 \leftrightarrows C_2H_3+H_2O$	2.230e+04	2.75	2.21	[20]
$O+C_2H_4 \leftrightarrows CH_3+HCO$	4.740e+06	1.88	0.18	[21]
$OH+CH_4 \leftrightarrows CH_3+H_2O$	2.050e+06	2.18	2.68	[21] multiplied by factor 1.5. reported uncertainty 1.58
$H+CH_2O \leftrightarrows HCO+H_2$	1.980e+15	0.00	9.70	[22] multiplied by factor 3.
$H+O_2+H_2O \leftrightarrows HO_2+H_2O$	3.700e+19	-1.00	0.00	[23]
$HO_2+HO_2 \leftrightarrows O_2+H_2O_2$	1.940e+11	0.00	-1.41	[24] (duplicate)
$HO_2+HO_2 \leftrightarrows O_2+H_2O_2$	1.030e+14	0.00	11.03	[25] (duplicate)
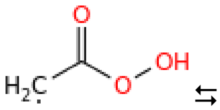 $\leftrightarrows$ 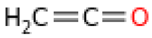 $+HO_2$	5.300e+16	-1.00	29.50	[26]
$C_2H_4+CH_3 \leftrightarrows C_3H_7\text{-}1$	0.880e+04	2.48	6.13	[27] divided by factor 2
$CH_3+CH_3 \leftrightarrows C_2H_6$	9.450e+14	-0.54	0.14	[28]
 $+CH_3 \leftrightarrows C_5H_9$	9.710e+02	3.27	2.35	CBS-QB3/1dHR(6-31G(d)/AsymmEck)
 $+C_2H_5 \leftrightarrows C_6H_{11}$	9.710e+02	3.27	2.35	Similar to C_4H_6 + CH_3 ↔ C_5H_9

Reaction	A	n	E	Comments
 +H ⇆ C_4H_7	9.710e+02	3.27	2.35	Similar to C_4H_6 + CH_3 ↔ C_5H_9
$OH+CH_2O$⇆$HCO+H_2O$	1.430e+09	1.18	-0.45	[29]
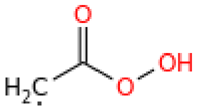 ⇆ 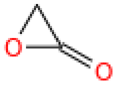 +OH	1.900e+17	-1.10	27.20	[26]
 ⇆ $CH_2O+C_2H_3$	2.700e+14	0	23.89	[30]
$C_3H_7+O_2$⇆ 	2.260e+12	0.00	0.00	[31]
C_3H_8+OH⇆$C_3H_7+H_2O$	1.400e+03	2.66	0.53	[32]
C_3H_6+OH⇆allyl+H_2O	3.100e+06	2.00	-0.30	[33]
$C_2H_6+O_2$⇆$C_2H_5+HO_2$	7.300e+05	2.50	49.16	[34]
$C_3H_8+HO_2$⇆$C_3H_7+HO_2$	4.000e+13	0.00	47.50	[35]
 ⇆  +OH	1.594e+20	-1.50	42.86	[30]
Allyl+HO_2⇆$C_3H_6+O_2$	5.260e+02	2.80	-2.14	[30]
Allyl+HO_2⇆ 	3.350e+10	0.60	-2.15	[30]
C_4H_6-1+H⇆C_4H_7-2+H_2	9.630e+01	3.60	2.07	[18]
C_4H_6-1+OH⇆C_4H_7-1+H_2O	1.730e+02	2.95	-1.06	[18]
C_4H_6-1+CH_3⇆C_4H_7-2+CH_4	3.330e+00	3.63	6.95	[18]
C_3H_6+OH⇆C_3H_6OH	8.730e+12	-0.18	-0.91	[36]
C_3H_6+H⇆allyl+H_2	6.457e+12	0.00	4.44	[35]

Rates for the ROO·⇆·QOOH⇆·OOQOOH⇆·OH +O=QOOH⇆2·OH +O=QO· sequence for all tetradecyl isomers were obtained from the RMG database and correspond to the calculations of Sharma *et al.* [37]. Rates for the $C_4H_6 \leftrightarrows CH_3+C_5H_9$ were computed at the CBS-QB3 level of theory using the CanTherm computer code. The 1d-hindered rotor approximation was used to account for torsional anharmonicity with torsional potentials obtained from relaxed scans at the B3LYP/6-31G(d) level of theory for the reactants and transition state. The computed rates were in good agreement with the recommendation of Tsang [38].

C.4 Packed bed reactor model results

To validate the reactor model, the hot box was kept open (*i.e.*, at room temperature) and the furnace wall temperature was maintained at 648.15 K. 400 SCCM N_2 was introduced and the axial temperature profile was measured by moving the thermocouple along the centerline of the reactor. This procedure was performed at furnace temperatures of 923.15 K, 1023.15 K and

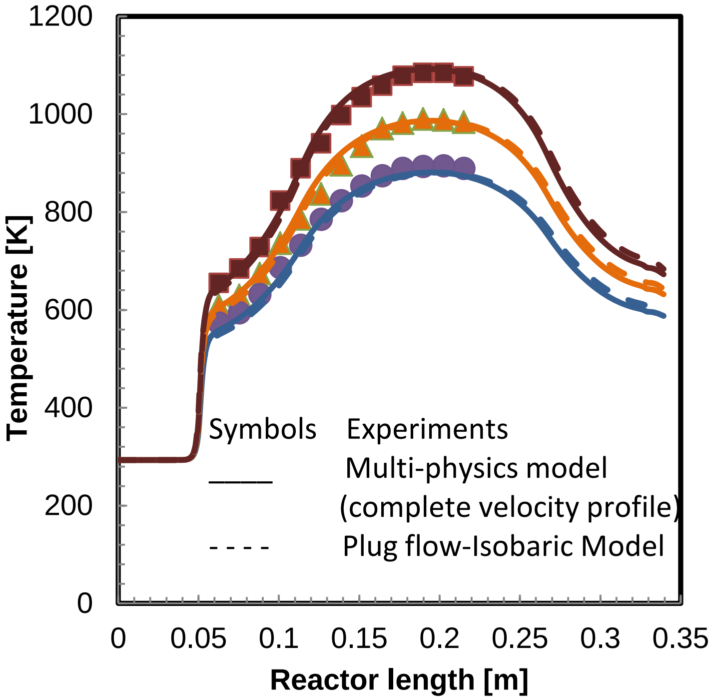

Figure C.4-1: Comparison of experimental and modeled temperature profile inside the reactor at three different furnace temperatures; ●, T_furnace = 923 K; ▲, T_furnace = 1023 K; ■, T_furnace = 1123 K

1123.15 K. The simulated and measured temperature profiles, as shown in Figure C.4-1, are in good agreement with each other. Even at the highest flow velocity at 660 SCCM, which is used in experiments, the maximum pressure drop modeled (Figure C.4-2) is about 3.5%. So the isobaric reactor assumption is justified. The radial porosity distribution inside the packed bed reactor for zones with and without the thermocouple is shown in Figure C.4-3. The average porosity of different zones was calculated using Equation (C.4-1) shown below.

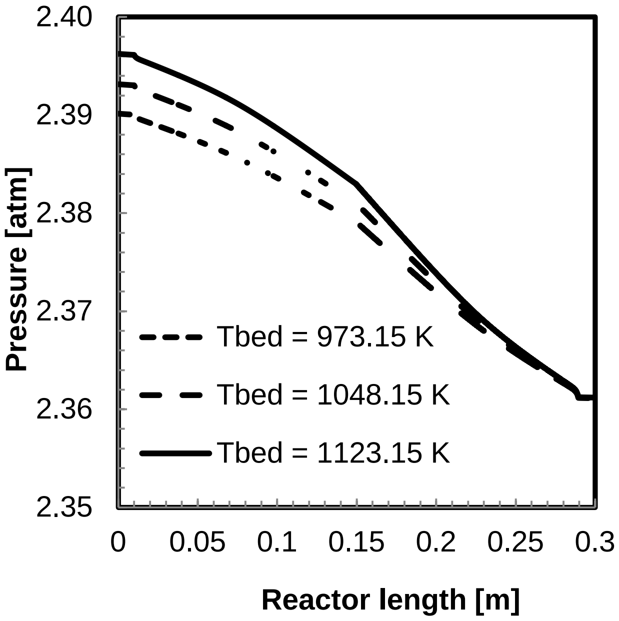

Figure C.4-2: Pressure drop inside the reactor at 660 SCCM N_2, and different T_{bed}

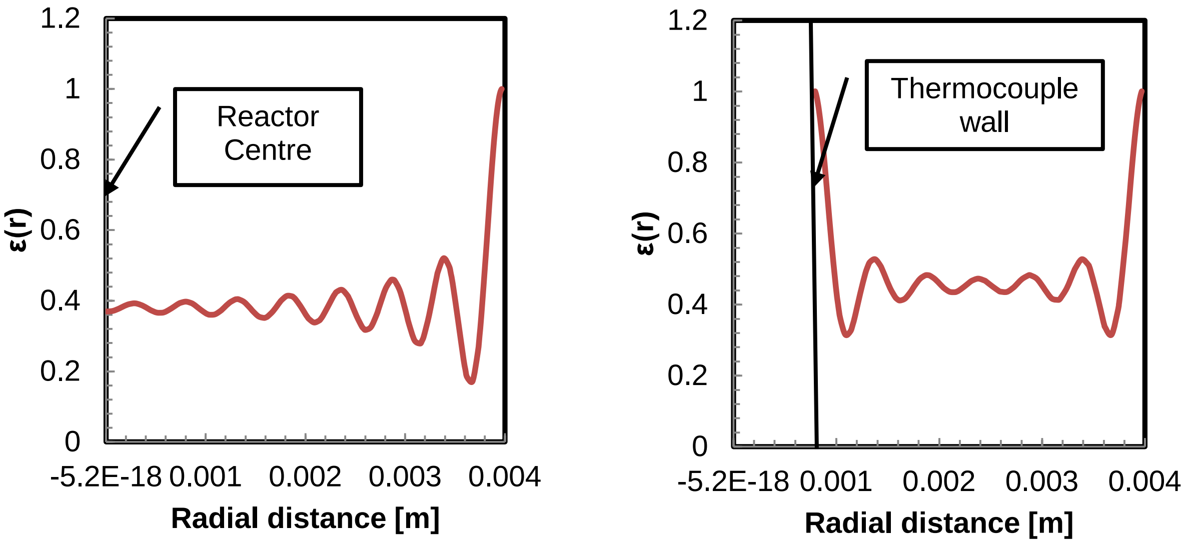

Figure C.4-3: Radial porosity (ε) distribution for (a) lower half part of the reactor without thermocouple and (b) upper part of the reactor with thermocouple

$$\varepsilon_{avg} = \int_0^R \frac{\varepsilon(r)\times 2\times\pi\times r}{Area}\,dr \qquad \text{(B.4-1)}$$

The calculated average porosity for reactor zone without thermocouple is 0.406 and reactor zone with thermocouple is 0.483. By applying plug flow isobaric reactor assumption, the temperature profile inside the reactor is calculated. The simplified model predicted temperature profile is shown as dotted line in Figure C.4-1. Plug flow isobaric reactor assumption does not result in any major change in modeled temperature profile as against solving modified Navier-Stokes equation. However, this assumption drastically reduces the computation time in iterative procedure to calculate the actual reactor temperature profile.

C.5 Sensitivity analysis plots for combustion of n-tetradecane

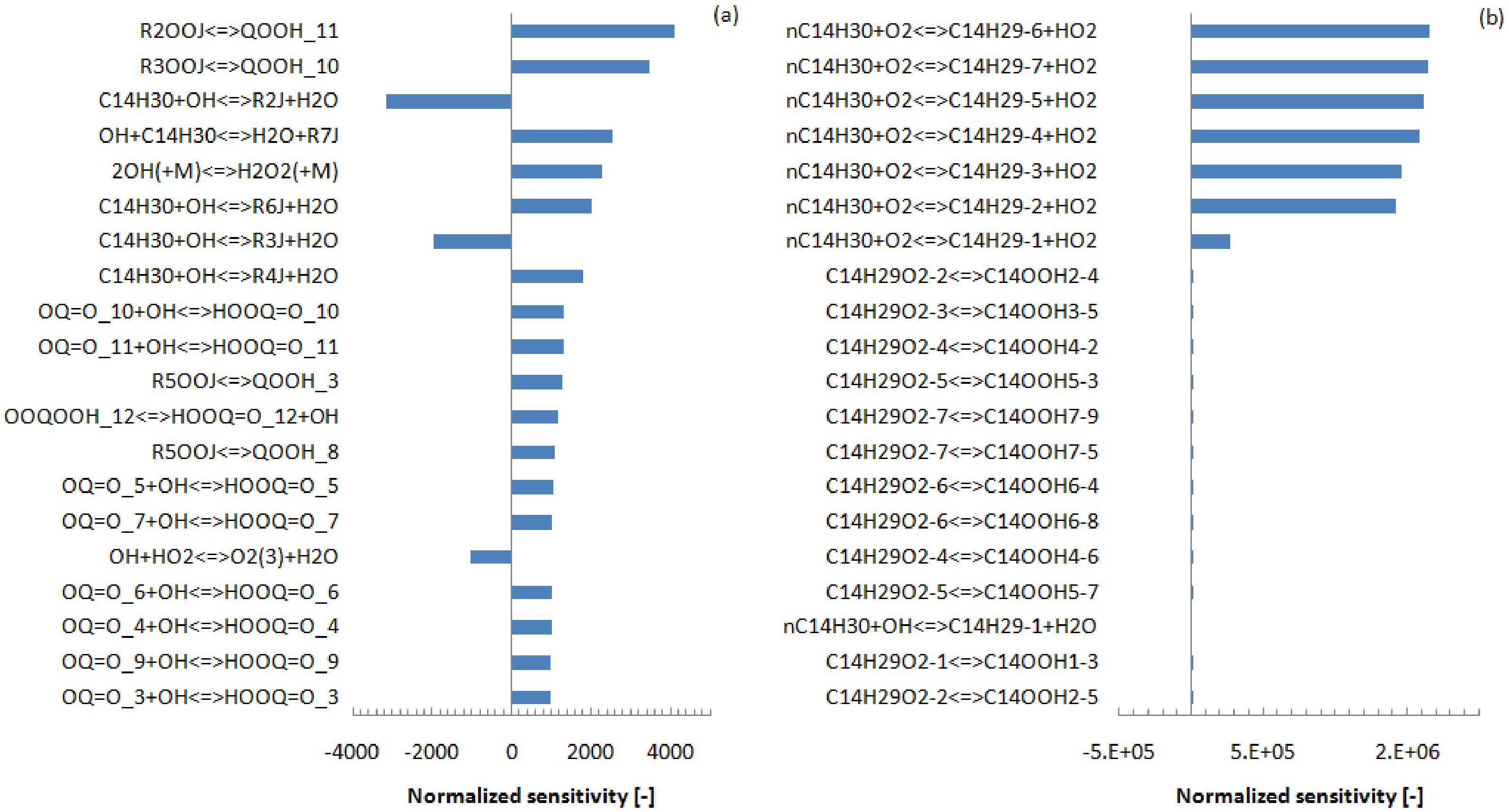

Figure C.5-1: Top 20 normalized sensitivity for OH species at 700K and at ignition time delay; (a) our model and (b) LLNL model

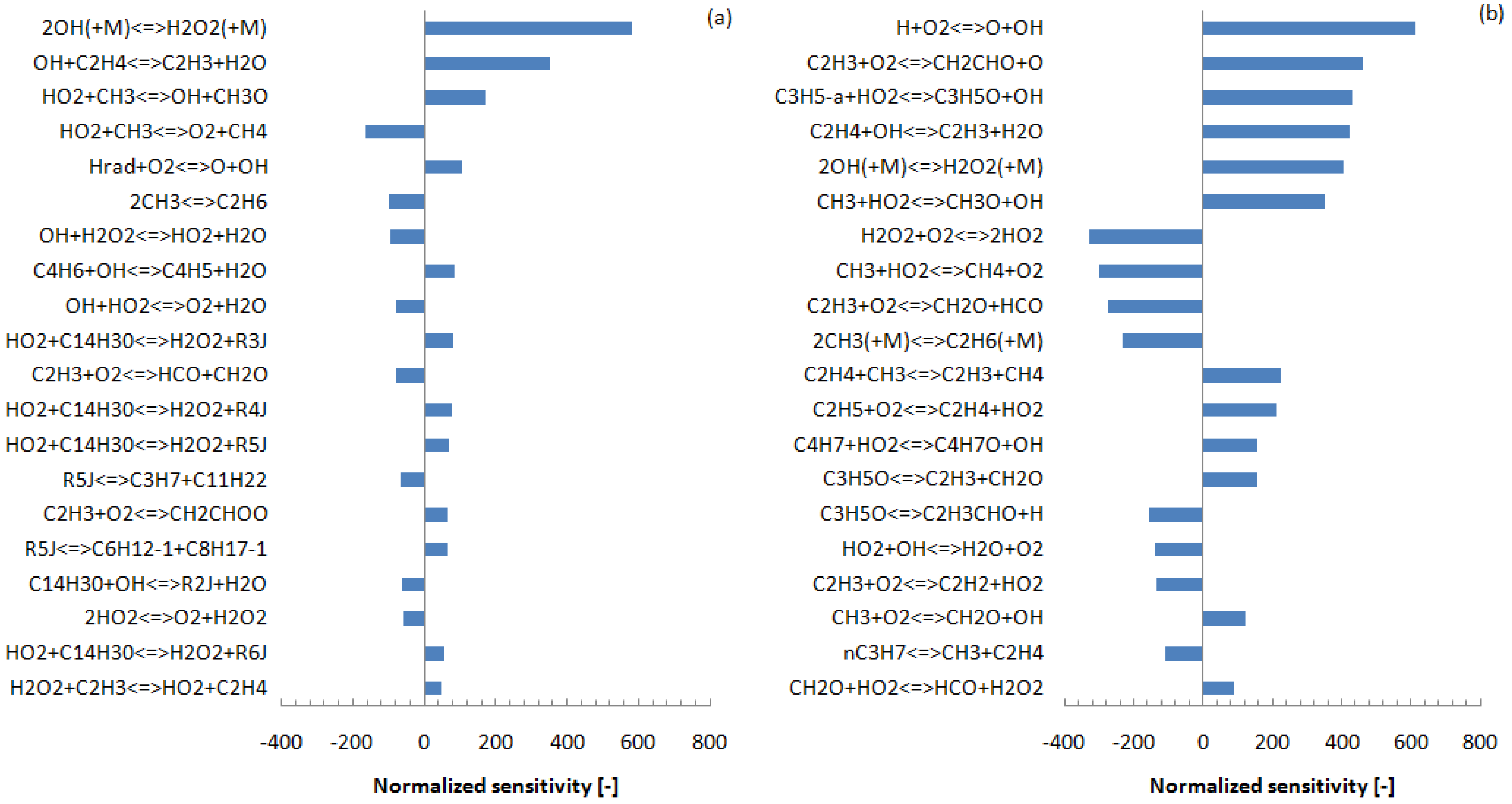

Figure C.5-2: Top 20 normalized sensitivity for OH species at 1200K and at ignition time delay; (a) our model and (b) LLNL model

References

[1] V.R. Tarnawski, T. Momose, W. Leong, G. Bovesecchi, P. Coppa, Thermal Conductivity of Standard Sands. Part I. Dry-State Conditions, International Journal of Thermophysics, 30 (2009) 949-968.

[2] C. Clauser, E. Huenges, Thermal conductivity of rocks and minerals, Rock physics and phase relations, A Handbook of Physical Constants, 3 (1995) 105-126.

[3] W. Woodside, J. Messmer, Thermal conductivity of porous media. I. Unconsolidated sands, Journal of Applied Physics, 32 (1961) 1688-1699.

[4] E. Tsotsas, E.U. Schlünder, Heat transfer in packed beds with fluid flow: remarks on the meaning and the calculation of a heat transfer coefficient at the wall, Chemical Engineering Science, 45 (1990) 819-837.

[5] M. Le Bars, M. Worster, Interfacial conditions between a pure fluid and a porous medium: implications for binary alloy solidification, Journal of Fluid Mechanics, 550 (2006) 149-173.

[6] O. Bey, G. Eigenberger, Fluid flow through catalyst filled tubes, Chemical Engineering Science, 52 (1997) 1365-1376.

[7] C.O. Castillo-Araiza, F. Lopez-Isunza, Hydrodynamic models for packed beds with low tube-to-particle diameter ratio, International Journal of Chemical Reactor Engineering, 6 (2008) 1-14.

[8] G.E. Mueller, Radial void fraction distributions in randomly packed fixed beds of uniformly sized spheres in cylindrical containers, Powder Technology, 72 (1992) 269-275.

[9] G.E. Mueller, Radial void fraction correlation for annular packed beds, AIChE Journal, 45 (1999) 2458-2460.

[10] J. Theuerkauf, P. Witt, D. Schwesig, Analysis of particle porosity distribution in fixed beds using the discrete element method, Powder Technology, 165 (2006) 92-99.

[11] H.H. Saber, W. Maref, M.C. Swinton, C. St-Onge, Thermal analysis of above-grade wall assembly with low emissivity materials and furred airspace, Building and Environment, 46 (2011) 1403-1414.

[12] COMSOL, in, Chemical Reaction Engineering User's Guide 4.2a, 2011.

[13] C. Geankoplis, Transport Processes and Separation Process Principles (Includes Unit Operations), Prentice Hall Press, New Jersey, 2003.

[14] C.H. Cho, Effect of Degree of Fluidization on Wall-to-Bed High Temperature Heat Transfer With A Single, Vertical Heater. Ph.D. Thesis, Texas Tech University, 1984.

[15] G.F. Froment, K.B. Bischoff, J. De Wilde, Chemical Reactor Analysis and Design, Wiley, New York, 1990.

[16] H.F. Rase, J.R. Holmes, Chemical Reactor Design for Process Plants, John Wiley & Sons, New York, 1977.

[17] Z. Hong, D.F. Davidson, K.Y. Lam, R.K. Hanson, A shock tube study of the rate constants for the reaction of HO_2 and CH_3, Combustion and Flame, Submitted (2012).

[18] H. Sun, C.K. Law, X. Zheng, Ignition of the butene isomers: an experimental and kinetic study. In *6th U.S. National Combustion Meeting*, University of Michigen, Ann Arbor, MI, 2009; 1-10

[19] G. da Silva, J.W. Bozzelli, Role of the [alpha]-hydroxyethylperoxy radical in the reactions of acetaldehyde and vinyl alcohol with HO_2, Chemical Physics Letters, 483 (2009) 25-29.

[20] S.S. Vasu, Measurements of Ignition Times, OH Time-histories, and Reaction Rates in Jet Fuel and Surrogate Oxidation Systems. Ph.D. Thesis, Stanford University, 2010.

[21] D. Baulch, C. Bowman, C. Cobos, R. Cox, T. Just, J. Kerr, M. Pilling, D. Stocker, J. Troe, W. Tsang, Evaluated kinetic data for combustion modeling: Supplement II, Journal of physical and chemical reference data, 34 (2005) 757-1398.

[22] G. Friedrichs, D.F. Davidson, R.K. Hanson, Direct measurements of the reaction $H + CH_2O \rightarrow H_2 + HCO$ behind shock waves by means of Vis–UV detection of formaldehyde, International Journal of Chemical Kinetics, 34 (2002) 374-386.

[23] D. Davidson, R. Hanson, Fundamental kinetics database utilizing shock tube measurements, Mechanical Engineering Department, Stanford University, Stanford CA, (2005).

[24] H. Hippler, J. Troe, J. Willner, Shock wave study of the reaction $HO_2 + HO_2 \rightarrow H_2O_2 + O_2$: Confirmation of a rate constant minimum near 700 K, The Journal of Chemical Physics, 93 (1990) 1755.

[25] C. Kappel, K. Luther, J. Troe, Shock wave study of the unimolecular dissociation of H_2O_2 in its falloff range and of its secondary reactions, Physical Chemistry Chemical Physics, 4 (2002) 4392-4398.

[26] J.W. Allen, C.F. Goldsmith, W.H. Green, Automatic estimation of pressure-dependent rate coefficients, Physical Chemistry Chemical Physics, 14 (2012) 1131-1155.

[27] H. Curran, Rate constant estimation for C_1 to C_4 alkyl and alkoxyl radical decomposition, International Journal of Chemical Kinetics, 38 (2006) 250-275.

[28] S.J. Klippenstein, Y. Georgievskii, L.B. Harding, Predictive theory for the combination kinetics of two alkyl radicals, Physical Chemistry Chemical Physics, 8 (2006) 1133-1147.

[29] M.R. Harper, K.M. Van Geem, S.P. Pyl, G.B. Marin, W.H. Green, Comprehensive reaction mechanism for n-butanol pyrolysis and combustion, Combustion and Flame, 158 (2011) 16-41.

[30] C.F. Goldsmith, S.J. Klippenstein, W.H. Green, Theoretical rate coefficients for allyl+ HO2 and allyloxy decomposition, Proceedings of the Combustion Institute, 33 (2011) 273-282.

[31] C.F. Goldsmith, W.H. Green, S.J. Klippenstein, On the Role of O_2+ QOOH in Low-Temperature Ignition of Propane: I. Temperature and Pressure Dependent Rate Coefficients, The Journal of Physical Chemistry A, (2012).

[32] W. Tsang, Chemical kinetic data base for combustion chemistry. Part 3: Propane, Journal of physical and chemical reference data, 17 (1988) 887.

[33] W. Tsang, Chemical Kinetic Data Base for Combustion Chemistry Part V. Propene, Journal of Physical and Chemical Reference Data, 20 (1991) 221.

[34] S. Dooley, M. Burke, M. Chaos, Y. Stein, F. Dryer, V. Zhukov, O. Finch, J. Simmie, H. Curran, Methyl formate oxidation: Speciation data, laminar burning velocities, ignition delay times, and a validated chemical kinetic model, International Journal of Chemical Kinetics, 42 (2010) 527-549.

[35] P. Dagaut, M. Cathonnet, J.C. Boettner, Kinetic modeling of propane oxidation and pyrolysis, International Journal of chemical kinetics, 24 (1992) 813-837.

[36] C. Kappler, J. Zádor, O. Welz, R.X. Fernandez, M. Olzmann, C.A. Taatjes, Competing Channels in the Propene+ OH Reaction: Experiment and Validated Modeling over a Broad Temperature and Pressure Range, Zeitschrift für Physikalische Chemie, 225 (2011) 1271-1291.

[37] S. Sharma, S. Raman, W.H. Green, Intramolecular hydrogen migration in Alkylperoxy and Hydroperoxyalkylperoxy radicals: Accurate treatment of hindered rotors, The Journal of Physical Chemistry A, 114 (2010) 5689-5701.

[38] W. Tsang, Mechanism and rate constants for the decomposition of 1-pentenyl radicals, The Journal of Physical Chemistry A, 110 (2006) 8501-8509.